X-ray Population Study of the Draco Dwarf Spheroidal Galaxy

Dissertation
der Mathematisch-Naturwissenschaftlichen Fakultät
Eberhard Karls Universität Tübingen
zur Erlangung des Grades eines
Doktors der Naturwissenschaften
(Dr. rer. nat.)

vorgelegt von

Sara Saeedi
aus Shiraz, Iran

Tübingen
2016

Tag der mündlichen Qualifikation: 29.1.2016

Dekan: Prof. Dr. Wolfgang Rosenstiel

1. Berichterstatter: Dr. Manami Sasaki

2. Berichterstatter: Prof. Dr. Andrea Santangelo

Abstract

This thesis presents the analysis of five *XMM-Newton* observations of the Draco dwarf spheroidal galaxy (dSph) in X-rays. We performed source detection separately for each image in each observation and for the total band mosaic image and produced a catalogue of 70 X-ray sources. The sources were classified through cross-correlation with catalogues of other wavelengths, spectral analysis, hardness ratio diagrams, and variability studies. We classified 18 sources as active galactic nuclei (AGNs) and 9 sources as galaxies and galaxy candidates. Six sources were classified as foreground stars and one source as a foreground contact binary system in the Milky Way. Four sources were classified as Low-mass X-ray binary (LMXB) candidates. One of them shows a significant pulsation, while the others were classified based on the X-ray-to-optical flux ratio and their position in the colour-magnitude diagram. We also found a symbiotic star, a candidate for a cataclysmic variable, and a binary system in the Draco dSph. Based on hardness ratios we classified 9 hard sources, which can be AGNs or LMXBs, in the field of the Draco dSph.

In the next step, the X-ray luminosity functions (XLFs) of the X-ray sources in the energy ranges of $2.0-10$ keV and $0.5-2$ keV were derived. The XLFs indicate that X-ray sources in the field of the Draco dSph are strongly contaminated by AGNs. The 0.2−5 keV XLF shows an excess of about ten sources in the flux ranges of $\sim 1.7\times10^{-15}-4.5\times10^{-15}$ erg s $^{-1}$ cm $^{-2}$, which are most likely objects in Draco dSph.

The studies of XLFs were continued by deriving the XLFs of five other dwarf galaxies, Phoenix, Fornax, Leo I, UMi, and UMa II, based on the observations of *XMM-Newton* in the energy range of $0.5-2$ keV. We studied the star formation history of each galaxy using literature, and showed that there is a correlation between the population of X-ray binaries and the recent star formation history of dwarf galaxies. The normalised XLF of Phoenix and Leo I dSphs represent the XLF of dwarf galaxies before completely leaving the star forming ages. The XLF shows that dwarf galaxies in this stage contain a population of LMXBs with luminosities of $\sim10^{34}-10^{35}$ erg s^{-1}. The XLFs of old dSph (Draco, UMi, and UMa II) show that their X-ray sources have very low luminosity ranges of $\sim10^{32}-10^{34}$ erg s^{-1}. Therefore, it seems that they are dominated by white-dwarf binaries and/or faint transient LMXBs. In the case of the Fornax dSph, we found an unexpected luminosity range for its X-ray sources, inconsistent with the recent star formation history of the galaxy. We suggested a possible correlation between the nature of the X-ray sources of Fornax and the structure of the galaxy (its dark matter halo). However, more studies of the nature of X-ray sources in this galaxy are necessary.

In the last part of the studies, we estimated dark matter halo mass that is required to keep the LMXBs of the Draco dSph, on the basis of the escape velocity of the LMXBs. We considered dark matter halo masses, suggested by different models, and showed that this galaxy could retain its LMXBs with speeds of $\lesssim$70 km s^{-1}, assuming a dark halo mass of $\gtrsim 10^9\ M_\odot$.

Zusammenfassung

In dieser Arbeit wird die Analyse von fünf XMM-Newton Röntgenbeobachtungen der spheriodalen Zwerggalaxie (dSph) Draco präsentiert. Wir haben für jede Beobachtung einzeln und im Mosaik-Bild nach Quellen gesucht und einen Katalog von 70 Röntgenquellen erstellt. Die Quellen wurden anhand von Kreuzkorrellationen mit Katalogen anderer Wellenlängen, Spektralanalysen, Härtegraddiagrammen und Variabilitätsuntersuchungen klassifiziert. Dabei konnten wir 18 Quellen als Aktive Galaxien Kerne (AGN) und neun Quellen als Galaxien und Galaxie-Kandidaten klassifizieren. Sechs weitere Quellen wurden als Vordergrundsterne und eine als Quelle Kontakt-Doppelsternsystem im Vordergrund in der Milchstraße klassifiziert. Von ihnen zeigt eine signifikante Pulsationen, während die anderen aufgrund des Röntgen-zu-optischen Fluss Verhältnisses und ihrer Position im Farben-Helligkeits-Diagramm klassifiziert wurden. Außerdem haben wir auch einen symbiotischen Stern, einen Kandidaten für einen kataklysmischen Variablen und ein Doppelsternsystem in Draco dSph gefunden. Basierend auf Härtegradverhältnissen haben wir neun harte Quellen im Feld von Draco dSph klassifiziert, die AGNs oder Röntgendoppelsterne mit massearmen Begleitern (low-mass X-ray Binaries, LMXBs) sein könnten.
Im mächtsen Schritt wurden die Röntgen-Leuchtkraft-Funktionen (XLFs) dieser Röntgenquellen in den Energiebereichen $2.0-10$ keV und $0.5-2$ keV erstellt. Die XLFs deuten darauf hin, dass Röntgenquellen im Feld von Draco dSph stark mit AGNs kontaminiert sind. Die $0.2-10$ keV XLF zeigt einen Überschuss von etwa zehn Quellen im Flussbereich von $\sim 1.7\times10^{-15}-4.5\times10^{-15}$ erg s^{-1} cm^{-2} welche höchstwahrscheinlich Objekte in Draco dSph sind.
Basierend auf den XMM-Newton Daten im Energiebereich von $0.5-2$ keV wurden zusätzlich XLFs von fünf anderen Zwerggalaxien, Phoenix, Fornax, Leo I, UMi und UMa II erstellt. Wir haben die Sternentstehungsgeschichte jeder Galaxie mithilfe von Literatur untersucht und konnten zeigen, dass es einen Zusammenhang zwischen der Population mit Röntgendoppelsternen und der jüngeren Sternentstehungsgeschichte von Zwerggalaxien gibt. Die normalisierte XLFs von Phoenix und Leo I dSph repräsentierten die XLF von Zwergalaxien während der Sternentstehungsperiode. Die XLFs zeigten, dass Zwerggalaxien in diesem Stadium eine Population von LMXBs mit Leuchtkräften von $\sim10^{34}-10^{35}$erg s^{-1} beinhalten. Die XLFs von alten dSph (Draco, UMi und UMa II) zeigen, dass ihre Röntgenquellen einen sehr niedrigen Leuchtkraftbereich von $\sim10^{32}-10^{34}$erg s^{-1} haben. Höchstwahrscheinlich sind sie dominiert von Doppelsternsystemen mit weißen Zwergen und/oder leuchtschwachen Kurzlebigen LMXBs. Im Fall von Fornax dSph haben wir einen auffälligen Leuchtkräftsbereich für die Röntgenquellen gefunden, welcher inkonsistent mit der jüngeren Sternentwicklungsgeschichte dieser Galaxie ist. Wir haben eine mögliche Korrelation zwischen der Art der Röntgenquellen von Fornax und der Struktur der Galaxie (Halo aus Dunkler Materie) diskutiert. Es sind jedoch weitere Untersuchungen der Röntgenquellen in dieser Galaxie nötig.
Im letzten Teil der Untersuchungen haben wir anhand der Fluchtgeschwindigkeit der LMXBs die Masse des Dunklen-Materie-Halos bestimmt, die benötigt wird,

um die LMXBs in Draco dSph zu halten. Dabei haben wir Halo-Massen verschiedener Modelle berücksichtigt und gezeigt, dass diese Galaxie ihre LMXBs bei Geschwindigkeiten $\lesssim$70 km s^{-1} halten kann, wenn man eine Halo-Masse von $\gtrsim 10^9$ $M_\odot$ annimmt.

Contents

Chapter 1

Introduction

The observation of extragalactic X-ray sources started around 4 decays ago by using data of UHURU (Fabian, 1975), the first satellite launched specifically for the purpose of X-ray astronomy (e.g., Laros et al., 1973). The following generation of telescopes gave the opportunity to study the X-ray population of nearby galaxies and extragalactic objects in a broad energy band with high spatial and spectral resolution.
There are several advantages in population studies of nearby galaxies which can not be obtained in observing the Milky Way.
First, Galactic sources suffer of a large uncertainty in the distance, a model is always required for the spatial distribution of the sources in Galactic population studies (Fabbiano, 2006), while in the case of the nearby galaxies -excluding the foreground and background sources which are identified by the classification- the distance of the X-ray sources is the one of the galaxy.
Second, the low absorption along the line of sight of nearby galaxies allows to detect many source classes, especially soft/supersoft X-ray sources, which might be not detected in the Milky Way population (Seward and Charles, 2010).
Third, the study of the nearby galaxies allows to investigate the X-ray population in different types of galaxies and also different galactic components e.g., centre, bulge, disk, globular clusters. This provides the possibility of deriving the relation of X-ray source population with galactic structure and with star formation (see Sect. 8).

The importance of the study of X-ray sources in the dwarf galaxies

In X-ray studies, dwarf galaxies are noticeable in some respects:
First, the presence of X-ray binary systems (XRBs) in the dwarf galaxies is a challenge for theory (Maccarone et al., 2005). According to theoretical models, XRBs are supposed to form a few Gyr after star formation bursts in galaxies. Since XRBs usually consumes the mass of the donor star in a few hundred million years, any presence of (especially) bright low mass X-ray binaries (LMXBs) in

dwarf galaxies needs to be justified (Maccarone et al., 2005).
Different models have been suggested to explain the presence of LMXBs in dwarf galaxies and the main scenario invokes behaviour similar to dynamical interaction in a globular cluster, which can form new X-ray binaries at the later stage of development (Hills, 1976). As Maccarone et al. (2005) mentioned, there are also other suggestions, such as primarily transient accretion disks with a very low duty cycle (Piro and Bildsten, 2002), or ultra compact objects, neutron star (NS) or black hole (BH), which formed out of a white dwarf, therefore with a delay in formation (Bildsten and Deloye, 2004). Theories and observations are discussed in more detail in Section. 8.

Second, as both Maccarone et al. (2005) and especially Nucita et al. (2013) discussed, there is high expectation to find intermediate mass black holes (IMBHs) in spheroidal dwarf galaxies (dSphs). Theoretically, IMBHs are the missing BHs with a mass of $10^2 - 10^5\ M_{\odot}$. They are the link between stellar-mass BHs and the super-massive BHs (10^6-10^8 $M_{\odot}$) in active galactic nuclei (AGNs). Based on the extrapolation to globular clusters of the fundamental $M_{BH} - M_{bulge}$ relation derived from the study of super massive black holes in galactic nuclei (e.g, Magorrian et al., 1998), IMBHs are expected to be found in globular clusters. Considering the similar dynamics of globular clusters and dwarf galaxies, these galaxies also are very good candidates to host an IMBH in the centre (Nucita et al., 2013). Observation of X-ray sources to identify IMBHs in the central region of dSphs is current challenge in astrophysics (e.g., Ghosh et al., 2006; Nucita et al., 2013).

Third, dwarf galaxies are believed to have higher dark matter to light ratio compared to the other galaxies. Considering their close distances, they are ideal laboratories to find evidence of decaying dark matter (e.g., Jeltema and Profumo, 2008). As an example, the background X-ray emission of the Draco dSph observed with *XMM-Newton* and *Chandra* was recently studied (e.g., Riemer-Sørensen and Hansen, 2009; Malyshev et al., 2014). It was shown that these observations are not significant enough to prove the presence of the sterile neutrino decay line at 3.5 keV. Malyshev et al. (2014) gave an upper-limit for the decay line and showed that an increase of the sensitivity by a factor of ~ 2 is necessary to firmly rule out the dark-matter decay line hypothesis for the line origin. This is possible with the *XMM-Newton* observation via a moderate increase of exposure towards selected dSph galaxies. It is also noticeable that recently two groups reported the detection of a line at 3.5 keV based on observation of galaxies and galaxy clusters (Bulbul et al., 2014; Boyarsky et al., 2014).

Fourth, not only the detection of the dark matter decay lines, but also the discov-

ery of the LMXBs by itself, can be used to estimate the amount of dark matter in dwarf galaxies suggested by Dehnen and King (2006) after Maccarone et al. (2005) detected five XRBs in the Sculptor dSph galaxy. We explain the details of the Dehnen and King (2006) methods and investigate this approach in the case of the Draco dSph in Chapter 9.

Thesis outline

In this thesis we present the results of a study of the Draco dSph based on five *XMM-Newton* observations. In chapter 2, we introduce the X-ray emission mechanisms, properties, and the emission processes of X-ray sources which are detected in the field of the nearby galaxies. We also explain the different observational and theoretical approaches to study the X-ray population of galaxies, and summarise the results of recent X-ray population study of early-type galaxies. In Chapter 3, The main properties of dwarf galaxies and especially dSphs are briefly explained. We summarise the details of the most recent researches and observations of Draco dSph, focusing on those used in this research. Chapter 4 introduces the *XMM-Newton* and *Swift* observatories, as this thesis work is based on data of these two X-ray telescopes. Chapter 5 contains the details of the *XMM-Newton* observations, data reductions and source detection. It also includes the details of the multi-wavelengths data which have been extracted from different catalogues and have been used in the source classification. In Chapter 6, we theoretically explained different methods which have been used in the data analysis with the purpose of source classification. The results of Chapters 5 and 6 have been used for source classification. Chapter 7 explains for different classes methods for the identification of the source's nature. The study of the X-ray luminosity function (XLF) of the Draco dSph in Chapter 8 is performed based on the results of source classification of Chapter 7. This function shows the expected number of X-ray sources in Draco dSph according to *XMM-Newton* observations. In addition, we computed the XLF of five other dwarf galaxies based on source classification in other works. The morphology and properties of each galaxy are discussed in Chapter 8. To study the correlation between star formation history and the X-ray binary population, the XLFs of these dwarf galaxies are compared with each other. In Chapter 9 based on the detection of LMXB candidates in the Draco dSph and the estimation of the population of LMXBs using the XLF, the gravitational potential of the Draco dSph is studied. We tried to give an estimate of the mass of the dark matter halo of the Draco dSph. Chapter 10 summarises the results of this work. In addition, plots, data, and images which have been extracted and applied in the process of data analysis and classification are categorised in different appendixes. Appendix 11 contains all plots, which are related to different analyses of the work. Appendix 12 contains the tables of properties of *XMM-Newton* X-ray sources and their multi-wavelength counterparts, which

are extracted from catalogues of different wavelengths and used in the course of source classification. Appendix 13 presents the optical high resolution images of the Sloan digital sky survey (SDSS9) for each *XMM-Newton* X-ray source.

Chapter 2

Nearby galaxies in X-ray observation

2.1 X-ray emission

In high-energy astrophysics X-ray emission is usually considered in the energy range of $0.1 - 100$ keV. Based on $E(keV) = k_B T$, where k_B is the Boltzmann constant (8.5×10^{-5} eV K^{-1}), the temperature of photons with energy of 1 keV is equal to 1.16×10^7 K. Different mechanisms are able to reach photons with this high energy. In the following we will explain the main processes for astronomical X-ray emission.

2.1.1 Thermal bremsstrahlung radiation

Electrons can experience large accelerations in hot plasmas through Coulomb collisions. As a result of the acceleration, electrons efficiently emit photons which can escape from an optically thin plasma or be radiated with a thermal spectrum from an optically thick hot structure (Bradt, 2008). The radiated energy of a single collision is calculated by Larmor's formula. The frequency of the emitted photon depends on parameters like the speed of the electron and the projected closest distance to the ion. With the increasing temperature of the electrons, the velocity and therefore the energy of their bremsstrahlung radiation increases. In a thermal equilibrium, the speeds of electrons have a Maxwell-Boltzman distribution. With the multiplication of electron energy and ion density and integration over the range of the speeds in the Maxwell-Boltzman distribution, the thermal bremsstahlung radiation is describe by this formula:

$$I(E,T) = AG(E,T) Z_i^2 n_i n_e \frac{e^{E/k_B T}}{k_B T^{1/2}}, \tag{2.1}$$

where T is the temperature of electrons, k_B is Boltzmann constant, $G(E,T)$ is the Gaunt factor, Z is the charge of ions, n_i and n_e are the densities of ions and electrons, and A is a constant. The bremsstrahlung emission is a continuum emission, however ions of the heavier elements can be excited in colliding with electrons producing emission lines.
Thermal bremsstrahlung spectra from the hot gas are observed from different regions within galaxies. Here we mention some of the examples of known thermal bremsstahlung:
H II regions show a flat spectrum of an optically thin gas in radio spectra. The high energy emission of recent star formation ionises the ambient gas, and the resulting plasma emits a bremsstrahlung spectrum.
Thermal X-ray bremsstahlung spectrum of plasmas with temperatures around 10^7 K is detected from the hot intergalactic gas in the cluster of galaxies (e.g., Sarazin, 1986). This emission was observed for the first time by UHURU in the Coma Cluster (Gursky et al., 1971).
In symbiotic systems, gas accreted by the white dwarf from a companion, periodically encounters a shock which slows down the material falling and prevents high density of matter on the surface. A hot optically thin plasma slowly falls down on to the surface of the white dwarf. The energy of infalling material is converted to thermal energy and radiated in X-rays (Kwok and Leahy, 1984).
The hot plasma, which is created by supernova remnant (SNR) shocks is optically thin and has the distribution of ionised atoms. This optically thin plasma in SNR, is a powerful tool for measuring abundances (Vink, 2012).

2.1.2 Blackbody radiation

Blackbody radiation is emitted by a photon gas in thermal equilibrium at temperature T. Each temperature corresponds to an energy spectrum of a specific amplitude. The intensity of the radiation from a blackbody is characterised by the Planck spectrum:

$$I(\nu,T) = \frac{h\nu^3}{c^2}\frac{1}{e^{h\nu/k_BT}-1} \tag{2.2}$$

where h is the Planck constant and ν is the frequency of the photons. In X-ray astrophysics the emission from young NSs or the emission form white dwarfs in the phase after the nova burst are blackbody radiation.

2.1.3 Inverse Compton scattering

Compton scattering is elastic scattering of a photon by a charged particle, usually an electron. The part of the energy of the photon is transferred to the recoiling electron. The main process which plays an important role in astrophysical emission phenomena is "inverse Compton scattering". In a plasma of relativistic electrons, the electrons typically have energies larger than the energy of photons. In this case, the photons are scattered up by electrons to larger energies. It should be considered that relativistic electrons in the presence of a magnetic field will emit in addition the synchrotron radiation (see Sect. 2.1.4).
The hard X-ray spectra of black-hole binaries that extends to $50 - 100$ keV is traditionally explained by inverse Compton scattering, however newest researches show that the hard tail of the spectrum can also be related to jets from the BH. Another example of the Comptonization[1] is the scattering of the cosmic microwave background photons at the electrons of hot plasma in cluster of galaxies which is known as "Sunyaev-Zeldovich effect".
If the radiation energy density of a given environment is sufficiently high photons will experience inverse Compton scattering. This could happen to photons produced by synchrotron before they leave the source region. This process is called synchrotron self-Compton and is seen in the spectrum of the Crab nebula (Aharonian et al., 2004) and the jets of blazars (e.g, Giommi et al., 2006).

2.1.4 Synchrotron radiation

When charged particles with a charge q move trough a magnetic field B with a velocity of V, the magnetic force $q(V \times B)$ causes the particles to accelerate. The accelerated particles emit cyclotron radiation. If particles especially electrons are relativistic ($v \simeq c$), the radiation is highly beamed in the direction of the electron velocity vector. The acceleration vector is in the direction $V \times B$. The observed radiation is linearly polarised parallel to the acceleration vector (Longair, 2011). The polarised radiation of Synchrotron emission was detected for the first time in the Crab nebula using a Polaroid filter transmitting only one polarisation of incident light. At some orientations of the filter some regions of the nebula seem brighter and this pattern changes by putting the filter in other orientations. SNRs are not the only sources of Synchrotron emission. The Galactic background of radio emission is in general polarised due the Galactic magnetic field, Also, relativistic jets in AGNs show Synchrotron emission in their spectra.

[1] The change in the spectrum of the incident radiation caused by the multiple Compton scattering with a thermal distribution of electrons, called "Comptonization".

The spectral distribution of the emission of non-thermal electrons follows a power-law. The spectrum is defined as the number of photons per photon energy:

$$N(E)dE = KE^{-\Gamma}dE \tag{2.3}$$

where Γ is photon index and K is a constant. When the source is "softer", the Γ increases (Bradt, 2008).

2.2 X-ray sources in the field of nearby galaxies

X-ray observations of nearby galaxies show numerous different classes of sources. They can be foreground stars (systems) belonging to the Milky Way, background objects (e.g, AGNs and galaxies), point-like, or diffuse sources belonging to the observed galaxy. In this section, different source types, their physical mechanisms that produce X-ray emission, and their properties are summarised:

2.2.1 Foreground stars

Usually, different classes of stars located in almost all regions of the Hertzsprung-Russell (HR) diagram have been detected as X-ray sources. There are just a few classes, like coolest giants of spectral type M, that don't show X-ray emission. But even for those classes, there are exceptions. In X-ray surveys of nearby galaxies a significant fraction of sources, detected in the field of view (FOV), are Galactic normal stars. Foreground stars are relatively soft sources and are homogeneously distributed in the FOV. The first stellar X-ray survey was performed by the Einstein X-ray mission, which allowed the search for stellar X-ray emission at a level comparable to the Sun (Vaiana et al., 1981). The stars which were detected in this survey covered a wide range of spectral types in HR diagram and the results showed that for most of the stars the X-ray emission is stronger than for the Sun. High resolution spectroscopy with *XMM-Newton* (see Sect.4.1) and *Chandra* (Weisskopf et al., 2000), together with their broad wavelength coverage and large effective areas, allowed studies of the stellar corona and stellar wind physics (Güdel and Nazé, 2009).
Figure 2.1 shows the HR diagram of detected X-ray stars, compiled from selected catalogues of different surveys (Güdel, 2004). The diagram shows the X-ray luminosity of the detected stars in X-ray and their positions in a colour magnitude diagram.

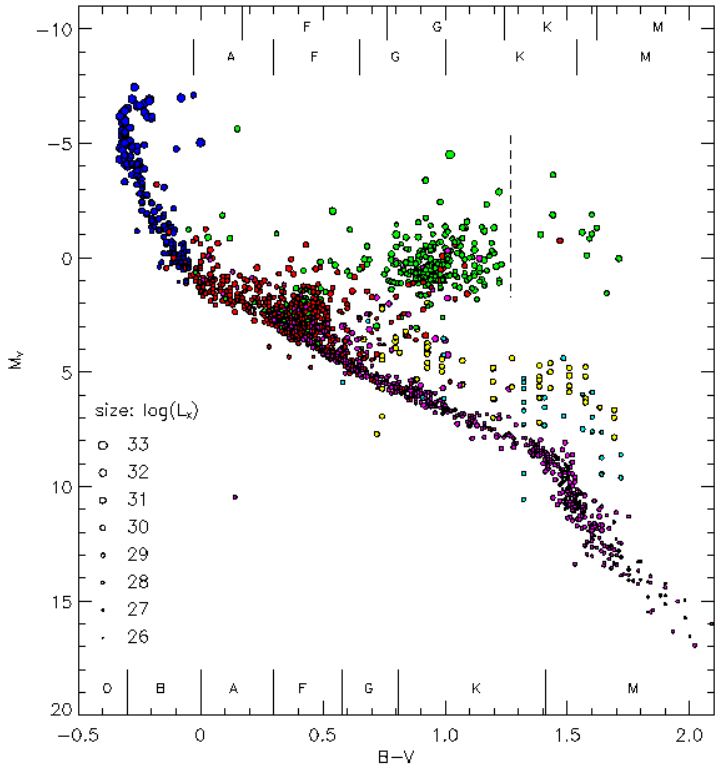

Figure 2.1: HR diagram based on about 2000 X-ray detected stars extracted from the different catalogues. The size of the circles characterises $log(L_x)$ indicated in the panel at lower left (Güdel, 2004).

Early-type stars

The X-ray production mechanisms in early-type stars is thought to be fundamentally different from that in late-type stars. For massive stars like O, B type or Wolf-Rayet stars, shocks forming in unstable winds create plasma with temperature of million degrees which is responsible for X-ray emission. (Güdel and Nazé, 2009). For B stars, which possess much weaker winds than O stars (Cohen et al., 2008), there are some additional models which explain the problem of hard X-ray emission in such objects, e.g., the impact of magnetic field on the stellar winds (ud-Doula and Owocki, 2002). The X-ray spectra of OB stars can be described by two temperatures model considering additional absorption by the warm wind (Corcoran et al., 1994).

Late-type stars

The X-ray production mechanism for late-type stars is believed to be almost similar to that of the Sun. The magnetic coronae are powered by flares owing to

reconnection in unstable magnetic fields that releases enormous amount of energy. Usually two temperature components are used to model the X-ray emission of the stellar coronae. The flares can cause the variability on time scales of several hours (Güdel and Nazé, 2009). There are just a few exceptions like A-type stars (Schröder and Schmitt, 2007) and coolest the M-type giants (Hunsch et al., 1998), which usually do not show X-ray emission, because they have neither convection zones nor strong winds. Therefore they are intrinsically X-ray dark. However, even in these cases there are some exceptions which are showing X-ray emission, especially in the case of A-type stars (Schröder and Schmitt, 2007).

Coronal emission of binary systems

Close interacting binaries keep their fast rotation rates throughout their main life and even sometimes into the subgiant and giant evolution (Güdel, 2004). The most common binary systems that are studied are RS CVn-type systems that typically contain a G- or K-type giant or subgiant with a late-type subgiant or main sequence companion. There is a similar class of binaries that contains two late-type main sequence stars instead, which are called BY Dra-type binaries. Studies suggested that the secondary star plays no role in determining the activity level of the system other than providing the mechanism to maintain rapid rotation. However, the surface X-ray activity of these stars is higher than those of isolated stars with the same rotation speed (Bopp et al., 1993).
If their separation is sufficiently small, the two components may come into physical contact, defining the class of W-UMa type contact systems. W-UMa systems are contact binaries of spectral type F-K with rotation periods from 0.2–1.5 days (Rucinski, 1998). Observations confirmed that for stars with rotation periods less than about 0.4 days, the ratio (L_x/L_{opt}) appears to decrease with decreasing period (Randich, 1998). Usually, the X-ray spectra can be modelled with two-temperature models, with temperatures of $\sim 10^6$ K and 10^7 K. The brightest source in the field of the Draco dSph is a foreground W-UMa binary (see Sect. 7.1).

2.2.2 Background sources

A noticeable fraction of the X-ray sources detected in nearby galaxies do not belong to the galaxy, but have an extragalactic origin like AGNs and background galaxies.

Active galactic nuclei

The majority of background objects are AGNs. An AGN is a super-massive BH

in the centre of a galaxy that accrets gas and dust . They are powerful sources of radiation in a wide spectral range: from radio to γ-rays. Their luminosities range from 10^{42} to 10^{48} erg/s, being the most luminous objects in the Universe, almost 10^4 more luminous than ordinary galaxies (Jovanović and Popović, 2009).

One of the important characteristics of AGNs is the fast variability observed in different parts of the electromagnetic spectrum. Fluctuations of the X-ray radiation on timescales from several parts of an hour into several days are a common property of all AGNs and this leads to the conclusion that the emission region in the AGNs have small dimension (Krolik, 1999).
Another property of AGN is the strong X-ray flux. X-ray emission of AGNs is between 10^{39} to 10^{46} erg/s (Urry and Padovani, 1995). The main mechanism which produce X-ray in AGNs is basically similar to the mechanism of X-ray emission in accreting XRBs. The main difference is that the AGNs require an accretion rate of several solar mass per year to explain the enormous output energy. This energy is produced by an accretion disk with the radius of $\sim 10^9$ km surrounding a super-massive BH with a mass $\sim 10^6 - 10^9\ M_\odot$. The accretion disk is surrounded by hot electrons which are believed to comptonise the UV photons emitted from the disk and producing the hard X-ray spectra of AGNs (Seward and Charles, 2010).
In X-ray spectroscopy, AGN are bright in both soft X-ray and hard X-rays. It is believed that both components mainly arise from the inner regions close to the central super-massive BH. The soft X-ray emission is probably formed in the accretion disk, which is also a strong source of soft UV and optical photons. The hard X-ray emission is caused by high-energy (most likely relativistic) electrons in hot corona above the disk, when the low-energy UV and optical photons scatter from the disk to X-ray energies by inverse-Compton process (Fabian, 1989, 2000). The X-ray spectrum of AGN in the energy range of $0.2 - 10$ keV can be usually fit by a power-law model with a photon index between $\sim 1.5 - 2.0$. In some cases, other spectral components are observed e.g. iron lines (especially Fe K_α emission at 6.4-6.7 keV).

Since the majority of background X-ray sources are AGNs, population studies of AGNs and galaxy structure are performed by both *Chandra* (Elvis et al., 2009) and *XMM-Newton* (Cappelluti et al., 2009) in deep surveys of regions which (1) are empty of bright nearby galaxies and stars and (2) have high latitude (hence low Galactic extinction).
The X-ray luminosity functions of AGNs of the *XMM-Newton* deep survey are used for reducing the AGN population from X-ray detected sources in the field of the Draco dSph, to estimate the number of XRBs (see Chapter 8).

Galaxies

Since most of the galaxies are believed to host a BH in their centre, the distinction between active and normal galaxies is difficult. It is assumed that in normal galaxies, the efficiency of the central super-massive BH is low and the thermal emission from the centre is produced by bremsstrahlung (Bender, 2005), while the main X-ray emission is caused by stars, accreting compact objects, SNRs, and soft diffuse emission (e.g., Trümper and Hasinger, 2008). Therefore, the study of the X-ray population of these galaxies is a key to understand the evolution and star formation rate of different galaxy types. Far background galaxies are usually visible in optical as red and extended sources. Their X-ray Luminosity is lower than AGNs. In galaxies with an active central region, the X-ray luminosity can reach 10^{41} erg s^{-1} (e.g., Stiele et al., 2011).

Galaxy clusters

Clusters of galaxies are large concentrations in the galaxy distribution containing hundreds to thousands of galaxies over a region of the order of $\sim$ 1 Mpc. Such structures are associated with deep gravitational potential wells. X-ray emission is observed from the intra-cluster gas. The dominant X-ray emission mechanism is thermal bremsstrahlung at temperatures of around $\sim$ 1 keV. The thermal X-ray luminosity of galaxy clusters is between $\sim 10^{43-45}$ erg s^{-1} (Voit, 2005). The X-ray study of galaxy clusters especially helps to study the structure of the intergalactic medium (e.g., Pointecouteau et al., 2005; Massey et al., 2007b).

2.3 X-ray binaries

X-ray binaries (XRBs) are systems consisting of a compact object orbiting a star that can be observed in the optical. They are close binary systems with a transfer of mass from the optical component to the compact object. Figure 2.2 shows the classification of different XRBs divided up into BH systems and NS systems[2]. Accreted matter falls down onto an enormous gravitational potential well and is accelerated to extremely high velocities. When the matter reaches the surface of the NS, it is rapidly decelerated and the free-fall kinetic energy radiated away as heat which is available to power the X-ray source (e.g, Reig, 2011).

[2] usually systems with a white dwarf (as compact object) are not a subclass of XRBs and are called cataclysmic variables (CVs).

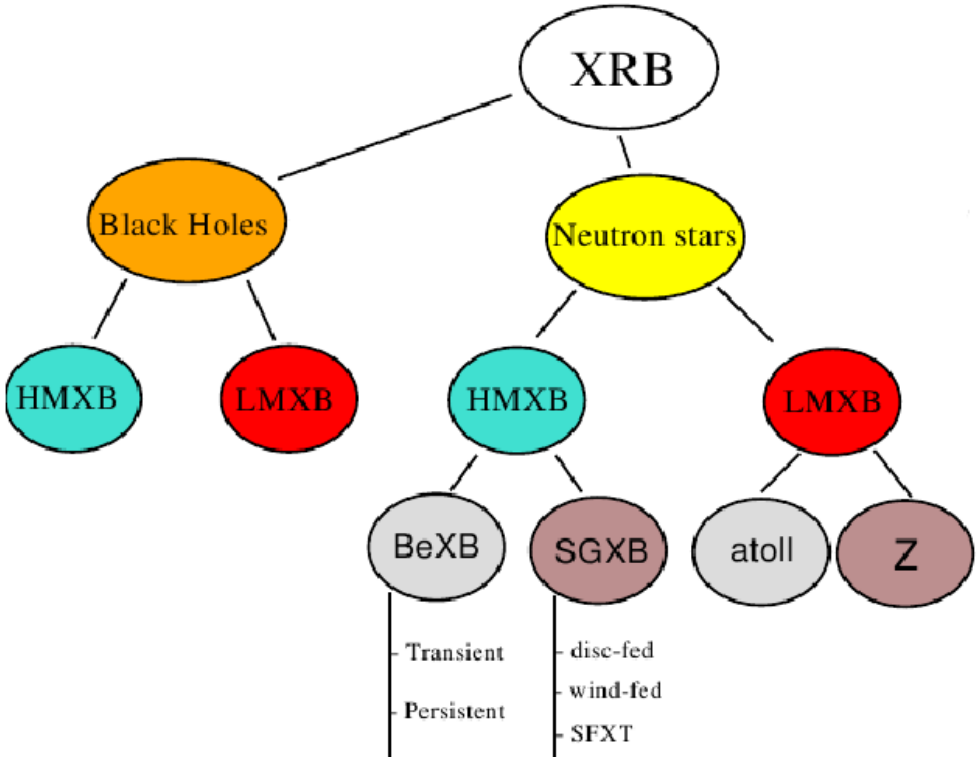

Figure 2.2: Classification of XRBs (Reig, 2011).

2.3.1 High-mass X-ray binaries

High mass X-ray binaries (HMXBs) contain an early-type O or B star ($> 5M_{\odot}$) as a companion with of a compact object (NS or BH). HMXBs are strong emitters of X-ray radiation. Sometimes they appear as the brightest objects in the X-ray sky. The majority of HMXB is associated with NSs. The class of HMXBs is divided into Be/X-ray binaries (BeXBs), if the optical companion is an emission line star of type Be (sometimes also OBe, luminosity class III, IV or V), and super-giant X-ray binaries (SGXBs), if they contain a luminosity class I-II star.
In BeXBs, the optical star emits a substantial stellar wind, removing the mass with a rate range $10^{-6} - 10^{-8} M_{\odot}$ yr^{-1} with a velocity up to 2000 km s^{-1} (Reig, 2011). A NS in a relatively close orbit will capture some fraction of this wind, sufficient to power a bright X-ray source.
SGXBs have different models: a NS in a relatively close orbit will capture some fraction of the strong wind. This is sufficient to power a bright X-ray source (wind-fed). If mass transfer occurs via Roche lobe overflow, then the X-ray emission is highly enhanced and an accretion disk is formed around the NS (disk-fed). INTEGRAL (Winkler et al., 2003) detected a population of highly obscured HMXBs

with supergiant companions. They show outbursts, that are significantly shorter than typical outbursts of BeXBs. They are known by bright flares with a duration of a few hours and peak luminosities of $10^{36} - 10^{37}$ erg s^{-1}. These new systems have been called super-giant fast X-ray transients (SFXTs) (Reig, 2011).
The lifetime of an HMXB is short (on the order of 10^{6-7} yr) and the Galactic HMXBs show a luminosity between $\sim 10^{35-37}$ erg s^{-1}(Fabbiano, 2006). The magnetic field of the NS is strong ($\sim 10^{12}$ G), therefore, the X-ray pulsation is very common in HMXBs. These system have been observed with pulsation periods between 0.1-1000 s. Their X-ray spectrum is hard ($KT>$ 15 keV) and they usually show X-ray eclipse. Their optical spectrum is star-like and the (L_x/L_{opt}) is between 0.001-10. Their common optical period is between 1-100 days (Ph.D thesis, Gianluca Israel, 1997). HMXBs are usually associated with young stellar populations (Fabbiano, 2006), therefore it is not expected to observe them in old populations like in dSph.

2.3.2 Low-mass X-ray binaries

Low-mass X-ray binaries (LMXBs) typically contain a late type (K, M) low mass donor star with mass $\lesssim 1\,M_\odot$ (in the case of very short period binaries, a white dwarf can be also the donor companion). The main part of the mass is usually transferred onto the compact object via an accretion disk yielding accretion rates of $10^{-10} - 10^{-8} M_\odot$ yr^{-1} (Tauris and van den Heuvel, 2006). Population studies of the Galactic LMXBs show that the majority of them have a luminosity of $\sim 10^{35} - 10^{37}$ erg s^{-1} (Fabbiano, 2006). The study of Zhu et al. (2012), using a population synthesis code, showed that persistent LMXBs with a red giant donor, and accretion via Roche lobe overflow, have an X-ray luminosity of $\sim 10^{37}$ erg s^{-1}, while the same system which transfers the mass via stellar wind has a low X-ray luminosity of $\sim 10^{33}$ erg s^{-1}. In the case of the transient LMXBs, the X-ray luminosity during quiescence is of the order of $\sim 10^{32} - 10^{33}$ erg s^{-1}. However, during the outburst the X-ray luminosity can increase by several orders of magnitude, and the sources become similar to persistent LMXBs. Some transient LMXBs show soft X-ray emission in quiescence. This emission seems to depend on the accretion rate and the disk structure (Asai et al., 1998). In LMXBs with white dwarf donors, the orbital periods are shorter than 1 hr, and the mass transfer is mainly driven by gravitational rotation. Their X-ray luminosities are between $6 \times 10^{35} - 10^{39}$ ergs s^{-1} and most of the LMXBs with a white dwarf donor are transient.

In general, LMXBs are characterised by a high ratio of X-ray to optical flux ($\frac{F_{\rm x}}{F_{\rm opt}} \approx 10 - 10^4$), faint blue optical counterpart, lack of strong optical emission

lines, and hard X-ray spectra (Schulz et al., 1989). LMXBs have relatively weak magnetic fields ($10^7 - 10^{11}$ G). Rarely, pulsation are observed in this systems with a period between 0.1-100 s (Ph.D thesis, Gianluca Israel, 1997). These systems show different kind of X-ray variability, in particular, bursts, which are sudden thermonuclear fusion of accreted mass on the surface of NS (Lewin and Joss, 1983).

2.4 Ultra luminous X-ray sources

Ultra-luminous X-ray sources (ULX) are XRBs in galaxies outside the nuclear region, with luminosity more than the Eddington luminosity of stellar mass XRBs ($L_x > 10^{39}$ erg s^{-1}). They are most commonly found in star-forming and star burst galaxies. One explanation for such a luminosity is that some of these extreme objects may be IMBHs with a mass of $M > 500 M_\odot$ (e.g, Colbert and Mushotzky, 1999). However, the existence and the formation of the IMBH is still not confirmed. The centre of dwarf galaxies is an important place to search for ULX sources as candidates for IMBHs (see Sect.1)

2.5 White-dwarf binaries

Interacting binaries like LMXBs, with a white dwarf as the accreting compact object are known as cataclysmic variables (CVs). The white dwarf accretes mass from a cool, late type companion star in a short period binary system. As the transferred material carries substantial angular momentum, it does not settle immediately onto the white dwarf but forms an accretion disc. The mass spirals through the disk and heats it to a temperature of $\sim 3000 - 100000$ K producing a luminosity of $0.001 - 10\ L_\odot$.

CVs can basically be divided into magnetic and non magnetic systems. If the case of non-magnetic white dwarfs, the mass of companion accreting inwards onto the surface of white dwarf with an accretion disk. The mass lands in the white dwarf's equatorial zone; while, if the white dwarf is strongly magnetic, the accreting material has to follow the field lines and goes onto the surface near the magnetic poles of the white dwarf (Connon Smith, 2007). X-ray observations of nearby galaxies in the past have revealed some CVs as X-ray sources (e.g., super-soft sources).

Super-soft sources

These source are luminous, $\sim 10^{36-38}$ erg s^{-1}, but extremely soft with low temperatures of $kT = 10 - 75$ eV (Long et al., 1981). van den Heuvel et al. (1992) showed based on a black-body model that the size of the source is comparable with a white dwarf, however if the accretion disk is considered as the only source of L_x the rate of accretion should be 100 times more than the outburst state in CVs. Shara et al. (1977) suggested that the nuclear fusion of accreted material undergoing stable nuclear hydrogen burning is the source of X-ray emission.

Symbiotic binaries

Very high accretion rates can also be found in another kind of white dwarf binaries called symbiotic binaries (Kenyon, 1986). Symbiotic binaries are very long period (hundreds of days) binaries containing a white dwarf that is accreting from a red-giant companion. Mass transfer can be either by Roche-lobe overflow or via a dense stellar wind if a red giant is on the asymptotic giant branch. Draco dSph contains at least one classified symbiotic star (see Sect. 7.4).

2.6 Supernova remnants

After a supernova explosion, a supernova remnant (SNR) is formed the result of the interaction between the shock wave of the explosion and the interstellar medium. The life of the SNR is divided into three phases: First, the ejecta shell expands rapidly in a free expansion and sweeps up the surrounding interstellar medium. This process heats up the shell to a temperature of 10^{7-8} K. It will continue to the time when mass of the swept-up matter is the same as the mass of ejecta. In the second phase, the expansion is adiabatic, since the swept-up mass is more than the ejecta mass, however the internal energy is more than the energy radiated by the shell material. In this situation two shock waves are formed, one that propagates into the gas in the direction of expansion and the second which is called the reverse shock and propagates back into the ejecta. In this phase, both the shell and the shocked ejecta are bright in X-rays. As the swept mass increases, the remnant becomes radiative and cooler. This stage lasts $\sim 10^5$ years and most of the energy will be radiated (Seward and Charles, 2010). SNRs are in general soft, extended X-ray sources, possibly, with a counterpart in the optical or radio, except if there of additional non-thermal emission from pulsar and/or pulsar wind nebula.
In dSph galaxies, which have very old stellar populations, the observation of SNRs (especially that of Type II) is rare due to very short life time of the progenitors

compared to the age of the galaxy. As the classification in Chapter 7 shows, we did not find any SNR in Draco dSph.

2.7 X-ray luminosity function

Most of the emission from our Galaxy and other nearby galaxies, which belong to the class of "normal" galaxies (without an AGN), seem to be caused by discrete objects. The population of these discrete sources helps us to study the galactic history and star formation rate. For any particular class of sources, the distribution of the number of sources versus the X-ray luminosity is called X-ray luminosity function (XLF).
Theoretical models for XRB formation and evolution depend on the star formation history of the host galaxies allow us to identify the main physical elements that determine the XLF slopes (Belczynski et al., 2004). Therefore the comparison of the observational XLF and the theoretical result can reveal the nature and evolution of the sources in a galaxy.

XLF in theoretical models

In simulations of the XLF there are different models based on different approaches e.g. "Scenario Machine" or "Strar Track synthesis population code".
The Scenario Machine (Lipunov et al., 1996) is a computer code based on the Monte-Carlo method, developed to calculate the evolution of a large ensemble of binaries, according to the description of evolutionary processes in close binary systems by Paczyński (1971). Bogomazov and Lipunov (2008) simulated the formation and evolution of different kind of binaries in an elliptical galaxy using the Scenario Machine. They calculated the population of different type of binary systems in a typical elliptical galaxy with respect to the star formation rate.
In their model, different types of XRBs are characterised as follows:
1. An accreting NS with a main-sequence companion.
2. An accreting NS with a super-giant.
3. An accreting NS with a companion filling its Roche lobe.
4. An accreting NS with a Be star.
5. A BH with a supergiant.
6. A BH with a companion filling its Roche lobe.
7. A NS with a companion filling its Roche lobe; supercritical accretion.
8. A BH with a companion filling its Roche lobe; supercritical accretion.
9. Two types of systems are studied for the purpose of modelling extremely luminous X-ray sources, assuming that the minimum initial mass of the donor is $120 M_{\odot}$.

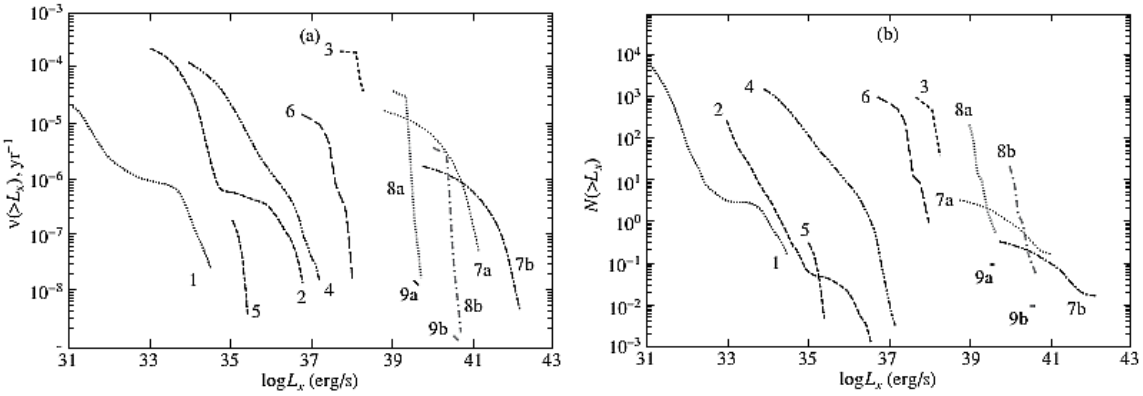

Figure 2.3: (a) Birth rates and (b) cumulative luminosity functions for various types of X-ray sources in the Galaxy (Bogomazov and Lipunov, 2008). The indices are according to the explanation of Section 8.

Figure 2.3 shows the result of the simulation for all different kinds of defined binaries in the simulation. Indexes (a) and (b) are related to different parameters for emission and stellar winds.

Scenario Machine also predicted the galactic evolution of the X-ray binary luminosity function over years. Figure 2.4 shows the evolution of the XLF of a typical elliptical galaxy in long scale time after the star formation burst. The population of different kind of sources can show different life times. The results show that the XLF of XRBs depends on the star formation rate. The evolution of the rotation of NSs and the life time for their X-ray stages should be taken to account in theoretical models and it shows that there is not any universal XLF.

The other leading model, the StarTrack code, was originally developed for the modelling of binaries with two compacts (Belczynski et al., 2002) and has undergone major revisions intended to treat in details the formation and evolution of XRBs for any choice of star formation history and metallicity (Belczynski et al., 2008).
As an excellent sample, this model estimated the age of the young and old stellar populations in NGC 1569 by fitting the simulated XLFs to the observational XLF (Belczynski et al., 2004).

Belczynski et al. (2004) examined the consistency of the models by allowing the relative SFR weight, the population age, and metallicity to vary. Figure 2.5 shows

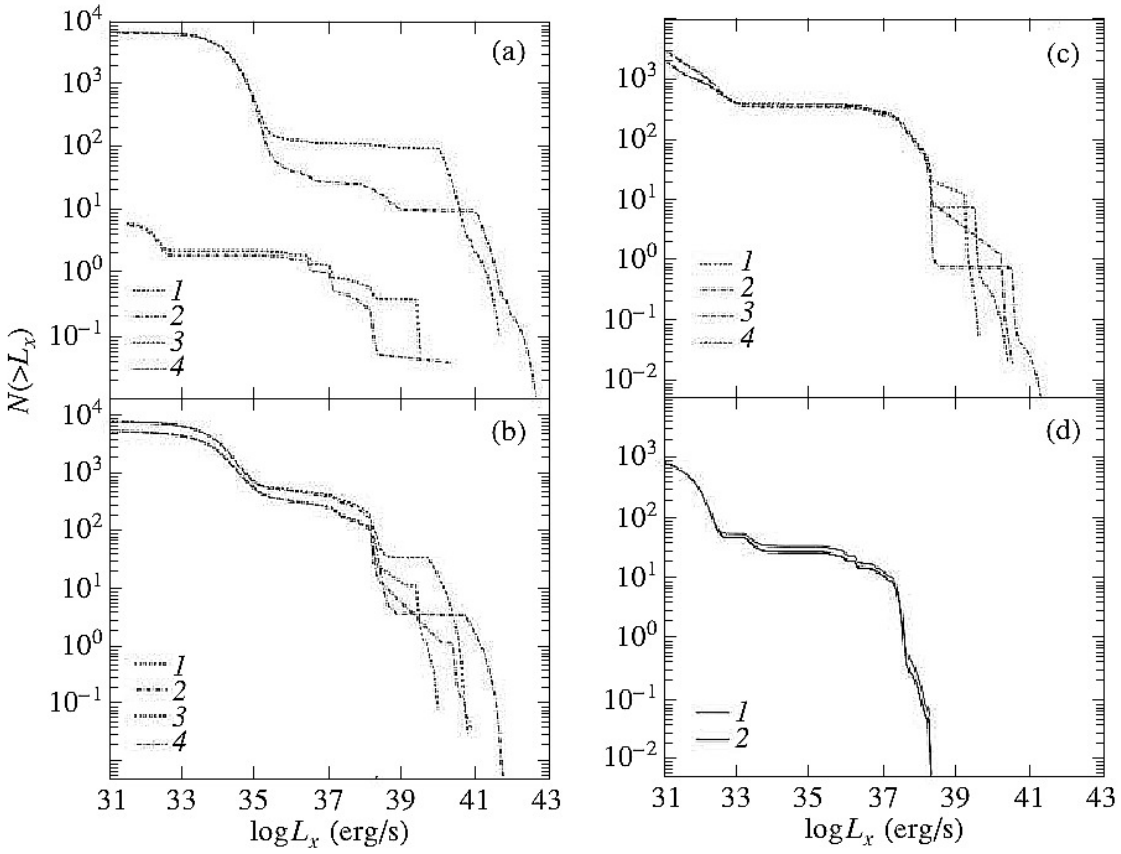

Figure 2.4: Evolution of the cumulative luminosity functions of the X-ray sources in an elliptical galaxy after its burst of star formation. The curves represent (1) weak wind for massive donors with a collimation angle in supercritical accretion regimes $\alpha = 10$, (2) weak wind with $\alpha = 1$, (3) strong wind for massive donors, with $\alpha = 10$, and (4) strong wind for massive donors, with $\alpha = 1$. Time intervals from the star formation burst are (a) 0–10 million years, (b) 10–100 million years, (c) 100 million–1 billion years, and (d) 1–10 billion years (Bogomazov and Lipunov, 2008).

the best fit model to the observational XLF. The model is corresponding to the young population at 70 Myr and the old one at 1.3 Gyr, with continuous star formation for 1 Gyr. The tendency of higher luminosity in the model compared to *Chandra* data is due to the bolometric luminosity adopted for the model which is higher than those in the *Chandra* band. The model enables the population of e.g., BH/NS accretors, transient systems, and thermal wind-fed systems to be estimated.

XLFs in observational works

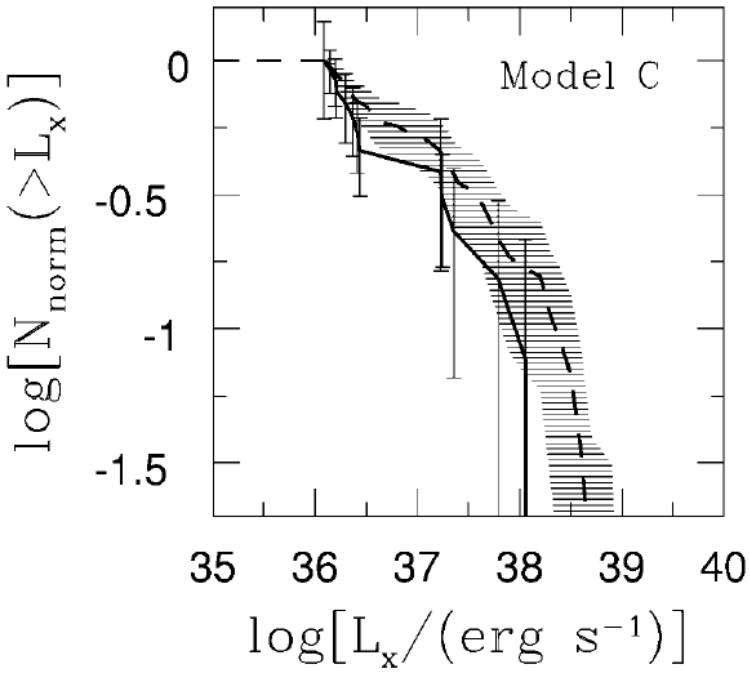

Figure 2.5: Observed NGC 1569 XLF with error bars (solid lines) plotted against predicted XLFs (dashed curves) shown with 1 σ sampling errors (shaded areas). All curves are normalised to the total number of the detected sources. In this model, the age of the young and old populations and the SFR ratio of the young relative to the old, is 70 Myr, 1.3 Gyr, and 40 respectively (Belczynski et al., 2004).

1. Milky Way: Observational population studies of the Milky Way galaxy show that the dominant Galactic X-ray sources are XRBs. The result of Grimm et al. (2002) is that XLF of HMXBs (donor with mass $M > 2.5M_{\odot}$) is fit to a power law with cumulative slope -0.64 ± 0.15 and for the LMXBs with a power law with slope of -0.26 ± 0.08 truncated at $\sim 2.7 \times 10^{38}$ erg s^{-1}.
As it is also mentioned in the introduction, since the XLF of the Galactic sources suffer of a large uncertainty in the distance, the population study of the sources in other galaxies a major topic of interest. Not only, nearby galaxies provide a large sample of X-ray sources, but also low column density allows for the detection of the soft X-ray sources (Seward and Charles, 2010).

2. Nearby galaxies; early type galaxies: XRBs in nearby galaxies have been known since the Einstein era, but detections of significant samples have been limited to just a few sources (e.g., Fabbiano et al., 1982). *Chandra* and *XMM-Newton*

observations have improved the XRB studies with the discovery of large numbers of X-ray point sources in different galaxies. The samples in most cases are large enough that we are now able to examine XRB populations in a wide range of galactic environments with different star formation histories. The samples are characterised by cumulative XLFs, which are fit by single or broken power-laws and allow us to identify the main physical elements that determine the XLF slopes (e.g., Fabbiano, 2006) .

In XLF studies, galaxies or globular clusters are usually separated into young and old stellar populations. Since this dissertation study focuses on the Draco dSph which has old stellar population, we briefly summarise the characteristics of XLFs in old populations.
Fabbiano et al. (1989) discussed that LMXBs should be present and might even dominate X-ray sources in early type galaxies (e.g, S0s or elliptical galaxies). This was confirmed by the statistical analysis of a large sample of early type galaxies.

Populations of several tens to hundreds of sources have been detected in E and S0 galaxies with *Chandra* showing that the X-ray colours and spectra of these sources are consistent with those expected of LMXBs, and consistent with those of the LMXBs of M31 (Fabbiano, 2006).
As the most remarkable studies, Fabbiano (2006) reviewed the work of Irwin et al. (2003) and Kim and Fabbiano (2004), who respectively studied 15 nearby early-type galaxies observed with *Chandra* and XLF of LMXBs for a sample of 14 galaxies type E and S0. Irwin et al. (2003) found that the average spectrum of sources fainter than 10^{39} erg s^{-1} is remarkably consistent for all studied galaxies, irrespective of the position of source in the galaxy. These spectra can be fit with either power-laws (photon index of ~ 1.6) or with bremsstrahlung emission (temperature of ~ 7 keV). Sources with luminosities around or higher than $\sim 10^{39}$ erg s^{-1} have softer spectra with a power-law (photon index of ~ 2), consistent with the soft emission of LMXBs with a BH compact object with masses of up to $15 M_{\odot}$. Kim and Fabbiano (2004) found that all the individual corrected XLFs are well fit with single power-laws with similar differential slopes between -1.8 to -2.2, in the observed luminosity range. The similar statistic of the individual power-laws allowed Kim and Fabbiano (2004) to normalise data of all galaxies and represented a high significance XLF of early-type galaxies (Figure 2.6, left). This composite XLF showes a break at $(5 \pm 1.6) \times 10^{38}$ erg s^{-1}. With two power-law, the best fit for the differential slope is -1.8 ± 0.2 in 10^{37} to 5×10^{38} erg s^{-1} luminosity range and at higher luminosity, the differential slope is steeper -2.8 ± 0.6.
As Fabbiano (2006) also mentioned, these results are consistent with an independent work of Gilfanov (2004), who analysed four early-type galaxies (Figure 2.6, right); however, the differential slope for the high luminosity portion of the XLF in this work is steeper (-3.9 to -7.3). Both works show a cut-off in the XLF at

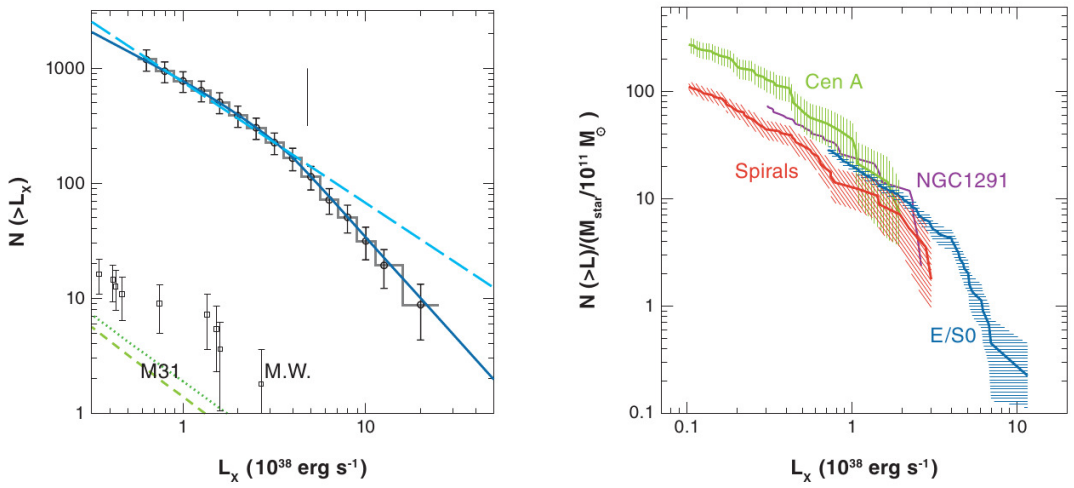

Figure 2.6: Left: Cumulative XLF of 14 E and S0 galaxies, with the single power-law best fit (dashed line), and the broken power-law model (solid line); the M31 and Milky Way low-mass X-ray binary (LMXB) XLFs are sketched in the left lower corner. Right: Cumulative LMXB XLFs Note the similarity of the XLFs and the break at $\sim 5 \times 10^{38}$ erg s^{-1} in the E/S0 XLF.

a few 10^{39} erg s^{-1}. The break in power-law is higher than the luminosity which would be expected from Eddington luminosity of a normal NS binary. It is consistent with the Eddington luminosity of the most massive NSs or low-mass BHs. Therefore, this break may be caused by the presence of both populations of NSs and black in early-type galaxies.

Piro and Bildsten (2002) showed that the large X-ray luminosities of the LMXBs in early-type galaxies ($10^{37} < L_x < 10^{39}$ erg s^{-1}) should have large accretion rates ($> 10^{-9}$ M yr^{-1}). This brings the idea that for the old populated systems the presence of LMXBs in transient forms. As Fabbiano (2006) explained, these transients would have recurrence times greater than 100 years and outbursts of 1-100 years duration. There are observations, which supported the presence of transients e.g, the NGC 5128 LMXB population (Kraft et al., 2001) and the discovery of five quiescent XRBs in the Sculptor dSph Maccarone et al. (2005)[3]. This means that more investigations are necessary to find the real nature and evolution of LMXBs in old stellar populations (Fabbiano, 2006). This brief summary shows the importance of the study of the XLF of LMXBs in the dSphs as the oldest known nearby stellar populations.

[3] Respected to the later works, two out of these five LMXBs have AGN counterparts. The results of Maccarone et al. (2005) work are discuss by details in Chapter 9

Chapter 3

The Draco dwarf spheroidal galaxy

3.1 Introduction

Dwarf galaxies

The Local Group is composed of more than 50 galaxies which are divided into three major classes: The three giant spirals (M31, M33 and the Galaxy), intermediate galaxies like the LMC and the SMC, and dwarf galaxies.
Dwarf galaxies are orbiting around the giant spirals. The Mateo (1998) catalogue listed 36^{+6}_{-2} dwarf galaxies in the Local Group. Many dwarf galaxies are extended, ranging from under 10 in diameter to over 40. Nearly all Local Group dwarfs have very low surface brightnesses. However it is not difficult to detect these galaxies, but obtaining a reliable follow-up photometry is complected. Due to this fact, measurements of the integrated photometric and structural properties of Local Group dwarfs are challenging.
Figure 3.1 shows the position of dwarf galaxies which are orbiting around our Galaxy. Based on the shape, dwarf galaxies are classified into different groups: dwarf elliptical galaxy, dwarf spheroidal galaxy, dwarf irregular galaxy, dwarf spiral galaxy, Magellanic-type dwarfs (intermediate between dwarf spiral galaxies and irregular galaxies with one spiral arm, named after their prototype, the LMC). There are also two more recently identified groups of dwarf galaxies which are different from the others due to their young, hot, and massive stars called Blue compact dwarf galaxies and Ultra-compact dwarf galaxies. The variety of dwarf galaxies make them a good laboratory in many different respects, e.g. how stellar evolution proceeds in chemically young environments; how dwarfs form from larger galaxies via mergers; and the nature of dark matter in the smallest natural size-scales (Mateo, 1998).

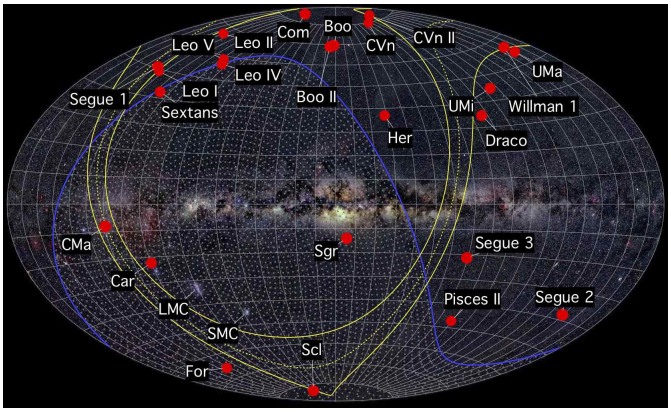

Figure 3.1: Optical all-sky image showing the locations of known dwarf galaxies associated with our Galaxy (Credit: A. Frebel, MIT).

Dwarf spheroidal galaxies

Dwarf spheroidal galaxies (dSphs) are believed to be the most abundant galaxies in the universe (Marzke and da Costa, 1997). They have two important characteristics: first, stellar velocity measurements have shown that some of the dSphs have a mass to light ratio of $\sim 100(M/L)_{\odot}$, which makes them the darkest known systems of stars in the universe. Their typical stellar mass is $< 5 \times 10^6 M_{\odot}$ corresponding to the absolute magnitude of $M_v > -9$. Generally they have a size of 10 times larger than a globular cluster, however the luminous mass density is around 1000 times smaller. Different models are suggested to justify this particular property of dSphs which is discussed in details in Sect.9.2.1. Second, The stellar population of the dSphs is one of the oldest known stellar populations, which makes them interesting galaxies to study the evolution of galaxies. The evolution of some dSphs and its relation to their X-ray luminosity function (XLF) are studied in Chapter 8.

3.2 Properties of the Draco dSph

Draco dSph has the coordinate of Right Ascension (RA)= $17^h20^m19^s$, and Declination (Dec)= 57° 54′ 55″ [J2000.0]. Its major and minor diameters are 35.5′ and 24.5′ (Falco et al., 1999). King (1962) fit the stellar density profile with a core radius of 7.′7 and a tidal radius of 40.′1 (Odenkirchen et al., 2001). Deep photometric surveys show a central stellar density increasing inward from ∼2 to 0.′5 (Ségall et al., 2007). Age, distance, metallicity and other properties of the Draco dSph have been investigated in several works. In the following, we give a summary of results from the most recent studies, used or considered in our work.

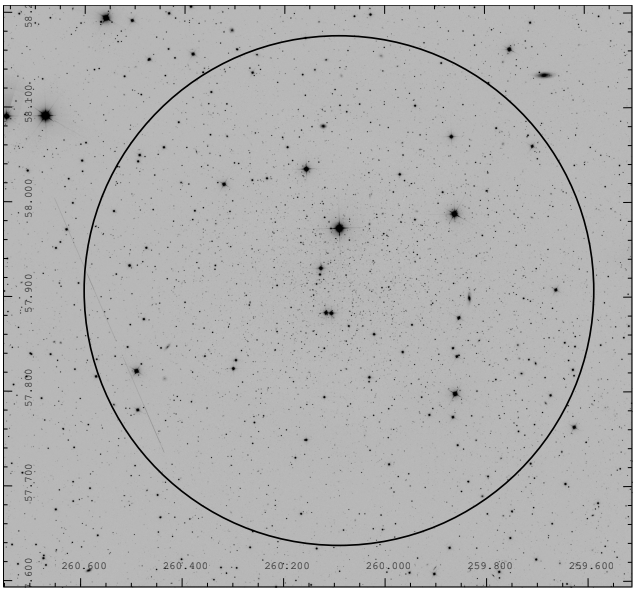

Figure 3.2: The Draco dSph in the optical r band of SDSS9 survey (Knapen et al., 2014). The circle shows the area which is detected in *XMM-Newton* observations of the Draco dSph.

Age

While dSphs are dominated by old populations, determining a single age is very difficult compared to single-population objects like globular clusters. Aparicio et al. (2001) studied the star formation history of the galaxy with two different models, based on the deep optical observations of three different fields which cover 1×1 of the Draco dSph in the B and R Johnson filters. The most important result of the Aparicio et al. (2001) survey is that the stellar population is fundamentally old (older than $\sim$ 10 Gyr). Some 90% or 75% (depending on the method) of the star formation in Draco dSph took place before $\sim$ 10 Gyr ago. After that, the star formation continued at a low rate, and apparently a small burst was produced around 2-3 Gyr ago. No star formation activity is detected in the analysis of the colour magnitude diagrams for more recent epochs.

Metallicity

Different studies with different approaches have been performed for finding the most accurate metallicity for the Draco dSph stellar population. Lehnert et al. (1992) suggested a mean spectroscopic metallicity of ~ -1.9 dex, based on 14 red giants and Shetrone et al. (2001) estimated a metallicity of at ~ -2.0 dex

based on six giants. Applying Padua isochrones[1] to Johnson B and R photometry Aparicio et al. (2001) found a mean photometric metallicity of -1.8 dex. Bellazzini et al. (2002) compared V and I photometry of Draco dSph red giants to globular clusters and derived a mean photometric metallicity of -1.7 dex. On the other hand, Klessen et al. (2003) who analysed a much larger area based on SDSS data, showed that the metalliicity from the central region of the Draco dSph might not be the same as the whole galaxy, due to the fact that the blue horizontal branch stars show a spatially more extended distribution than the red horizontal branch stars. Spatial gradients in the horizontal branch morphology are commonly found in dSph and are likely due to age spreads in the central regions of these (Girardi et al., 2004). The latest work has been done by Girardi et al. (2004) who fit well the theoretical isochrones line of their work, assuming an age of $log(t) = 10.1$ (Aparicio et al., 2001) to the SDSS7 observation of Draco dSph member (taking the source with uncertainties < 0.1 mag). They found that $Z = 0.0004 Z_{\odot}$(or $[Fe/H] = -1.7$ dex) is closest to the main body of the red giant branch of Draco dSph in different filters (see Fig. 3.3). However the mean metallicity from the comparison with the SDSS isochrone would be closer to the lower metallicity (-1.8 to -1.9 dex). We used the Girardi et al. (2004) isochrones in the colour-magnitude diagram to study the optical counterparts of the *XMM-Newton* sources (see Sect. 5.4.4).

Distance

Stetson (1979) estimated the distance of the Draco dSph at 72 ± 3 kpc using the position of red helium-burning stars. Nemec (1984) obtained a distance of 84 ± 12 kpc using RR Lyrae variability periods. Aparicio et al. (2001) estimated a distance of 80 ± 7kpc. The result of the most recent works of Bellazzini et al. (2002) by optical photometry suggests $(m - M)_0 = 19.84 \pm 0.14$ (yielding ~ 93 kpc). Observation of Cioni and Habing (2005) suggests $(m - M)_0 = 19.49 \pm 0.06(stat) \pm 0.15(sys)$. We used the most update distance measurement of 82.4 ± 5.8 kpc (Kinemuchi et al., 2008).

Properties of the Draco dSph in optical surveys

Based on the data of SDSS7, Rave et al. (2003) presented a catalogue containing 5634 objects in the Draco dSph. They selected sources with $15 < g < 23$. This catalogue of the Draco dSph sources are plotted in Figure 3.4. Dwarf spheroidal galaxies typically contain many variable stars, predominately RR Lyrae variables

[1] Padua isochrones is large grids of theoretical isochrones for different stellar initial chemical compositions and ages, which is performed by Bertelli et al. (1994) for the standard Johnson photometry.

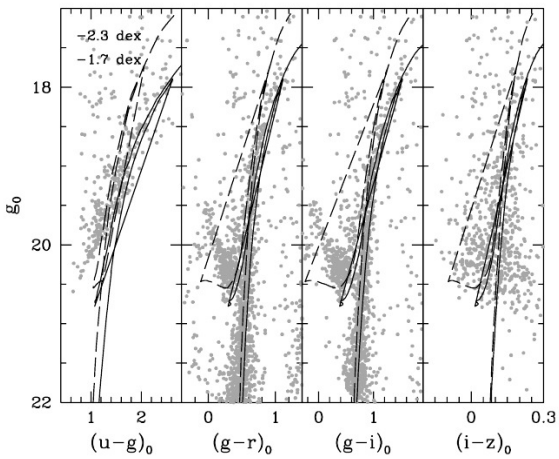

Figure 3.3: SDSS *ugriz* color-magnitude diagrams of the central $9.' \times 9.'$ of the Draco dwarf spheroidal galaxy for stars with photometric uncertainties < 0.1 mag (grey dots). With SDSS isochrones for ages of log(t)=10.1 and metallicity of -2.3 dex and -1.7 dex. The main concentration of the red giant branch of Draco lies blueward to the -1.7 dex isochrone (solid line)(Girardi et al., 2004).

typical of older, metal-poor stellar populations (Stetson, 1979). Draco is no exception. The first extensive study of Draco by Baade and Swope (1961) found 138 variable stars in the central part of Draco. Rave et al. (2003) also reported 142 variable star candidates, two of which were known AGNs. Figure 3.4 shows the position of the optical variable source in the colour magnitude diagram based on SDSS7 data. This study of the X-ray sources identified 19 AGNs whose optical counterparts occupied the same area of the colour-magnitude diagram as the variable stars. In addition, other works were dedicated to the problem of dark matter in the Draco dSph, as discussed in details in Chapter 9, all of the optical surveys of the Draco dSph consistently show that there is no evidence of a tidal stream in the galaxy.

Properties of the Draco dSph in near infrared surveys

The near infrared surveys of the Draco dSph are usually focused on the red giant branch, which is the dominant stellar population in this galaxy. The main goal has been to measure the age and the metallicity of the system. In our approach, classification of the red giant branch population in the Draco dSph is important for identifying X-ray sources as LMXB or CV candidates. We used the colour-colour diagram of (Fig. 3.5, Cioni and Habing, 2005) in some cases as mentioned in Chapter 5.

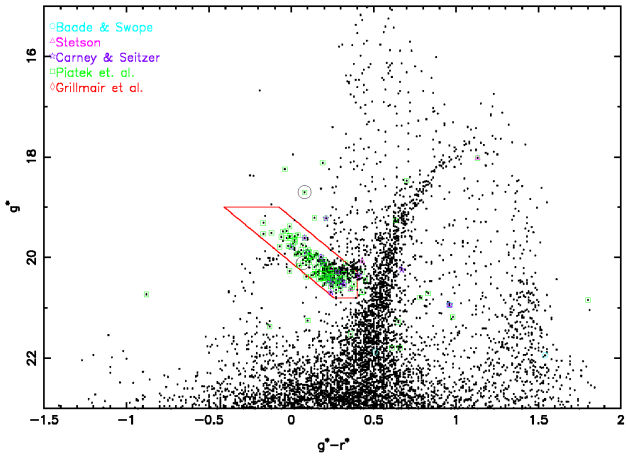

Figure 3.4: Colour-magnitude diagram of optical sources of the Draco dSph. The objects that are variable candidates are indicated with a different colour for each catalogue. Some objects are selected as variable in more than one catalogue. The colour-magnitude selection box for RR Lyrae variable candidates is indicated with red lines. The two known QSOs that were selected as variables are indicated by large black circles (Rave et al., 2003).

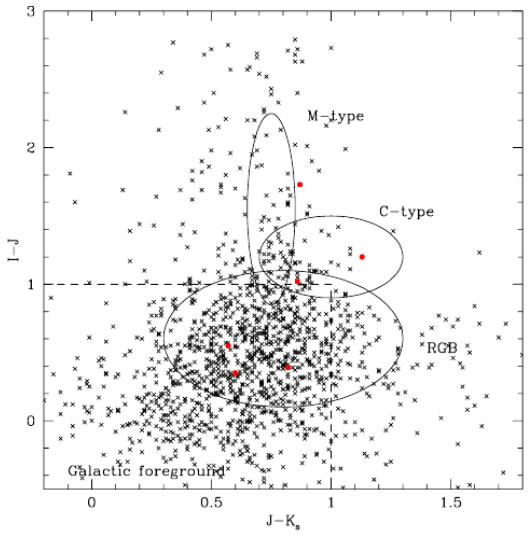

Figure 3.5: Colour-colour diagram of Draco dSph stars detected in three near infrared bands I, J, K with $\sigma_I < 0.18$ mag. Regions of expected RGB, C-type and M-type AGB stars as well as Galactic foreground stars are indicated. Known carbon stars are marked with thick dots (Cioni and Habing, 2005).

Chapter 4

Observatories

Data of the X-ray telescopes *XMM-Newton* and *Swift* have been used in this work. This chapter is a summary of the hardware equipment and the observation process for both telescopes.

4.1 *XMM-Newton* observatory

The X-ray Multi-mirror Mission (*XMM-Newton*) observatory[1] was launched on December 10, 1999 into a highly eccentric, 48 hour orbit. *XMM-Newton* is a key project of the European Space Agency (ESA) in ESA's Horizon 2000 program. In this chapter, we review the major characteristics of the observatory and its instruments. The design-structure of the spacecraft, the structure of the X-ray telescopes, and the details of the X-ray detectors, known as European Photon Imaging Cameras (EPICs), Reflection Grating Spectrometer (RGS), and Optical/UV Monitors, will be explained.

4.1.1 Spacecraft

With 4 tonne mass and 10 m length, *XMM-Newton* is one of the largest spacecrafts launched by ESA (Jansen et al., 2001). The scientific goal is to maximise the collecting area for spectroscopy and complementing the imaging capability of the Chandra X-ray Observatory (Weisskopf et al., 2000). The design contains 6 co-aligned instruments: Three imaging X-ray cameras, the European Photon Imaging Cameras (EPICs), two grating X-ray spectrometers (RGSs), and an optical monitor (OM). The spacecraft consists of four main sections as it is shown in Figure 4.1 and explained in the following:
1. The focal plane assembly (FPA), which contains a platform to carry two RGS

[1] XMM is the abbreviation of the X-Ray Multi-Mirror Mission

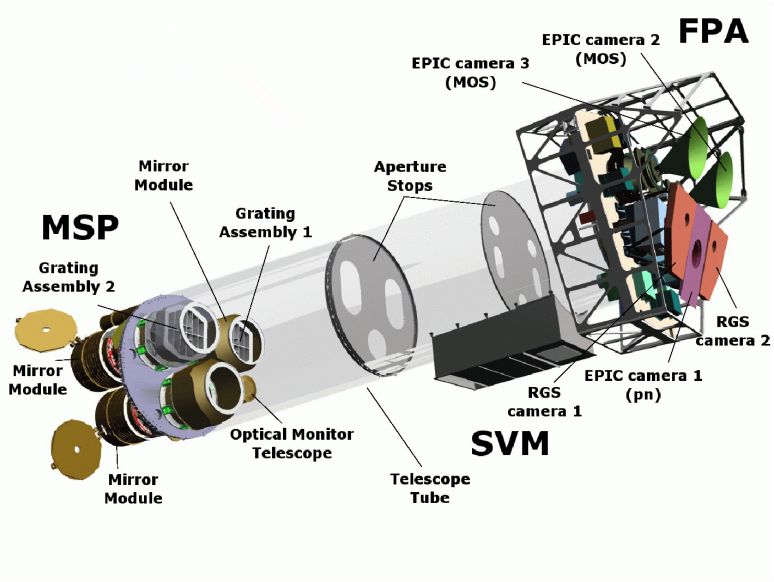

Figure 4.1: View of the *XMM-Newton* spacecraft subsystem. The external structure is removed for clarity. Credit: Image courtesy of ESA. The labels of the equipment according to Lumb et al. (2012)

cameras, three EPICs cameras, electronics boxes and the radiators, which passively cool the charged coupled devices (CCDs) of the EPICs camera.
2. The mirror support platform (MSP), which carries three mirror assemblies, the OM, and two star-trackers.
3. The service module, which carries the spacecraft subsystems, two solar-array wings, telescope sun shield and two S-band antennae.
4. The long carbon fibre tube, which keeps the separation of the FPA and MSP.

4.1.2 X-ray telescope

The three X-ray telescopes have a scheme as shown in Figure 4.2. Each telescope consists of the following elements:
1. Mirror door to protect the X-ray optics and telescope interior against contamination when telescope is not in operation.
2. Entrance baffle which suppresses the visible stray lights.
3. X-ray baffles which are located in front of the mirror systems. They act as collimators and considerably reduce the amount of stray light in the FOV of the focal plane cameras.

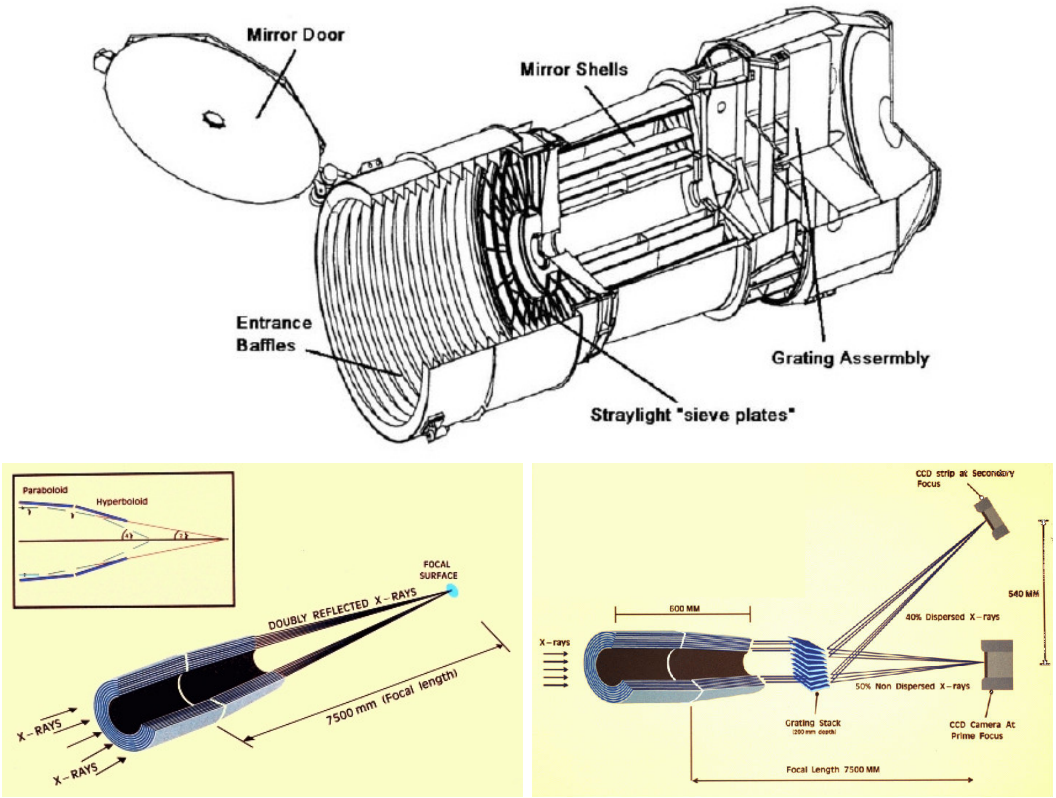

Figure 4.2: Upper image: *XMM-Newton* telescope assembly (Lumb et al., 2012); lower images: (Left) the light path in the *XMM-Newton* telescope with EPIC-pn camera in its primary focus. (Right) The light path in the two EPIC-MOS telescopes each with a reflection grating array (RGA) mounted in the optical path (Credit: Image courtesy of ESA).

4. Mirror shells which consist of 58 mirrors. A mirror module is a Wolter I type[2] grazing incident telescope with a focal length of 7.5 m and the resolution of ~ 15 in the energy range of $0.1 - 12$ keV. The mirror length is 600 mm and the effective area at 1 keV is 1500 cm^2 (Lumb et al., 2012). The X-ray mirrors are nickel shells covered with thin monolithic gold (250 nm layer) and the mass of the mirror module is 420 kg (de Chambure et al., 1998).

[2] Due to the very small incident angle required for the reflection of X-rays, it is not possible to focus the light using a focal mirror like in optical telescopes. The critical angle for a photon with the energy of 1 keV is 1 and it shows that a very large focal length is necessary to focus the X-ray beams. To decrease this focusing length special methods were suggested by Wolter (1952a,b). The configuration which is used in *XMM-Newton* is the Wolter I configuration, which reflects the X-ray emission twice, first with paraboloid mirror shells and then with hyperboloid mirrors. By using this method the length decreases considerably. Figure 4.2 shows the scheme of the reflected X-rays in Wolter I mirror in *XMM-Newton*.

5. Electron deflector which produces a toroidal magnetic field to divert the soft electrons. This deflector is located behind the mirror module.
6. Reflection grating assembly (RGA), with a mass of 60 kg, are mounted in the light path of the two X-ray telescopes with EPIC-MOS cameras at their primary focus. Each RGA intercepts about 58% of the total light focused by the mirror module.
7. Exit baffle which provides an appropriate thermal environment for the grating.

The performance of each X-ray telescope is characterised by 3 different factors:
1. The image quality: The quality of an X-ray mirror module depends on its ability to focus photons. The point spread function (PSF) of the X-ray telescope depends on the source off-axis angle, i.e., its distance from the centre of the FOV. Each of the three Wolter I type X-ray telescopes on board *XMM-Newton* has its own PSF. In general, the core of its on-axis PSF is narrow and varies a little over a wide energy range ($0.1 - 6$ keV). Above 6 keV, the PSF becomes slightly energy dependent (Read et al., 2011).
2. The effective area: The second important characteristic of the mirror performance is their effective area, which shows the ability of the mirrors to collect radiation at different photon energies. EPICs in full frame mode and with thin filter are effective between the energy range of $0.1 - 10$ keV and have the best response at around 1.5 keV. The effective area of the EPIC-MOS camera is less than that of EPIC-pn because they receive less X-ray emission compared to the EPIC-pn camera (see Fig.4.2). It should be considered that, like the PSF, the effective area is also a function of the off-axis angle. With increasing off-axis angle, less photons entering the telescopes actually reach the focal plane. This effect is called vignetting. The effective area of the camera decreases by increasing off-axis angle.
3. The stray-light rejection efficiency: X-ray stray light on EPICs is produced by X-rays reflected only once by the mirror hyperbolas and reaching the sensitive area of the camera. The X-ray baffle is responsible to shadow those singly reflected rays (XMM-Newton Users Handbook, 2013).

EPIC instruments: EPIC-pn and EPIC-MOS cameras

As mentioned before, three X-ray CCD cameras onboard *XMM-Newton* are called EPICs. Two of the EPIC-MOS cameras contain the RGA and more than half of the incident flux is diverted to the RGS detectors. Around 44% of the total incoming flux is detected by the EPIC-MOS cameras.
All EPIC cameras are located in the focal point of the related mirror module and performs imaging observation over the telescope field of view of 30 in the energy

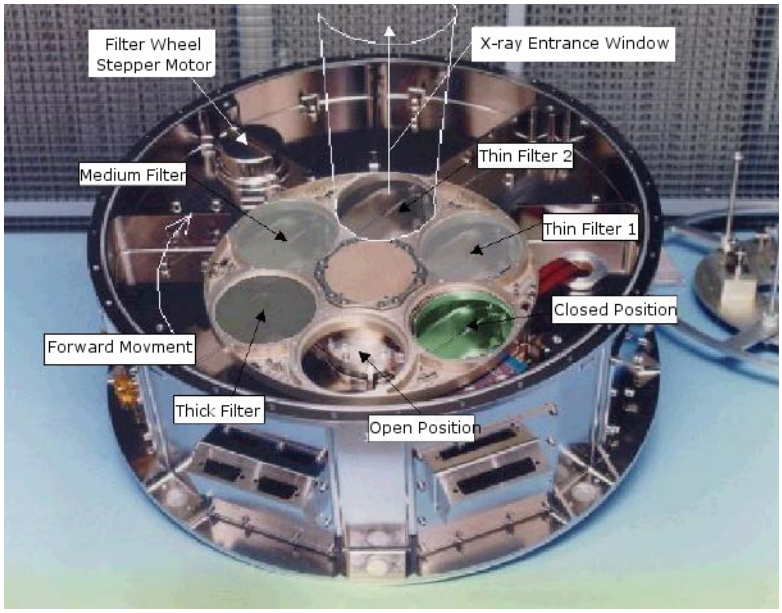

Figure 4.3: The EPIC stand-off structure. The aluminium structure is nickel plated to reduce vacuum out-gassing. It houses the filter wheel, calibration source, and the door; the bulkhead is part of the vacuum enclosure. It is located on the spacecraft bulkhead using drilled bushes to bring the optical centre of the camera to the optical axis of the mirror (Turner et al., 2001)

range of $0.15 - 15$ keV (Lumb et al., 2012).
Each EPIC camera has three parts:
1. The stand-off structure, which contains the filter wheels, door, calibration source, interface of the spacecraft, radiation shield, and the internal vacuum bulkhead. As it is shown in Figure 4.3, there are six locations for filters and six apertures through which a source can shine on the CCDs. The apertures were closed before and during the launch. The CCDs are protected against damaging protons by a 3 cm aluminium shielding in all direction except along the FOV.
2. The cryostat section which holds the CCDs and electronic interfaces. Figure 4.4 shows the EPIC-MOS CCD inside the cryostat.
3. The radiators cool the EPICs and provide the minimum temperature of -140 K for the CCDs. There are some outer radiator to provide thermal shielding for the inner radiator which are cooling the CCDs with connection to cold finger and the thermal shroud around CCDs.

There are seven CCDs in the focal plane of each EPIC-MOS camera. The central CCD is at the focal point on the optical axis of the telescope and the outer six CCDs are shifted toward the mirror by 4.5 mm to follow the focal plane curvature.

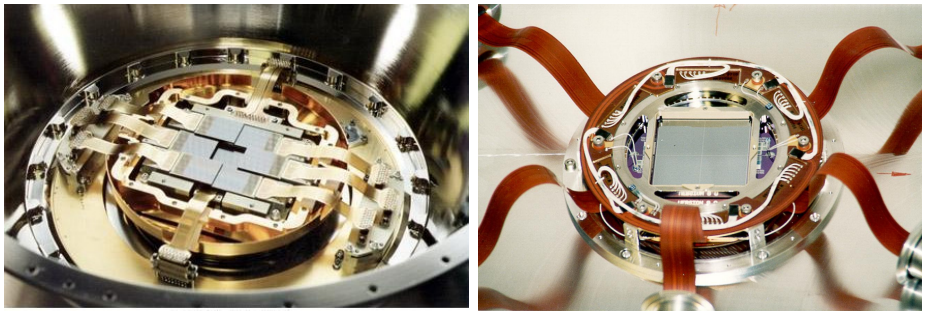

Figure 4.4: CCD structures of the EPIC cameras. (Left) The CCDs of one of the EPIC-MOS cameras in the cryostat. (Right) The CCDs of the EPIC-pn camera. (Credit: Image courtesy of ESA)

The imaging area of EPIC-MOS is $\sim 2.5 \times 2.5$ cm and the mosaic of the seven CCDs cover the focal plane of 62 mm diameter which is equal to $28'.4$ (Turner et al., 2001). The essential part of EPIC-pn detector is a 4 inch silicon wafer divided into 12 monolithically implanted CCDs. The total effective size is 6×6 cm^2 (Lumb et al., 2012). In EPIC-pn each three CCDs are arranged as one quadrant and each quadrant can be considered as a separated unit, which has separated power supplies, back contact, preamplifiers, and event analyser electronics, Therefore each quadrant can operate independently from the others. The focal point of the X-ray telescope is at the central CCD of quadrant 1 (Strüder et al., 2001). Around 97% of the detectors is illuminated by the telescope. The remaining area of ~ 6 cm^2 is out of FOV and applied for the background studies (Strüder et al., 2001).
In order to cover the gap between the CCDs, the FOVs of the CCDs of the two EPIC-MOSs are orthogonal with respect to each other. It means that the gaps between the outer CCDs in one camera are covered by the CCD of the other camera. However, the gaps around the central CCDs in both EPIC-MOS cameras overlap. To solve this problem, the EPIC-pn CCDs are oriented 45 degree with respect to the EPIC-MOS, Therefore, the total area of the FOV is covered by three cameras.
The basic read out speed of the EPIC-MOS and EPIC-pn are 2.6 s and 74 ms respectively. This speed can be changed if either a source is bright and the problem of pile-up would occur, or a fast timing observation is necessary (Turner et al., 2001). Different operating mode are available for the CCDs. Figure 4.5 shows which part of the CCD array in EPIC-MOS and EPIC-pn cameras are read out in the different modes. In *XMM-Newton* cameras six different observing modes are defined: full frame, extended full frame, large, small, timing, and burst mode. The extended full frame and burst mode are only available for the EPIC-pn. Table 4.1 shows the imaging area and time resolution in each mode for EPIC-pn and

EPIC-MOS cameras. In the full frame and extended full frame mode all pixels of all CCDs are read out and thus the full FOV is covered. For EPIC-pn, in the large window mode only half of the area in all 12 CCDs is read out, whereas in Small Window mode only a part of CCD number 4 is used. In EPIC-MOS, the central CCD of both MOS cameras can be operated in a different mode. In the timing mode, imaging is made only in one dimension. The data from a predefined area on one CCD chip are collapsed into a one-dimensional row to be read out at high speed. Since the two EPIC-MOS cameras orientation differ by 90 degrees, the imaging directions in them are perpendicular to each other. For the EPIC-pn, there is timing mode which is called burst mode and it offers very high time resolution, but has a very low duty cycle of 3% (XMM-Newton Users Handbook, 2013).

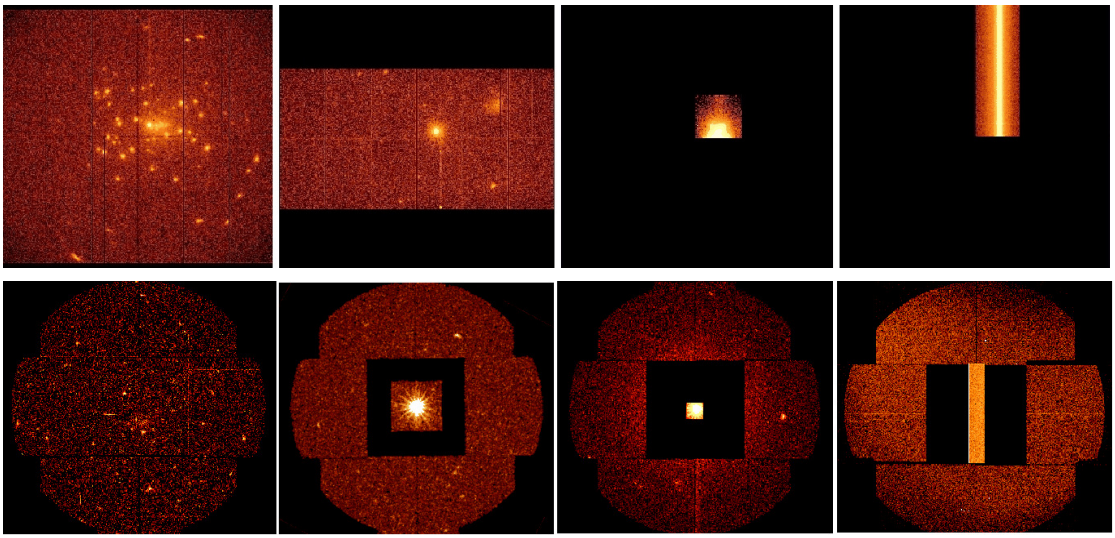

Figure 4.5: Up: Images of the EPIC-pn camera in the different operating read out modes: Full frame image, Large window, Small window, and Timing. Down: Images of the EPIC-MOS camera in the different operating modes: Full frame image, Large window, Small window, and Timing (Credit: XMM-Newton Users Handbook, 2013).

RGS instruments

XMM-Newton carries two identical RGS behind two of its three nested sets of Wolter I type mirrors (mirrors of EPIC-MOS instruments, den Herder et al., 2001). The instrument allows high resolution ($E/\Delta E = 100 - 500$) measurements in the soft X-ray range ($2.1 - 0.3$ keV). Each reflection grating array (RGA) contains 182 identical gratings. As mentioned before, the role of these grating stacks is

Table 4.1: Summary of EPIC-MOS and EPIC-pn readout modes.

CCD Mode	Imaging Area		Time Resolution	
	EPIC-pn (Pixels)	EPIC-MOS (Pixels)	EPIC-pn	EPIC-MOS
Full frame	376×384	600×600	73.4 ms	2.6 s
Extended full frame	376×384	-	199.1 ms	-
Large window	198×384	300×300	47.7 ms	0.9 s
Small window	63×64	100×100	5.7 ms	0.3 s
Timing*	64×200	100×600	1.75 ms	0.03 ms
Burst	64×180	-	7 μs	-

$\star$: The timing mode provides even higher time resolution but with low duty cycle (*XMM-Newton* users handbook, 2013).

the diversion of more than half of X-ray incoming flux to the focal plane camera which contains nine CCDs (see Fig. 4.2). The separation of spectral orders is accomplished by using the energy resolution of the CCDs. In addition this energy resolution provides the means for background suppression since it is required that events have the correct pulse height, corresponding to their spatial position in the spectrum.

4.1.3 Optical/UV monitor

The Optical/UV Monitor Telescope (XMM-OM Mason et al., 2001) is an instrument that is mounted on the mirror support platform of *XMM-Newton* alongside the X-ray mirror modules. It covers the wavelength between 170 nm and 650 nm of the central 17 square region of the X-ray FOV. Because of the low sky background in space, *XMM-Newton*-OM is able to achieve impressive imaging sensitivity compared to a similar instrument on the ground, and can detect a $B = 23.5$ mag A-type star in a 1000 s integration in its "white light" filter (6 sigma). The XMM-OM consists of a Telescope Module and a separate Digital Electronics Module, of which there are two identical units for redundancy. The Telescope Module contains the telescope optics and detectors.

4.2 *Swift* observatory

4.2.1 Introduction

The *Swift* gamma-ray burst (GRB) Explorer was launched in November 2004 (Gehrels et al., 2004). Due to the importance of the detection of GRBs, NASA with the cooperation of the an international team designed and built *Swift*. It is a medium size explorer mission which carries three instruments: a Burst Alert Telescope (BAT), which identifies GRBs and determines their location on the sky to within a few arcminutes; an Ultraviolet/Optical Telescope (UVOT); and an X-ray Telescope (XRT). Here we summarise the characteristics of each instrument in particular to the XRT, which had been used in this work to detect one of the LMXB candidates in the field of the Draco dSph (see Sect. 7.3.1). Figure 4.6 shows the arrangement of the instruments in the satellite. To understand the capability of *Swift* to detect γ-ray flashes, we quickly review the main characteristics of the GRBs and the *Swift* on board telescopes.

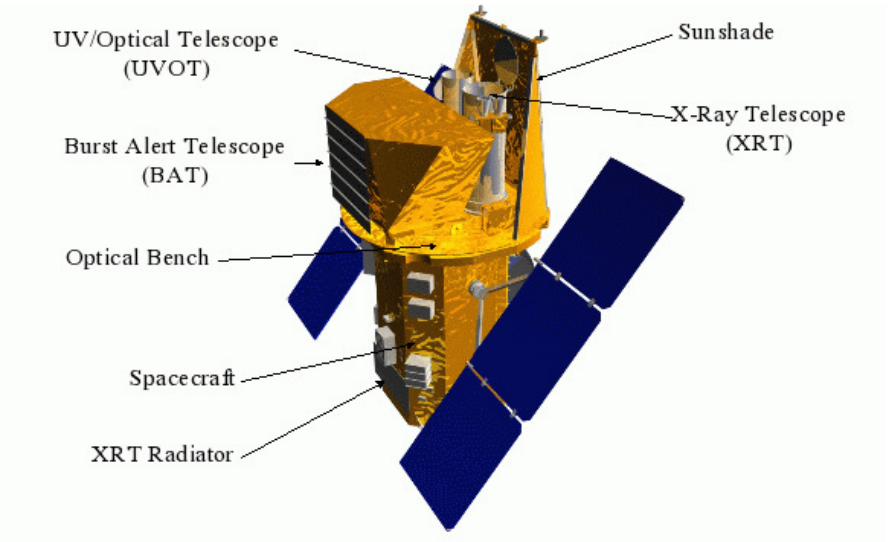

Figure 4.6: The *Swift* satellite, (credit: *Swift* website)

Gamma-ray bursts

Gamma-ray bursts (GRBs) are bright flashes in γ-rays that are isotropically distributed on the sky and are observable on earth at a rate of almost one per day. The duration of the burst can be a fraction of a second to several hundred seconds. The bursts are divided into two groups according to their overall duration

T: long bursts with T $>$ 2 s and short bursts with T $<$ 2 s. By assuming a redshift of $z \sim 1$, the energy released from the γ-ray flashes is around $10^{51} - 10^{52}$ ergs. Assuming radiation is beamed, the energy of a GRB is comparable to the total energy released by a supernova (Piran, 2004). There are different models suggested to explain GRBs on different time scales. The main model invokes the merger of either two NSs, or a NS with a black-hole (BH) (e.g, Eichler et al., 1989). Other models such as the formation of rapidly rotating highly magnetised NS (Usov, 1992), the cataclysmic collapse of a single massive star (Woosley, 1993; Paczyński, 1998), and the collapse of a super-massive NS to a BH (Vietri and Stella, 1998) are also considered to explain the various properties of GRBs. It is also shown that according to the accretion theories, cataclysmic collapse of a single massive star (collapsar) can produce long GRBs and only NS–NS (or NS–BH) merger can produce short bursts (Narayan et al., 2001). The GRBs are followed by an afterglow, a lower luminosity, long lasting emission in the X-ray, optical and radio band.
The following three parameters can be measured directly in prompt observations of GRBs and allow the study of their progenitors: the total energy released, the nature of the host galaxy (if one exists), and the location of the burst within the host galaxy. The angular resolution of XRT and UVOT allows to determine the precise location of the BAT-discovered bursts (Gehrels et al., 2004).

4.2.2 Burst alert telescope

The Burst alert telescope (BAT) is the instrument which first detects the GRB and localises the burst direction to an accuracy of 1-4 arcmin within 20 sec after the start of the event (Barthelmy, 2004). The energy range is $15 - 150$ keV for imaging. Within the first 10 s of detecting a burst, BAT will calculate an initial position, decide whether the burst merits a spacecraft slew, and, if worthy, send the position to the spacecraft. BAT uses a two-dimensional coded mask and a large-area solid state detector array to detect weak bursts and has a large FOV to detect a good fraction of bright bursts. The detection algorithm of the BAT is upgraded based on the HETE–2 (High Energy Transient Explorer, Ricker et al., 2003) which looks for excesses in the detector count rate above the expected background and constant sources.
BAT has two main operative modes: burst mode, which produces burst position, and survey mode, which produces hard X-ray survey data. In the survey mode BAT collects count rate data with a time bin of 5 minutes for 18 different energy bands. This hard X-ray survey has two benefits: first, it provides a sensitive hard X-ray all sky survey, and second, sources which are found in these images are compared against an on board catalogue of sources. Those sources either not listed in the catalogue or showing large variability are deemed transients. A

subclass of long smooth GRBs that are not detected by the burst trigger algorithm may be detected with this process (Gehrels et al., 2004).

4.2.3 X-ray telescope

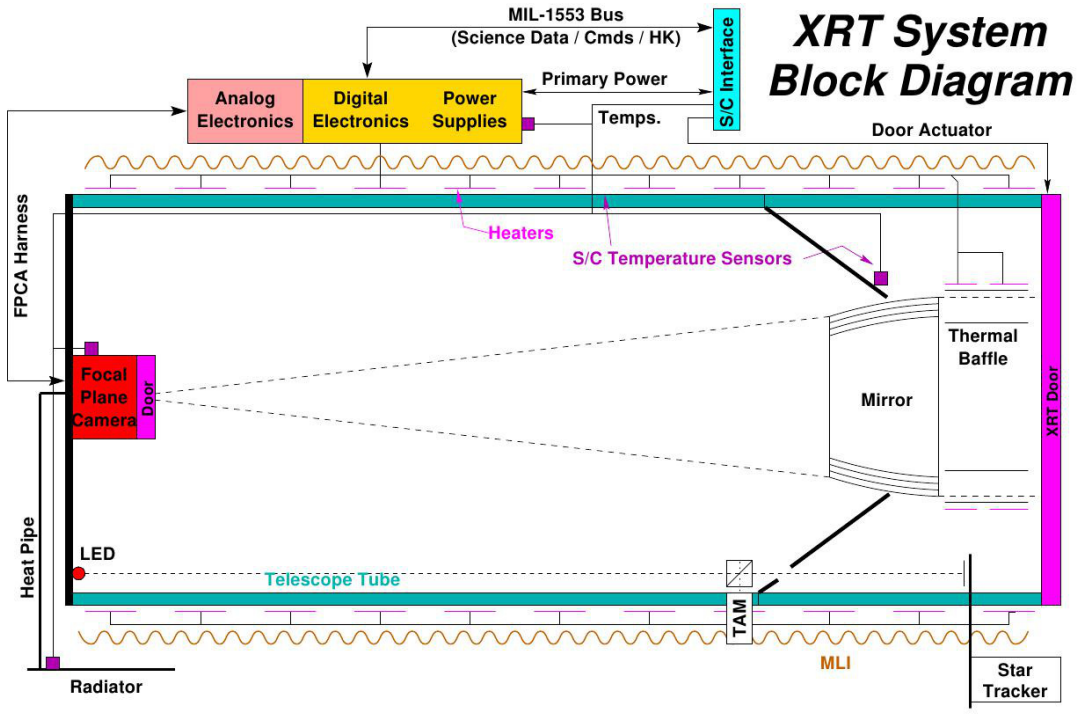

Figure 4.7: A block diagram of the *Swift* X-ray telescope (XRT)(Burrows et al., 2005).

The X-ray telescope (XRT) is a focusing X-ray telescope which uses a grazing incidence Wolter 1 telescope to focus X-rays onto a CCD. The complete mirror module for XRT consists of the X-ray mirrors, thermal baffle, a mirror collar, and an electron deflector (Figure. 4.7). A telescope tube holds the focal plane camera containing a CCD–22 detector. The CCD-22 detector was designed for the EPIC-MOS instrument on *XMM-Newton*. The CCD has an imaging area of 600×602 pixels (40×40 mm) which is sensitive in the energy range of $0.2-10$ keV. The effective area of the of the telescope is 110 cm^2, and the FOV is 23×23.
Three main read out modes are defined for the XRT to ensure that it coves the rapid variability of the GRB afterglows:
1. Imaging mode which produces an integrated image measuring the total energy deposited per pixel. Spectroscopy is not possible because of the highly piled-up

image. However, this mode produces an accurate position and also a good flux estimation. 2. Windowed timing mode can not provide an accurate position, but produces high time resolution data (2.2 ms) and a bright source spectroscopy through fast CCD readout. 3. Photon-counting mode uses sub-array windows with a time resolution of 2.5 s to permit full spectral and spatial information especially for sources with a flux around or below 1 mcrab (Burrows et al., 2005; Gehrels et al., 2004).

In serendipitous surveys, the XRT can start to observe the GRB before the end of it. This long observation provides an accurate position of GRB within the 5 seconds of the typical burst, allowing the ground-base optical telescope to immediately observe the afterglow (Burrows et al., 2005). Furthermore, it is also possible for the ground-base Gamma-ray (e.g, the HESS observatory) telescopes to catch the GRB afterglow in the case that they can catch the flash position promptly (e.g., Fan et al., 2008).

4.2.4 Ultra-Violet/Optical telescope

The Ultra-Violet/Optical telescope (Roming et al., 2005) design is based on the OM on board *XMM-Newton* (see Sect. 4.1.3). UVOT is co-aligned with the XRT. Low resolution spectra of bright GRBs and broadband UV and optical photometry is possible with this telescope. The CCD has 385×288 pixels which provides a 17×17 FOV.

The guest investigator programme of *Swift* allows scientist to submit observational proposals in the field of GRBs and also of other kind of transient sources. To have more information about source XMMUJ172140.6+580244 as a pulsing LMXB candidate, we submitted a proposal for a 10 ks observation with XRT in imaging mode (see Sect. 7.3.1). The XRT pipeline produces cleaned, calibrated event list files and standard products for the observation. We performed the pipeline source detection process according to the steps of the *Swift* XRT data reduction guide (version 1.2, NASA).

Chapter 5

Observations and data analysis

5.1 Observations

We analysed the public archival *XMM-Newton* (Jansen et al., 2001) observations of the Draco dwarf spheroidal galaxy (dSph). Table 5.1 summarises the used *XMM-Newton* observations and shows the details including identification, date of observation, instrument mode, filter, and the flare-filtered exposure time – after screening of high background (see Sect. 5.2.2)– for the three cameras EPIC-pn and two EPIC-MOS cameras, (see Sect. 4.1.2). All observations have the same pointing at the centre of the galaxy (RA= 17^h 20^m $12^s.40$, Dec= +57° 54 55.″3, J2000). In all observations EPIC-pn and EPIC-MOS cameras were operated in the full-frame mode with a time resolution of 73.4 ms and 2.6 s, respectively. The observations were taken from 2009-08-04 to 2009-08-28.

5.2 Data analysis software

Data analysis was performed using the *XMM-Newton* Scientific Analysis System (SAS) [1] version 11.0.1 to 13.5.0, which is a collection of tasks, scripts and libraries, specifically designed to process and analyse data collected by the *XMM-Newton*. The software `xspec`[2] version 12.8.1 was used for spectral analysis (Arnaud, 1996). We also used `ftools`[3] (Blackburn, 1995) software package version 5.3.1, as well as `ds9`[4] (Joye and Mandel, 2003). Shell scripts were used for analysis chains. We used `IDL` version 8.1 for calculations and diagrams.

[1] the `SAS` homepage http://xmm.esac.esa.int/sas/
[2] http://heasarc.nasa.gov/xanadu/xspec/
[3] http://heasarc.gsfc.nasa.gov/ftools/fv
[4] http://ds9.si.edu/site/Home.html

5.2.1 Data pre-processing

For each *XMM-Newton* observation data are provided in the file ODF, which includes the raw event files of all instruments, housekeeping files, radiation monitor files, and spacecraft files. These data are processed applying the newest calibration files using the latest version of `SAS`. Since `SAS` tasks need calibration information from the calibration access layer (CAL), first, we ran the tasks `cifbuild` and `odfingest` to match the input data with calibration files of CAL. For EPIC-MOS cameras, the task `emproc`, and for EPIC-pn camera the task `epproc` were run to create the calibrated photon event lists. At this stage, the output files are event files contaning the information of each event, i.e. the position of the detected event on CCD, the detection time, the energy, and the pattern of the detected photons.

Table 5.1: *XMM-Newton* observations of the Draco dSph

ID ⋆	Observation ID	Observation Date	EPIC-pn		EPIC-MOS1		EPIC-MOS2	
			mode/filter†	T.exp [ks]*	mode/filter†	T.exp [ks] *	mode/filter†	T.exp [ks]*
OBS1	0603190101	2009-08-04	FF/Thin1	17.0	FF/Thin1	18.6	FF/Thin1	18.6
OBS2	0603190201	2009-08-06	FF/Thin1	18.0	FF/Thin1	19.4	FF/Thin1	16.4
OBS3	0603190301	2009-08-08	FF/Thin1	12.5	FF/Thin1	12.7	FF/Thin1	12.8
OBS4	0603190401	2009-08-20	FF/Thin1	3.1	FF/Thin1	9.3	FF/Thin1	7.2
OBS5	0603190501	2009-08-28	FF/Thin1	18.0	FF/Thin1	19.6	FF/Thin1	19.6

⋆: IDs used in the text.
†: FF: full frame.
∗: T.exp: exposure time after screening for high background.

5.2.2 High background contamination

We screened the high energy background to exclude the time of high background due to soft proton flares. High energy background light curves were constructed from the source-free regions of each observation. For creating the light curves, the task `evselect` was run with a time-bin-size of 10 seconds. The light curves for each observation are shown in Appendix 11. According to the light curve, good time intervals (GTI) which have low background were determined and selected. The net exposure was obtained by filtering out the flare by running `tabtigen`. The net exposure times are shown in Table 5.1. Since for OBS4, there were two event files of EPIC-MOS, we merged the two event files (by running task `merge`) and filtered the flares. Because of the long duration of flares in this observation, the net exposure time is shorter than the others (see Table 5.1).

5.2.3 Images of single observation

For each observation, data were split into five energy bands: B1 $(0.2 - 0.5$ keV), B2 $(0.5 - 1.0$ keV), B3 $(1.0 - 2.0$ keV), B4 $(2.0 - 4.5$ keV), and B5 $(4.5 - 12$ keV). Single to quadruple pixel events (PATTERN ≤ 12) were used for all five energy bands of EPIC-MOS. In the EPIC-pn, for the first energy band only single-pixel events (PATTERN $= 0$), and for the other energy bands single and double-pixel events (PATTERN ≤ 4) were used. This selection is applied because of the relatively higher noise in the softest EPIC-pn band. For creating images, we ran `evselect` on the filtered event files. In EPIC-MOS we used an image bin-size of 22 in both X and Y axises which is equal to $1\farcs1$, and in EPIC-pn, we used a image bin-size of 84 which is equal to $4\farcs2$.

5.2.4 Mosaic image

Since longer exposure time increases the chance of the detection of faint sources which were not detected in single observations, we merged all EPIC images of all observations to create mosaic images. In the first step of preparing the event files for the mosaic image, we ran the task `emosaic-prep` to separate the calibrated event files in "EPIC–Mosaic" mode. We were allowed to select one pattern for the calibrated event file in each EPIC. Therefore, the EPIC-pn (PATTERN ≤ 4) was selected for the first energy band instead of (PATTERN $= 0$). Due to this new pattern, to avoid high fluctuation in the soft band of the EPIC-pn, we set the lower cut of the first energy band into 0.3 keV. In the next step, the task `emosaicproc` was performed to run source detection on mosaic image. The output files contain exposure maps, detector mask images, background maps, and the mosaic source

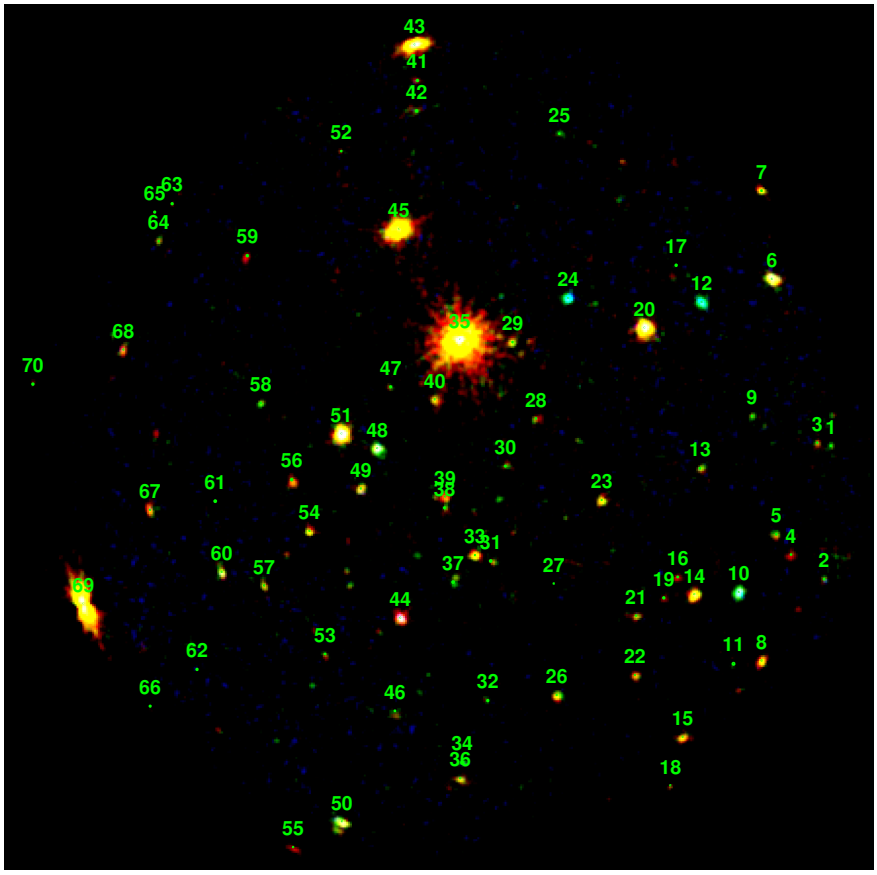

Figure 5.1: The logarithmically scaled mosaic RGB image of *XMM-Newton* observations in the field of the Draco dSph. The images are smoothed with a 2D-Gaussian with a kernel radius of 1.5 pixels.

list. In the last step, we produced combined mosaic images by running the task `emosaic`. The mosaic RGB (red-green-blue) images of EPIC-pn and EPIC-MOS is shown in Figure 5.1. The colours represent the X-ray energy ranges, $0.3 - 1.0$ keV (red), $1.0 - 2.0$ keV (green), $2.0 - 12$ keV (blue). The images are smoothed with a 2D-Gaussian with a kernel radius of 1.5 pixels.

5.2.5 Source detection

In the process of source detection, we ran the `SAS` task `edetectchain` separately for the images of each observation/EPIC and simultaneously for five energy bands. The task `edetectchain` is a script consisting of the `SAS` tasks `eexpmap`, `emask`, `eboxdetect` (local mode), `esplinemap`, `eboxdetect` (map mode), `emldetect`, and `esensmap`.

The task `eexmap` creates an exposure map by using the images, the attitude file, and the event files. In the next step, the detection mask for exposure map is created by the task `emask`. This mask contains the integer values 0 and 1. The value 0 is selected when the value of exposure map is less than 30% of maximum value of the exposure and the gradient of the exposure map is steeper than 0.5.
In the next step, `eboxdetect` performs a preliminary source detection and creates a list of source positions, where the background is calculated from a window around each source. We selected the maximum detection likelihood of 10 as a threshold for detecting the sources. The detection likelihood of sources in an *XMM-Newton* data set is calculated based on several parameters (e.g, PSF of sources, their extension, cash statistics in each defined energy band). Finally, the detection likelihood is defined by $L = -ln(p)$ where p is the probability of poission random fluctuation of the counts and can be used to calculate the confidence level of observation. This probability is calculated from the raw counts of the source and the raw counts of the background.
By removing the detected sources, `esplinemap` creates a spline background map by using the list of sources created by `eboxdetect`. We used the number of spline nodes of 16. At this time, the spline map of background helps to improve the detection sensitivity. The task `eboxdetect` is run again this time in map mode (`usemap=yes`). We took the default minimum detection likelihood of 8. The task `emldetect` generates the final list of sources (emllist). It performs a simultaneous PSF fits to the source count distribution in all energy bands for each EPIC for all sources with a maximum likelihood (ML) > 10. This task does not find any new source but characterises the detected sources by taking three parameters, the source count rate, source position (RA, Dec), and source extent.
Finally, the task `esensmap` is run to create the sensitivity map specially to have an upper-limit flux of the expected sources which are not detected by the process of source detection. We can run it just for one band or simultaneously for all energy bands.
As the result of source detection, the output files generated for each EPIC are background maps, exposure maps, sensitivity maps, detector mask image, and final source list which includes the source coordinates, source counts, source image pixels X and Y, source extent (image pixel), ML of detection, likelihood of extent, background at source location (counts/pixel), exposure at source location (seconds, vignetting corrected), source count rate (counts/sec), hardness ratios, vignetting, integration time (not vignetting corrected), and quality flag.

5.2.6 Catalogue of sources

Sources were detected on images of all observations in all energy band, as well as different energy band mosaic images. Source detection was limited to ML>10

(corresponding to $\sim 3.9\sigma$ level of confidence for a detection in one camera image). Table 12.1 shows the detection ML of each source, for EPIC-pn camera as well as the average of ML in each observation, and the ML of mosaic image. Table 12.2–12.4 shows the XID flux ($0.2 - 4.5$ keV) for each EPIC observation. ″N″ represents the case that source is located out of filed of view (FOV) of instrument, and ″G″, shows when it is located on a gap or damaged pixel(s). If the source inside FOV is not detected by an instrument, the upper limit is given as ″<″. The method of the calculation of the upper-limit is explained in Sect. 6.3. In each observation, we detected about 60 – 65 sources with EPIC-pn and 15 – 25 with MOS1/2. Eight sources were artifacts, i.e., false sources detected on, e.g., bad pixels or chip edges, and were removed from the source list.
Since we performed source detection separately for all observations for each EPIC and each energy band, we had to combine the results to obtain a final source catalogue. First, we examined each list of detections by visual inspection and removed spurious sources caused by bad pixels, hot columns, gaps, or edges of the CCD chips. After all the artifacts were removed, the source lists of all observations for all EPICs and all five energy bands were combined into one source list.

We obtained 70 sources as X-ray sources in the field of the Draco dSph. Most of the sources were detected in more than one pointing which allows us to study their X-ray variability (see Sect 6.3). The general properties of the sources is shown in Table 7.3, which contains the position of each source, total count rate and total flux ($0.2 - 12$ keV), and hardness ratios. The selected position of sources corresponds to the position of the detection on a camera and observation with the best (highest) ML. The weighted flux and its error calculated using the energy conversion factor (ECF) is explained in Sect. 6.3. Hardness ratios (HRs) are calculated and given for all sources. The HRs for each source are the weighed HRs of the observation with the best statistics. Since the HRs are considered a sensitive tool for representing the spectral type of source, it is only trustful if the corresponding count rates in each energy band have significance higher than 3σ. Therefore, we considered the hardness ratios of sources significant if the detection MLs of the related energy bands were more than 6. Section 6.5 shows how the HRs are used as a tool for the source classification. For each of the detected sources, we derived the X-ray flux (in units of erg s^{-1} cm^{-2}) in each energy band using the relation:

$$F_{\rm i} = \frac{B_{\rm i}}{ECF_{\rm i}}\,, \tag{5.1}$$

where $B_{\rm i}$ is the count-rate and $ECF_{\rm i}$ is the ECF, which was calculated according to the recent calibration matrices of EPIC-MOS and EPIC-pn. We obtained the ECF by assuming a power-law model with the Galactic foreground absorption of $N_{\rm H} = 2.46 \times 10^{20}$ cm^{-2} (Willingale et al., 2013) and a photon index of $\Gamma = 1.81$

Table 5.2: ECFs for each EPIC energy band

Energy-band	EPIC-pn	EPIC-MOS
B1 (0.2 − 0.5 keV)	1.12e+12	1.79e+11
B2 (0.5 − 1.0 keV)	9.05e+11	1.91e+11
B3 (1.0 − 2.0 keV)	5.72e+11	2.05e+11
B4 (2.0 − 4.5 keV)	1.98e+11	7.73e+10
B5 (4.5 − 12 keV)	5.59e+10	1.54e+10

which is obtained by fitting a power-law model to the spectra of hard sources (see Sect. 6.4). Table 5.2 lists the value ECFs for each EPIC energy band.
The faintest detected source in the field of the Draco dSph, which is neither classified as a foreground nor as a background object, is source No 28 with a luminosity of $(3.94 \pm 1.69) \times 10^{33}$ erg s^{-1}.

5.3 Astrometric Correction

5.3.1 Offset of source positions based on the *XMM-Newton* observations

We selected bright point and point-like sources which were detected in all observations in order to correct the X-ray position. We checked the difference between RA and Dec of OBS 2, 3, 4, and 5 with respect to OBS 1 to see if there is a shift in the position of sources in each of the observations to verify possible offset in their positions in different observations. The weighed means of ΔRA and ΔDec were calculated. We could not find any shift in none of the observations.

5.3.2 Correcting the positions of the detected sources using the optical counterparts

We corrected the positions of the sources for each EPIC in the observation, with respect to the their counterpart in the optical, which have more accurate position measurements than X-ray source. To obtain a more accurate position for the X-ray sources, we determined the systematic errors between the X-ray positions and their counterpart in the optical catalogues (see Sect. 5.4). For this purpose, the final *XMM-Newton* source list was cross-correlated with optical catalogues. For the correction of X-ray coordinates, we were interested in associations between X-ray sources and foreground stars or point-like background objects (like quasars

and AGNs). We selected 14 bright X-ray sources with counterparts in the optical, which were known to be foreground stars or AGN/quasars (see Sect. 5.4).

For each observation and instrument, we separately calculated the weighted mean of ΔRA and ΔDec between the positions of optical and X-ray sources. The plots (Fig. 11.2) show the difference between optical and X-ray positions for each EPICs in five observations. The position of the optical counterpart is selected as the centre of the plots and the X-ray ΔRA and ΔDec offsets are shown. The error bars represent the combined errors of statistical X-ray error and corresponding optical error. ΔRA and ΔDec have been calculated and corrected for each EPIC separately. Table 5.3 shows the ΔRA and ΔDec offsets of EPIC-MOS1, EPIC-MOS2, and EPIC-pn for five observations and mosaic image. The final coordinate of the X-ray sources in Table 7.3 are the corrected positions in the observation with the highest ML.

Table 5.3: **Offsets of the different *XMM-Newton* observations of the Draco dSph.**

OBS-ID	EPIC	Δ RA (″)	Δ Dec (″)
OBS1	PN	-0.09 ± 0.01	0.03 ± 0.01
	MOS1	-0.18 ± 0.03	-0.07 ± 0.03
	MOS2	-0.23 ± 0.02	-0.014 ± 0.02
OBS2	PN	-0.10 ± 0.01	-0.13 ± 0.01
	MOS1	-0.06 ± 0.03	-0.15 ± 0.03
	MOS2	-0.12 ± 0.02	-0.09 ± 0.02
OBS3	PN	-0.22 ± 0.02	-0.08 ± 0.02
	MOS1	-0.23 ± 0.05	-0.08 ± 0.05
	MOS2	-0.22 ± 0.04	0.04 ± 0.04
OBS4	PN	0.05 ± 0.08	-0.15 ± 0.08
	MOS1	0.11 ± 0.05	-0.07 ± 0.05
	MOS2	0.05 ± 0.07	-0.08 ± 0.07
OBS5	PN	0.03 ± 0.01	-0.07 ± 0.01
	MOS1	0.09 ± 0.06	0.06 ± 0.06
	MOS2	-0.06 ± 0.03	-0.02 ± 0.03
MOSAIC		-0.035 ± 0.002	-0.030 ± 0.002

5.4 Cross correlation with other wavelengths

In the first step of identifying X-ray sources in the Draco dSph, we searched for correlation around each X-ray source position with other catalogues. We searched

within the radius of $3 \times \sqrt{\sigma^2_{\rm stat} + \sigma^2_{\rm syst}}$ in catalogues at different wavelengths in VIZIER[1] and SIMBAD[2] archives. The parameter σ_{stat} is the statistical error derived by `emldetect`, and σ_{syst} comes from the positional error of the correlated source and also from the uncertainty of the offset between optical and X-ray positions. Sources are considered as counterpart if their positions overlap within $3\sigma(= 0.9973)$ positional error (Watson et al., 2009). The positional uncertainties were either taken from the respective catalogues or from the technical data of the telescopes.

5.4.1 Milky Way stars catalogue

The catalogue of hot star and hot white dwarf candidates (Bianchi et al., 2011) is a list of UV sources from the Galaxy Evolution Explorer (GALEX) sky survey and contains stars in the Milky Way. To classify foreground stars we checked for cross-correlations with sources of this catalogue. The positional error of the sources was $\sim 0\farcs5$.

5.4.2 Quasars and AGNs catalogues

There are a noticeable number of AGN and quasar catalogues that cover the field of the Draco dSph. We selected the most updated and popular catalogues:
the Quasars and AGNs Catalogue (13th Ed, Veron-Cetty and Veron, 2010), QSO Candidates Selection in Virtual Observatory Era (D'Abrusco et al., 2009), Photometric Classification Catalogue of SDSS DR7 (Abraham et al., 2012), Large Quasar Astrometric Catalogue 2 (LQAC-2, Souchay et al., 2012), Photometric Selection of Quasars from SDSS II (Richards et al., 2009), All-sky Atlas of Radio/X-ray Associations (Flesch, 2010), and the Quasar Catalogue of Kinemuchi et al. (2008) in the field of the Draco dSph.

5.4.3 The Draco dSph stars catalogues

A catalogue of stars in the Draco dSph exists from deep photometric studies with the new Canada-France-Hawaii telescope wide-field imaging Camera (MegaCam) with three different filters ($g = 487$ nm, $r = 625$ nm, $i = 770$ nm), the Wide Field Camera of the Isaac Newton telescope (INT) with standard filters (V, I), and the Wide Field and Planetary Camera on board the Hubble space telescope (HST)

[1] http://vizier.u-strasbg.fr/viz-bin/VizieR
[2] http://simbad.u-strasbg.fr/simbad/

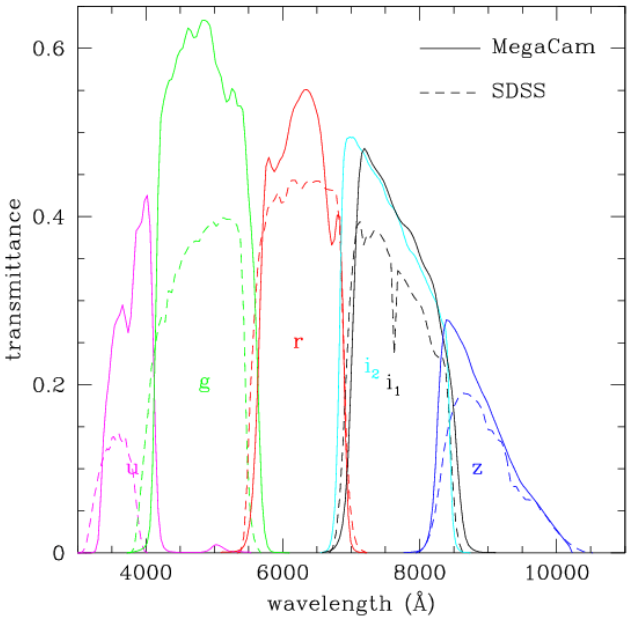

Figure 5.2: The spectral coverage of the MegaCam g, r, i and SDSS u, g, r, i, z filter sets (Gwyn, 2008)

(Ségall et al., 2007), which lists the members of the Draco dSph based on the analysis of colour-magnitude diagrams for each observation. The HST survey is limited to the centre of the galaxy, where no *XMM-Newton* X-ray source was detected. In MegaCam and INT catalogues, we found more than one counterpart generally in the 3σ error circle of the X-ray sources. Therefore, we selected the brightest optical source as a counterpart. If there were counterparts in many optical or infrared (see Sect. 5.4.5) catalogues, we selected the brightest source with consistent magnitudes in the same energy bands of the different catalogues as the counterpart.
The counterparts of INT and MegaCam are given in the Tables 12.7 and 12.8. The tables show the position of the counterparts and apparent magnitudes in different filter bands. For INT sources we considered extinction correction of *V, I* optical bands according to 12.5.
The effective wavelengths of the MegaCam bands (g, r, i) correspond to the SDSS9 g, r, i bands (Fig. 5.2). Therefore we applied the extinction correction of SDSS bandss for MegaCam band according the to Table 12.5.

Figure 5.3 shows the colour-magnitude diagram of the optical counterparts of the MegaCam catalogue. To have a more accurate idea about the nature of the optical counterparts, we over-plotted the isochrone line on colours-magnitude diagrams.

As Girardi et al. (2004) showed, the best-fit isochrone line for the stellar population of the Draco dSph has an age of 10^{10} yr and metalicity of 0.0004 (more details of explained in Sect. 3.2). The colour and absolute magnitude of the isochrone lines are based on the SDSS9 energy bands. As it is shown in Figure 5.2 the spectral coverage of the SDSS and MegaCam energy bands are very similar. The magnitude of the bands of MegaCam are related to SDSS according to following equations, which are provided in MegaPipe image stacking pipeline of the MegaCam ugriz set (Gwyn, 2008):

$$u_{Mega} = u_{SDSS} - 0.241(u_{SDSS} - g_{SDSS}) \tag{5.2}$$
$$g_{Mega} = g_{SDSS} - 0.153(g_{SDSS} - r_{SDSS}) \tag{5.3}$$
$$r_{Mega} = r_{SDSS} - 0.024(g_{SDSS} - r_{SDSS}) \tag{5.4}$$
$$i_{Mega} = i_{SDSS} - 0.003(r_{SDSS} - i_{SDSS}) \tag{5.5}$$
$$z_{Mega} = z_{SDSS} + 0.074(i_{SDSS} - z_{SDSS}) \tag{5.6}$$

It allowed us to compare the SDSS9 sources with the MegaCam sources. Out of the isochone line of SDSS (Girardi et al., 2004), we calculated the isochrone line of the Draco dSph sources for the MegaCam using this set of formulae.
Due to the larger exposure time of the Mega-Cam (950, 1090 and 1700 s respectively for g, r and i bands) compared to SDSS9 (53.9 s per band) there are plenty of X-ray sources which have faint optical counterparts in Mega-Cam and not in SDSS9. It should also be noticed that Ségall et al. (2007) removed known background and foreground sources from the MegaCam catalogue of Draco dSph, therefore some known sources are missing in the colour-magnitude diagram (Fig. 5.3). The positional error of the optical sources in this catalogue is $\leq 0\farcs5$.
One of the aim of the deep surveys with INT, MegaCam, and HST was the study of the mass-to-light ratio in this galaxy (Ségall et al., 2007). Therefore, these catalogues should not contain any known foreground stars and background objects (galaxies, AGNs, quasars) that were classified before. However, there are still many foreground and background objects which have been classified as stars of Draco dSph in these catalogues as we will see later.
For more accuracy, we also considered other catalogues of the Draco dSph, in which the members of the galaxy are classified by different methods in different wavelengths. The catalogue of Kleyna et al. (2002) contains a few hundred stars which were selected based on radial velocity measurements. Rave et al. (2003) classified all sources with $g < 23$ mag of the SDSS7 survey in the field of the Draco dSph as stars in the galaxy, background galaxies or unclassified faint source by several photometric methods. The selected members of Draco dSph are consistent with five other previous catalogues. On the basis of the infrared and optical observations Cioni and Habing (2005) classified late-type stars in the Draco dSph. Piatek et al. (2001) selected the members of the Draco dSph in R and V band

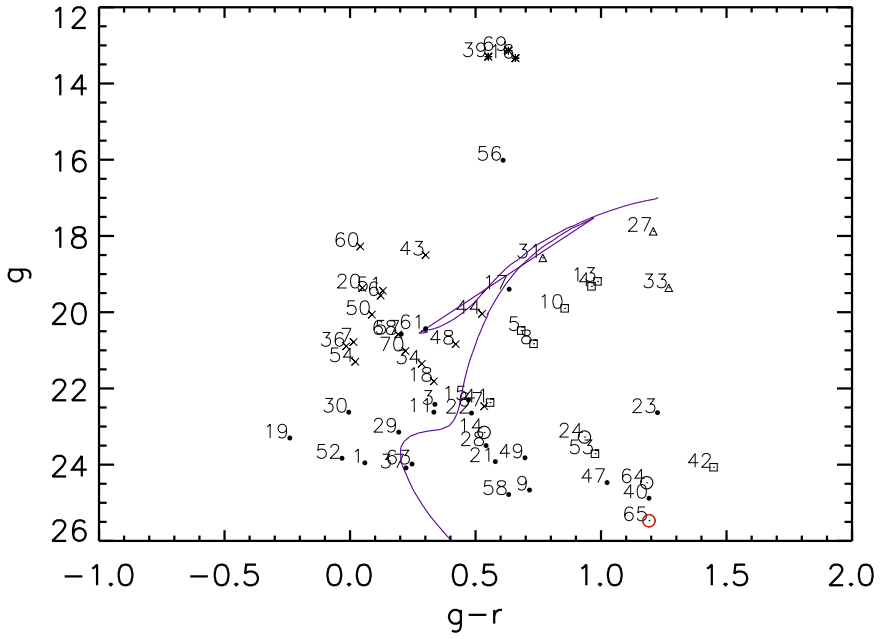

Figure 5.3: The colour-magnitude diagram of MegaCam optical counterpart of the X-ray sources. The violet line is the steller isochrone for the age and metalicity of the Draco dSph (Sect. 5.4.4). Foreground stars are marked with asterisk, AGNs with crosses, galaxies with squares, X-ray binary candidates with circles, super-soft sources with triangles, and the remaining unclassified sources are just shown as black dots. Source No 65 is a candidate of LMXB which had a optical counterpart only in the MegaCam catalogue and is coloured in red (see Sect. 7.3.1).

photometry.

5.4.4 Optical catalogues

The catalogue of SDSS9 (Ahn et al., 2012) is the most updated optical catalogue which covers the field of the Draco dSph. We selected this catalogue as the main optical reference as we had access not only to its images but also to the apparent magnitudes and errors in five different optical energy bands from near ultraviolet (UV) to near infrared ($u = 3551$, $g = 4686$, $r = 6165$, $i = 7481$, $z = 8931$). Furthermore, the red-shifts of the background objects are available for the brightest sources. Table 12.6 lists the SDSS9 optical counterparts of *XMM-Newton* sources in the field of the Draco dSph. The magnitudes in different filters

are corrected according to the extinction in Table 12.5. For source No 57, g and r band magnitudes are adopted from the SDSS7 catalogues (Abazajian et al., 2009), because the magnitudes of the sources in SDSS9 seems to be contaminated by a neighbouring source. The positional uncertainty of a source in the SDSS9 catalogue depends on its brightness and is between 0.″003 and 0.″2 for the sources considered as counterparts of the *XMM-Newton* sources. Appendix 13.1 shows the SDSS9 images centred on the region of X-ray sources of the Draco dSph.
Figure 5.4 shows the colour-magnitude and colour-colour diagrams of the SDSS9 counterparts. The classification of sources in these figures is based on the result of Chapter 7. We also over-plotted the isochrone which is fitted to the stellar population of the Draco dSph according to Girardi et al. (2004). The line shows that the main fraction of the stars in the galaxy are already in the red-giant branch (see Sect. 3.2).

5.4.5 Inferared catalogues

Infrared counterparts were found in two catalogues, the wide-field infrared survey explorer (WISE)All-Sky Data, released in four energy bands (3.4, 4.6, 12, and 22 μm, called *W1, W2, W3, W4* respectively, Cutri and et al., 2012), and the two micron all sky survey (2MASS)All-Sky Catalogue of Point Sources taken with J, H, K filters (Cutri et al., 2003). Table 12.9 shows the list of WISE infrared counterparts. The list of 2MASS counterparts with X-ray sources of the Draco dSph is shown in the Table 12.10. The magnitudes are corrected for the extinction according to Table 12.5. Figure 5.5 shows the colour-magnitude diagrams of the WISE and 2MASS infrared counterparts of X-ray sources of the Draco dSph. The positional uncertainty of WISE sources is 0.″3 – 1 and the average positional uncertainty of 2MASS is ∼3

5.4.6 Radio catalogue

We used the source catalogue of the 1.4GHz NRAO VLA sky survey (NVSS) (Condon et al., 1998). Table 12.11 shows the sources which have radio counterparts. This catalogue gives the position and the flux density with respective errors of the radio sources.

5.4.7 X-ray catalogues

The second ROentgen SATellite (ROSAT) Source Catalogue of Pointed Observations (Böhringer et al., 2000) includes some of the brightest sources, which were

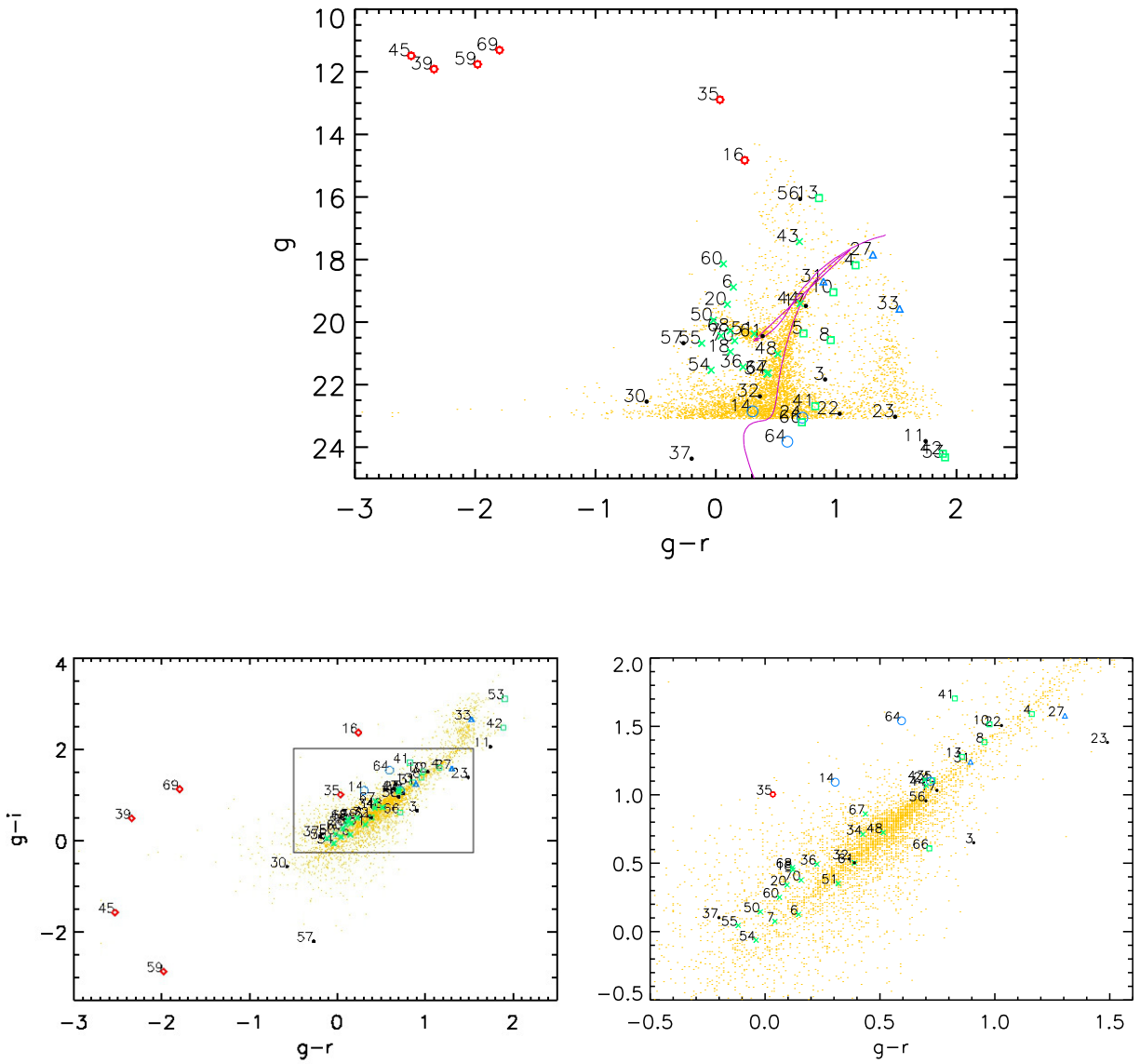

Figure 5.4: Colour-magnitude (up) and colour-colour (down) diagrams of SDSS9 optical counterparts of X-ray sources. In down, the right colour-coulor diagram shows a zoom in to the square area of the left diagram. Foreground stars are marked with red stars, AGNs with green crosses, galaxies with green squares, X-ray binary candidates with blue circles,super-soft sources with blue triangles, and the remaining unclassified sources are just shown by black dots. Orange dots represent the SDSS7 members ($g < 23$ mag) of the Draco dSph classified by Rave et al. (2003). The violet line is the stellar isochrone for the age (10^{10} yr) and metalicity (0.0004) of the Draco dSph according to Girardi et al. (2004) and as it shows main part of the stars of the galaxy are already in red giant branch.

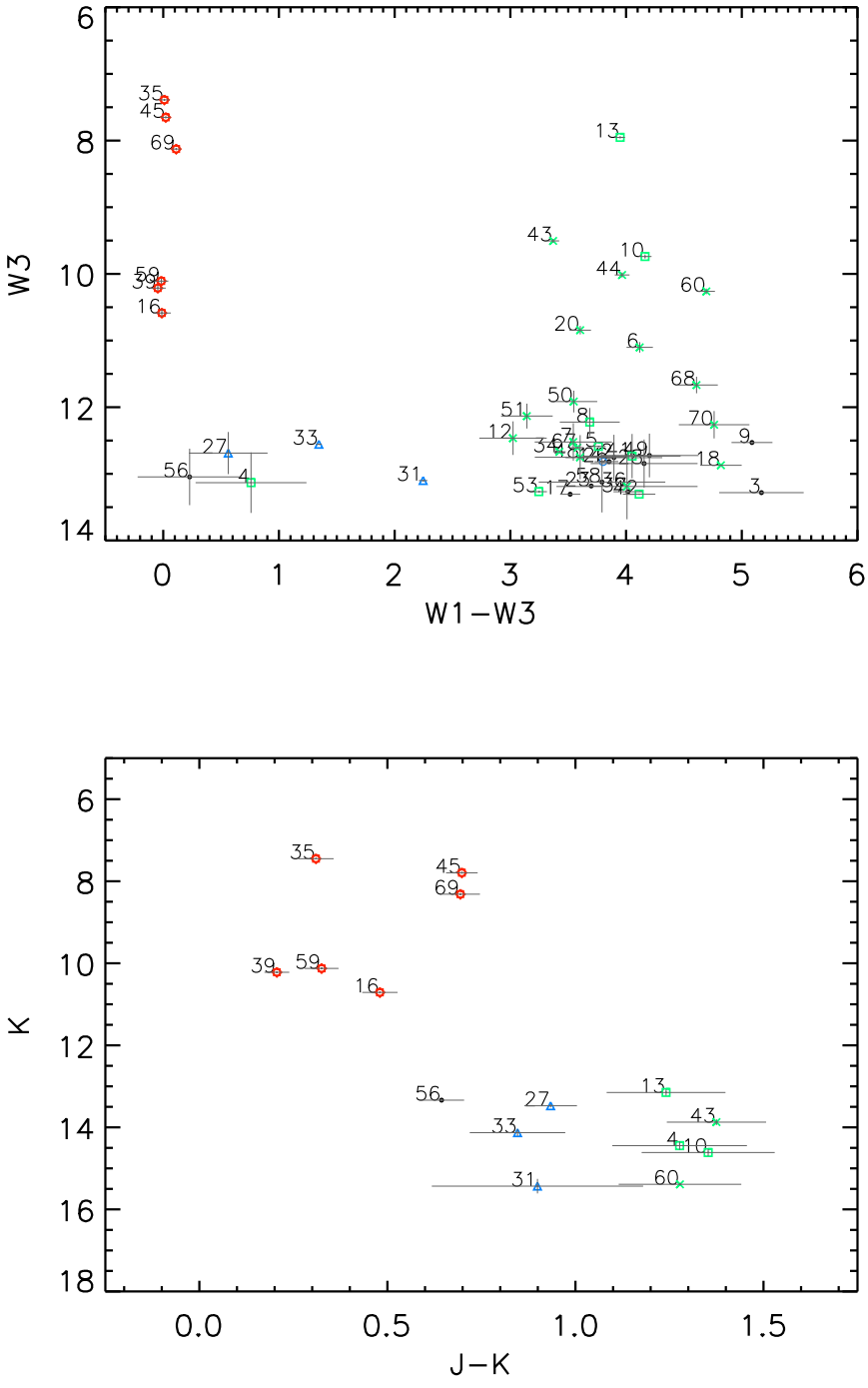

Figure 5.5: Colour-magnitude diagrams of the infrared counterparts of the *XMM-Newton* sources. Upper panel: WISE $W2\,(4.6\ \mu m)$ versus the colour index $[W1\,(3.4\mu$ m$)-W3\,(12\mu$ m$)]$. Lower panel: 2MASS K band versus the colour index $J-K$. For the different source classes same symbols are used as in Fig. 5.4.

detected with *XMM-Newton*. Table 12.12 lists the count rate and hardness ratios of the ROSAT sources which have *XMM-Newton* counterparts. The hardness ratios are defined as:

$$RHR1 = (B - A)/(B + A), \tag{5.7}$$

where A is the count rate in Pulse Height Amplitude (PHA) range of $11-41$ $(0.1-0.4$ keV) and B is the count rate in PHA range of $52-201$ $(0.5-2.0$ keV), and

$$RHR2 = (D - C)/(D + C), \tag{5.8}$$

where C is the count rate in PHA range of $52-90$ $(0.5-0.9$ keV) and D is the count rate in PHA range of $91-201$ $(0.9-2.0$ keV).
The counterparts in the *Chandra* catalogue (Evans et al., 2010) are listed in Table 12.13. The hardness ratios CHR1 and CHR2 of the Chandra catalogue is:

$$CHR1 = (h - m)/b, \tag{5.9}$$

$$CHR2 = (m - s)/b, \tag{5.10}$$

where the range for b is $0.5-7.0$keV (broad band), for s $0.5-1.2$keV (soft band), for m $1.2-2.0$keV (medium band), and for h $2.0-7.0$keV (hard band).
About one third of the *XMM-Newton* sources were detected before by ROSAT and *Chandra* observations. In the case of unknown sources, the data of these two catalogues were considered for the classification.

Chapter 6

Analysis

As it is explained in Section 5.4, searching for counterparts of X-ray sources and studying their properties are among the most important steps in the classification of X-ray sources. Different methods of X-ray data analysis were applied. These various methods are discussed in the following. The results of the X-ray data analysis plus the distinctive figures of the counterparts of an X-ray source at other wavelengths help to determine the class of the source.

6.1 Variability of the source

In this section, we explain the different methods which have been applied to find any evidence for pulsations, periodicity, and long-term variation of the flux for each source.

6.2 Short-term variability

For each observation, we searched for both pulsation and periodicity of the brightest sources (counts ≥ 200) using the Lomb-Scargle method and for pulsation of all sources using the Rayleigh method.
First, the extracted event file of EPICs were corrected to the barycentre. This correction is necessary because the position of the satellite changes during its orbit. This means that the satellite moves toward or away from the source and the distance between the source and the satellite changes. Therefore, the arrival time of photons changes due to this motion. By applying the barycentric correction the arrival time of a photon is recalculated to that at the barycentre of the solar system instead of the measured time at the position of the satellite.

6.2.1 Light curves

For sources with ≥ 300 counts in EPIC-MOS and EPIC-pn, we ran `evselect` to extract the light curve of the source and its background. The background light curve was extracted from an annulus region around the source or from a circle region on the same CCD as for the source in the case that the source was located near the edge, a damaged pixel or another source. For each source, we changed the size of the time-bins to find the best time scale of the light curve, varying from 20 to 700 seconds for different sources on different EPICs. None of the sources showed a regular variability of the light curves.
We checked the possibility of any periodicity or pulsation on the time scale of the observation(s) for each source by applying the Lomb-Scargle method describe in the following section:

6.2.2 Lomb-Scargle periodogram for unevenly sampled time series

We applied the Lomb-Scargle method to detect a possible periodic signal hidden in the noise. Discrete Fourier transform is the main technique to decompose time series into a linear combination of sinusoidal function which transforms the data from time domain to frequency domain. The technique usually assumes evenly spaced time series. Since we had light curves for different observations, we applied the Lomb-Scargle method which has been improved for unevenly spaced times.

Periodogram

For a sample of data $X(t_i),\ i = 1, 2, ..., N_0$, the discrete Fourier transformation can be written as:

$$FT_x(\omega) = \sum_{j=1}^{N_0} X(t_i) e^{(-i\omega t_j)}, \tag{6.1}$$

and the classical periodogram is defined as:

$$
\begin{aligned}
P_x(\omega) &= \frac{1}{N_0}|FT_x(\omega)|^2 \\
&= \frac{1}{N_0}|\sum_{j=1}^{N_0} X(t_i)e^{(-i\omega t_j)}|^2 \\
&= \frac{1}{N_0}[(\sum_j X_j cos\omega t_j)^2 + (\sum_j X_j sin\omega t_j)^2],
\end{aligned}
\tag{6.2}
$$

If we have a periodicity at the frequency ω_0, X has a sinusoidal component at this frequency. Therefore near ω=ω_0, $X(t)$ and $\exp(-i\omega t)$ are in phase and make a large distribution with the summation in periodogram (Press et al., 1992).
However, applying these equations to observational data is difficult even if they are evenly sampled. First, in observational data, X is a random variable which contains noise, therefore, $P_x(\omega)$ is also a random variable. Equations 6.2 are almost useless for practical computations (Richards, 1967). Second, for sinusoidal signals at a given frequency, ω_0, the power of the periodogram not only appears at ω_0, but also leaks to other frequencies. This problem which is known as "spectral leakage" is caused by the finite size of the amount of data. Either the finite total intervals over which the data is sampled, or the finite size of the interval between samples can cause the spectral leakage. Third, we usually have unevenly sampled data, and it means that there are some missed data.
First and second problems have been almost reduced with the modified version of periodogram by Lomb (1976). For the third problem, it was suggested to apply a grid of evenly spaced time intervals on the data, interpolate a value equal to zero for the missing data, and make a series of evenly spaced data. However, this technique produces a poorly distributed sample. Scargle (1982) suggested to evaluate data exactly at times t_j which are measured. By assuming N_0 data points $X(t_i), i = 1, 2, .., N_0$, the mean and the variance of data are:

$$
\bar{X} = \frac{1}{N_0} \times \sum_{j=1}^{N_0} X_j, \tag{6.3}
$$

$$
\sigma^2 = \frac{1}{N_0}\sum_{j=1}^{N_0}(X_i - \bar{X})^2. \tag{6.4}
$$

Normalised periodogram is defined as :

$$
P_N(\omega) = \frac{1}{2\sigma^2}\frac{[\sum_j (X_j - \bar{X})cos\omega(t_j - \tau))]^2}{\sum_j cos^2\omega(t_j - \tau)} + \frac{[\sum_j (X_j - \bar{X})X_j sin\omega(t_j - \tau)^2]}{\sum_j sin^2\omega(t_j - \tau)}, \tag{6.5}
$$

where the τ is :

$$tan(2\omega\tau) = \frac{\sum_j sin2\omega t_j}{\sum_j cos2\omega t_j}. \tag{6.6}$$

τ makes $P_N(\omega)$ completely independent of shifting in t_j. This method was elaborated by Scargle and was checked for false alarm probability and detection efficiency (Scargle, 1982). We used the available Lomb-Scargle algorithm. We have searched for periodicity in the light curves of bright sources in all observations. This method allows us to see a periodic signal hidden in the noise not only in one observation, but also in the combined light curves of all observations. We selected the light curves with the minimum size of time-bin of different observations and applied the Lomb-Scargle algorithm. As mentioned before, the presence of variability will produce a peak in a peridogram.
For example if the data are measured every 100 seconds and the long-term trend has a time-scale of 10 days, the periodogram shows peaks very close to 100 second as well as a broad peak at about 10 days. This method was applied for the light curves of all the brightest sources. Figure 11.4 shows the Lomb-Scargle peridogram of the analysed sources for all observations. The short-term peaks in the periodograms are related to the selected bin size of different light curves and the long term peaks are related to the length of observations. We did not find any evidence for pulsations or periodicity for the sources in the Draco dSph by the Lomb-Scargle method.

6.2.3 Testing the phase distribution for the presence of pulsed signal

The Lomb-Scargle method is only useful for the brightest sources, so the number of sources which were tested by that method was limited. To improve the search for pulsations, especially for the faint sources, we extracted the barycentric corrected event files of sources for each observation and EPIC and applied the $Z^2_{\rm n}$ analysis. We checked the periodograms for the 1st and 2nd harmonics of the arrival times in the event files of each EPIC in $0.2 - 12$ keV as it is explained in the following. We found significant pulsation for the source No 65 in OBS2 (see Sect. 7.3.1).

Z^2_n Test

Rayleigh (Z^2_n) test was suggested by Buccheri et al. (1983, 1988) in order to find the pulsations of γ ray emissions. The aim of this method was to search for the pulsed signal in γ rays emitted from the magnetosphere of an NS. This method

is useful if the statistics of the signals is not high enough to obtain a light curve of the source. In usual methods based on Gaussian distribution, the time of the observation is split into n bins and the number of counts per bin derived by sorting into phase bins with respect to the average number of counts per bin. However, Rayleigh (Z_n^2) test is independent of the chosen phase bin. In this method, the time intervals between arrival photons are considered to find the pulsations in the following way:

First, the photon arrival times are reduced to a phase value in the interval from 0 to 1 by this formula:

$$\phi_j = fractional\,part\,of\left(\nu\Delta t_j + \frac{\dot{\nu}\Delta t_j^2}{2} + \frac{\ddot{\nu}\Delta t_j^3}{6}\right), \tag{6.7}$$

where j is the number of arrival photon and Δt_j is the difference between the arrival time of the first arrived photon and the other photons $\Delta t_j = t_j - t_0$. The parameter ν is the pulse frequency which is variable in the case of a source with pulse variation. We are generally interested in finding any evidence of pulsation in several sources. In this case, taking the first term in equation 6.7 is enough.
In the next step, different pulse frequencies are evaluated for N phase values (which is equal to the number of photons):

$$Z_n^2 = (\frac{2}{N})\sum_{k,1}^{n}\left(\sum_{j,1}^{N} cosk\phi_j\right)^2 + \left(\sum_{j,1}^{N} sink\phi_j\right)^2 \tag{6.8}$$

where n is the chosen number of harmonics and Z_n^2 is the probability density function with $2n$ degrees of freedom. We have:

$$P = 1 - [1 - exp(exp(Z_n^2/2))]^{nT_{exp}\Delta f} \tag{6.9}$$

where T_{exp} is the exposure time of the event file, and Δf is the frequency range. The maximum of frequency, with respect to the Nyquist frequency[1], is twice of the time resolution of EPIC-pn, which is 0.073 s in the full-frame mode. The minimum frequency is limited by the duration of the observation.

[1] The Nyquist frequency is half of the sampling rate of a discrete signal processing system. In order to recover all Fourier components of a periodic waveform, it is necessary to use a sampling rate ν at least twice the highest waveform frequency. The Nyquist frequency, also called the Nyquist limit, is the highest frequency that can be coded at a given sampling rate in order to be able to fully reconstruct the signal.

6.3 Long-term variability

Since the observations were spread out over 2 weeks (Table 5.1), we also checked the flux variability on long time scales. We either calculated the flux of the sources in each observation, or the upper-limit at the position of a source if the source was not detected.
Since the fluctuation of the flux in the highest energy band is high, the flux of the first four energy bands ($0.2 - 4.5$ keV) is used to compare the flux of different observations. The weighted flux (0.2–4.5 keV) is calculated for each observation using the ECF of Table 5.2. The upper-limit was calculated by using the sensitivity map. The count rate of the background photons was extracted from the sensitivity map at the position of the source. To have a better sensitivity, the upper-limit is derived from the sensitivity map of EPIC-pn. If that source was not in the FOV of EPIC-pn, the counts were extracted from EPIC-MOS sensitivity maps. Tables 12.2– 12.4 show the details of detection and ($0.2 - 4.5$ keV) flux for each source in each observation and EPIC. Figure 11.3 shows the long term light curves of the 0.2 – 4.5 keV flux of all sources for the five observations. The flux in these diagrams is the weighed flux of three EPICs.
Furthermore, to compare the $0.2 - 4.5$ keV fluxes between different observations, the ratio of the maximum and minimum flux and its significance are calculated by using the following formulae:

$$Var = \frac{F_{\max}}{F_{\min}} \tag{6.10}$$

$$S = \frac{F_{\max} - F_{\min}}{\sqrt{EF_{\max}^2 + EF_{\min}^2}}\,, \tag{6.11}$$

where $F_{\max}$ and $F_{\min}$ are the maximum and minimum X-ray flux (or upper limit), and $EF_{\max}$ and $EF_{\min}$ are the errors of the maximum and minimum flux of the source, respectively. The variability factor was calculated for the sources which were detected in at least two observations (see Figure 11.3). We considered the source as variable if the statistical variability significance (S) was higher than 3. Figure 6.1 shows the variability factor (Var) of the sources as a function of the hardness ratio HR_2 and HR_3 (see Sect. 6.5) and the variability factor (Var) as a function of the maximum flux.

Figure 6.1: Variability factor of sources in the 0.2 – 4.5 keV energy band plotted versus HR_2 (upper left panel), versus HR_3 (upper right panel), and versus maximum flux (lower panels). Sources with the statistical significance of variability lower than three are marked in orange. In the lower right panel, the sources are plotted with the error bars. For the different source classes same symbol types are used as in Fig. 5.4.

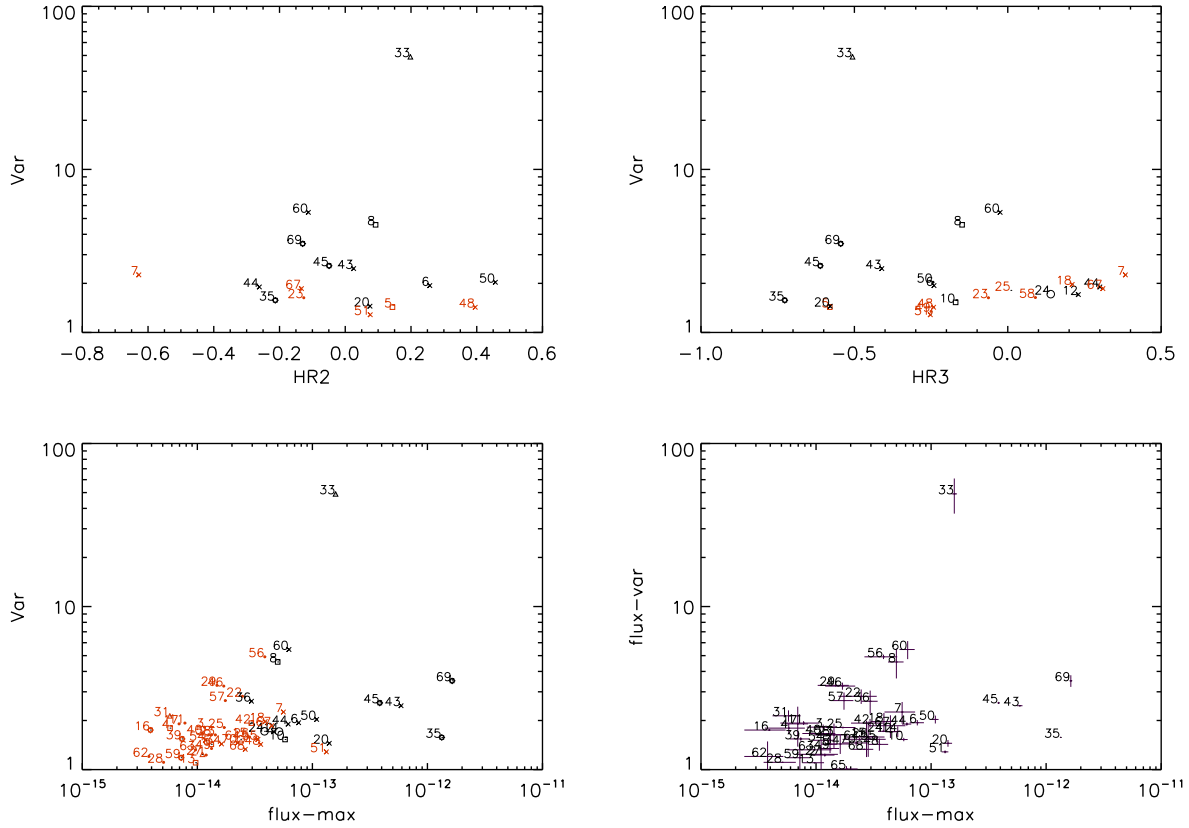

6.3.1 Long-term variability of *Chandra* sources

For sources for which we also have a *Chandra* detection, we included the *Chandra* flux in the long-term light curves. We estimated the equivalent *XMM-Newton* flux of *Chandra* sources. In the *Chandra* catalogue, a spectral power-law model with photon index of $\Gamma = 1.7$ is considered for hard sources while a blackbody model with a fixed temperature of $kT = 1$ keV is considered for soft sources in the flux calculation (Evans et al., 2010). We converted *Chandra* fluxes (energy range $0.5 - 7$ keV) to equivalent *XMM-Newton* fluxes (energy range of $0.2 - 12.0$ keV) assuming the spectral model as explained in Section 5.2.6. For all these sources, the *Chandra* flux is consistent with the average *XMM-Newton* flux, indicating that none of them show variability between the *Chandra* and *XMM-Newton* observations. Table 6.1 gives the fluxes of the *Chandra* sources converted into the used energy band of 0.2–12.0 keV.

6.4 Spectral analysis

We have extracted the spectra for 27 sources with ≥ 300 counts in the energy range of 0.2 – 12 keV, for each EPIC of each observation. For many sources poor statistics did not allow to find a reliable model for the source spectra. The only bright source for which we could perform spectral analysis was source No 69. It was located on a damaged pixel of EPIC-pn in both observations (OBS4 and OBS5), in which the source was detected. We fit 13 sources with power-law, APEC, VAPEC, and MEKAL models using XSPEC (ver.12.8.1).
Power-law is a photon power-law model, defined by photon index (Γ) and normalisation parameter (K):

$$A(E) = KE^{-\Gamma} \tag{6.12}$$

where E is the energy of the photons. Non-thermal emission (e.g, Synchrotron or Inverse Compton emission) usually has a power-law spectral distribution (Xspec, User Guide manual, 2015).
The Astrophysical Plasma Emission Code (APEC) is a model for X-ray spectra of hot, collisionally ionised plasma (Brickhouse et al., 2000). This model facilitates the diagnosis of temperature, density, elemental abundance, charge state, and optical depth (Brickhouse et al., 2000; Brickhouse, 2003). The APEC model contains abundances for C, N, O, Ne, Mg, Al, Si, S, Ar, Ca, Fe, and Ni as one parameter (related to the solar value). The VAPEC variant allows the user to fit the abundances of elements separately.
MEKAL is an emission spectrum from hot diffuse gas based on the model calculations of Kaastra and Mewe (2000). The model includes line emissions from several elements (C, N, O, Ne, Na, Mg, Al, Si, S, Ar, Ca, Fe, Ni).

Table 6.1: The *Chandra** flux of the sources detected with *XMM-Newton*

ID*	Flux $(0.2-4.5$ keV) $[\mathrm{erg\,s^{-1}\,cm^{-2}}]$	Confidence limits†	
		$[\mathrm{erg\,s^{-1}\,cm^{-2}}]$	$[\mathrm{erg\,s^{-1}\,cm^{-2}}]$
13	6.94e-15	1.10e-14	2.85e-15
20	9.20e-14	9.78e-14	8.70e-14
23	1.55e-14	1.77e-14	1.34e-14
29	3.37e-15	4.57e-15	2.18e-15
30	5.21e-15	6.49e-15	3.93e-15
33	3.64e-15	4.63e-15	2.64e-15
35	8.24e-13	8.39e-13	8.17e-13
38	6.08e-15	7.15e-15	5.03e-15
39	3.50e-15	4.11e-15	2.90e-15
40	7.39e-15	8.45e-15	6.31e-15
47	9.62e-15	1.22e-14	7.29e-15
48	4.57e-14	4.97e-14	4.17e-14
49	1.59e-14	1.80e-14	1.39e-14
51	9.78e-14	1.03e-13	9.37e-14
54	6.80e-15	8.45e-15	5.13e-15
56	7.44e-15	8.78e-15	6.14e-15
58	6.22e-15	8.22e-15	4.22e-15
67	2.38e-14	2.77e-14	1.99e-14
68	2.38e-14	3.84e-14	9.28e-15
70	-	-	2.90e-14

$*$: *Chandra* observations were perfumed on 10-15 of December 2007.
$\star$: IDs are according to the *XMM-Newton* catalogue.
†: Confidence limits for the flux are calculated according to Evans et al. (2010). Fluxes, upper, and lower limits have been converted to the *XMM-Newton* energy range.

The PHABS model (Balucinska-Church and McCammon, 1992) considers photo-electric cross-section (NOT including Thomson scattering) to calculate the X-ray absorption in the energy range 0.03-10 keV. This absorption model was applied in all spectral fit. We fitted the spectra of three EPICs simultaneously for each source for each observation.
Because of the poor statistics of the data, we also created combined spectra of three EPICs for each observation and average response. The significance of the

Table 6.2: Spectral parameters of the hard sources in the field of the Draco dSph**

ID	OBS	EPIC⋆	$N_{\rm H}(10^{22}{\rm cm}^2)$	Γ	Norm.	χ^2_ν(d.o.f.)
6	2	PN	0.02*	$1.2^{+0.5}_{-0.3}$	$7.8^{+1.9}_{-1.9} \times 10^{-6}$	1.1 (4)
10	5	PN	0.02*	$1.0^{+0.4}_{-0.4}$	$1.2^{+0.6}_{-0.4} \times 10^{-5}$	0.4 (3)
12	2	Merged	0.02*	$0.9^{+0.2}_{-0.2}$	$6.5^{+1.7}_{-1.5} \times 10^{-6}$	1.4 (8)
14	5	PN	0.02*	$1.9^{+0.3}_{-0.3}$	$1.2^{+0.2}_{-0.2} \times 10^{-5}$	1.2 (6)
20	5	PN,MOS1,MOS2	0.02*	$2.4^{+0.1}_{-0.1}$	$2.7^{+0.2}_{-0.2} \times 10^{-5}$	0.9 (33)
24	1	Merged	0.02*	$0.7^{+0.2}_{-0.2}$	$4.7^{+1.5}_{-1.3} \times 10^{-6}$	0.8 (7)
33	4	PN,MOS1,MOS2	0.02*	$2.1^{+0.3}_{-0.2}$	$3.9^{+0.5}_{-0.5} \times 10^{-5}$	0.8 (12)
43	1	PN	0.02*	$2.4^{+0.1}_{-0.1}$	$1.7^{+0.1}_{-0.1} \times 10^{-4}$	0.8 (65)
48	2	Merged	0.02*	$1.1^{+0.2}_{-0.2}$	$5.2^{+1.1}_{-1.0} \times 10^{-6}$	1.7 (7)
50	5	PN	0.02*	$1.3^{+0.2}_{-0.2}$	$2.2^{+0.3}_{-0.3} \times 10^{-5}$	0.9 (11)
51	1	PN,MOS1,MOS2	0.02*	$1.9^{+0.1}_{-0.1}$	$2.7^{+0.2}_{-0.2} \times 10^{-5}$	0.7 (33)

⋆: EPICs which were used for the simultaneous fit. "Merged" means that the three EPIC spectra were combined (see 6.4.1).
*: Parameter is frozen to the Galactic foreground $N_{\rm H}$ (Willingale et al., 2013).
**: The plots of the spectra are in Figure 11.5.

fit parameters improved by this method for fainter sources (see Sect. 6.4.1). We merged the spectra for sources which were detected in more than one EPIC. Table 6.2 shows the results of spectral analysis of the hard sources which are fitted with a power-law model. Figure 11.5 shows the spectra of these sources.
The spectra of sources which were fitted with other models will be explained when the classification of sources is discussed (see Sect. 7.1).

6.4.1 Combining the EPIC spectra

To improve the statistics for the spectral analysis, we combined the spectra of the three EPICs by using the tasks of SAS (V.13.5). This method can "only" be applied if the spectra and response files, which are going to be merged, are generated for the same PI channel interval and with the same spectral binning. We can never merge the spectra of two different observations.
First, a source and a background spectrum with a common bin size were generated using the task `evselect` for each EPIC. Second, a set of spectral files were generated for each EPIC by tasks `rmfgen` and `arfgen`. The combined spectra were created by the task `epicspeccombine`. It is reasonable to merge the spectra if the statistical error of the source is larger than the systematic error of the EPICs [2].
As an example, we present the result for source No 35, which was classified as a close binary system and is the brightest source in the field of the Draco dSph with a total X-ray flux of $(3.02 \pm 0.02) \times 10^{-13}$ ergs s^{-1} cm^{-2} in 0.2 – 12.0 keV. We fit a model with a VAPEC component for the spectrum of this source and applied the PHABS model for the foreground absorption. Figure 6.2 shows the spectra of the source. Figure 6.3 shows the contour diagram for the parameters kT_1 and kT_2 versus $N_{\rm H}$ for the simultaneous fit of spectra and for the fit of the merged spectra (see Fig. 6.3). One can see that the contours of the two methods overlap. This means that the statistical errors dominate the systematic errors. We can thus use the combined spectra of EPICs in this case. We applied this method for all the sources for which we could extract spectra for at least two EPICs in the same observation.
It also should be noted that in this case the significance of spectra parameters does not improve (Table 6.3). This shows that for such bright sources the systematic error dominate over the statistical uncertainties. In this case, therefore, it is not necessary to combine the spectra. However, for fainter sources for which the statistical errors dominate the systematic errors we can combine the spectra of the EPIC detectors.

[2] http://xmm.esac.esa.int/sas/current/documentation/threads/epic_merging.shtml

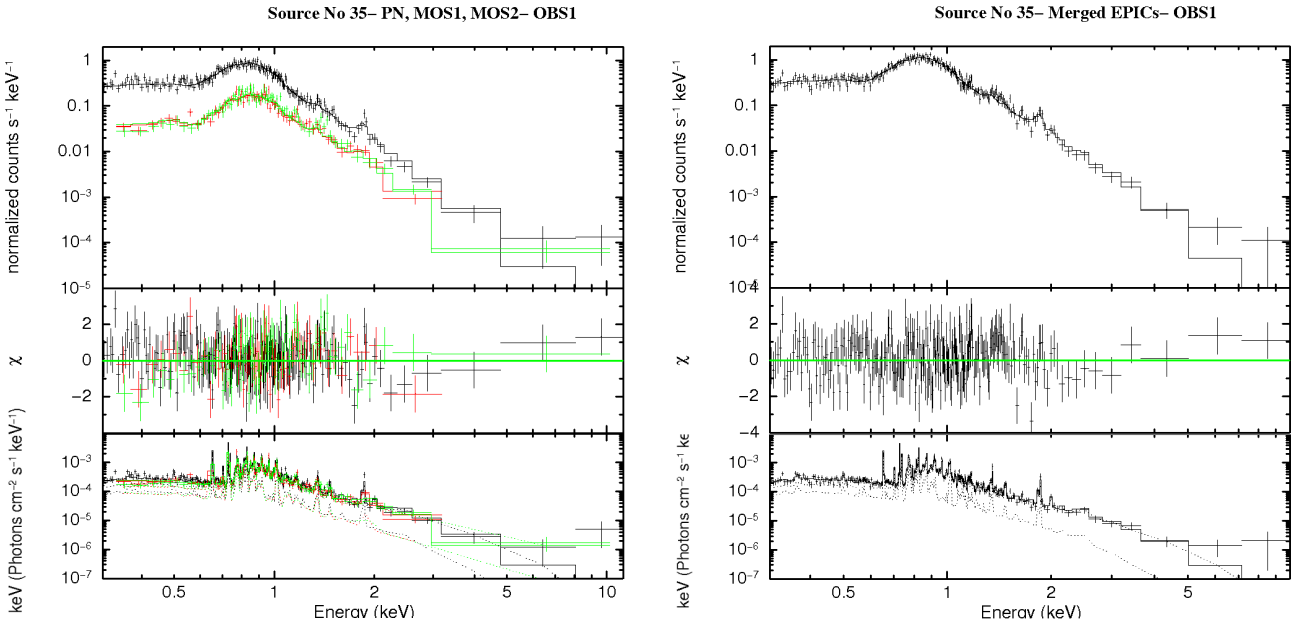

Figure 6.2: Individual (upper) and merged (lower) EPIC spectra of source No 35

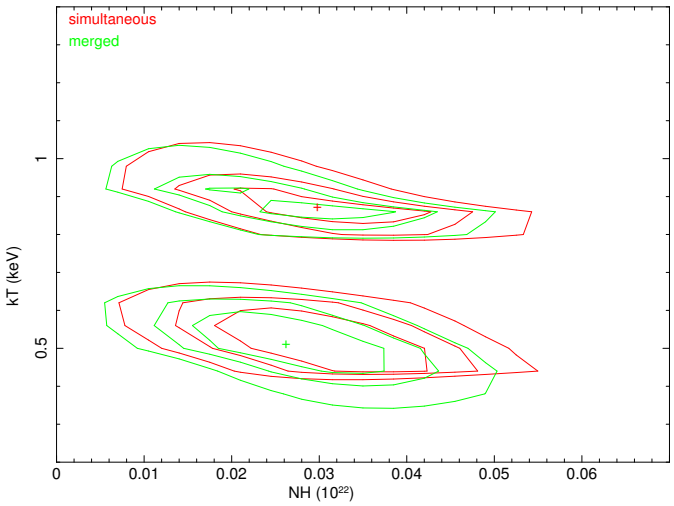

Figure 6.3: Contour-plot of simultaneous and combined EPIC fits of source No 35 in OBS2

Table 6.3: Fit parameters of source No 35

Parameters	simultaneous EPICs	Merged EPICs
$N_{\rm H}(10^{22}{\rm cm}^{-2})$	$0.03^{+0.01}_{-0.01}$	$0.02^{+0.01}_{-0.01}$
kT_1(keV)	$0.51^{+0.09}_{-0.09}$	$0.51^{+0.09}_{-0.08}$
Carbon	$0.24^{+0.03}_{-0.02}$	$0.25^{+0.03}_{-0.03}$
Norm.	$3.47^{+0.85}_{-0.67} \times 10^{-4}$	$3.19^{+0.73}_{-0.58} \times 10^{-4}$
kT_2(keV)	$0.87^{+0.05}_{-0.06}$	$0.87^{+0.05}_{-0.05}$
Norm.	$6.05^{+1.93}_{1.59} \times 10^{-4}$	$5.52^{+0.15}_{0.13} \times 10^{-4}$
χ^2_ν(d.o.f)	1.07(336)	1.17(234)

6.5 Hardness ratio diagrams

Hardness ratio diagrams are very useful tools to separate different classes of sources using their X-ray properties, especially in the case in which the source is too faint to extract a spectrum.
The hardness ratio and error are defined as:

$$HR_{\rm i} = \frac{B_{\rm i+1} - B_{\rm i}}{B_{\rm i+1} + B_{\rm i}} \tag{6.13}$$

$$EHR_i = 2\frac{\sqrt{(B_{\rm i+1}EB_{\rm i})^2 + (B_{\rm i}EB_{\rm i+1})^2}}{(B_{\rm i+1} + B_{\rm i})^2}\,, \tag{6.14}$$

for $i = 1, .., 4$; $B_{\rm i}$ is the count rate and $EB_{\rm i}$ is the corresponding error in the band i.
For each source, we calculated the average of hardness ratios from the observation, in which the source had the highest flux. Hardness ratios were calculated if the detection maximum likelihood of the source in each of the respective energy bands was higher than 6 ($> 3\sigma$). Figure 6.4 shows the hardness ratios of the sources. We only plotted the sources with uncertainties of the hardness ratios < 0.3 .
In the same plot, the lines present the hardness ratios calculated using different spectral models with various column densities from $N_{\rm H} = 10^{20}$ cm^{-2} to $N_{\rm H} = 10^{24}$ cm^{-2}. We used absorbed power-law models with different photon-indices $\Gamma = 1, 2, 3$ corresponding to e.g., XRBs or AGNs. Two absorbed disk black body models with temperatures $kT_{\rm in} = 0.5$ and 1.0 keV were used for XRBs in soft state. Four thermal plasma models APEC with different temperatures $kT_{\rm apec} = 0.2, 0.5, 1.0, 1.5$ keV were used for SNRs, and two black-body models

with temperatures of $kT_{\rm bb} = 50$ and 100 eV for super-soft sources (Ducci et al., 2013).

6.6 X-ray to optical flux ratio

A very useful tool to separate optically bright sources (like stars) from X-ray bright sources (like XRBs) is the X-ray to optical flux ratio. For each source associated with an optical source, we calculated the X-ray to optical flux ratio using the modified equation of Maccacaro et al. (1988):

$$log_{10}\left(\frac{F_{\rm x}}{F_{\rm opt}}\right) = log_{10}(F_{\rm x}) + \frac{g+r}{2\times 2.5} + 5.37\,, \tag{6.15}$$

where the standard band B ($\lambda_{\rm eff} = 0.43$ μm) and R ($\lambda_{\rm eff} = 0.65$ μm) were replaced by g band ($\lambda_{\rm eff} = 0.47$ μm) and r band ($\lambda_{\rm eff} = 0.61$ μm) of SDSS9 (Ahn et al., 2012). We used the counterparts as it is explained in Sect. 5.4.4. Table 12.6 lists the value of $log_{10}\left(\frac{F_{\rm x}}{F_{\rm opt}}\right)$ of sources with SDSS9 counterparts. In Figure 6.5 $log_{10}\left(\frac{F_{\rm x}}{F_{\rm opt}}\right)$ is plotted over of HR_2 and HR_3 (see Sect. 6.5). The stars usually have $log_{10}\left(\frac{F_{\rm x}}{F_{\rm opt}}\right) < 1$ and the X-ray bright sources $log_{10}\left(\frac{F_{\rm x}}{F_{\rm opt}}\right) > 1$.
Figure 6.6 shows $log_{10}\left(\frac{F_{\rm x}}{F_{\rm opt}}\right)$ of sources which had counterparts in MegaCam catalogue over of HR_2. The position of Source No 65, which is an LMXB candidate with a counterpart in MegaCam catalogue, is marked in red. This source did not have counterpart in SDSS9. This shows obviously that the source is a dominant X-ray source. In chapter 7, the X-ray to optical flux ratio of different classes of sources is investigated.

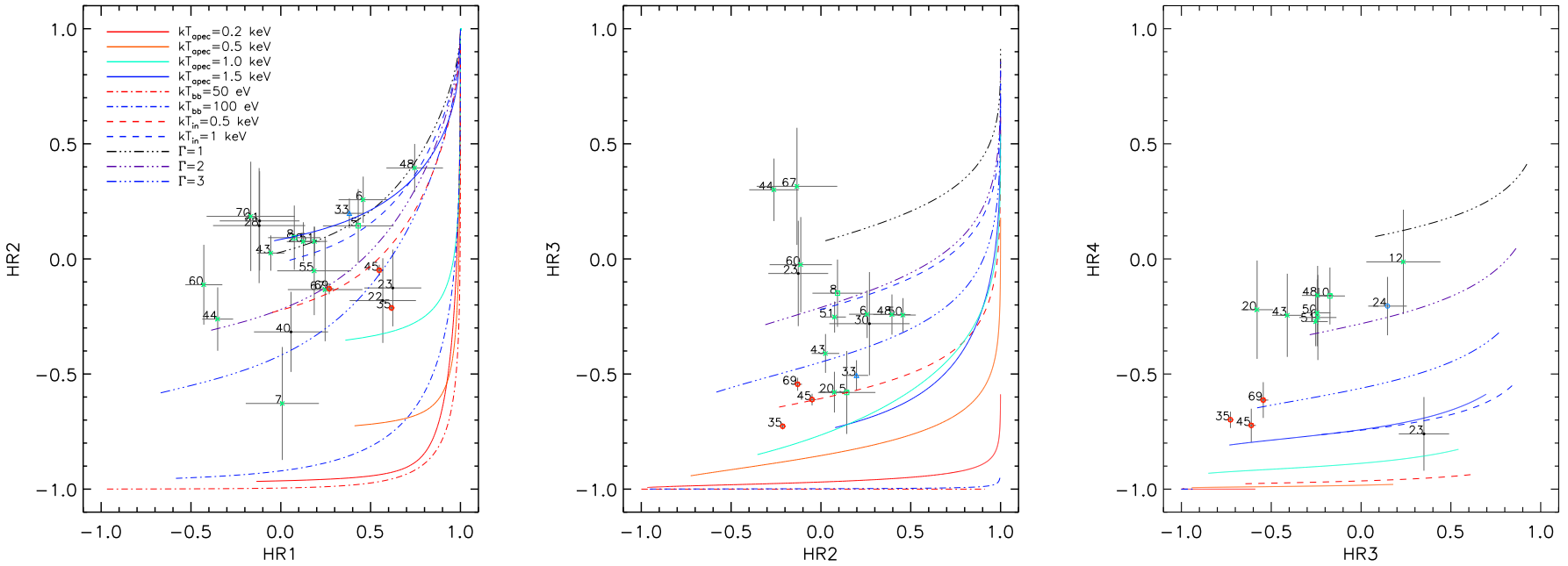

Figure 6.4: Hardness-ratio diagrams. The lines are the hardness ratios calculated for different spectral models and column densities. For the different source classes same symbol types are used as in Fig. 5.4.

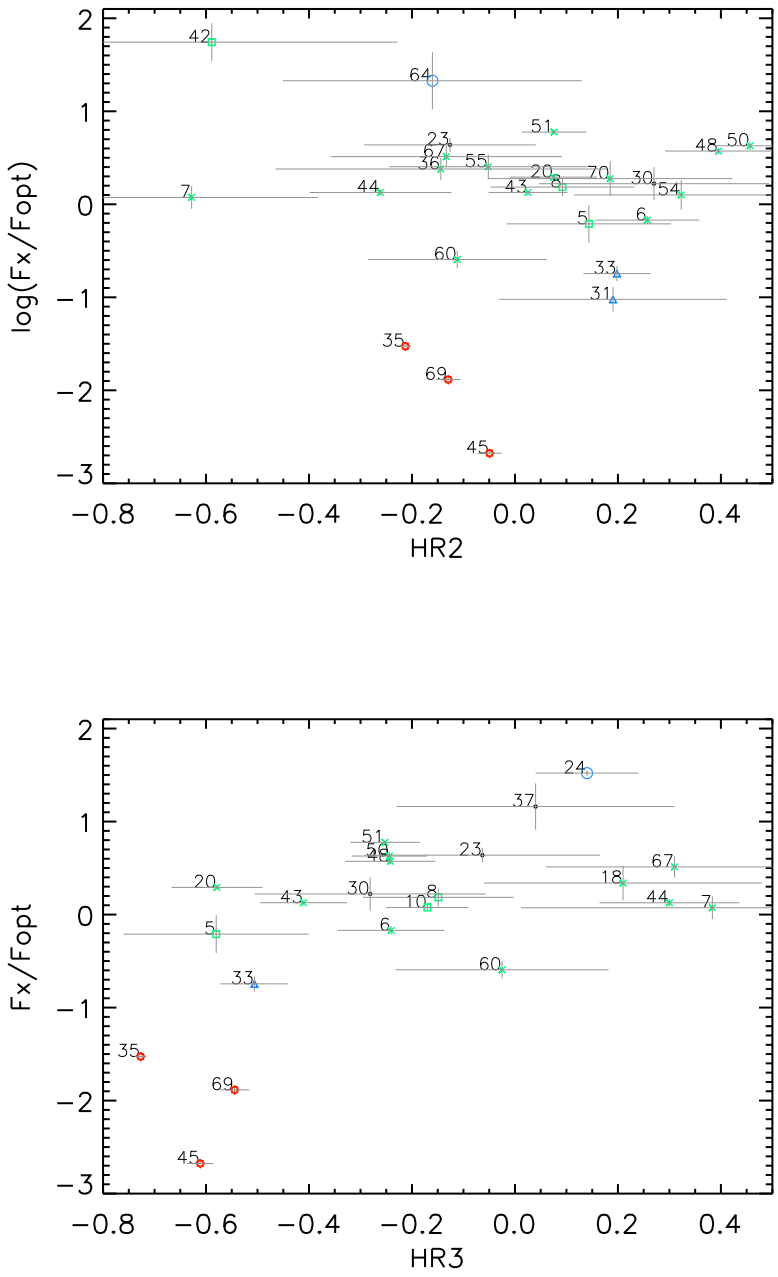

Figure 6.5: X-ray to optical logarithmic ratio $log(\frac{F_x}{F_{opt}})$ over hardness ratios HR_2 and HR_3. For the different source classes same symbol types are used as in Fig. 5.4.

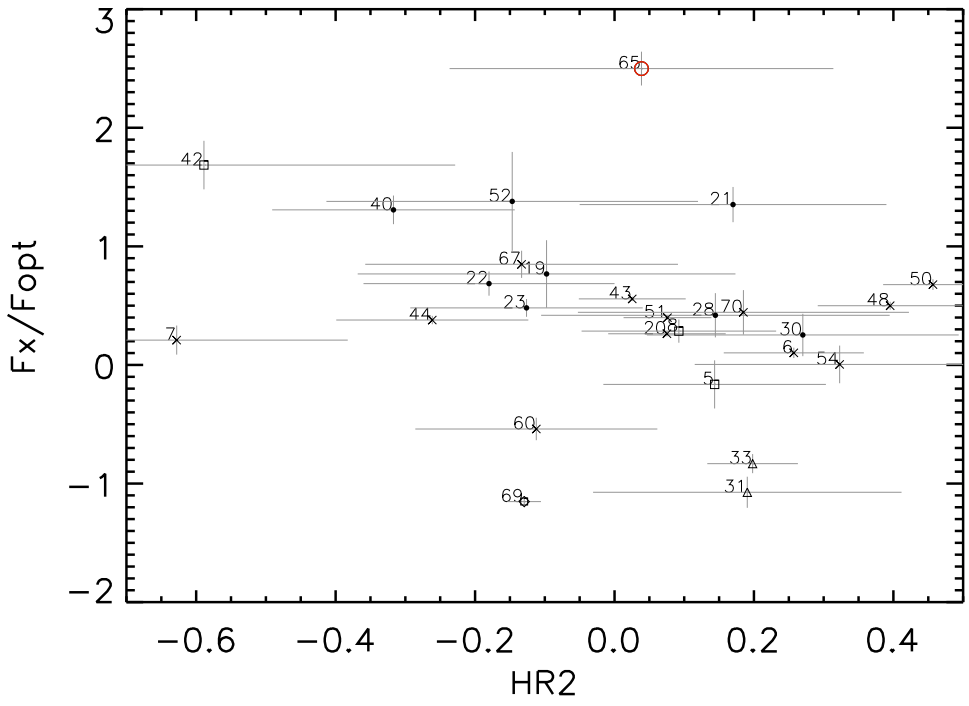

Figure 6.6: The X-ray to optical logaritmic ratio over HR_2. The optical counterparts are from MegaCam catalogue (Table. 12.8). For the different source classes same symbol types are used as in Fig. 5.4. The position of Source No 65 which is a candidate of LMXB and has a counterpart in MegaCam catalogue is marked in red.

Chapter 7

Source classification

We classified the sources detected in the *XMM-Newton* observations into different classes of X-ray objects: foreground stars, galaxies, AGNs, XRBs, white dwarf binary systems, and hard sources.
The sources are classified based on different methods: cross correlation with catalogues at other wavelengths (5.4), variability (6.1), spectral analysis (6.4), hardness ratio diagrams (6.5), and X-ray to optical flux ratio (6.6).
In some cases, the sources were already classified in other wavelengths (e.g., majority of AGNs). But in most cases, we define the criteria on the basis of the new analysis. Many sources remained unclassified since not have enough information was available for them. Table 7.3 gives the class of each source.

7.1 Foreground star and star systems

The physical mechanisms which cause X-ray emission in stars have been explained in Section 2.2.1. To identify X-ray sources as foreground stars, we considered that, in general, stars are brighter in optical $(\frac{F_x}{F_{opt}}) < 10^{-1}$ (e.g., Maccacaro et al., 1988) and they are soft X-ray sources (see Sect. 2.2.1). The classified foreground stars have $log_{10}\left(\frac{F_x}{F_{opt}}\right) < 1$, $HR_2 \leq 0.0$, $HR_3 \leq -0.5$ and $HR_4 \leq -0.5$. The optical colour- magnitude diagrams show that there is a significant offset distance between the foreground sources and the isochrone line of the galaxy members (Fig. 5.4). Foreground stars are obviously brighter than other sources in the optical. We used these criteria for foreground stars: $g - r \leq 0.0$, $g < 15.0$.
In addition, we also used the colour magnitude diagram in the near-infrared (2MASS survey) and infrared (WISE survey) to classify foreground stars (Fig. 5.5). In near infrared K band, they are significantly brighter than other sources. The infrared WISE survey counterparts of the foreground stars are located in a region obviously separated from other classes of sources (Fig. 5.5). The criteria of the 2MASS and WISE counterparts for the foreground stars are: $J - K \leq 1.0$,

$K < 12.0$, and $W3 - W1 \leq 0.5$.
A source is classified as a foreground star if it satisfies almost all of the defined criteria. In addition, SDSS9 optical mosaic images of foreground stars show that they are much brighter than other sources and are dominant in the optical band (see Appendix 12.6 and Appendix 13).

We classified sources Nos 16, 35, 39, 45, 59, and 69 as foreground stars. According to the catalogue of Ségall et al. (2007) they are classified as stars of the Draco dSph. However, these bright sources have never been selected as a member of the Draco dSph in other catalogues (see Sect. 5.4.3). As they fulfil all of our X-ray foreground star criteria, we consider them as foreground stars.
Spectral analysis has been performed for the brightest foreground stars. Sources Nos 35, 45, and 69 were the brightest X-ray foreground stars. Source No 69 was located on damaged pixels. Therefore we could not perform a spectral analysis for this source.

Source No 35

This source is the brightest X-ray source in the field of the Draco dSph. The source is an eclipsing binary of W UMa type (contact binary, Lucy, 1968) and is named V* GM Dra (Gazeas et al., 2005). It is an eclipsing binary discovered by ESA's Hipparcos mission (ESA 1997). Its optical light curve was studied by Gazeas et al. (2005). The evolution and structure of this kind of binary systems was studied over decades based on optical observations (e.g, Vilhu, 1983; Geske et al., 2006). Contact binary systems are expected to have a high level of coronal X-ray emission as a result of their short periods (see Sect. 2.2.1). Studies of the X-ray luminosity of these systems, spectral emission lines, variability of the X-ray flux over time, and optical results help to understand their structure better. In a population study of contact binaries, Shaw et al. (1996) showed that W UMa type systems have luminosities around 30 ergs/sec.
In the case of V* GM Dra, we fitted the X-ray spectrum with a two-component VAPEC model, the thermal plasma model APEC with variable abundances. Figure 6.2 and Table 6.3 show the details of the spectral analysis of this source in OBS1 data which have the best statistics. The best fit was achieved when two temperatures of the plasma components and the carbon abundance were left free to vary. While the reduced χ^2 is 1.62 for 337 degrees of freedom if the C abundance parameter is frozen to 1.0, it becomes 1.07 for 336 degrees of freedom if C is freed (see Table 6.3). Therefore, the F-test probability that the two cases are consistent with each other is 4.05986×10^{-32} and indicates that fitting the C abundance improves the fit significantly. The average element abundance in W UMa type binaries are usually found to be lower than the solar photosphere value

(e.g., Gondoin, 2004a,b).

Figure 7.1: Simultaneous by fitted EPIC spectra of source No 45

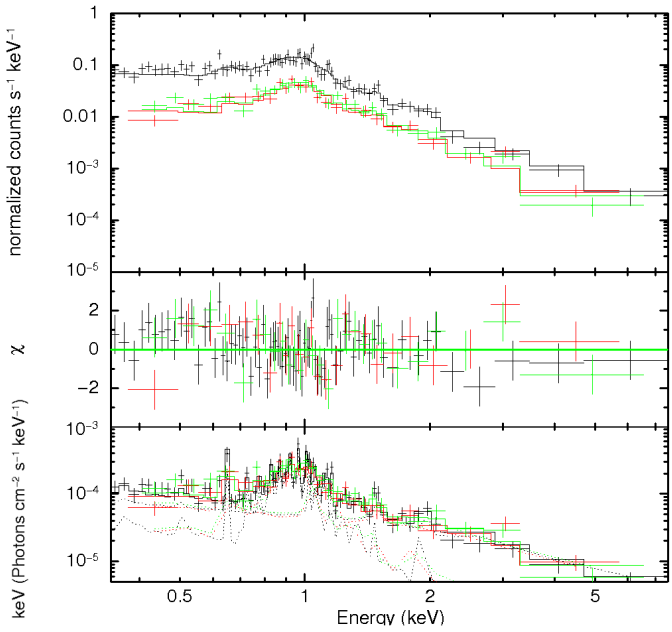

Table 7.1: Fitted parameters of source No 45

Model parameters	
$N_{\rm H}(10^{22}$ cm$^{-2})$	<0.01
kT(keV)	$0.83^{+0.03}_{-0.04}$
Norm.	$5.84^{+0.64}_{0.04} \times 10^{-5}$
kT(keV)	$2.48^{+0.82}_{-0.19}$
Norm.	$1.63^{+0.83}_{-0.43} \times 10^{-4}$
χ^2_ν(d.o.f.)	1.11 (127)

Fit parameters of the X-ray spectra of source No 45 with the model phabs×(mekal+mekal). Errors are 90% confidence limits.

Source No 45 We performed spectral analysis for all of the observations. Figure 7.1 and Table 7.1 show the fit model of this source in OBS2, which had the

highest amount of counts. The source is fit well with a MEKAL model. The source was not identified as a member of Draco dSph in any optical catalogue (see Sect. 5.4.3) but as a star e.g, Röser et al. (2008) and Flesch (2010). Its place in the optical and infrared colour-colour diagrams perfectly shows the behaviour of a foreground source (Figures 5.5, 5.4 and 6.5). It is neither reported as a variable source (e.g., Kinemuchi et al., 2008) nor as a binary system. Therefore, it is most likely an isolated foreground star.

7.2 Background objects

7.2.1 AGN and Quasars

The properties of X-ray emission of AGNs are explained in Section 2.2.2. We considered the criteria of Pietsch et al. (2004) for the classification of background objects: $HR_2 \geq -0.4$ and the existence of a radio counterpart. We identified sources Nos 12, 13, and 51 as AGNs, since radio counterparts were found in the catalogue of 1.4GHz NRAO VLA Sky Survey (NVSS-1998). Table 12.11 lists the details of the radio counterparts. In addition to the HR_2 criterion, sources identified as AGNs fulfill the following criteria: $HR_3 \geq -0.5$ and $HR_4 \geq -0.5$. Source No 13 was classified before as a quasar-galaxy (see Sect. 7.2.2). Since there are catalogues in literature based on a dedicated search for AGNs, we checked for correlations of the *XMM-Newton* sources with AGN catalogues (see Sect. 5.4.2). Sources Nos 6, 7, 20, 43, 44, 60, 68, and 70 have counterparts that were classified as AGNs and counterparts of sources Nos 18, 34, 36, 48, 50, 54, 55, and 67 were considered as AGN candidates in at least one of the AGN/quasar catalogues (see Sect. 5.4.2). All classified AGNs are point sources in the optical (see Appendix 11.3) and infrared, and they have $-1.0 \leq log_{10}(\frac{F_{\rm x}}{F_{\rm opt}}) \leq 1.0$. In optical colour-colour and colour-magnitude diagrams, they apear bluer than the galaxies and have $-0.5 \leq g - r \leq 1.0$ and $-1.0 \leq g - i \leq 1.0$ (ss Fig. 5.4). In infrared colour-colour and colour-magnitude diagrams they are not separated from other sources. In hardness ratio diagrams, AGNs don't show any special behaviour.
The brightest classified AGN is source No 43 with a total flux of $6.66 \pm 28 \times 10^{-13}$ erg s^{-1} cm^{-2} in 0.2 – 12 keV. For some AGNs we performed spectral analysis and all are well fit with power-low model (Table 6.2).

7.2.2 Galaxies

The X-ray properties of galaxies are explained in Section 2.2.2. Typically, an X-ray source can be classified as a galaxy if the optical or infrared counterpart in the SDSS9 and WISE images is extended. Sources Nos 4, 5, 8, 10, and 13 were classified in the star/galaxy classification catalogue (Vasconcellos et al., 2011) and SDSS9 survey (Ahn et al., 2012). These source appear extended in the optical image (see Appendix. 13.1). Source No 13 is an optically dominant galaxy (Fig. 6.5) with a radio counterpart (see Table 12.11) which is classified as a quasar (Bukhmastova, 2001). Sources Nos 41, 42, 53, and 66 were classified as galaxies in SDSS7 and SDSS9 survey (Abazajian et al., 2009; Ahn et al., 2012). We considered these sources as galaxy candidates.
In colour-colour and colour-magnitude diagrams, the classified galaxies appear redder than AGNs in the optical with $g - i \geq 1.0$, and $g - r > 0.5$ (Fig. 5.4). However, they do not show any special tendency in X-ray luminosity or hardness ratios.

7.3 X-ray binary candidates

Since there is no recent star formation in dSphs, XRBs in these galaxies are expected to be LMXBs containing an NS or a BH and a low-mass companion like a red giant or low-mass main sequence star with $\lesssim 1\ M_{\odot}$, or a white dwarf.
As it is mentioned before, it is difficult to distinguish the AGNs from XRBs only based on X-ray data. In hardness ratio diagrams these two classes of sources occupy the same place. Both type of sources can be variable. One of the main indictators of XRBs is periodicity or pulsation. As explained in Section 6.2, we could find neither periodicity nor pulsation for sources in all observations using the Lomb-Scargle method. However the $Z^2_{\rm n}$ Rayleigh test revealed pulsations of the source No 65. The details are explained in section 7.3.1. The short exposure times of these observations make it very difficult to perform significant spectral analysis of the hard sources. Therefore, we considered some other factors to find LMXB candidates. For hard sources, not classified as AGNs, the X-ray to optical flux ratio diagram is a good tool for the classification. We have shown that the classified AGNs have $-1.0 \leq log_{10}(\frac{F_{\rm x}}{F_{\rm opt}}) \leq 1.0$. As candidates for LMXBs, we considered the sources which had $(\frac{F_{\rm x}}{F_{\rm opt}}) \geq 1.0$ because the optical flux of a low mass star should be relatively low. As explained in Section 3.2 the majority of the stars in the Draco dSph are red giants, quite faint in optical bands. For hard sources with $log(\frac{F_{\rm x}}{F_{\rm opt}}) \geq 1.0$ (6.6), we also checked the optical colour-magnitude diagram (Fig. 12.5). We considered hard sources with optical counterparts, classified as a member of the Draco dSph, as candidates for LMXBs:

Sources Nos 14, 24, and 64 showed hard spectra in both spectral analysis and hardness ratio diagrams. Their optical counterparts were classified as stars in the Draco dSph based on photometry (e.g, Piatek et al., 2001; Rave et al., 2003). Their flux ratio is high with $log_{10}(\frac{F_{\rm X}}{F_{\rm opt}}) \geq 1.0$ (see Table 12.6). They are likely XRBs in the Draco dSph.
Source No 24 was classified as a quasar candidate at a low redshift by Abraham et al. (2012), who mainly classified the sources (quasars, galaxies or stars) based on the colour-colour diagrams using the SDSS7 data. The colour of the source indicates a quasars in SDSS7, however the u band magnitude of the SDSS9 survey is significantly different from that of SDSS7. With the colours of SDSS9 ($u-g \sim 1.9$ and $g-r \sim 0.7$) the source is likely a star based on the diagrams of Abraham et al. (2012). Also, the position of the source in the colour-magnitude diagram is far from that of classified AGNs (Fig. 5.4). The source is not reported as an AGN in any other AGN catalogue. Therefore, we classified the source as a LMXB candidate.

7.3.1 The pulsation of XMMUJ172140.6+580244

By applying the $Z^2_{\rm n}$ test for the 1st and 2nd harmonics, source 65 showed pulsation at ∼19.18 s in the EPIC-pn data of OBS2 (see Sect. 6.2.3). The number of photons was 87.
The probability that a peak is not caused by noise but more likely by pulsation in $N = nT_{\rm exp}\Delta f$ independent trials is $P = [1 - \exp(-Z^2_2/2)]^{nT_{\rm exp}\Delta f}$, where n is the number of searched harmonics and $T_{\rm exp}\Delta f$ is the number of searched periods, where $T_{\rm exp}$ is the exposure time of the event file, and Δf is the frequency range $\Delta f = 0.00005 - 6.8$. The maximum frequency which can be investigated is the Nyquist limit obtained from the time resolution of EPIC-pn in full-frame mode. The maximum frequency is limited by the duration of the observation. The Z^2_2 value of 43.35 for the peak occurring at ∼19.18 s corresponds to a detection probability of ∼99.991% ($\gtrsim 3.5\sigma$ detection, see Fig. 7.2). If we also consider the number of detected sources in the random search for pulsation, the detection probability decreases to $\sim 2.7\sigma$.

We found a counterpart for the X-ray source in the optical MegaCam catalogue (see Sect. 5.4.3) with magnitudes of $g\,(0.47\mu{\rm m}) = 25.37 \pm 0.14$, $r\,(0.62\mu{\rm m}) = 24.2 \pm 0.10$ and $i\,(0.81\mu{\rm m}) = 24.13 \pm 0.12$, and in the first look survey of *Spitzer* Space Telescope (Fadda et al., 2004) with magnitude $R = 24.4 \pm 0.15$. Figure 6.6 shows the position of the source in X-ray to optical flux ratio diagram, and Figure 5.3 shows the optical counterpart in the MegaCam colour-magnitude diagram. As indicated by the $g-r$ colour index, the optical counterpart is a

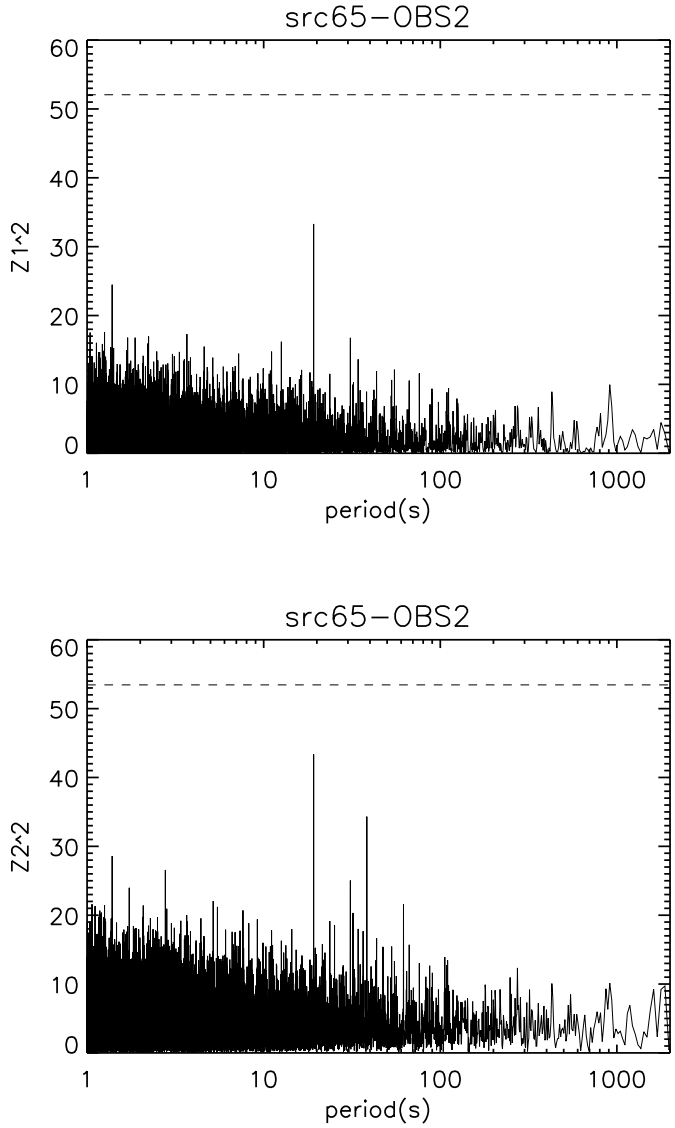

Figure 7.2: The significance of pulsations of XMMUJ172140.6+580244 (source No 65) in the first harmonic (up) and the second harmonic (down). The dashed line shows the 5σ significance.

very faint red single star. The flux ratio is $log_{10}(\frac{F_X}{F_{opt}}) = 2.5$. If this counterpart is associated with the X-ray source, the source is an accreting pulsar in a binary system in Draco dSph the optical counterpart is not associated with the X-ray source, the source can be an isolated pulsar.

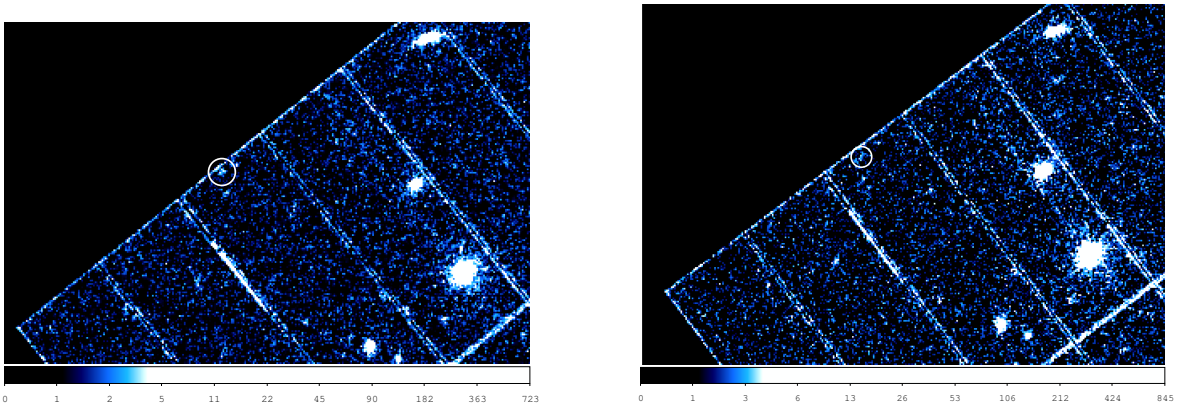

Figure 7.1: The location of the source No 65 in EPIC-pn image of OBS1 (left) and OBS2 (right).

The source was not detected in other data than that of the EPIC-pn camera in OBS1 and OBS2, because it was either located outside of the FOV (EPIC-MOS) or on damaged pixels (EPIC-pn). In OBS1 we could not find any evidence of pulsation for the source. However, the source is fainter in OBS1 than in OBS2. Figure 7.1 shows the position of the source in EPIC-pn camera in OBS1 and OBS2. The total flux in the band of 0.2 – 12 keV in OBS1 is $F = (7.83 \pm 4.29) \times 10^{-14}$ erg s^{-1} cm^{-2}, and in OBS2 $F = (1.13 \pm 0.45) \times 10^{-13}$ erg s^{-1} cm^{-2}.

Since we found an indication for pulsation, we applied for a 10 ks observation by *Swift* (Burrows et al., 2005) for source No 65. Two 5 ks observations were performed by *Swift*. However, the source was not detected. In the *Swift* data, we calculated the upper limit of the flux of 4.1×10^{-14} erg s^{-1} cm^{-2}. Figure 7.2 shows the light curve of *XMM-Newton* and *Swift* observations for source No 65. There are some explanations for the non-detection in *Swift* observation: First, this source is variable and became fainter. Second, since the source is located too near to the edge of EPIC-pn (see Fig.7.1), there is the possibility of flux overestimation in the second observation. In conclusion, to prove the pulsation detected in *XMM-Newton* additional observation is necessary.

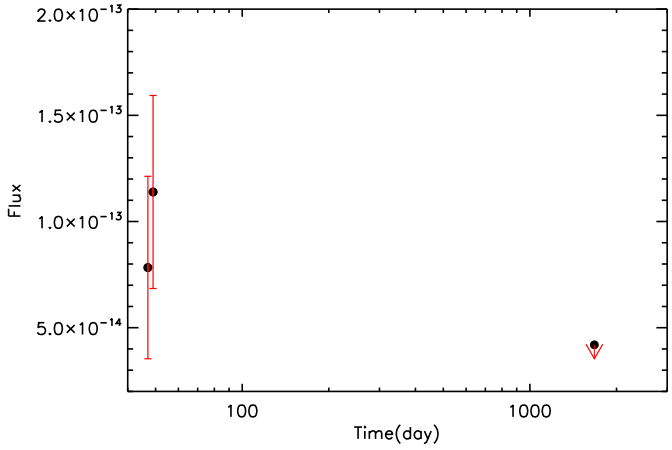

Figure 7.2: The light curve of the *XMM-Newton* and Swift observation of source No 65.

7.4 Other binary systems

Three sources are most probably binary systems. One of the them (source No 27) is a known symbiotic star. Two other sources show an indication of binary systems but are not hard X-ray sources. The details of these sources are explained in the following:

Source No 27

Its counterpart is a known symbiotic star in the Draco dSph, Draco C1 (Belczyński et al., 2000). Symbiotic stars are interacting binary systems considering of a late-type giant star and a compact companion (usually a white dwarf). They show far ultraviolet and super-soft X-ray emission.
The source was studied in long-term optical photometry over years and shows a significantly variable light curve (e.g., Kinemuchi et al., 2008; Henden and Munari, 2008). It was classified in the *GALEX* hot white dwarfs catalogue of the Milky Way (Bianchi et al., 2011). However the high variability and luminosity of the source are more consistent with a symbiotic system in the Draco dSph ($\sim$ 82 kpc, Munari and Buson, 1994). In addition, the radial velocity of the source is similar to that of Draco dSph members (-311.7 ± 13.5 km s^{-1} Margon et al., 2002).
In this work, the $log_{10}(\frac{F_{\rm x}}{F_{\rm opt}})$ ratio shows that the optical flux is higher than the X-ray flux. The source was not bright enough in any observation, therefore, we could neither study its X-ray spectrum nor the hardness ratios.

Source No 31

The $log_{10}(\frac{F_x}{F_{opt}})$ ratio of the source is less than one but not consistent with a foreground star (Fig. 6.5). This source was classified as a member of the Draco dSph in different radial velocity measurements (e.g., Kleyna et al., 2002; Olszewski et al., 1995). The position of the source in both the optical and infrared colour-magnitude diagrams is far from that of typical foreground stars and seems more similar to source No 27, which is a symbiotic star (see Fig. 5.4 and Fig. 5.5). The infrared colours of the counterpart $J - K \lesssim 0.9$ and $I - J \lesssim 0.3$, obtained from the infrared surveys of 2MASS and the William Herschel Telescope, indicate that the source is located in the region of the red giant branch of the Draco dSph, according to the classification of Cioni and Habing (2005). The source is likely a binary system with a red giant in the Draco dSph, but the exact nature of the system is not clear.

Source No 33

This source is the most variable source (Fig. 6.1), found in this catalogue (variability factor = 49.07±11.94). Its high variability factor is related to the higher flux of the source in OBS4 (see Appendix 12). It appears that the source has been detected during a flare or an outburst in OBS4. We fitted a power-law model to the spectrum of the source in OBS4 (Table 6.2). Figure 6.4 shows the hardness ratio of the source in OBS4. The hardness ratio of the source in OBS1 and OBS2, before the increase of the flux, is much softer than OBS4. With $HR_1 = 0.5 \pm 0.2$ and $HR_2 = -0.8 \pm 0.2$, it shows a very soft spectrum in OBS1. The source is also detected by *Chandra*, with a flux of $4.35^{3.16}_{5.54} \times 10^{-15}$ erg s $^{-1}$cm $^{-2}$ in the energy range of $0.5 - 7$ keV. The hard and soft hardness ratios of the *Chandra* data are not significant enough but they suggest a soft behaviour (Evans et al., 2010). The flux ratio $log(\frac{F_x}{F_{opt}}) = -1.01 \pm 0.07$ indicates that this source is dominant in the optical. The optical and infrared colours as well as variability are not indicative of a foreground star (see Fig. 5.4 and Fig. 5.5). These properties make it a possible candidate for a CV in the Draco dSph.

7.5 Hard sources

We classified sources with no previous classification as hard sources if they have $HR_2 - EHR_2 > -0.2$ or only HR_3 and/or HR_4 were defined (Pietsch et al., 2004). These sources can either be background AGNs or XRBs in the Draco dSph. We classified sources Nos 21, 25, 28, 30, 37, 38, 47, 49, and 58 as hard sources.

7.6 Summary

In total, we classified 18 sources as AGNs and 9 sources as galaxies and galaxy candidates. Six sources were classified as foreground stars and one source as a foreground contact binary system in the Milky Way. Four sources were classified as LMXB candidates. One of them shows a significant pulsation, while the others were classified based on the optical to X-ray flux ratio and their position in the colour-magnitude diagrams. We also found a symbiotic star, a CV candidate, and a binary system in the Draco dSph. Based on hardness ratios, we classified 9 hard sources, which can be AGNs or LMXBs in the field of the Draco dSph.
Table 7.2 shows a summary of the classifications of sources and Table 7.3 shows the final catalogue of sources with their position, total weighted count rate and flux in the energy band of $0.2-12$ keV, the weighted hardness ratio of each source, and their classification.

Table 7.2: The criteria or/and behaviours of the different classes of the X-ray sources in the *XMM-Newton* study of the Draco dSph

Class*	number of sources	The criteria or behaviours
FG	6 Cl	Criteria: $log_{10}(\frac{F_{\rm X}}{F_{\rm opt}}) \leq -1$, $HR_2 \leq 0.0$, $HR_3 \leq -0.5$, $HR_4 \leq -0.5$, $g-r \leq 0.0$, $g < 15.0$, $J-K \leq 1.0$, $K < 12.0$, $W3-W1 \leq 0.5$
AGN	10 Cl – 8 Can	Criteria: $HR_2 \geq -0.4$ and the existence of a radio counterpart. Behaviour: $-1.0 \leq log_{10}(\frac{F_{\rm X}}{F_{\rm opt}}) \leq 1.0$, $-0.5 \leq g-r \leq 1.0$, and $-1.0 \leq g-i \leq 1.0$.
GLX	5 Cl – 4 Can	Criteria: Extended optical or infrared counterpart. Behaviour:$g-i \gtrsim 1.0$ and $g-r > 0.5$
LMXB	4 Can	Criteria: Presence of pulsation and classified optical counterpart in the galaxy. Behaviour: $log_{10}(\frac{F_{\rm X}}{F_{\rm opt}}) \geq 1.0$ and and classified optical counterpart in the galaxy
BS	1 Cl – 2 Can	Criteria: Very soft in HRs, Variable Behaviour: $log_{10}(\frac{F_{\rm X}}{F_{\rm opt}}) \leq -1$, $J-K \leq 5.0$, $0.0 \geq W3-W1 \leq 2.5$
H	17 Cl	Criteria: $HR_2 - EHR_2 > -0.2$ or only HR_3 and/or HR_4

*: GLX: galaxy, AGN: active galactic nuclei, FG: foreground star, XRB: X-ray binary,
BS: binary system, H: hard source, Cl: classified, Can: candidate.

Table 7.3: Catalogue of X-ray sources in the field of the Draco dSph spheroidal galaxy detected by *XMM-Newton*

ID	Class†	RA (J2000)	Dec (J2000)	r1σ ()	Count rate $(0.2-12$ keV) $(\mathrm{ct\,s^{-1}})$	Flux $(0.2-12$ keV) $(\mathrm{erg\,s^{-1}\,cm^{-2}})$	ML	**HR1**	**HR2**	**HR3**	**HR4**
1		17 18 46.52	+57 54 46.5	1.16	4.18e-3± 6.64e-4	2.09e-14± 3.92e-15	1.15e+1	-	-	-	-
2		17 18 48.45	+57 50 13.3	1.05	5.95e-3± 9.47e-4	2.56e-14± 5.02e-15	1.47e+1	-		-	-
3		17 18 49.99	+57 54 52.9	0.88	4.71e-3± 6.57e-4	8.01e-15± 3.90e-15	4.03e+1	-	-	-	-
4	GLX	17 18 56.89	+57 51 04.0	1.07	3.34e-3±7.41e-4	4.34e-15 ± 6.46e-15	2.50e+1	-	-	-	-
5	GLX	17 19 00.63	+57 51 45.7	1.19	5.01e-3± 6.43e-4	2.04e-14 ± 9.55e-15	6.45e+1	0.43±0.19	0.14±0.15	-0.58±0.18	-
6	AGN	17 19 01.51	+58 00 29.0	0.35	1.19e-2± 5.14e-4	8.77e-14 ± 8.85e-15	1.23e+3	0.45±0.13	0.25±0.10	-0.24±0.10	-0.25±0.18
7	AGN	17 19 04.05	+58 03 29.3	1.15	6.51e-3± 5.21e-4	3.66e-14 ± 1.03e-14	3.74e+2	0.01±0.20	-0.62±0.24	0.38±0.37	-0.25±0.51
8	GLX	17 19 04.54	+57 47 27.5	0.48	6.67e-3± 4.72e-4	4.18e-14 ± 9.42e-15	4.82e+2	0.07±0.14	0.09±0.13	-0.14±0.14	-
9		17 19 06.76	+57 55 48.0	0.92	2.37e-3± 5.22e-4	1.43e-14 ± 9.55e-15	2.32e+1	-	-	-	-
10	GLX	17 19 10.33	+57 49 48.0	0.37	1.04e-2± 4.88e-4	1.33e-13 ± 1.10e-14	7.32e+2	-	-	-0.17±0.08	-0.16±0.12
11		17 19 11.75	+57 47 20.9	2.44	3.80e-3± 8.93e-4	7.22e-15 ± 9.79e-15	1.14e+1	-	-	-	-
12	AGN (r)	17 19 19.62	+57 59 42.2	0.39	6.31e-3± 3.15e-4	1.08e-13 ± 8.43e-15	5.87e+2	-	-	0.23±0.20	-0.01±0.22
13	GLX (r)	17 19 20.17	+57 54 01.5	1.30	2.51e-3± 3.81e-4	1.24e-14 ± 5.01e-15	5.39e+1	-	-	-	-
14	XRB-CAN	17 19 21.71	+57 49 43.8	0.33	1.00e-2± 4.44e-4	6.14e-14 ± 6.43e-15	1.27e+3	-	-	-	-
15		17 19 24.84	+57 44 52.0	0.54	5.96e-3± 4.98e-4	3.05e-14 ± 6.97e-15	2.66e+2	-	-	-	-
16	FG	17 19 25.98	+57 50 19.1	1.39	2.43e-3± 4.02e-4	3.32e-15 ± 2.11e-15	1.45e+1	-	-	-	-
17		17 19 26.14	+58 00 57.3	1.90	5.63e-3± 9.45e-4	1.19e-14 ± 1.04e-14	1.14e+1	-	-	-	-
18	AGN-CAN	17 19 28.02	+57 43 12.6	0.72	4.76e-3± 5.89e-4	4.23e-14 ± 1.81e-14	8.94e+1	-	-	0.21± 0.27	-
19		17 19 29.56	+57 49 36.4	1.88	3.93e-3± 9.64e-4	1.30e-14 ± 8.53e-15	1.59e+1		-0.10± 0.27	-	-
20	AGN	17 19 34.35	+57 58 50.1	0.17	2.32e-2± 5.51e-4	1.53e-13 ± 8.16e-15	6.77e+3	0.12±0.09	0.07±0.08	-0.57±0.08	-0.2±0.21
21	H	17 19 36.65	+57 49 00.2	0.78	7.08e-3± 8.84e-4	2.83e-14 ± 9.67e-15	8.43e+1	-0.12± 0.22	0.17± 0.22	-	-
22		17 19 37.01	+57 46 58.7	0.66	6.96e-3± 5.93e-4	1.97e-14 ± 4.62e-15	1.82e+2	0.57± 0.18	-0.18± 0.18	-	-
23		17 19 45.43	+57 52 56.9	0.56	2.21e-3± 1.76e-4	1.24e-14 ± 2.15e-15	2.04e+2	0.62± 0.16	-0.13± 0.17	-0.06 ± 0.23	-0.56 ±
24	XRB-CAN	17 19 53.96	+57 59 50.8	0.36	5.20e-3± 2.41e-4	9.22e-14 ± 6.16e-15	6.96e+2	-	-	0.14±0.10	-0.20±0.12
25	H	17 19 56.21	+58 05 27.1	1.16	4.92e-3± 8.91e-4	1.93e-14 ± 1.00e-14	1.83e+1	-	-	-0.01± 0.27	-
26		17 19 57.05	+57 46 17.8	0.64	5.37e-3± 4.42e-4	2.82e-14 ± 5.73e-15	2.07e+2	-	-	-	-

ID	Class	RA (J2000)	Dec (J2000)	r1σ ($''$)	Count rate ($0.2-12$ keV) (ct s^{-1})	Flux ($0.2-12$ keV) (erg s^{-1} cm^{-2})	ML	**HR1**	**HR2**	**HR3**	**HR4**
27	SYM	17 19 57.76	+57 50 06.2	0.88	4.40e-3± 2.83e-4	1.03e-14 ± 2.46e-15	1.14e+1	-	-	-	-
28	H	17 20 02.29	+57 55 44.3	0.97	3.05e-3± 4.69e-4	4.85e-15 ± 2.09e-15	1.55e+1	-0.12± 0.26	0.14± 0.25	-	-
29		17 20 08.31	+57 58 20.4	1.07	2.31e-3± 3.00e-4	1.29e-14 ± 4.07e-15	4.65e+1	-	-	-	-
30	H	17 20 10.16	+57 54 06.5	1.52	3.07e-3± 6.29e-4	7.43e-15 ± 3.05e-15	1.66e+1	-	0.27± 0.22	-0.28± 0.22	-
31	BS-CAN	17 20 13.92	+57 50 52.4	2.20	2.33e-3± 3.38e-4	1.46e-14 ± 4.40e-15	1.96e+1	-	0.19± 0.22	-	-
32		17 20 14.67	+57 46 06.5	1.83	3.71e-3± 9.68e-4	6.91e-15 ± 7.00e-15	1.72e+1	-	-	-	-
33	BS-CAN	17 20 17.96	+57 51 04.4	0.66	3.37e-3± 2.29e-4	1.23e-14 ± 2.29e-15	5.57e+2	0.38± 0.08	0.20± 0.07	-0.50± 0.06	-
34	AGN-CAN	17 20 21.20	+57 43 59.3	2.69	4.02e-3± 7.32e-4	5.36e-14 ± 1.65e-14	2.68e+1	-	-	-	-
35	FG	17 20 21.88	+57 58 26.5	0.04	2.22e-1± 1.24e-3	9.63e-13 ± 6.24e-15	1.87e+5	0.61±0.01	-0.21±0.01	-0.72±0.01	-0.69±0.03
36	AGN-CAN	17 20 21.70	+57 43 27.6	0.71	6.91e-3± 6.91e-4	2.97e-14 ± 8.13e-15	1.68e+2	-	-	-	-
37	H	17 20 23.57	+57 50 09.1	2.22	3.07e-3± 7.90e-4	1.20e-14 ± 6.89e-15	1.73e+1	-	-	0.04± 0.27	-
38	H	17 20 25.77	+57 52 41.3	1.77	3.20e-3± 7.61e-4	1.68e-14 ± 7.31e-15	1.00e+1	-	0.51± 0.36	-	-
39	FG	17 20 25.64	+57 53 04.4	0.65	2.37e-3± 2.40e-4	6.65e-15 ± 2.15e-15	1.66e+2	0.53±0.24	-	-	-
40		17 20 28.33	+57 56 23.3	0.63	2.30e-3± 2.64e-4	1.05e-14 ± 2.93e-15	7.13e+1	0.06± 0.21	-0.32± 0.17	-	-
41	GLX-CAN	17 20 32.86	+58 07 16.0	1.85	1.09e-2± 2.72e-3	6.50e-14 ± 3.89e-14	2.14e+1	-	-	-	-
42	GLX-CAN	17 20 33.08	+58 06 13.7	2.03	5.83e-3± 1.15e-3	5.32e-14 ± 2.50e-14	4.29e+1	-	-0.59±0.36	-	-
43	AGN	17 20 33.62	+58 08 29.7	0.23	9.60e-2± 1.85e-3	6.66e-13 ± 2.84e-14	1.29e+4	-0.05±0.075	0.02±0.07	-0.41±0.08	-0.24±0.18
44	AGN	17 20 37.10	+57 48 56.3	0.33	8.80e-3± 3.54e-4	1.07e-13 ± 8.69e-15	1.25e+3	-0.35± 0.09	-0.26± 0.14	0.30± 0.14	-
45	FG	17 20 37.62	+58 02 12.4	0.11	5.88e-2± 8.16e-4	2.49e-13 ± 7.19e-15	2.16e+4	0.55± 0.02	-0.05± 0.02	-0.61± 0.03	-0.72± 0.07
46		17 20 38.45	+57 45 45.4	1.22	4.36e-3± 9.78e-4	1.63e-14 ± 1.10e-14	2.49e+1	-	-	-	-
47	H	17 20 39.66	+57 56 48.8	1.62	3.03e-3± 8.10e-4	1.27e-14 ± 8.30e-15	1.14e+1	-	-	0.03± 0.29	-
48	AGN-CAN	17 20 43.08	+57 54 43.2	0.35	5.33e-3± 2.35e-4	6.78e-14 ± 5.12e-15	7.59e+2	0.74±0.15	0.39±0.10	-0.24±0.08	-0.15±0.12
49	H	17 20 47.27	+57 53 20.6	0.64	3.09e-3± 2.69e-4	2.15e-14 ± 4.28e-15	1.52e+2	-	-		
50	AGN-CAN	17 20 51.94	+57 41 59.0	0.41	2.18e-2± 1.02e-3	2.09e-13 ± 2.17e-14	9.77e+2	-	0.45±0.071	-0.24±0.07	
51	AGN (r)	17 20 52.28	+57 55 13.2	0.17	2.30e-2± 4.65e-4	1.95e-13 ± 7.67e-15	6.86e+3	0.18±0.06	0.07±0.06	-0.25±0.06	
52		17 20 52.50	+58 04 51.1	1.05	7.90e-3± 2.43e-3	3.26e-14 ± 3.13e-14	1.53e+1	-	-0.15± 0.27	-	-
53	GLX-CAN	17 20 56.35	+57 47 41.7	1.01	3.62e-3± 6.07e-4	1.75e-14 ± 3.66e-15	1.36e+1	-	-	-	-

ID	Class	RA (J2000)	Dec (J2000)	r1σ ($''$)	Count rate ($0.2-12$ keV) (ct s^{-1})	Flux ($0.2-12$ keV) (erg s^{-1} cm^{-2})	ML	**HR1**	**HR2**	**HR3**	**HR4**
54	AGN-CAN	17 21 00.45	+57 51 53.5	0.66	4.88e-3± 5.10e-4	1.42e-14 ± 5.19e-15	1.18e+2	-	0.32± 0.21	-	-
55	AGN-CAN	17 21 04.38	+57 41 06.0	0.83	1.72e-2± 1.61e-3	6.28e-14 ± 1.91e-14	1.22e+2	0.19± 0.21	-0.05± 0.19	-	-
56		17 21 05.04	+57 53 38.2	2.07	1.95e-3± 4.51e-4	1.28e-14 ± 6.87e-15	8.96e+1	-	-	-	-
57		17 21 12.02	+57 50 01.5	0.80	4.56e-3± 7.49e-4	2.30e-14 ± 1.17e-14	7.58e+1	0.53±0.26	-	-	-
58	H	17 21 13.06	+57 56 15.2	0.87	4.10e-3± 5.95e-4	1.96e-14 ± 8.23e-15	3.79e+1	-	-	0.09± 0.23	-
59	FG	17 21 16.66	+58 01 16.5	1.95	6.07e-3± 1.17e-3	8.20e-15 ± 1.24e-14	3.20e+1	0.51± 0.18	-	-	-
60	AGN	17 21 22.92	+57 50 29.2	0.61	9.40e-3± 8.57e-4	6.56e-14 ± 1.43e-14	1.94e+2	-0.43± 0.10	-0.11± 0.17	-0.02± 0.21	-
61		17 21 24.66	+57 52 53.6	2.23	1.11e-2± 4.25e-3	5.03e-14 ± 4.96e-14	1.14e+1	-	-	-	-
62		17 21 29.13	+57 47 08.9	1.80	7.09e-3± 1.76e-3	6.17e-14± 2.80e-14	1.14e+1	-	-	-	-
63		17 21 36.11	+58 03 02.2	1.77	5.48e-3± 1.20e-3	8.40e-15± 1.20e-14	1.14e+1	0.21± 0.25	-	-	-
64	XRB-CAN	17 21 39.51	+58 01 45.2	0.87	8.88e-3± 1.78e-3	2.92e-14± 2.06e-14	5.59e+1	0.91± 0.18	-	-	-
65	XRB-CAN	17 21 40.60	+58 02 44.8	1.63	1.39e-2± 2.21e-3	9.51e-14± 3.12e-14	1.14e+1	-	0.04± 0.28	-	-
66	GLX-CAN	17 21 41.08	+57 45 53.2	1.61	8.99e-3± 2.81e-3	1.88e-14± 3.24e-14	1.86e+1	-	-	-	-
67	AGN-CAN	17 21 41.40	+57 52 35.2	0.66	7.35e-3± 7.36e-4	3.38e-14 ± 8.91e-15	2.48e+2	0.24±0.20	-0.13±0.22	0.31±0.25	-
68	AGN	17 21 48.46	+57 58 03.2	0.72	8.52e-3± 8.20e-4	3.84e-14 ± 1.34e-14	1.99e+2	0.41± 0.21	-	-	-
69	FG	17 21 58.32	+57 49 22.7	0.11	8.55e-1± 1.81e-2	1.82e-12± 9.29e-14	3.76e+4	0.27± 0.02	-0.13± 0.02	-0.54± 0.03	-0.61± 0.08
70	AGN	17 22 11.69	+57 56 51.1	1.88	1.24e-2± 1.71e-3	5.06e-14 ± 2.18e-14	3.44e+1	-0.17± 0.25	0.18± 0.24	-	-

† :GLX: galaxy, AGN: active galactic nuclei, FG: foreground star, XRB: X-ray binary, SYM: symbiotic star, BS: binary system, H: hard source, CAN: candidate, (r): source with radio counterpart.

Chapter 8

X-ray luminosity function (XLF)

8.1 Introduction

As it was explained in Section 2.7, several works have studied the XLFs of different types of galaxies (Kim and Fabbiano, 2004; Gilfanov, 2004). In these works, the X-ray observations had similar exposure times achieving a comparable significances. There are reasons which do not allow to extrapolate the XLF of these works for the case of the dSphs. First, the models, which have been used to normalise the stellar mass and luminosities in this kind of works are not suitable for the case of dSphs. In fact the optical mass of galaxies is much higher than the optical mass of dwarf galaxies. Gilfanov (2004) estimated the stellar mass of the galaxies according to the model by Bell and de Jong (2001), based on the $K-$band mass-to-light ratio and the $B-V$ optical colour. Bell and de Jong (2001) mentioned that their model is not appropriate for dSphs. Second, due to the very old stellar population of dSphs, we expect to detect LMXBs in lower luminosity ranges than in other kinds of galaxies. Gilfanov (2004) showed that, in the case of early and late type galaxies, LMXBs have luminosities of $10^{36} - 10^{38}$ erg s^{-1}, however, in the case of the dSphs, the majority should have a luminosity of $\sim 10^{35}$ erg s^{-1}. We explained in section 2.3.2 the different kinds of LMXBs which can have low luminosities. Third, the study of the XLF of other types of galaxies shows a correlation between the X-ray luminosity of XRBs and the SFR of galaxies (e.g., Grimm et al., 2003). Dwarf spheroidal galaxies are the oldest known galaxies and have no recent star formation. The study of their XLF as system with no recent star formation is interesting. Taking these problems to account, XLFs of dSphs seems to form a separated class.

With the aim to study the LMXB population in the dSphs, we calculated the XLFs for OBS 1, 2, 3, 5 of the Draco dSph, plus the XLF of all combined observations. We also calculated the XLFs of the Phoenix, Fornax, Leo I, Ursa Minor, and Ursa Major II dSphs. All these dSphs were observed by XMM-Newton and their X-ray sources were classified in other works. The details of the observations and sources

are explained in Section 8.3. In the Draco dSph, we excluded OBS4 in individual study of the XLF, because the detection sensitivity of this observation (see Fig. 8.2), and consequently the number of the detected sources (see Figure 8.1), is noticeably lower due to the low exposure time of this observation. However, the EPIC event images of this observation were included in the production of XLF of mosaic image.

In general, to have a significant estimate of the population of XRBs in a given field, two important points should be considered: First, a correct estimation of the number of sources with lower fluxes. Since the sensitivity of an X-ray detector is not uniform in the total area of its FOV, this problem is solved by estimating the sky-coverage function of the detector (Sect. 8.2.2). Second, to have an XLF of the XRBs, only sources, which are most likely X-ray binaries should be included. The source classification enables us to separate the soft sources and foreground stars. However, it is likely that not all AGNs have been identified. Since they are the most numerous X-ray sources in a field like the Draco dSph, their XLF has to be estimated based on a deep survey e.g., the COSMOS survey of *XMM-Newton* (Cappelluti et al., 2009). Since the *logN-logS* relation of the COSMOS survey is limited to two energy ranges of $0.5-2.0$ keV and $2.0-10$ keV, we calculated the XLFs in these two energy ranges (Sect. 8.2.3).

8.2 XLF of the Draco dwarf spheroidal galaxy

8.2.1 Catalogue of the hard sources

The source detection process was performed with an ML of 10 in the total energy band of $0.2-12$ keV (see Sect. 5.2.1). To calculate the XLFs of the sources in the energy ranges of the $0.5-2.0$ keV and $2.0-10$ keV, we repeated the source detection procedure with ML of 10 in these two energy bands for EPIC-pn images of observation 1, 2, 3, 5. For each observation, we corrected the catalogue of detected sources with the final catalogue (Table 7.3) and removed all foreground stars and soft source candidates (SNRs and WD binary systems). In each observation, the final list contains all hard sources which should be XRBs and AGNs in the field of the Draco dSph. To convert the count rate to flux we used the ECF of $7.09E+11$ in the energy range of $0.5-2$ keV and $1.27E+11$ in the energy range of $2-10$ keV by assuming the same model as explained in the Section 5.2.6. The ECF for the mosaic image was $1.10764e+12$ in the energy range of $0.5-2$ keV and $2.19890e+11$ in the energy range of $2-10$ keV. Figure. 8.1 shows the distribution of the number of detected hard sources in the different energy bands $0.5-2.0$

keV and $2.0 - 10$ keV for each observation. It is obvious that the number and the flux range of the detected sources (ML$>$ 10) in the energy band $2.0 - 10$ keV is noticeably smaller compared to the energy band $0.5 - 2.0$ keV.

8.2.2 Sky-coverage function

The probability of detection of faint sources is not homogeneous over the entire FOV and is less than that of bright sources, because the exposure time is higher in the centre of the EPICs and decreases for increasing off-axis angles. The PSF degrades for increasing off-axis angle due to the optical properties of the X-ray telescope. The sensitivity varies with flux. Therefore, the sensitivity of the EPICs is not uniform across the FOV, and the detection of the source of a given flux depends on its position in the FOV. The effective area of the fainter sources is smaller than that of the brightest sources, which are observable across the entire FOV. The underestimation of the number of sources, observed at the faintest flux level, affects the XLF in a way that it flattens at low luminosities. The incompleteness of XLFs can be corrected using the sky-coverage function, which is the effective area as a function of flux. For each observation we created sensitivity maps of the EPICs with the SAS task `esensmap`. We also produced the sensitivity map of all observations and all EPICs. For creating the sensitivity maps, exposure maps, background images, and detection masks are required, which are all produced in the process of source detection (see Sect. 5.2.5). In each observation, the sensitivity maps are used to calculate the sky-coverage function.
Figure 8.2 shows the sky-coverage function of the EPICs of each observation and also the sensitivity map of the mosaic image of all observations and EPICs in two different energy bands. As the plots show the sensitive area of the camera drops for lower fluxes (rate) and the sensitive area of the energy band $0.5 - 2$ keV is larger than that $2 - 10$ keV. The sensitivity map of the mosaic image has much larger area in the lower fluxes compared to the sensitivity maps of an individual observation.
The cumulative XLF is corrected for incompleteness by:

$$N(> F_{\rm x}) = A_{\rm tot} \sum_{\rm i=1}^{N_{\rm s}} \frac{1}{\omega(F_{\rm i})}\,, \tag{8.1}$$

where $N(> F_{\rm x})$ is the number of sources with flux higher than $F_{\rm x}$. For each source with a flux $F_{\rm i}$ the number is weighted by the normalised effective area $\omega(F_{\rm i})/A_{\rm tot}$ where $A_{\rm tot}$ is the total area observed by the EPIC and $\omega(F_{\rm i})$ is the sky coverage function. $N_{\rm s}$ is the total number of detected sources. Every source is hence weighted and the XLF corrected for incompleteness. The variance of the

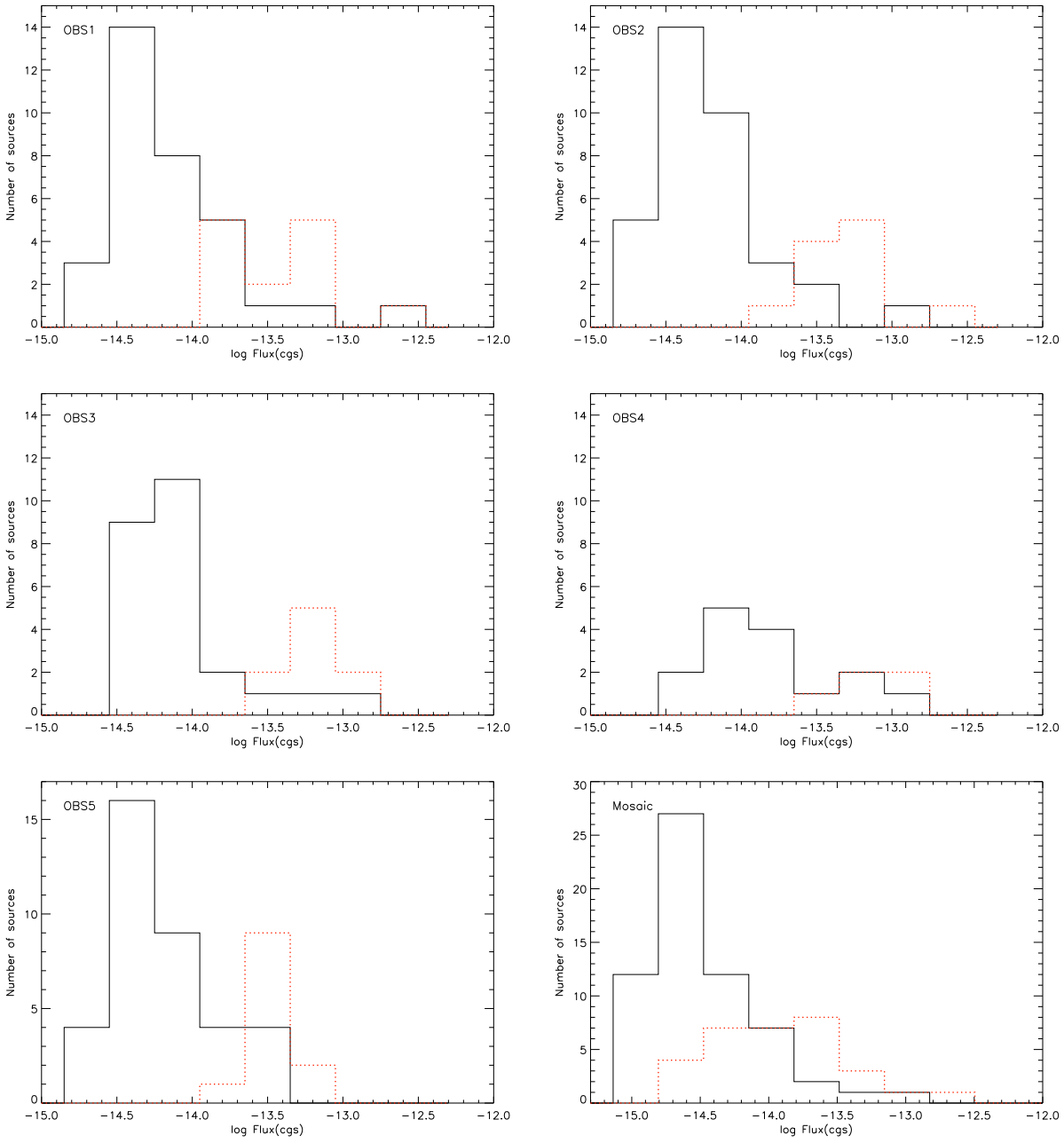

Figure 8.1: Distribution of the source fluxes in the energy bands of 0.5 − 2 keV (hard black line) and 2 − 10 keV (dashed red line). The diagrams show the number of source per flux bin, plotted versus the flux using a logarithmic scale.

source number counts is calculated by:

$$\sigma^2 = \sum_{\mathrm{i}=1}^{N_\mathrm{s}} \left(\frac{A_\mathrm{tot}}{\omega(F_\mathrm{i})} \right)^2 . \tag{8.2}$$

8.2.3 Results

The XLFs obtained by the method described above consists of X-ray sources in the Draco dSph and background AGNs. We eliminated the AGN contribution by subtracting the AGN XLF of the XMM-COSMOS survey (Cappelluti et al., 2009). They calculated the *logN-logS* of AGNs in two energy bands, $0.5-2.0$ keV and $2.0-10$ keV, which allows us to subtract the AGN *logN-logS* from the distribution of X-ray sources of a galaxy. The XLF of AGNs is described by a broken power-law:

$$\frac{dN}{dF} = \begin{cases} AF^{-\alpha_1} & F > F_\mathrm{b} \\ BF^{-\alpha_2} & F \leq F_\mathrm{b}\,, \end{cases} \tag{8.3}$$

where $A = BF_\mathrm{b}^{\alpha_1-\alpha_2}$ is the normalisation. In the 2.0 – 10 keV, the best fit parameters are $\alpha_1 = 2.46 \pm 0.08$, $\alpha_2 = 1.55 \pm 0.18$, $F_\mathrm{b} = (1.05 \pm 0.16) \times 10^{-14}$ erg cm^{-2}s^{-1} and $A = 413$. In the $0.5-2$ keV energy band the parameters are $\alpha_1 = 2.40 \pm 0.05$, $\alpha_2 = 1.60^{+0.04}_{-0.10}$, $F_\mathrm{b} = 1.00^{+0.21}_{-0.26} \times 10^{-14}$ erg cm^{-2} s^{-1} and $A = 141$. Two factors should be considered in using the XLF of AGNs. First, the function is per unit of area (arcmin^{-2}), therefore the XLF of AGN for a specific observation depends on the detected area of the sensitivity map. Second, the absorption in the direction of the observation changes the number of detected AGNs. Cappelluti et al. (2009) assumed an absorption of $N_\mathrm{H} = 2.5 \times 10^{20}$ cm^{-2} in the energy range $0.5-2$ keV, which is the same absorption in the direction of the Draco dSph ($N_\mathrm{H} = 2.46 \times 10^{20}$ cm^{-2} Willingale et al., 2013). Therefore, it was not necessary to correct the AGN function for the absorption in this energy range. Figure 8.3 shows the XLFs of the X-ray sources in $2.0-10$ keV band and Figure 8.4 those of the $0.2-5$ keV band for observation 1, 2, 3, and 5. Figure 8.5 shows the same plot of the mosaic of all EPICs/observations. We plotted both the XMM-COSMOS survey function of the AGNs and the XLF of AGNs identified in our work. To calculate the XLF of LMXB sources in the Draco dSph, we subtracted the normalised XLF of the XMM-COSMOS of AGNs from the total XLF of hard sources. The total XLF in the energy band $2.0-10$ keV is consistent with the AGN XLFs. Therefore, the source above 2 keV are highly contaminated by AGNs. In the energy range $0.5-2$ keV many more sources were detected with ML > 10.

As Figure 8.5 shows due to the larger area of the sensitivity map, there is a higher estimation of the AGNs compared to the XLF of each observation. There are $\sim$45

AGN sources in the flux range of $\geq 1.7 \times 10^{-15}$ erg s^{-1} cm^{-2}. The 0.2−5 keV XLF of Fig. 8.5 shows an excess of sources (compared to the AGN distribution) in the luminosity range between $\sim (1.4 - 3) \times 10^{33}$ erg s^{-1} (assuming $D = 82.4$ kpc) of $\sim$10. This luminosity for the flux range is less than 10^{34} erg s^{-1}, which makes it difficult to classified all as LMXBs. Binary systems which have a white dwarf as a compact object with typical accretion rates of $10^{11} - 10^{9}$ $M_{\odot}$yr^{-1} have accretion luminosities of $10^{31} - 10^{34}$ erg s^{-1}. Also, as it is shown by Zhu et al. (2012), transient LMXBs can have a luminosity in the range of $10^{32} - 10^{33}$ erg s^{-1}. Therefore these sources can be from both classes.

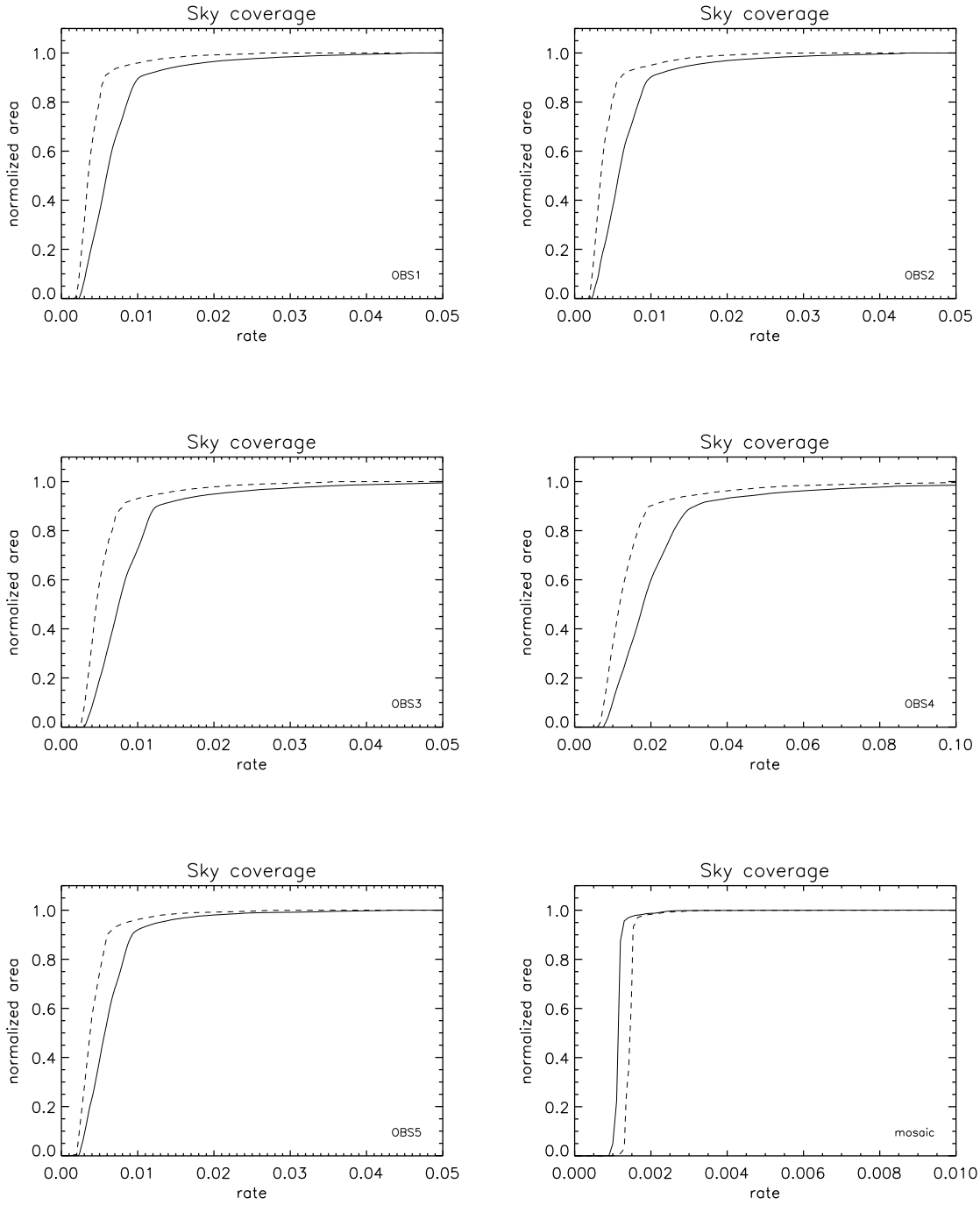

Figure 8.2: Sky coverage as a function of the X-ray count rate ($2-10$ keV, hard line) and ($0.5-2$ keV, dashed line) in EPIC of OBS 1, 2, 3, 4, 5, and the mosaic image of all EPICs.

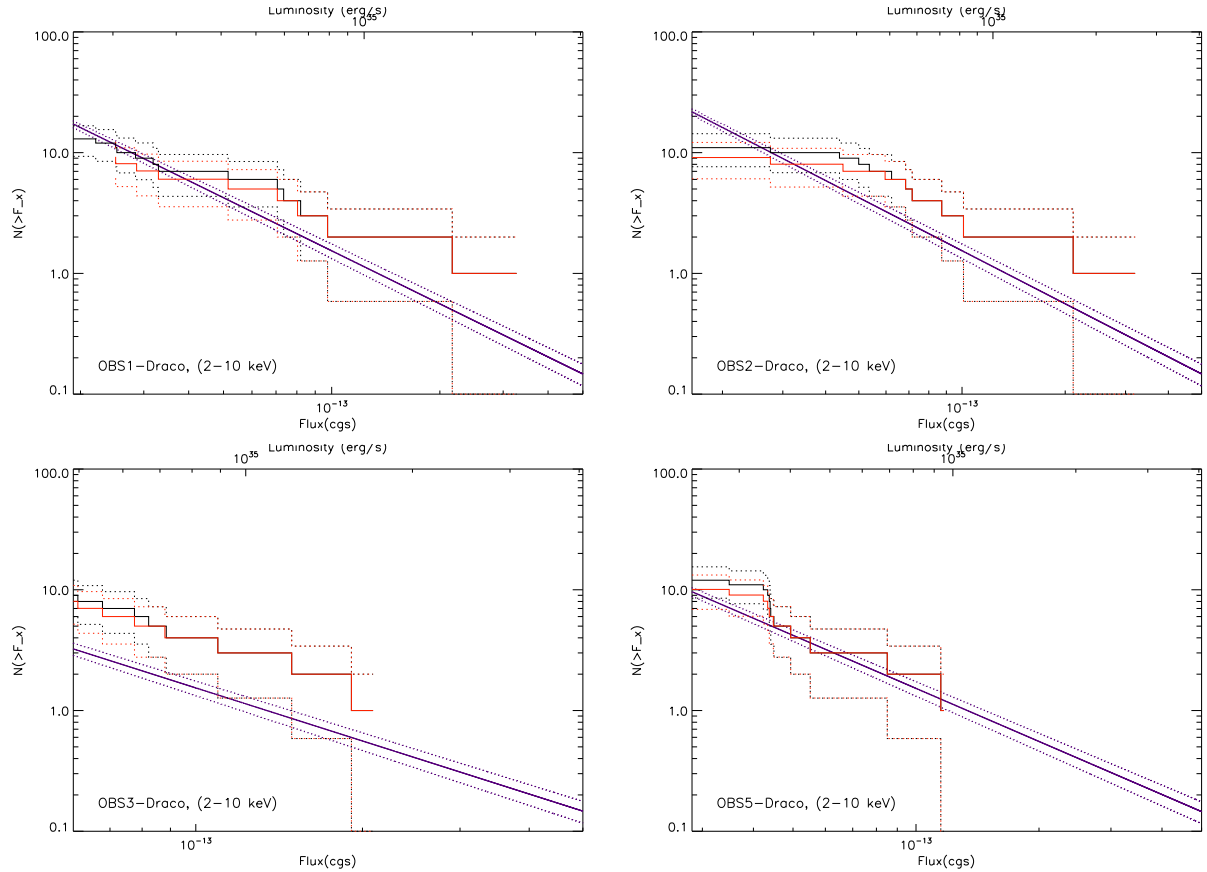

Figure 8.3: Cumulative XLFs corrected for incompleteness in the $2-10$ keV energy band. Black lines correspond to the XLFs without foreground stars and SSSs. Red lines show the XLFs of the classified AGNs. Blue lines are AGN XLFs of Cappelluti et al. (2009).

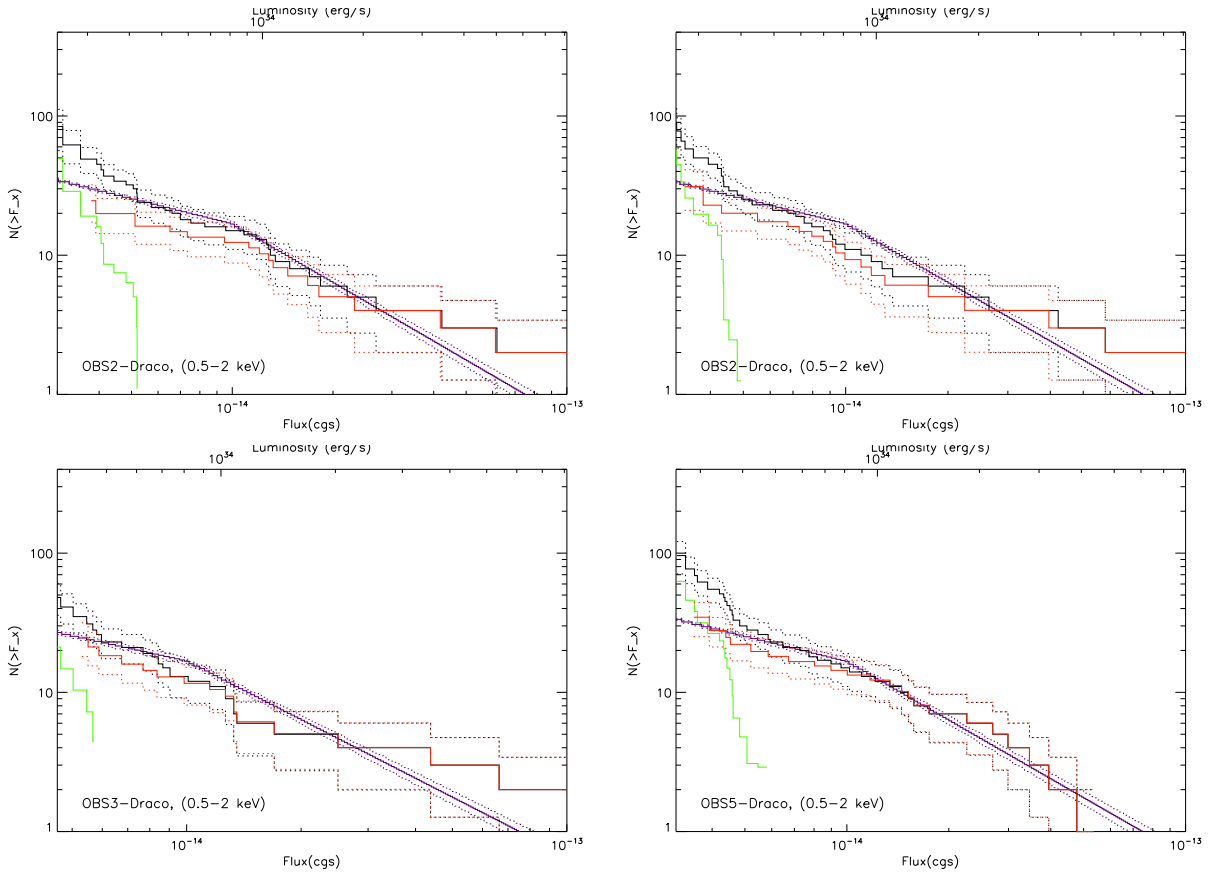

Figure 8.4: Cumulative XLFs corrected for incompleteness in the $0.5 - 2$ keV energy band. Black lines correspond to the XLFs without foreground stars and SSSs. Red lines show the XLFs of the classified AGNs. Blue lines are AGN XLFs of Cappelluti et al. (2009). Green lines show the XLFs of X-ray sources after subtracting the contribution of the AGNs (blue lines) from X-ray sources in the dwarf galaxy (black lines).

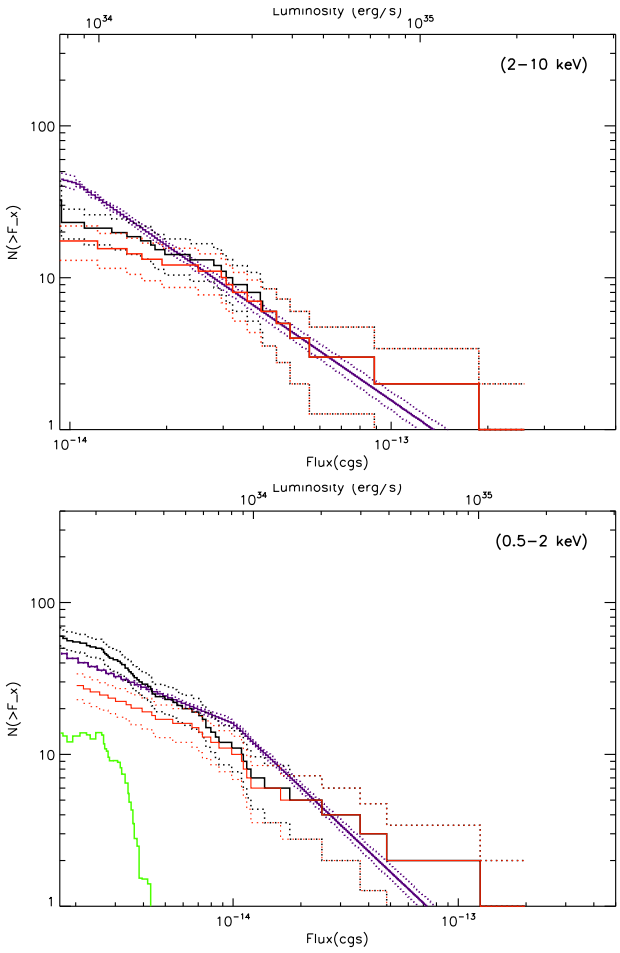

Figure 8.5: Cumulative XLFs of the mosaic event file of five *XMM-Newton* observations of the Draco dSph, corrected for incompleteness, in the $2 - 10$ keV (upper panels) and $0.5 - 2$ keV (lower panels) energy bands. Black lines correspond to the XLFs without foreground stars, symbiotic systems, and binary candidates as classified in Chapter 7, corrected for incompleteness. Red lines show the XLFs of the classified AGNs. Blue lines are the AGN XLFs of Cappelluti et al. (2009). Green lines show the XLFs of X-ray sources after subtracting the contribution of the AGNs (blue lines) from X-ray sources in the dwarf galaxy (black lines). The dashed lines are the 90 % confidence errors.

8.3 XLF of other dwarf galaxies

As (Young et al., 2007) explained, most of the dwarf galaxies can be divided into two different families, the dSphs and the dwarf irregular galaxies (dIrrs). The

dSphs has no HI gas and no current star formation, while dIrrs are HI rich, and show obvious signs of recent star formation. Observational works (e.g, Fenner et al., 2006; Weisz et al., 2014) showed wide different ages in stellar populations of different dSphs, various from very old populations of ∼10 Gyr to young stellar populations of ∼1 Gyr, which applies that in many of them the star formation bursts continued over several Gyr. (Young et al., 2007) mentioned this fact as a possibility, that ∼5 billion years ago current dSphs had a similar structure of the dIrrs. It means they were more gas-rich, and had more recent star formation activities. They focused on the Phoenix dwarf galaxy, which shows a transformation epoch from dIrr to dSph (see the details in Sect. 8.3.1). Considering these differences in the history of star formation of dwarf galaxies, we decided to study the XLFs of dwarf galaxies which are satellites of our Milky Way and had X-ray detections in previous works. We selected the Phoenix dwarf galaxy, Fornax, Leo I, Ursa Major II, and Ursa Minor dSphs for which X-ray population study were performed by Bartlett et al. (2012), Nucita et al. (2013) and Manni et al. (2015). General properties of these dwarf galaxies are listed in Table 8.1.

Table 8.1: Data for the dwarf galaxies

Name	Type	D(Kpc)[1]	Log$M_\star(M_\odot)$[2]	OBS ID[3]	ET (ks)[4]
Phoenix	dE/dS[5]	427	5.46	0601350101	44.9
Leo I	dSph	268	6.69	0555870201	88.6
Fornax	dSph	144	7.39	0302500101	82.2
Draco	dSph	82.4	5.51	Mosaic	
Ursa Minor	dSph	73	5.73	0301690401	9.9
Ursa Major II	dSph	34.7	3.73	0650180201	14.7

1: For each galaxy the distance was selected from the most updated measurement and the references are available in the text.
2: The stellar mass is taken from Kirby et al. (2013). For the Phoenix dwarf galaxy the reference is McConnachie (2012).
3: The details of the *XMM-Newton* observations which have been used to produce the mosaic image and sensitivity map are in the text.
4: ET: the exposure time of the observations after removing the flare times.
5: As it is explained in the text, the type of the Phoenix dwarf galaxy is between a dwarf irregular and dwarf spheroidal galaxy which is called "transient".

8.3.1 Phoenix dwarf galaxy

The Phoenix dwarf galaxy (hereafter Phoenix; RA= $01^h51^m06.3^s$, Dec= -44° 26′41″ [J2000.0]) has optical major and minor diameters of 4.9′ and 4.1′. The distance of Phoenix is ∼427 kpc (Ripepi et al., 2014). The Phoenix is an intermediate class of galaxy between the dwarf spheroidal and dwarf irregular, called

transition dwarf (dTrans). This galaxy offers a unique opportunity for the study of mechanisms that can transform a gas-rich irregular dwarf galaxy into a gas-poor dSph. Its stellar population is primarily old, but some star formation activity has continued until ∼100 Myr ago (Martinez-Delgado et al., 1999). Dolphin et al. (2005) indicated that, while stars as young as 100 Myr were found, the majority of star formation in Phoenix occurred more than 10 Gyr ago. Consistently, later studies of Hidalgo et al. (2009, 2013) showed that Phoenix had a continuous SFH. They considered three epochs for the SFH of the Phoenix. The highest rate of star formation occurred from the time of formation of the galaxy till 10.5 Gyr ago. After that star formation decreased to a lower rate level until 6 Gyr ago, and from 6 Gyr ago up to the present time, it continued to a very low level. Figure 8.7 (lower plot) shows the star formation history (SFH) of the Phoenix based on the colour-magnitude diagram analysis of the Hubble space telescope (Weisz et al., 2014). There is also an HI cloud which is associated with the galaxy but displaced from the stellar body, suggesting that gas removal might have taken place recently in Phoenix (Gallart et al., 2001). Young et al. (2007) suggest that this cloud is associated with the recent star formation. The other nearby dwarf galaxies have either lost their gas long ago, so that no signs of the removal process remain, or they still retain their gas, so that no signs of the removal process are visible yet.
To have an estimation of current Star formation rate (SFR) of the Phoenix, we used the works of Hidalgo et al. (2009), which measured the SFR of the Phoenix as a function of age. Figure 8.7 (upper plot Hidalgo et al., 2009) shows the changes of the SFR of Phoenix over time. In the last 1 Gyr galaxy shows an SRF of $\sim 0.25 \times 10^{-9}$ $M_{\odot}$ yr^{-1}pc^{-2} of normalised SFR value. We calculated the mean SFR for the whole Phoenix area to be $\sim 58 \times 10^{4}$ $M_{\odot}$ yr^{-1}, based on the data of Hidalgo et al. (Table 6; 2009). Therefore, current SFR (last 1 Gyr) of Phoenix is estimated to be $\sim 1.6 \times 10^{4}$ $M_{\odot}$ yr^{-1}.

In X-rays, the Phoenix dwarf galaxy was observed by *XMM-Newton* in July 2009. With the aim of searching for HMXBs (related to the recent star formation), the X-ray population of the galaxy was studied by Bartlett et al. (2012). They classified 81 sources in the field of Phoenix in the energy range $0.2 - 12$ keV. We repeated data the analysis of the *XMM-Newton* data of Phoenix using data with OBS ID 0601350101. After filtering flares caused by soft protons, the observation time (47.8 ks) decreased to 44.9 ks. We performed the source detection (ML>10) in the energy range of $0.5 - 2$ keV for the mosaic image of all EPICs. We detected 86 sources. Foreground stars and SNRs were removed after comparing the detected sources with the classified sources in the Bartlett et al. (2012) catalogue. Our final catalogue of Phoenix hard sources contained 78 sources.
Kalberla et al. (2005) reported a Galactic $N_{\rm H} \sim 1.56 \times 10^{20}$ cm^{-2} in the direction of Phoenix. We used a power-law model with photon index 1.7 (Bartlett et al.,

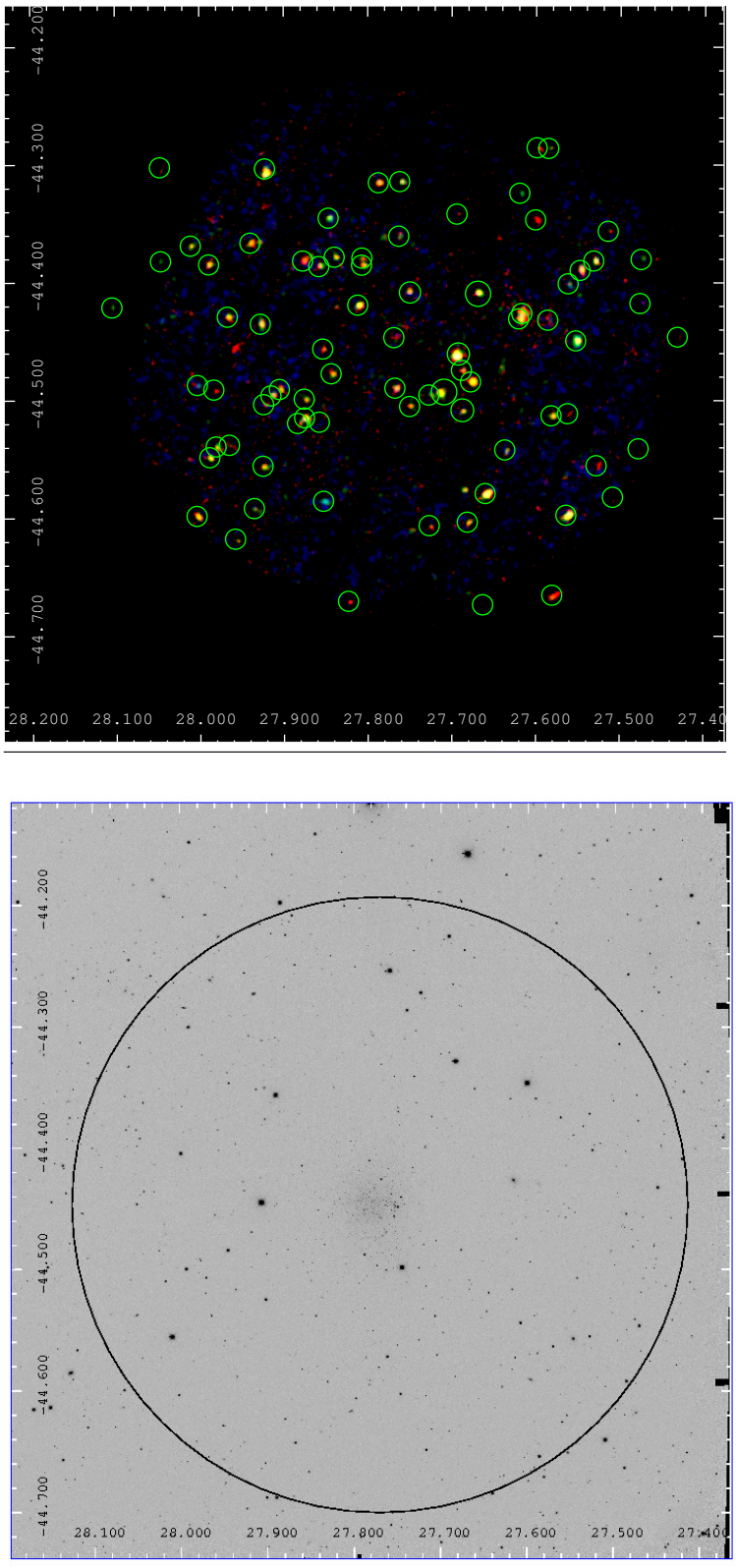

Figure 8.6: Top: *XMM-Newton* observation in the field of the Phoenix. The image are smoothed with a 2D Gaussian with a kernel radius of 1.5 pixel. The colours present the energy range of red: 0.2–1.0 keV, green: 1.0–2.0 keV and blue: 2.0–12 keV. Bottom: Optical image of the Phoenix in V band observed by CTIO optical telescope (Massey et al., 2007a). The black circle shows the area, observed by *XMM-Newton*.

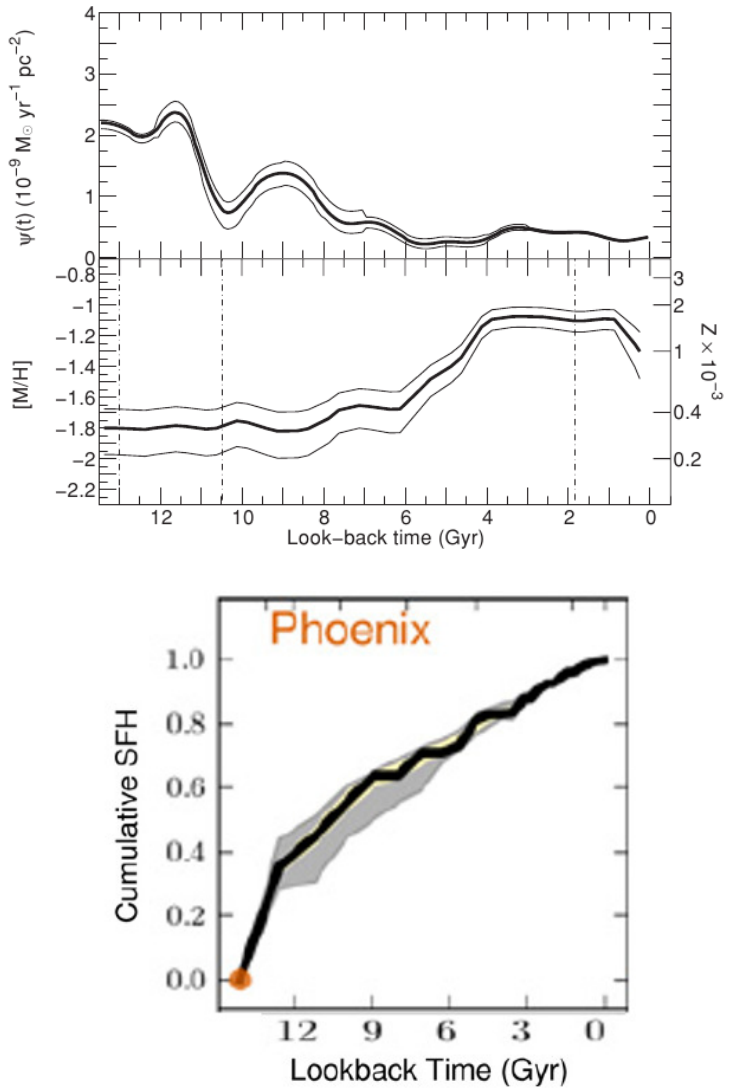

Figure 8.7: Top: Upper diagram shows the SFH of Phoenix as a function of time only and the bottom diagram shows the chemical enrichment law in logarithmic scale (Hidalgo et al., 2009). Bottom: Star formation history (SFH) track of Phoenix. The solid black line represents the best fit SFH, while the shaded area represent the 68% confidence interval due to random uncertainties (yellow) and total uncertainties (random and systematic; gray). The plot has been normalised such that its total stellar mass formed is unity at the present day. The orange dot indicates the approximate age of the oldest main sequence turn-off based on the colour-magnitude diagram of the galaxy (Weisz et al., 2014).

2012) for hard sources, yielding an ECF of $1.10370e+12$ in the energy range $0.5-2$ keV. We applied this ECF in order to calculate the flux of the hard sources in the Phoenix. The same method of XLF calculation for Draco was applied for the Phoenix too. Since the $N_{\rm H}$ in the direction of the Phoenix was even smaller than the assumed $N_{\rm H}$ in the luminosity function of AGNs ($N_{\rm H} = 2.5 \times 10^{20}$ cm^{-2}; Cappelluti et al., 2009), it was not necessary to apply an absorption correction for the fluxes of AGN XLF for this galaxy. First plot of Figure 8.15 shows the XLF of the Phoenix in the energy range of $0.5-2$ keV.

8.3.2 Leo I dwarf spheroidal galaxy

The Leo I dSph (Hereafter Leo I; RA= $10^h08^m28.1^s$, Dec= $+12°18'23''$ [J2000.0]) has major and minor diameters of $9.8'$ and $7.4'$ and is located at the distance of ∼268 kpc (Stetson et al., 2014). The SFH of Leo I was studied in several works. Gullieuszik et al. (2009) showed, using a deep observation with Very Large Telescope (VLT), that stars in the inner part of Leo I dSph are on average younger than those in the outer regions. They concluded that the first generation of Leo I stars formed uniformly in this dSph, while the majority of intermediate-age stars originated from an interstellar medium. Also, younger stellar populations mainly formed in the central regions in the last few Gyr. This result is consistent with the parallel study of Held et al. (2010), which showed a radial gradient in the number of C-type AGB stars relative to RGB stars, implying an increasing fraction of the intermediate-age (1-3 Gyr) stars in the inner regions of the galaxy. The study of colour-magnitude diagram by Dolphin (2002) showed an extremely broad turnoff, ranging from ancient star to young star populations, although, they mentioned that a few blue helium burners are still present. They also, numerically measured the SFH of Leo I from 15 Gyr until 0.5 Gyr ago. The largest epoch of star formation occurred recently, from 3 to 1 Gyr ago. During this time the SFR was 2.5 times the lifetime average. This work showed that the recent SFR (last 1 Gyr) of Leo I should be $\lesssim 5. \times 10^{-5}$ $M_{\odot}$yr^{-1}. Figure 8.9 (lower plot) also shows the SFH path of the Leo I by Weisz et al. (2014) using the colour-magnitude diagram of HST observations.

In X-rays, Leo I was observed in February 2008 by *XMM-Newton* (data set ID of 0555870201). Manni et al. (2015) performed a population study of the X-ray sources with the aim of finding IMBHs in the centre of the galaxy. They listed 116 source in the field of the Leo I in the energy range of $0.2-12$ keV.
In order to study the XLF of Leo I we repeated the data reduction and source detection on mosaic image of EPICs in the energy range of $0.5-2$ keV taking the detection ML>10. The exposure time of the observation was $\sim$ 94 ks which was reduced to 88.6 ks after removing the time of flares. We removed all classified foreground stars and SNRs of Manni et al. (2015) from our sources. Our final

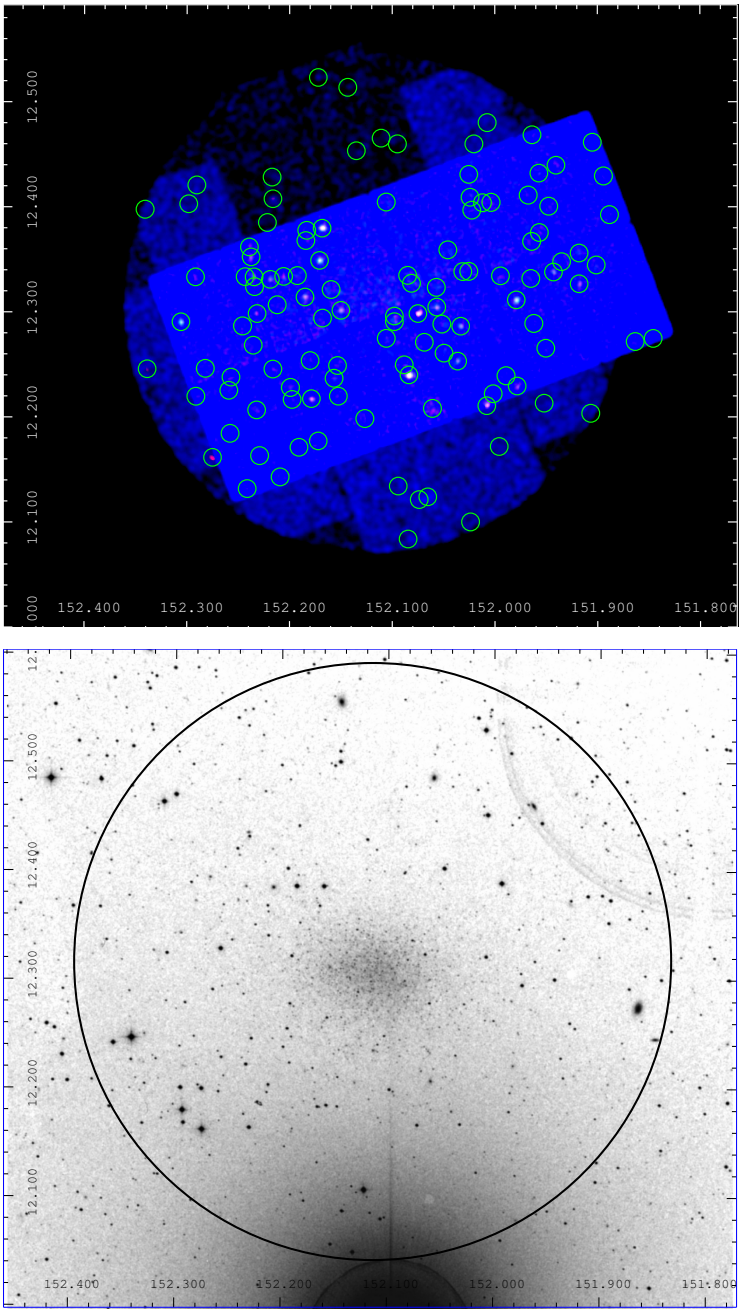

Figure 8.8: Top: *XMM-Newton* observation in the field of the Leo I. The images are smoothed a 2-D Gaussian with a kernel radius of 1.5 pixel. The colours present the energy range of Red: 0.2–1.0 keV, green: 1.0–2.0 keV and blue: 2.0–12 keV. Bottom: Optical image of the Leo I dSph in V band observed with the UK Schmidt optical telescope (199, 1994). The black circle shows the area, observed with *XMM-Newton*.

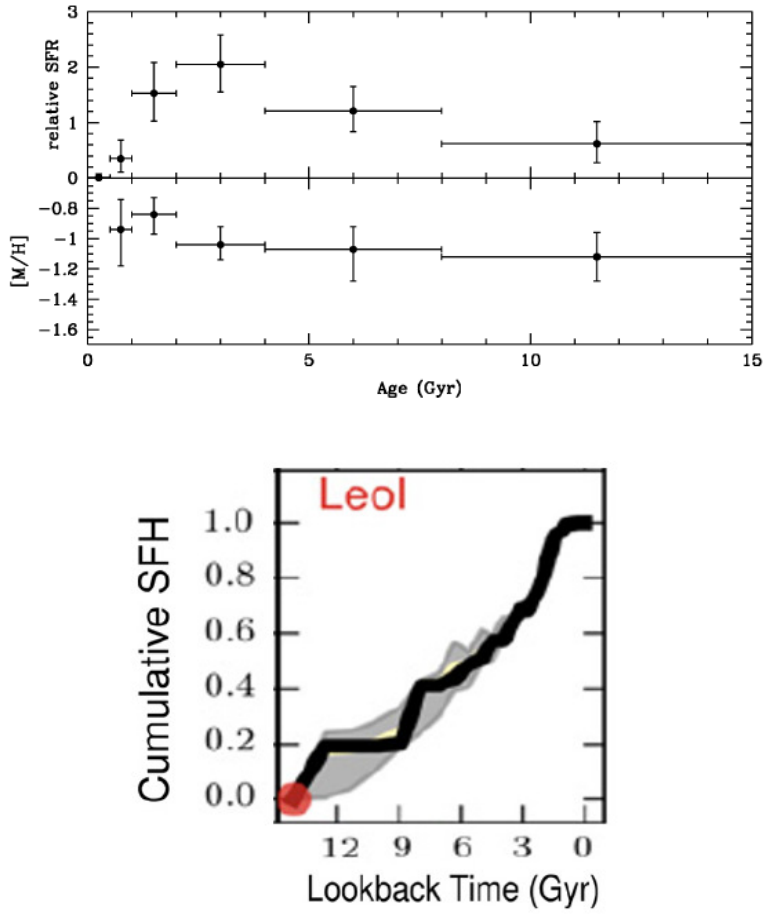

Figure 8.9: Top: Star formation and chemical enrichment histories of Leo I. The top panel shows the SFR, normalised to the lifetime average rate of 8.5×10^{-5} $M_{\odot}\mathrm{yr}^{-1}$. The bottom panel shows the chemical enrichment history (Dolphin, 2002). Bottom: Star formation history (SFH) track of the Leo I. The solid black line represents the best fit SFH, while the shaded area represents the 68% confidence interval due to random uncertainties (yellow) and total uncertainties (random and systematic; gray). The plot has been normalised such that its total stellar mass formed is unity at the present day. The red dot indicates the approximate age of the oldest main sequence turn-off based on the colour-magnitude diagram of the galaxy (Weisz et al., 2014).

catalogue contained 93 sources. Kalberla et al. (2005) reported a Galactic $N_{\mathrm{H}} \sim 3.60 \times 10^{20}$ cm^{-2} in the direction of the Leo I. We used a power-law model for hard sources with a photon index of 1.7 (Manni et al., 2015) and obtained an ECF of $1.09194e+12$ in the energy range of $0.5-2$ keV . We applied this ECF to calculate

the flux of the hard sources in the Leo I.
The long exposure time of this galaxy allowed us to detect very faint sources with a flux less than $\sim 1. \times 10^{-15}$ erg s^{-1} cm^{-2} in the energy range of 0.5 − 2 keV. However, the XMM-COSMOS survey has a limiting flux of 1.7×10^{-15} erg s^{-1} cm^{-2} (Cappelluti et al., 2009). Therefore, we only could calculate the XLF of the Leo I X-ray sources down to the flux of 1.7×10^{-15} erg s^{-1} cm^{-2}.
We used the same method of XLF calculation as for the Draco dSph. Figure 8.15 shows the XLF of the Leo I in the energy range of $0.5-2$ kev. Since the $N_{\rm H}$ in the direction of the Leo I ($N_{\rm H} \sim 3.60 \times 10^{20}$ cm^{-2}) was higher than the assumed $N_{\rm H}$ in the luminosity function of AGNs ($N_{\rm H} = 2.50 \times 10^{20}$ cm^{-2} Cappelluti et al., 2009), we applied an absorption factor for the fluxes of AGNs. The absorption factor was calculated using the absorption model, PHABS, via XSPEC (see Sect. 6.4). The assumed column density of Cappelluti et al. (2009) and the column density of Leo I are very close, therefore, the flux of XLF of AGNs did not change so much after applying the absorption factor.

8.3.3 Fornax dwarf spheroidal galaxy

Fornax dSph (hereafter Fornax; RA= $02^h39^m59.3^s$, Dec=-34°26′57″ [J2000.0]) has major and minor diameters of 17′ and 12.6′. The distace was estimated to be ∼144 kpc (Weisz et al., 2014). The recent proper-motion estimate by Piatek et al. (2002) indicates that Fornax is currently close to perigalacticon and may be bound to the Local Group rather than to the Milky Way. Figure 8.10 shows the optical and X-ray observations of Fornax.
Based on a deep imaging survey, Coleman and de Jong (2008) presented the first homogeneous SFH of the Fornax. They showed that this galaxy experienced multiple epochs of star formation. Its stars were generally formed in the early universe; however, a dominant population has intermediate-age stars. They found that the recent star formation are mainly toward the centre of the galaxy, also the central region has a faster rate of chemical enrichment than the outer parts of Fornax. They measured a mean metallicity of [Fe/H]=-1.4 for ancient stars (age $>$ 10 Gyr), located at the centre while, the most recent star formation burst has produced stars with close to solar metallicity. They also showed that the star formation gradually decreased over time, but ∼4 Gyr age, Fornax experienced a sudden star formation burst. This result is consistent with the results of more recent works by de Boer et al. (2012) and del Pino et al. (2013), which have shown that the last star formation events, as young as 1 Gyr old, are mainly located in the central region. de Boer et al. (2012) calculated the SFR of the Fornax in different epoch and estimated a current SFR of $\sim 1.5 \times 10^{-4}$ $M_{\odot}$yr^{-1} for the Fornax (see Fig. 8.11, upper plot). Figure 8.11 (lower plot) shows the track of SFH of the Fornax (Weisz et al., 2014).

Fornax was observed in X-rays in August, 2008 by *XMM-Newton* (observation ID: 0302500101). We reducted the data to obtain the source list (ML>10) in the energy range of $0.5-2$ keV as for the other galaxies. The net exposure time of the observation was 98.2 ks. These data have been used for the source classification of Fornax by Nucita et al. (2013). The foreground stars and SNRs were removed after comparing of the detected sources with the classified sources in the Nucita et al. (2013) catalogue. Our final catalogue of phoenix hard source contained 95 sources.
Kalberla et al. (2005) reported Galactic $N_{\rm H} \sim 2.90 \times 10^{20}$ cm^{-2} in the direction of Fornax. We took a power-law model for hard sources with Photon index 1.7 (Bartlett et al., 2012). ECF of $1.10968e+12$ in the energy range of $0.5-2$ keV was estimated. We applied this ECF to calculated the flux of the hard sources in the Fornax. Since the $N_{\rm H}$ in the direction of Phoenix was higher than the assumed $N_{\rm H}$ in the luminosity function of AGNs (Cappelluti et al., 2009), we applied an absorption factor for the fluxes of AGNs. The absorption factor has been calculated as explained in the section related to the Leo I dSph (Section 8.3.2). Figure 8.15 shows the XLF of the Fornax in the energy range of $0.5-2$ kev.

8.3.4 Ursa Minor dwarf spheroidal galaxy

The Ursa Minor dSph (hereafter UMi; RA$= 15^h09^m10.2^s$, Dec$= 67°12'52''$ [J2000.0]) has major and minor diameters of $30.2'$ and $19.1'$ and is located at a distance of $\sim$73 kpc (Weisz et al., 2014). UMi hosts a predominantly old stellar population. In general, all the stars have formed before 10 Gyr ago and 90% have even formed earlier than 13 Gyr ago (Carrera et al., 2002). Regarding the distance, stellar mass, and the recent SFH, UMi is the most similar dSph to the Draco. With a comprehensive study of star formation histories, using colour-magnitude diagrams, Dolphin (2002) showed that these two galaxies (Draco and UMi dSphs) did not experienced any recent star formation and for both systems the only significant star formation episode happened at ancient ages ($>$ 11 Gyr ago). Weisz et al. (2014) and Dolphin (2002) have shown the similarity of SFH of the Draco and UMi (see Fig. 8.13).

In X-rays, the UMi was observed between the end of August and the begging of September 2005 by the *XMM-Newton*. We used the data set of 0301690401 for extracting the XLF as these set of data were used by Manni et al. (2015) to perform the population study on the X-ray sources of this galaxy. As same as other galaxies, we calculated the XLF of UMi after performing the data reduction and source detection in the energy range of $0.5-2$ keV. The exposure time of observation 0301690401 (11.8 ks) reduced to 9.9 ks after removing the flare times. Manni et al. (2015) listed 54 X-ray sources in the field of UMi. After comparing our source list with the Manni et al. (2015) catalogue and removing the candidate

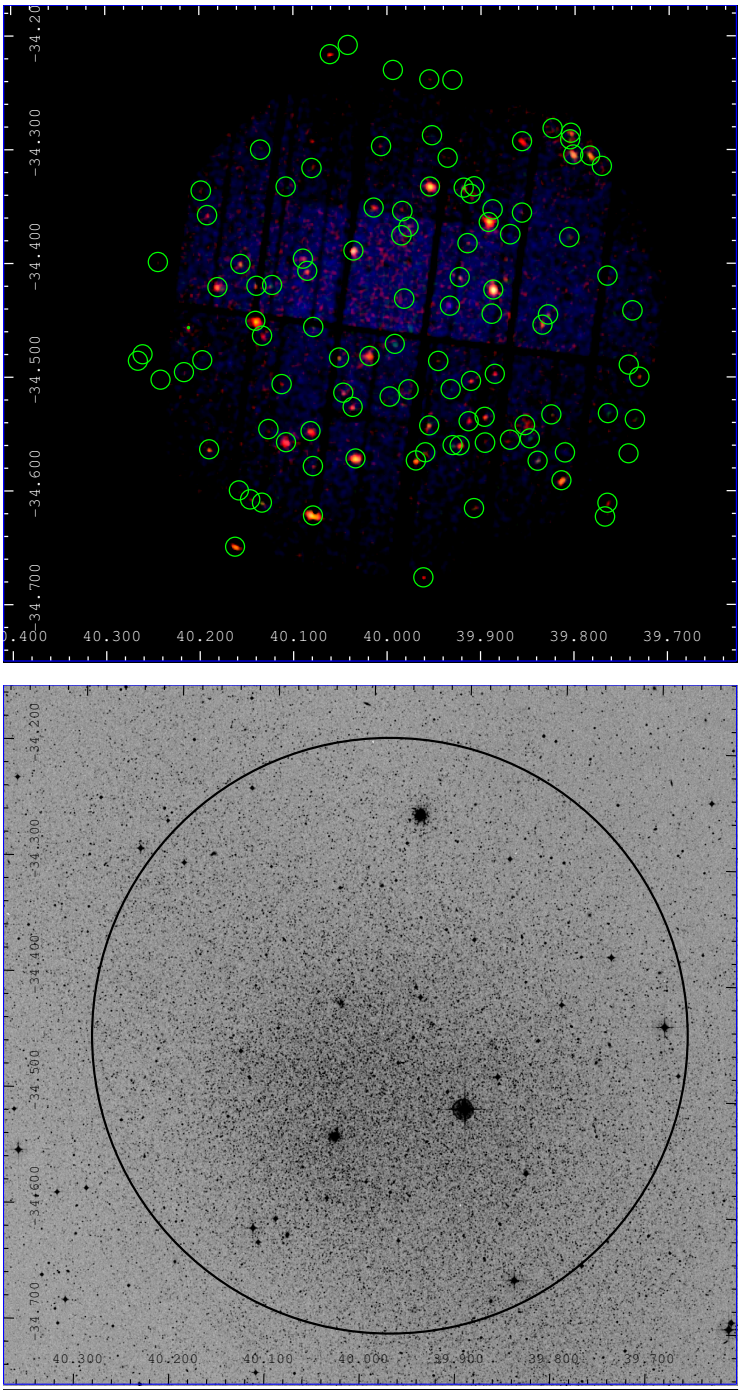

Figure 8.10: Top: *XMM-Newton* observation in the field of the Fornax. The image are smoothed a 2-D Gaussian with kernel radius of 1.5 pixel. The colours present the energy range of Red: 0.2–1.0 keV, green: 1.0–2.0 keV and blue: 2.0–12 keV. Bottom: Optical image of the Phoenix dwarf galaxy in V band observed with the UK Schmidt optical telescope (199, 1994). The black circle shows the area, observed by *XMM-Newton*.

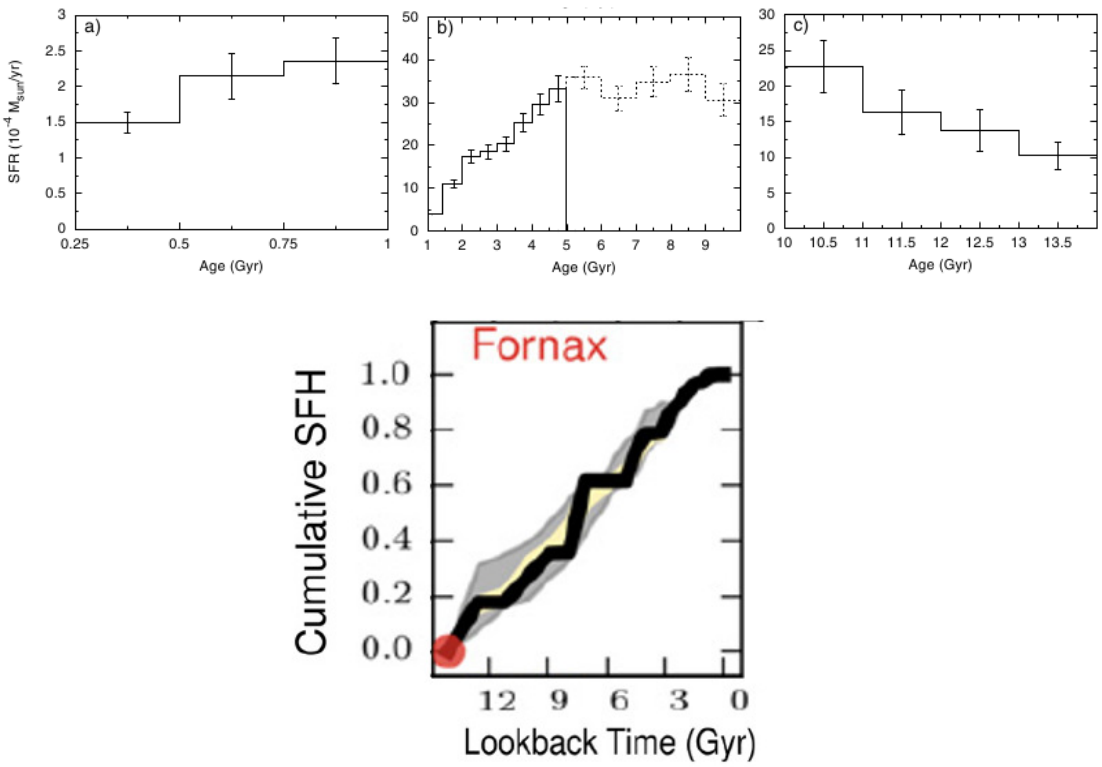

Figure 8.11: Top: The overall SFH of the Fornax, divided into young, intermediate, and old age ranges (de Boer et al., 2012). Bottom: Star formation history (SFH) track of the Fornax. The solid black line represents the best fit SFH, while the shaded area represent the 68% confidence interval due to random uncertainties (yellow) and total uncertainties (random and systematic; gray). Plot has been normalised such that its total stellar mass formed is unity at the present day. The red dot indicates the approximate age of the oldest main sequence turn-off based on the colour-magnitude diagram of the galaxy (Weisz et al., 2014).

of foreground stars, 32 sources were used for the XLF.
Kalberla et al. (2005) reported a Galactic $N_{\rm H} \sim 1.88 \times 10^{20}$ cm^{-2} in the direction of the UMi. With taking a power-law model with photon index 1.7 (Manni et al., 2015), ECF of $7.05947e+11$ in the energy range of $0.5-2$ keV was estimated. We applied this ECF to calculate the flux of the hard sources. Since the $N_{\rm H}$ in the direction of the UMi was even smaller than the assumed $N_{\rm H}$ in the luminosity function of AGNs ($N_{\rm H} = 2.5 \times 10^{20}$ cm^{-2}; Cappelluti et al., 2009), it was not necessary to apply an absorption correction for the fluxes of AGN XLF for this galaxy. Figure 8.15 shows the XLF of the UMi in the energy range of $0.5-2$ keV.

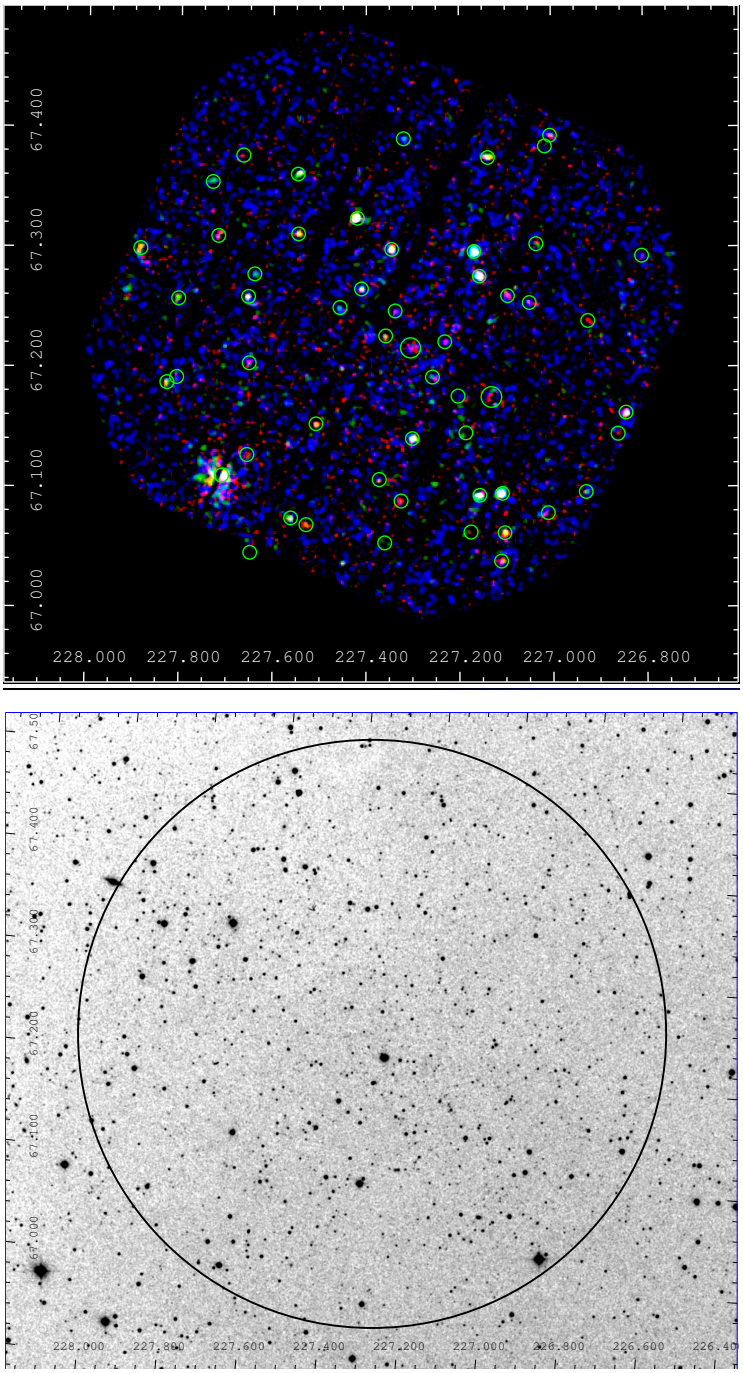

Figure 8.12: Top: *XMM-Newton* observation in the field of the Ursa Minor dSph. The image are smoothed a 2-D Gaussian with a kernel radius of 1.5 pixel. The colours present the energy range of Red: 0.2–1.0 keV, green: 1.0–2.0 keV and blue: 2.0–12 keV. Bottom: Optical image of Ursa Minor dSph in V band observed with Palomar 48-inch Schmidt optical telescope in SDSS survey(199, 1994). The black circle shows the area, observed by *XMM-Newton*.

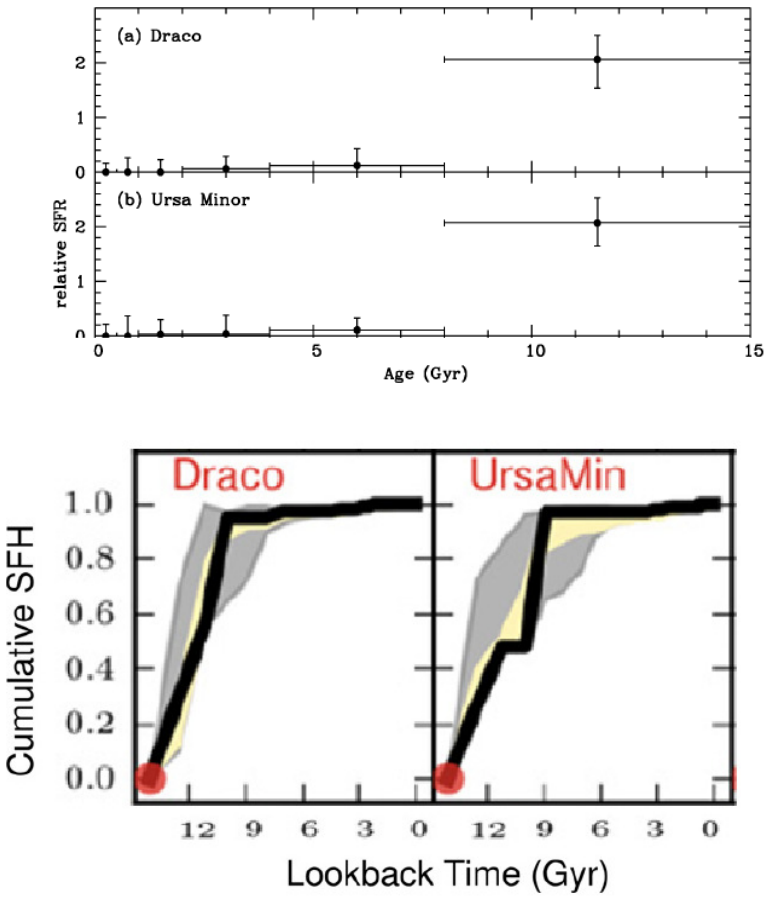

Figure 8.13: Top: Star formation histories of three old systems: Draco and Ursa Minor dSphs. Each is normalised relative to its lifetime average SFR (Dolphin, 2002). Bottom: Star formation history (SFH) track of the Draco dSph and Umi dSph. The solid black line represents the best fit SFH, while the shaded area represent the 68% confidence interval due to random uncertainties (yellow) and total uncertainties (random and systematic; gray). Plot has been normalised such that its total stellar mass formed is unity at the present day. The red dot indicates the approximate age of the oldest main sequence turn-off based on the colour-magnitude diagram of the galaxy (Weisz et al., 2014).

8.3.5 Ursa Major II dwarf spheroidal galaxy

Ursa Major II (hereafter UMa II) is an ultra faint dwarf spheroidal galaxy with RA= $08^h51^m30^s$ and Dec= $63°\ 07'48''$ [J2000.0] and has an apparent optical dimension of $\sim 32.'$. This galaxy was discovered by Zucker et al. (2006). The distance of the galaxy is estimated to be 34.7 kpc (Dall'Ora et al., 2012). Figure 8.14 shows the optical and X-ray observations of UMa II.
Zucker et al. (2006) suggested the age/metallicity spread in UMa II could be accounted for by an intermediate-metallicity stellar population with an age of at least 10 Gyr. Dall'Ora et al. (2012) showed that the metallicity and the age of the galaxy is $Z = 0.001 - 0.0001$ and $11 - 14$ Gyr and respectively suggested that there is a possibility that UMa II dSph experienced distinct bursts of star formation during its history. Study of formation history of several ultra-faint dwarf galaxies showed that they all stop the star formation more than 10 Gyr ago (Brown et al., 2014).

In X-rays, UMa II was observed in April 2011 by *XMM-Newton* (OBS ID of 0650180201). Manni et al. (2015) performed population study of the X-ray sources of this galaxy in the energy range $0.2 - 12$ keV. We have calculated the XLF of UMa II after performing data reduction and source detection in the energy range $0.5 - 2$ keV. The exposure time of observation (34.4 ks) was $\sim$ 14.7 ks. Manni et al. (2015) listed 49 X-ray sources in the field of UMa II. After comparing our source list in the energy range $0.5 - 2$ keV with the catalogue of Manni et al. (2015) and removing the foreground stars and candidates, we had 34 sources, which were used to calculate the XLF. Kalberla et al. (2005) reported the Galactic $N_{\rm H} \sim 4.65 \times 10^{20}$ cm^{-2} in the direction of the UMa II. Taking a power-law model with Photon index 1.7 (Manni et al., 2015), the ECF is $1.08489e+12$ in the energy range $0.5 - 2$ keV. We applied this ECF to calculate the flux of the hard sources. Since the $N_{\rm H}$ in the direction of the UMa II was higher than the assumed $N_{\rm H}$ in the luminosity function of AGNs (Cappelluti et al., 2009), we applied an absorption factor for the fluxes of AGNs. The absorption factor was calculated as explained in the section of Leo I dSph (Section 8.3.2). Figure 8.15 (last pannel) shows the XLF of the UMa II in the energy range of $0.5 - 2$ kev.

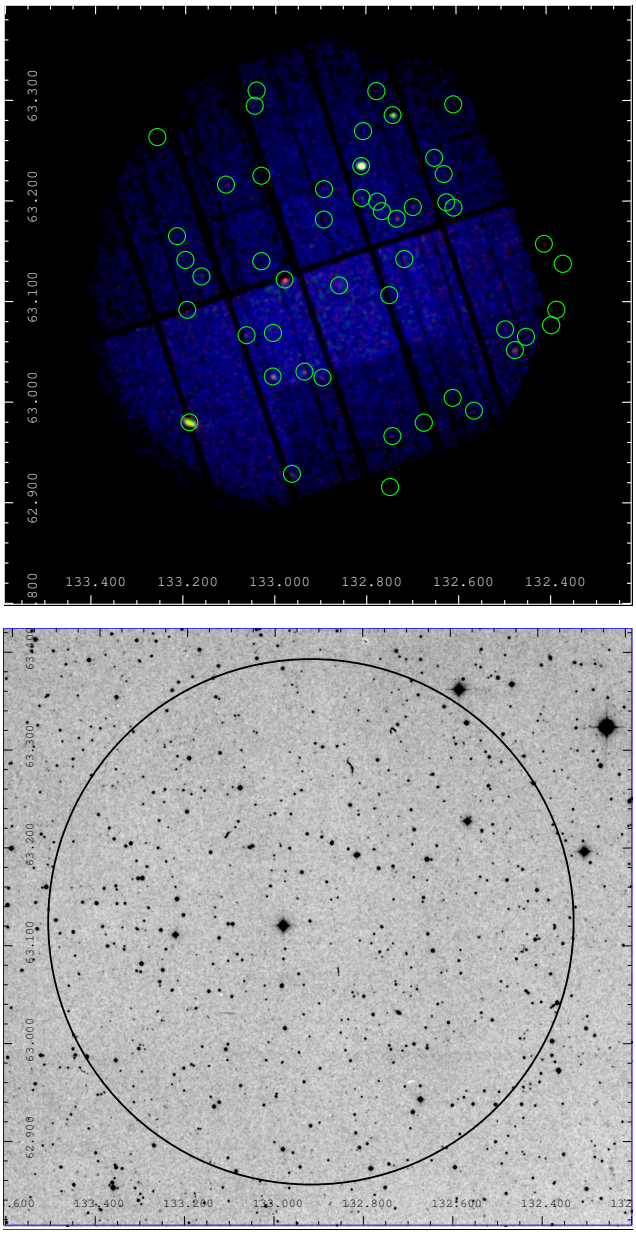

Figure 8.14: Top: *XMM-Newton* observation in the field of the Ursa Major II dSph. The image are smoothed a 2-D Gaussian with a kernel radius of 1.5 pixel. The colours present the energy range of red: 0.2–1.0 keV, green: 1.0–2.0 keV and blue: 2.0–12 keV. Bottom: Optical image of the Uma II in V band observed with the Palomar 48-inch Schmidt optical telescope in SDSS survey (199, 1994). the black circle shows the area, observed by *XMM-Newton*.

Figure 8.15: Cumulative XLFs corrected for incompleteness in the $0.5 - 2$ keV energy band for the dwarf galaxies Phoenix, Leo I, Fornax, UMi, and UMa II. Black lines correspond to the XLFs without foreground stars and SSSs. Blue lines are AGN XLFs of Cappelluti et al. (2009). Green lines show the XLFs of X-ray sources after subtracting the contribution of the AGNs (blue lines) from X-ray sources in the dwarf galaxy (black lines).

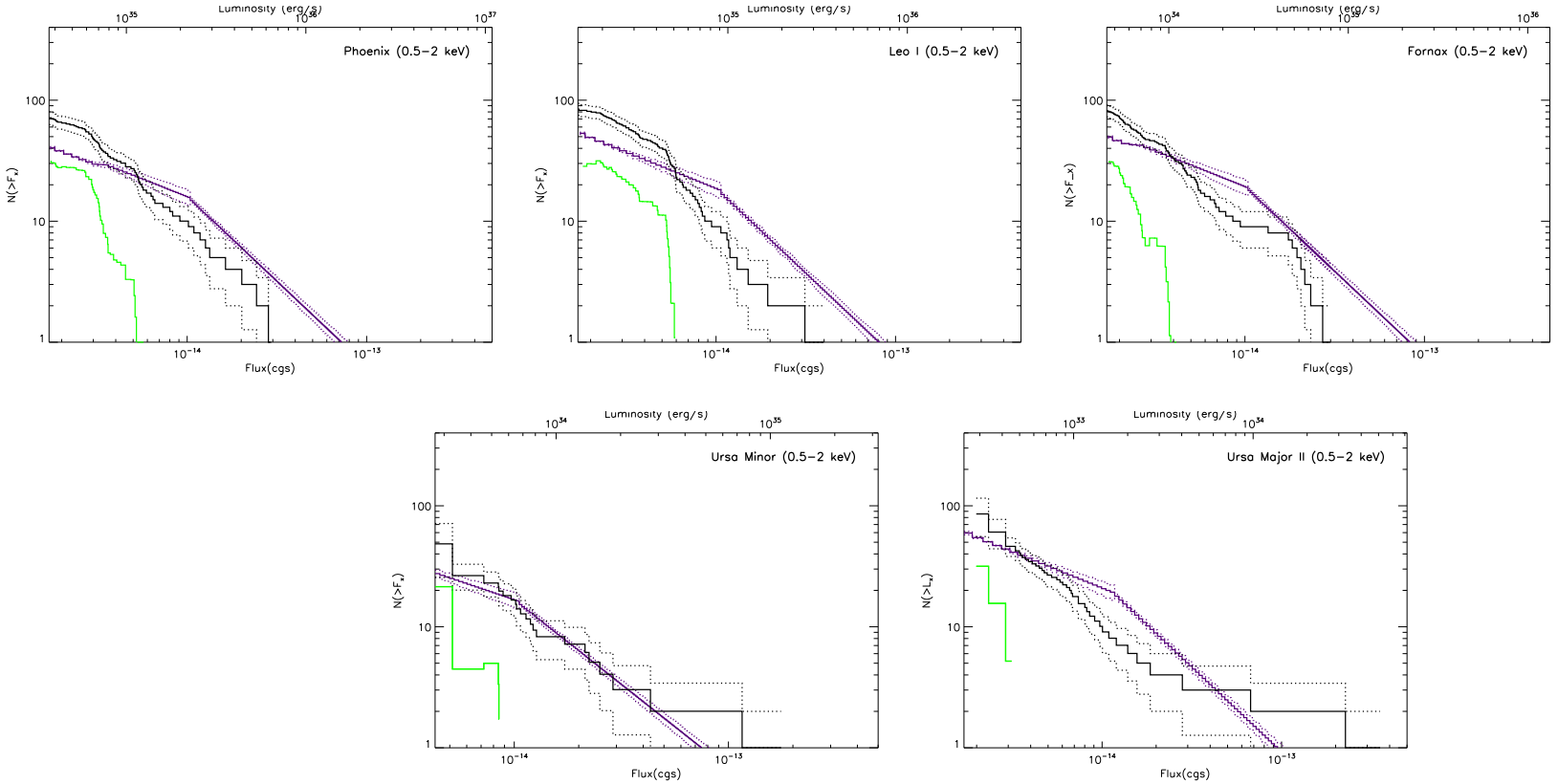

8.3.6 Discussion

Figure 8.17 shows the cumulative XLF of the X-ray sources for the six dwarf galaxies, discussed in this section. Some points have to be considered before comparing the XLFs of dwarf galaxies:

1. The very different observational exposure times of these galaxies (see Table 8.1) provided XLFs neither with a same significance nor a similar resolution. The XLFs of the UMi and UMa II, which had very low exposure times, show a population of sources in a very limited luminosity range, while a longer exposure time can give possibilities to have more extended and more significant XLFs.
2. Since the luminosities of sources of the Draco, UMi, UMa II and Fornax are all less than 10^{34} erg s^{-1}, the population can contain both white-dwarf binaries and transient LMXBs (Zhu et al., 2012). While, XLFs of Leo I and Phoenix (with luminosities above 10^{34} erg s^{-1}) show a population of LMXBs. As it is explained, Leo I, Phoenix, and Fornax had many sources with a luminosity less than 10^{34} erg s^{-1}, but since the XMM-COSMOS survey of AGNs was limited to fluxes $> 1.7 \times 10^{-15}$ erg s^{-1}cm^{-2}, the function was cut at this flux and XLF just contained the sources with higher fluxes.
3. We are interested in finding a relation between SFH and XRBs population of dwarf galaxies. Since the typical life time of LMXBs is $\sim 10^7 - 10^8$ yr (Padmanabhan, 2002), the last 1 Gyr of SFH of each galaxy is considered in this discussion.

Comparison of Leo I and Phoenix:

For these two galaxies, XLFs show the presence of ∼30 sources (LMXBs) in the flux range of $log(L_x)$∼34–35. The Phoenix, as explained in Sect. 8.3.1, has a recent star formation, which has continued to ∼100 Myr ago. Therefore, it is expected to have more LMXBs and also a population of more luminous sources compared to Leo I, which is an older galaxy without any star forming activity since ∼500 Myr ago (see Sect. 8.3.2). We normalised the XLF of Leo I to the stellar mass and also the current SFR (see Sect. 8.3.1 and 8.3.2) of the Phoenix (see Fig. 8.17, right panel). Since the Phoenix is an example of changing from a dIrr to a dSph (see Sect. 8.3.1), and the normalised XLF of Leo I shows consistency with the XLF of Phoenix, the plot can present an XLF of the dwarf galaxy before completely leaving the star forming ages and reaching quiescent life of dSphs. We could not normalise the XLF of very old dSphs (Draco, UMi, and UMa II) to Leo I and Phoenix since the amount of current SFR was not clear.

Old dSphs:

The XLFs of the Draco and UMi are very similar (see Fig. 8.17, left panel),

which was expected regarding to their similarities in SFHs and stellar masses (see Sect. 8.3.4). As it was mentioned, the low luminosity ranges of their XLF suggest that the main X-ray sources in these old dSphs are white-dwarf binaries and probable low-luminous transient LMXBs. In the case of UMi a very short observation time did not allow us to obtain a more extended and significant XLF. UMa II, as an ultra faint dSph should have even older stellar population compared to other dSphs (see Sect. 8.3.5). The mass of the galaxy is also much lower than the mass of other dSphs (see Table 8.1). Low significance of XLFs of UMi and UMa II could not give us a comparable view of old dSphs. More observations can help to study the XLF of old dSphs better.

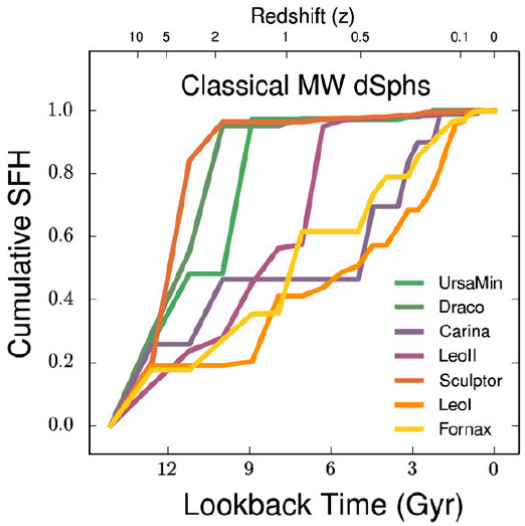

Figure 8.16: Cumulative SFH of classical Milky Way dSphs shows that there are two types of evolution for the known dSph: predominantly old galaxies (e.g., Sculptor, Draco) and those with extended SFHs (e.g., Carina, Fornax) (Weisz et al., 2014).

Fornax:

Based on the optical studies on Fornax, this galaxy had some recent star forming actives (see Sect.8.3.3). As the plots of Weisz et al. (2014) shows, the SFH track of the Fornax is similar to Leo I in last 1 Gyr (see Fig. 8.16). Some studies even compare the Fornax star formation with the Phoenix irregular dwarf galaxy as Grebel et al. (2003) mentioned that "Fornax, Phoenix, and LGS 3 closely resemble each other in several ways: all experienced star formation until 100-200 Myr ago; all have prominent intermediate-age populations, as evidenced by, e.g., their red clumps and subgiant branches; and they all have substantial old populations traced by well-populated horizontal branches." The recent SFR of the

Fornax ($\sim 1.5 \times 10^{-4}$ $M_\odot$ yr^{-1}, see Fig. 8.11) is also comparable with Phoenix ($\sim 1.6 \times 10^{-4}$ $M_\odot$ yr^{-1}, see Sect. 8.3.1). However, the XLF of Fornax has a luminosity range much lower than the Leo I and Phoenix. The XLF of Fornax is more close to the old dSphs, like Draco and UMi, which are almost devoid of LMXBs (see Fig. 8.17, left panel). Therefore, it seems that we observed low luminous sources (like white dwarf binaries) as the major population in Fornax and this galaxy does not contain LMXBs with the same population of Leo I and Phoenix. This inconsistency poses many questions about Fornax XLF.
Before suggesting any certain idea about this strange X-ray population of Fornax another classification of X-ray sources of this galaxy is necessary to know, first, the population of foreground and background (AGNs) sources in the field of the Fornax better, and second, the nature of sources which are showing such low luminosities.
As an interesting approach (hypothesis), the low luminosities of sources in Fornax can be related to the galactic structure of this galaxy, which made it not possible to keep its LMXBs (more luminous sources). Therefore, the major population was white dwarf binary systems, which could be detected in Fornax due to its shorter distance compared to other similar galaxies (Leo I and Phoenix, see Table 8.1). As we discuss in Chapter 9, due to the kick velocity of compact objects after the supernova explosion, typical XRBs have a higher speed than the radial velocity of dSphs which means that these small size galaxies can not keep their XRBs. However, detection of some LMXBs in old dSphs led to the theory that gravitational effect of the dark matter halo can allow LMXBs to stay in their host dSph depending on their speed [1].
The mass of dark matter halo might be the solution in the case of Fornax, which based on its visible mass and star formation rate, should still have LMXBs (similar to Leo I and Phoenix), but it behaves like old dSphs in which LMXBs already finished their life. There is the possibility that the major of LMXBs of Fornax have left the galaxy before finishing their life. The mass-to-light ratio of Fornax is noticeably low compared to other dwarf galaxies (8.8 ± 3.8 $(M/L)_\odot$; Łokas, 2009) and there are several works, which have shown that Fornax is relatively baryon-dominated dSph, and does not fit to the dark matter halo models (e.g, Jardel et al., 2013; Mashchenko et al., 2005; Walker and Peñarrubia, 2011; Peñarrubia et al., 2009). While, Leo I, with a similar recent SFH but a higher luminosity range in its XLF (see Fig. 8.17), seems to have noticeably higher mass-to-light ratio. Different observations and models suggested a high mass-to-light ratio for Leo I. The study of (Mateo et al., 2008) showed that the mass distribution of Leo I is much more extended than the visible matter and their best fit model suggests a mass-to-light ratio of 129 ± 45 $(M/L)_\odot$. Also the result of (Smolčić

[1] In chapter 9 we explain this theory in details and show what masses of the dark matter halo are necessary to keep the LMXBs in dSphs.

et al., 2007) based on the SDSS observation of Leo I suggested an upper-limit of $\sim$65 $(M/L)_{\odot}$ for mass-to-light ratio in the V band, within 12.. They discussed that the mass-to-light ratio is possibly $>$75 $(M/L)_{\odot}$, if a constant density dark matter halo dominate the mass and extend further beyond 12. This hypothesis is one possibility for the strange luminosity of Fornax sources. However, we have to note that considering the (usually) low significant observational data of velocity dispersion in dSphs, the estimation of dark matter halo mass are strongly depending on the selected model(s)(Smolčić et al., 2007). In addition, as we mentioned, before drawing any conclusion, an accurate classification of X-ray sources in Fornax is necessary.
In summary, first, we showed that there is an observable correlation between the population of X-ray binaries and star formation history of dwarf galaxies, and second, the population of LMXBs in dSph can be related to the dark matter halo of dSphs as it will be explained in the next Chapter.

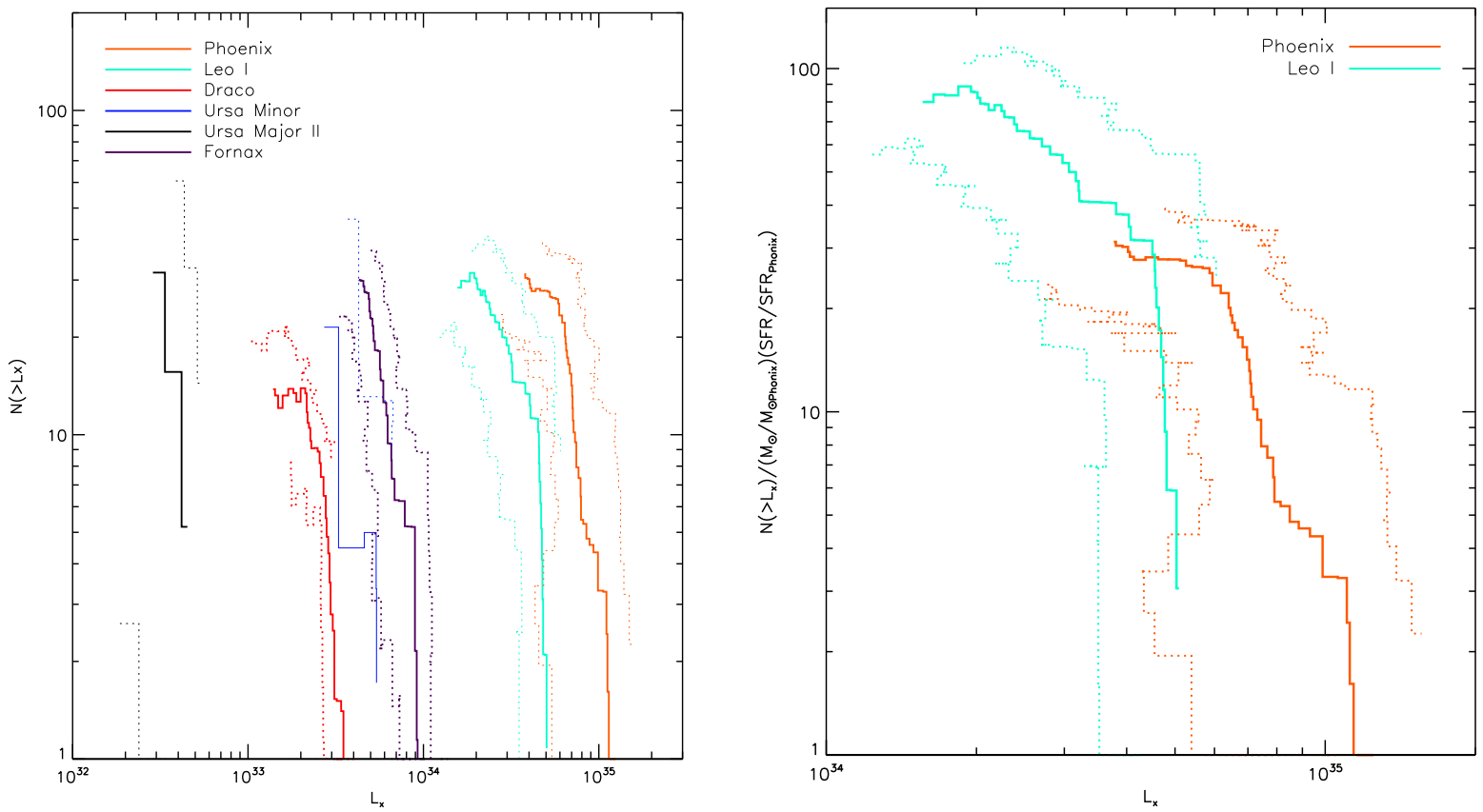

Figure 8.17: Left: Cumulative X-ray luminosity function for dwarf spheroidal galaxies. Right: The XLF of Leo I dSph is normalised to the mass and SFR of Phoenix dwarf galaxy. The hard lines are the XLF of X-ray sources of the galaxies and the dashed lines show the corresponding error.

Chapter 9

Dark matter halo and LMXBs

9.1 Introdunction

Based on an *XMM-Newton* study of the Sculptor dSph, Maccarone et al. (2005) reported that the optical counterparts of five X-ray sources have colours and magnitudes consistent with either giant branch or horizontal branch stars of the Sculptor dSph, and all have proper motion estimates that indicate a probability of at least 96% for being members of the Sculptor dSph. Therefore, these five sources were classified as LMXBs in Sculptor dSph. Table. 9.1 shows the details of these five LMXB candidates. However, more updated observations have shown that two of them are AGNs. The source at RA=01^h 00^m 26.19^s, Dec=–33° 41 07″.5 (J2000) is a quasar with a red-shift of $z = 0.60$ (Véron-Cetty and Véron, 2010; Souchay et al., 2012), and the source at RA=00^h 59^m 52.75^s, Dec=–33° 44 26″.1 (J2000) is a quasar candidate with $z = 0.07$ (Flesch, 2010; Jones et al., 2009).

In general, detections of LMXBs in the Sculptor dSph (Maccarone et al., 2005) and now in the Draco dSph (see Sect. 7.3) would mean that they are able to retain their XRBs. Dehnen and King (2006) raised the question whether the XRBs can be retained by the host dwarf galaxy in spite of their proper motion. They considered the LMXBs in the Sculptor dSph reported by Maccarone et al. (2005) and concluded that the most likely explanation for the presence of LMXBs in Sculptor dSph galaxy would be a massive dark matter halo with a mass of the order of $\geq 10^9\ M_\odot$. In this chapter we discuss about the presence of the LMXBs in dwarf galaxies and its relation to the mass of dark matter. First we review the kick velocity of NSs and BHs and the run-away speed of the XRBs. We consider the suggested dark matter halo mass and galactic structure of the Sculptor dSph in the most updated works and compare with suggestion of Dehnen and King (2006). With the approach of Dehnen and King (2006) we calculate the necessary dark matter halo mass to keep the XRBs in the field of the Draco dSph by considering the most updated reported parameters for the Draco dSph.

Table 9.1: The five LMXB candidates in the Sculptor dSph. Columns are RA and Declination (for the optical counterparts), optical catalogue number from Schweitzer et al. (1995), the X-ray luminosity in erg sec^{-1}, the number of counts in the soft $(0.5 - 2.0$ keV) and hard $2.0 - 8.0$ keV bands, the ratio of soft to hard counts (Maccarone et al., 2005)

RA (J2000)	Dec (J2000)	Opt.no.	L_X erg s^{-1}	Soft	Hard	HR
01 00 09.39	–33 37 31.9	355	6×10^{34}	325	82	3.9
01 00 26.19	–33 41 07.5	758	1×10^{34}	108	59	1.8
00 59 58.68	–33 43 37.1	609	1×10^{34}	189	40	4.7
00 59 52.75	–33 44 26.1	226	6×10^{33}	73	49	1.5
01 00 13.84	–33 44 43.3	NA	9×10^{34}	804	212	3.8

9.2 The run-away speed of the XRBs

Compact objects obtain a kick velocity at their birth. The run-away speed of X-ray binary systems, caused by an asymmetry of supernova explosions, have been calculated in several works. It was first discussed by Blaauw (1961) and Boersma (1961) who considered the strangely high space speed of some of the O and B stars. They concluded that this high speed originates from the asymmetric supernova explosion in the binary systems. The loss of mass on time scales faster than the orbital period of the binary system means that the lost mass in supernova explosion will carry away linear momentum related to the centre of mass of the binary system. It means that the new formed binary system (new formed NS or BH and the companion) will receive equal and opposite momentum kicks. This kick is sometimes called "Blaauw and Boersma kick (recoil)".
Following several observational updates which reported different space speeds for XRB systems and isolated NSs, several mechanisms have been suggested to calculate the run-away speed theoretically (see e.g., Postnov and Yungelson, 2006). Assuming that the birth velocities of NSs are distributed with a mean value of 450 $km\,s^{-1}$ according to Lyne and Lorimer (1994), Brandt and Podsiadlowski (1995) studied the effect of the supernova kick on the binary system and concluded that LMXBs that remain bound after the supernova explosion have an average system velocity of $V = 180 \pm 80$ $km\,s^{-1}$. Pfahl et al. (2002) also showed that NSs born in the wide binary systems receive only a small kick velocity (≤ 50 km s^{-1}), while NSs born in isolation receive large kick velocities, with a mean speed of $\sim$300 $km\,s^{-1}$.
As a noticeable sample of the most updated observational works in this field, Maccarone et al. (2014) investigated the proper motion (using the data of Yale southern

survey, Girard et al., 2011) of optical counterparts of HMXBs and LMXBs. For the optical counterparts, they checked the confidence for the optical source being the companion of a binary system and discovered the high linear momentum of two binary systems.

9.2.1 Structural models of the dwarf galaxies

As modeled by Kalogera (1996) for different globular clusters, the escape velocity of LMXBs from the core of a globular cluster is $\sim 30 - 60$ km s^{-1}. Therefore, because of the small size of the globular cluster, XRBs have a very low chance to remain in globular clusters. But what about dwarf galaxies?
The stellar mass of the dSph galaxies is comparable to that of massive globular clusters. However, globular clusters are dense and compact, while dSphs are very extended and their radii exceed those of globular clusters by a factor of several hundreds (Irwin and Hatzidimitriou, 1995) and reach up to kilo parsecs. The velocity dispersion of their stars again is similar to what is measured in globular clusters (Klessen et al., 2003).
There are three main models to justify this peculiar behaviour of the dSphs:
First, the dSph galaxies are the results of the birth of small systems, especially in the cold dark matter (CDM) model (Dekel and Silk, 1986). The dark matter dominated model suggests that dSphs originated from the most massive primordial dark matter sub-halos (e.g., White and Rees, 1978; Stoehr et al., 2002). In this model, N-body simulations predict masses of $\sim 10^{10}$ $M_{\odot}$ for the dSphs (Klypin et al., 1999).
Second possible origin of dwarf galaxies is the tidal scenario (e.g., Sofue, 1994; Mayer et al., 2001b,a). Since dSph galaxies are in general located close to their host galaxy, the tidal field of the host galaxy has most likely played an important role in their formation and evolution. The model suggests that tidal interactions transform field disk galaxies into spheroidal systems.
A third model suggests that dSph galaxies are fragments liberated during collisions between larger galaxies (Gerola et al., 1983). The interaction of gas rich galaxies can throw out long thin tidal arms, which fragment, collapse and form new stars (Metz and Kroupa, 2007). Some of the tidal dwarf galaxies in these models contain even no dark matter and are almost unbound (Kroupa, 1997).
These models are not necessarily independent of one another; for example a dwarf galaxy may form via the collapse of CDM and then evolve through tidal interactions (Grebel et al., 2003). Usually, for each dwarf galaxy, the proper model(s) are examined using both observation and simulation.

Model of the Draco dSph

In the case of the Draco dSph, all of the different studies, e.g., very deep observational studies (Ségall et al., 2007), or N-body simulations (e.g., Mashchenko et al., 2006; Read et al., 2006) consistently concluded that the Draco dSph is a flawless dwarf galaxy, i.e, it can not be the remnant of a tidally disrupted satellite galaxy. Instead, it is most likely strongly dark matter dominated. The total i-band luminoscity of the Draco dSph is $L/L_{\odot} = (2.4 \pm 0.5) \times 10^5$ (Odenkirchen et al., 2001). Under the assumption of Virial equilibrium, the high stellar velocity dispersion implies an extremely high mass to light ratio, from 146 ± 42 $(M/L)_{\odot}$ (Odenkirchen et al., 2001), 330 ± 125 $(M/L)_{\odot}$ (Kleyna et al., 2002), $\sim$416 $(M/L)_{\odot}$ (e.g., Ségall et al., 2007; Read et al., 2006), and even up to 440 $(M/L)_{\odot}$ (Faria et al., 2007). Several other studies (e.g., Klessen et al., 2003; Łokas, 2002) also concluded that Draco dSph is probably a very strongly dark matter dominated galaxy. With this background we try to understand how consistent the estimated mass of the dark matter halo is with the required mass to retain the LMXBs.

9.2.2 Dark matter halo in the Sculptor dwarf galaxy

In the case of the Sculptor galaxy, the minimum required mass of the dark matter halo to hold LMXBs with velocities between $20-60$ km s^{-1} has been estimated by Dehnen and King (2006). They assumed a pseudo-isothermal sphere model with a radius of 1.5 kpc for the galaxy, a mass of 5×10^7 $M_{\odot}$, and a truncation radius that exceeds 15 kpc. They selected different radii for the dark matter halo core to show how massive the total mass should be to keep the LMXBs in the potential. According to this model, a dark matter core with a radius of $\sim 3-5$ kpc is needed to hold the LMXBs in the Sculptor dSph with a speed between $40-60$ km s^{-1}. It also implies that the total mass of the galaxy should be of the order of 10^{10} $M_{\odot}$, which is more massive than other estimates. A recent estimate for the dark matter in the Sculptor dSph showed that a pseudo-isothermal sphere model is consistent with a dark matter core radius of $r_c = 0.5$ kpc and a mass of $M = (3.4 \pm 0.7) \times 10^8$ $M_{\odot}$ inside the radius of 1.8 kpc (Battaglia et al., 2008). This estimate suggested dark matter halo masses and core sizes (e.g., Amorisco et al., 2014) are significantly smaller than that of Dehnen and King (2006).

9.2.3 Dark matter halo in the Draco dSph

In the case of the Draco dSph, there have been several attempts to estimate the mass and its distribution. The most recent optical observations suggest a visible

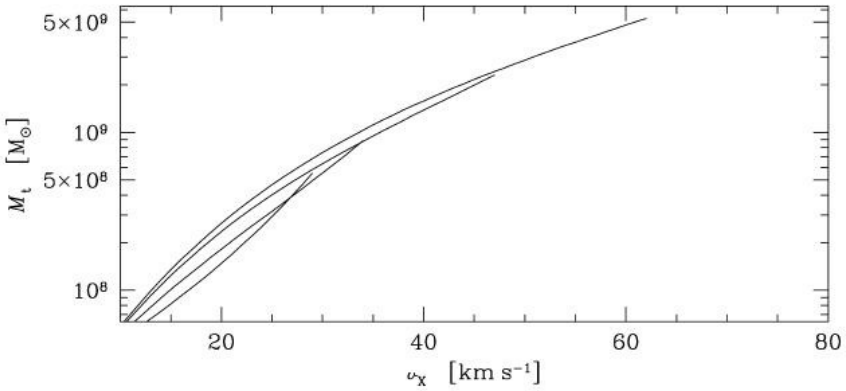

Figure 9.1: The minimum mass of an extended dark matter halo for Sculptor dSph required to hold on to an LMXB with velocity v_X at radius 1 kpc for haloes with core radii r_c of 0.7, 1.5, 3 and 5 kpc. The halos are assumed to have a mass 5 $\times 10^7$ within 1.5 kpc. The curves end to the right when the required truncation radius $r_t M_\odot$ exceeds 15 kpc (the larger the core radius, the larger the maximum v_X still bound (Dehnen and King, 2006).

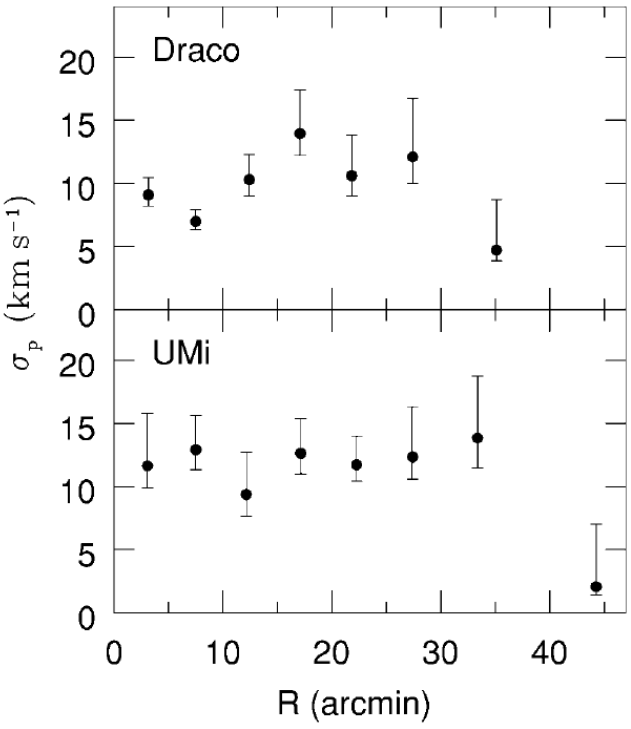

Figure 9.2: Line-of-sight velocity dispersion profiles (with 1σ error bars) for the Draco and UMi dSphs (Wilkinson et al., 2004).

galaxy core of 7.′7 (corresponding to 0.18 kpc at a distance of 82 kpc, Kinemuchi et al., 2008), and a stellar truncation radius of ∼40.′1 (corresponding to 0.96 kpc) (Odenkirchen et al., 2001). The velocity dispersion of Draco dSph measured in many observations is between $9-11$ km s^{-1}. Kleyna et al. (2001) found the first evidence of an extended dark matter halo in the Draco dSph. They showed that the velocity dispersion with two different dark matter halo models consistently implies a mass of $M = 8^{+3}_{-2} \times 10^7$ $M_\odot$ inside a dark matter halo core of $r_c = 29$. Consistently with this result, a sharp decline in the velocity dispersion outside ∼30 was reported by Wilkinson et al. (2004, Fig. 9.2). On the basis of this new data of Wilkinson et al. (2004), Łokas et al. (2005) has performed another study of the Draco dSph dark matter distribution and calculated a mass of $M = 6.6 \times 10^7$ $M_\odot$ which is lower than the estimated mass by Kleyna et al. (2001). On the other hand, N-body simulations of Read et al. (2006) in different initial conditions were fitted to observational data of Wilkinson et al. (2004) and suggest a mass of $\sim 10^8$ $M_\odot$ inside 0.8 kpc for the Draco dSph (Model D in the paper) and showed that it is possible for the dSphs to have a dark matter halo with a mass of 10^{10} M$_\odot$.
However, it should be also considered that there are other observational data that show no evidence of rapidly falling dispersion (Muñoz et al., 2005; Walker et al., 2007). In these work the estimation of mass is 6.9×10^7 $M_\odot$ at radius 0.6 kpc, or 9.0×10^7 $M_\odot$ at the outermost profile point.
Additionally, with a cosmological approach, Mashchenko et al. (2006) fitted a flexible stellar anisotropy model to the velocity dispersion reported by Bellazzini et al. (2002) and showed that there are two possible mass ranges for the dark matter halo the Draco dSph; either it formed rather recently (at $z = 2-7$) and is massive (up to 5×10^9 $M_\odot$) or formed before the reionzaition of the universe ($z = 7-11$) and is less massive (down to $\sim 7 \times 10^7$ $M_\odot$).

In the following calculation, we took the radius at which the observed velocity dispersion changes as the dark matter radius. Considering the above results and following the method by Dehnen and King (2006), we calculate the necessary total mass in the Draco dSph to confine LMXBs with the speed V. The model for the halo follows the formula:

$$GM(< r) = V_0^2 \frac{r^3}{r^2 + r_c^2} \,. \tag{9.1}$$

By assuming a dark matter core radius of $r_c = 29$ (0.70 kpc at the distance of 82 kpc, Kinemuchi et al., 2008), and a radius of the galaxy of $r = 40$ (0.96 kpc at the distance of 82 kpc), the circular velocity is:

$$V_0 = \sqrt{\frac{GM}{0.96\,\mathrm{kpc}}} \times \sqrt{1 + \left(\frac{0.70}{0.96}\right)^2} \,. \tag{9.2}$$

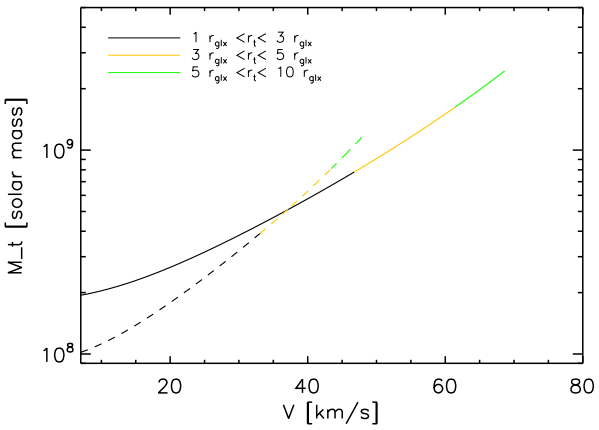

Figure 9.3: The minimum mass of the extended dark matter halo of the Draco dSph, which is needed to confine an LMXB with the velocity V at the radius 1 kpc. The halo core radius is 0.70 kpc and the assumed mass is $M = 5 \times 10^7$ $M_\odot$ (dashed line) or 8×10^8 $M_\odot$ (solid line) within 0.96 kpc. The truncation radius changes with colours. Black, red, and green correspond to reach up to 3, 5 and 10 times the visible radius of the galaxy.

With r_t being the truncation radius of the galaxy, the velocity v_esc at radius $r < r_\mathrm{t}$ required to escape outside r_t is:

$$V_\mathrm{esc}^2 = V_0^2 ln\left(\frac{r_\mathrm{t}^2 + r_\mathrm{c}^2}{r^2 + r_\mathrm{c}^2}\right). \tag{9.3}$$

Inside the visible galaxy, we assumed two different dark matter core masses of $M_\mathrm{min} = 5 \times 10^7$ $M_\odot$ and $M_\mathrm{max} = 10^8$ $M_\odot$. We calculated the halo mass required to keep an LMXB moving out with the velocity v from $r = 1$ kpc, which is already larger than the radius of the galaxy. The truncation radius of the halo can vary between $3 - 10$ times the stellar radius (e.g., Duc et al., 2004; Bournaud et al., 2003). However, we note that large halo truncation radii (in the order of 10 times the galaxy radius) are suggested in tidal dwarf galaxy models (e.g., Bournaud et al., 2003; Duc et al., 2004). It seems unlikely for the Draco dSph, without any tidal evidence, to extend up to 10 times the visible radius. In Figure 9.3, we show how the amount of the mass changes by assuming a dark matter truncation radius of $3 - 10$ times the galaxy radius. Different colours present different ranges of the truncation radius from minimum to maximum.

Circular velocity

The circular velocity calculated by Eq.(9.2) is between $\sim 27 - 38$ km s^{-1}. The

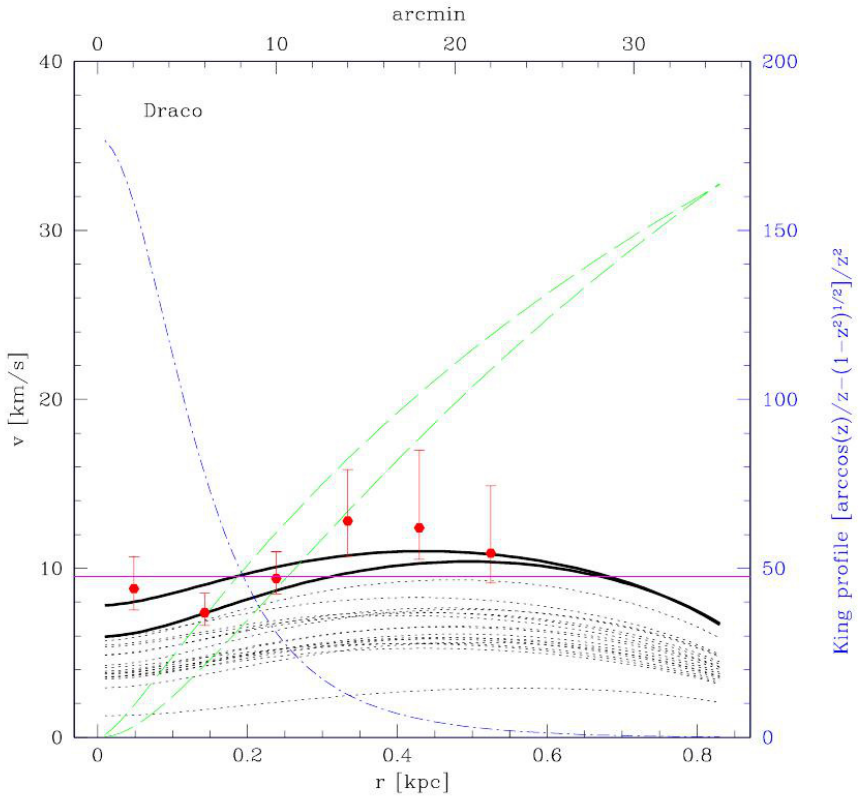

Figure 9.4: Predicted velocity dispersion profiles (dotted) of the Draco dSph. The two best fitting models for each dwarf spheroidal are shown with thick solid lines. The green dashed lines correspond to the circular velocity curves of these best-fit dispersion profiles. King profile fits to the stellar distributions are shown in blue dot-dashes. The red horizontal line corresponds to the central dispersion value given by Mateo (1998). The data are from Kleyna et al. (2001) and show the velocity dispersion profile of the Draco dSph. The plot is by Felix Stoehr (Ph.D thesis, 2003, Physics Department, Ludwig-Maximilan University of Munich).

amount of the circular velocity plays an important role in the estimation of both the total mass and the escape velocity in this model. Our estimation is consistent with the result of Kazantzidis et al. (2004), who have shown that by adapting an isotropic and a tangentially anisotropic model, a maximum circular velocity of $\sim 20 - 35$ km s^{-1} fits the data well and also with the result reported in Ph.D thesis of Felix Stoehr [1] who calculated the velocity dispersion of the Draco dSph using the data of Kleyna et al. (2001, Fig. 9.4).

However Hayashi et al. (2003) showed that the circular velocity can reach significantly higher value than expected from the stellar line of sight velocity dispersion. They suggested a maximum circular velocity V_{max} of the order of 79 km s^{-1}. Contrarily, Mashchenko et al. (2006) assumed the velocity dispersion as a lower limit for the circular velocity of 9.6 km s^{-1} at a radius of 0.74 kpc. Kleyna et al. (2001) mentioned that the Draco appears to rotate at 6 km s^{-1} at the radius of 30 Also Hayashi et al. (2003) mentioned that for an isothermal model, the circular velocity of the Draco can be on the order of 13.4 km s^{-1}.
As shown in Figure 9.3, even assuming the highest total mass inside the visible radius of the Draco dSph and extending the truncation radius of the dark matter halo to 10 times of the visible radius, the galaxy is only able to keep LMXBs with speeds lower than $\sim$70 km s^{-1}, which is much smaller than the mean speed of the majority of the LMXBs of 300 km s^{-1} according to Pfahl et al. (2002). However, neither do we know the accurate distribution of the run-away speed of LMXBs, nor the mass, nor the truncation radius of the galaxy. We will need a better estimate of the number of LMXBs in the dSphs to have a more clear value of the required total mass of such galaxies.

[1] http://edoc.ub.uni-muenchen.de/1644/

Chapter 10

Conclusions, results and outlook

1. We presented the X-ray analysis of five *XMM-Newton* observations of the Draco dSph. We performed source detection separately for each image in each observation and total band mosaic of EPIC, obtaining a catalogue, containing 70 X-ray sources. The position of the X-ray sources for each observation were corrected by the position of optical counterparts. The position of the source in the final catalogue is taken from the observation where the source had the highest statistics.

2. As second step, the correlation of sources with catalogues in other wavelengths was checked. For each source, all the counterparts at other wavelengths and in other catalogues available in literature (e.g., AGNs, galaxies, Milky Way) were considered in the classification. Optical and infrared magnitudes were used to plot the colour-colour or colour-magnitude diagrams. These diagrams clarified the class of several sources. In addition, the optical magnitude of the source counterparts of the SDSS9 and MegaCam catalogues and their X-ray flux were used to calculate the $log_{10}\left(\frac{F_{\rm x}}{F_{\rm opt}}\right)$. This method was essential to significantly distinguish X-ray sources with bright optical counterparts (especially foreground stars).

3. To properly classify the sources, different type of analysis were performed for the X-ray sources. The spectrum of sources with a sufficient amount of counts was studied. Spectra of hard sources were used to select the spectral model (a power-law model with $\Gamma = 1.81$) to calculate the source flux. In addition, the spectral models of two bright foreground stars were presented. Finally, the method of combining the spectrum of 3 different EPICs of an observation was tested. Results showed that for faint sources this method can improve the significance of the fit parameters, while for bright sources it is not necessary.

4. The investigation of the spectral properties of the sources was completed by studying hardness ratio diagrams. Hardness ratio diagrams can indicate the spec-

tral model of sources for which the poor statistics of counts does not allow to extract a spectrum. The hardness ratio is defined for a source in energy bands, in which the detection ML of the source in that band is > 6.0.

5. The variability of sources was studied searching for long-term and short-term variabilities. For long-term variability studies, the flux of the sources (0.2–4.5 keV) in five observations were plotted and fluctuations over time were investigated. During the time of the five *XMM-Newton* observations ($\sim$ 24 days), just one source (source No 33) showed a very high fluctuation in its flux possibly related to an outburst, as the source is a candidate cataclysmic variable. In addition, for sources which have counterparts in the *Chandra* catalogue, the equivalent *XMM-Newton* flux in the energy range of 0.2–4.5 keV were calculated. These *Chandra* sources resulted to have fluxes comparable to the *XMM-Newton* fluxes. Therefore, we did not find long-term variable sources. In the case of short-term variability, two different methods were applied to find a periodicity or pulsations of the sources. The Lomb-Scargel method did not unveil any periodicity or pulsation for the bright sources, however the Z_n^2 test shows a significant pulsation for one of the source (source No 65). To further investigate this source we asked for 10 ks *Swift* observation. However, the source was not detected and we concluded that the source was probably in the quiescent state.

6. All methods mentioned above were used for all sources to classify them. We classified 18 sources as AGNs and 9 sources as galaxies and galaxy candidates. Six sources were classified as foreground stars and one source as a foreground contact binary system in the Milky Way. Four sources were classified as LMXB candidates. Based on hardness ratios, we classified 9 hard sources, which can be AGNs or LMXBs in the field of the Draco dSph.

7. We derived the XLFs of the X-ray sources in Draco dSph in the energy ranges of $2.0 - 10$ keV and $0.5 - 2$ keV. We removed the foreground stars and cataclysmic variable candidates to extract the XLF of the LMXBs. The combination of the background AGNs were subtracted by the function, obtained from the XMM-COSMOS survey. The expected number of AGNs in the observed field can be calculated assuming the distribution function of Cappelluti et al.(2009, see Sect. 8.2.3). Considering the area of the field of view (FOV) the total expected number of AGNs is $\sim$45. Therefore, more than half of the X-ray sources in the field of Draco are most likely AGNs. The number of X-ray sources in the Draco dSph with luminosities between $10^{33} - 4 \times 10^{33}$ erg s^{-1} is estimated to be $\sim$10, which can be a population of both white dwarf X-ray binaries and transient LMXBs.

For a better study of the LMXBs population, longer observations are necessary.

8. We derived the XLFs of the X-ray sources for the Phoenix, Leo I, Fornax, UMi and UMa II dwarf galaxies in the energy ranges of $0.5-2$ keV. We reviewed the star formation histories of these galaxies, investigated relations of formation history of each galaxy to its XLF, and compared the galaxies. It is shown that there is a correlation between the recent formation history and the XLFs of dwarf galaxies. We obtained the XLF of LMXBs for dwarf galaxies, when they are in the last star formation stage (see Fig. 8.17). In addition, we discussed the possible cases for low luminosities found for X-ray sources in Fornax dSph.

9. Considering the escape velocity of LMXBs, we estimated the required dark matter halo mass to keep the LMXBs in the Draco dSph. Our calculation shows that the Draco dSph seems not to be able to retain its LMXBs with a speed $\gtrsim 70$ km s^{-1}, however this result require further investigation (observations) to have a better classification of LMXBs in the Draco dSph.

Outlook

1. The X-ray population study of dwarf galaxies can strongly help to understand the star formation, galactic evolution, and the structure of these galaxies. Our studies were limited to the XLFs of six dwarf galaxies, however there are more than 20 dwarf galaxies around the Milky-Way with a distance less than 200 kpc (Table 2, McConnachie, 2012). This makes them ideal targets to improve and extend the X-ray population study of dwarf galaxies as the oldest known nearby galaxies. There is no available survey to offer a general X-ray luminosity function for the evolution of dwarf galaxies and this thesis can be a basis for this larger work.

2. Not only, the observation of other dwarf galaxies can complete this survey, but also, longer observations of studied cases like, Draco, UMi, UMa II dSph, which suffered of short observational time, can help to significantly improve the comparison of XLFs of these galaxies. New observations can help to improve the source classification of the dwarf galaxies which is very important in population studies.

3. Optical observations and simulations are being carried out to find a suitable model for the structure of dSphs. There are cases in which the result are not consistent with common dark matter dominant models of dSphs (Battaglia et al., 2013). It seems that the population of LMXBs can be a probe for the structure of dSphs.

Chapter 11

Figure 11.1: The light curves of the entire EPICs in each observation. The time-bin-size of the light curves is 10 s. Light curves of OBS3 and OBS4 were contaminated by flares more than other observations. For each observation, we removed the times of strong background flares from the event files which were obtain from these light curves.

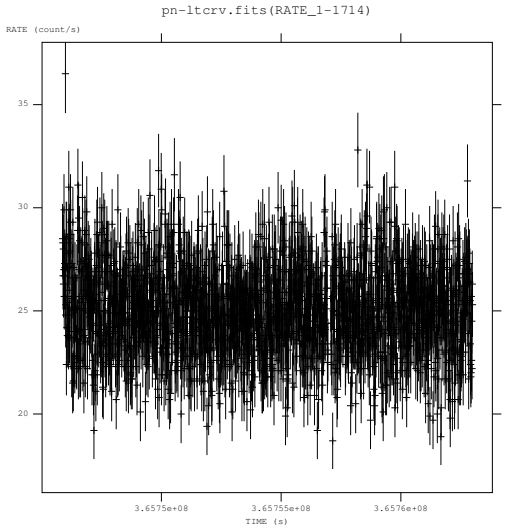

() OBS1-PN

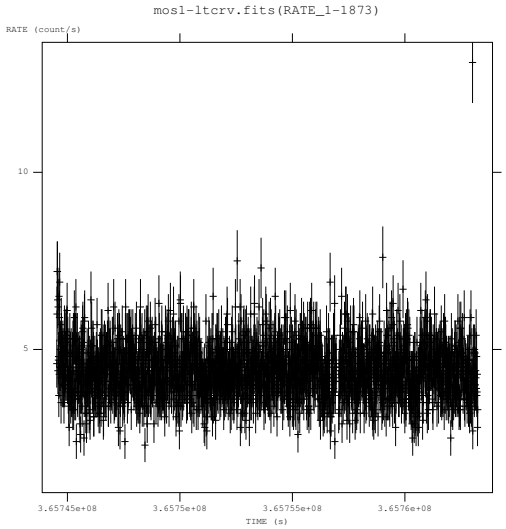

() OBS1-MOS1

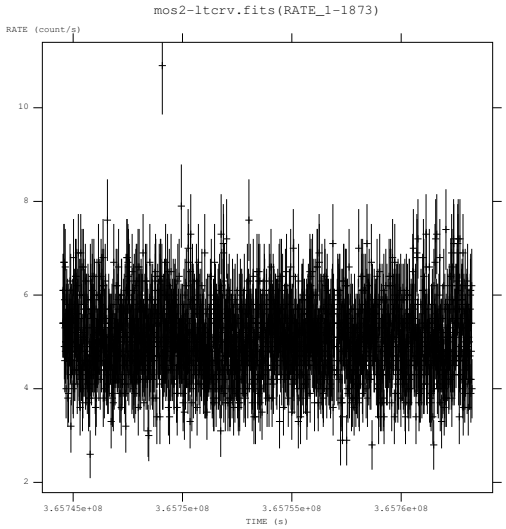

() OBS1-MOS2

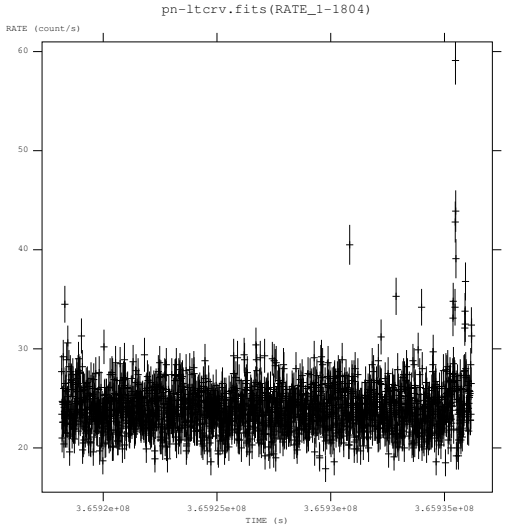

() OBS2-PN

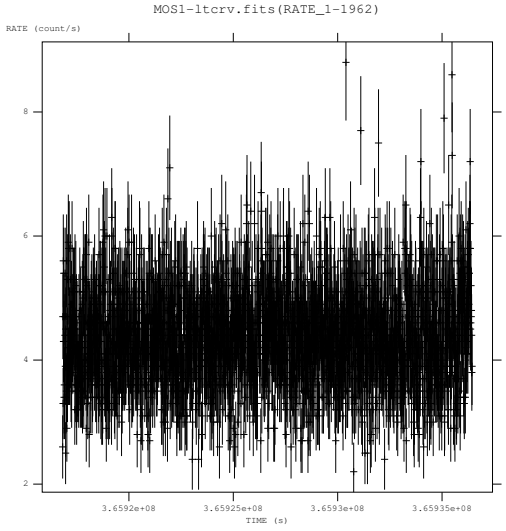

() OBS2-MOS1

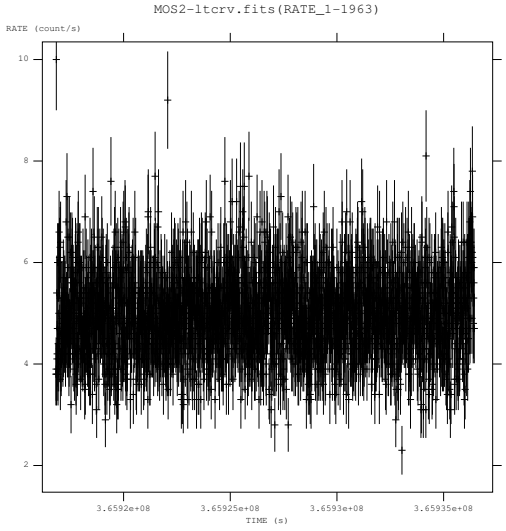

() OBS2-MOS2

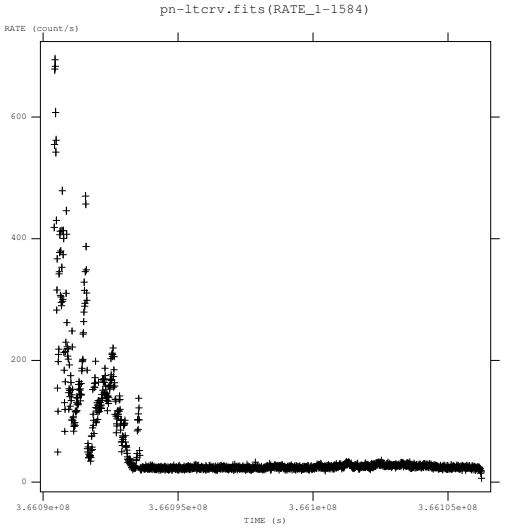

() OBS3-PN

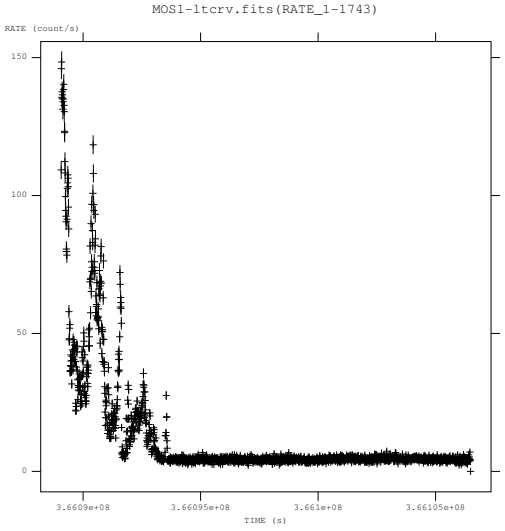

() OBS3-MOS1

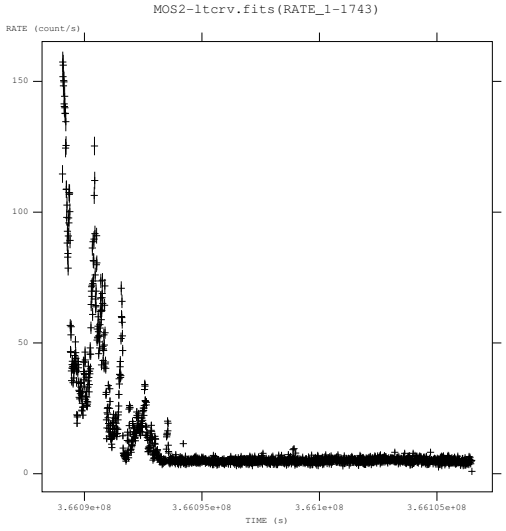

() OBS3-MOS2

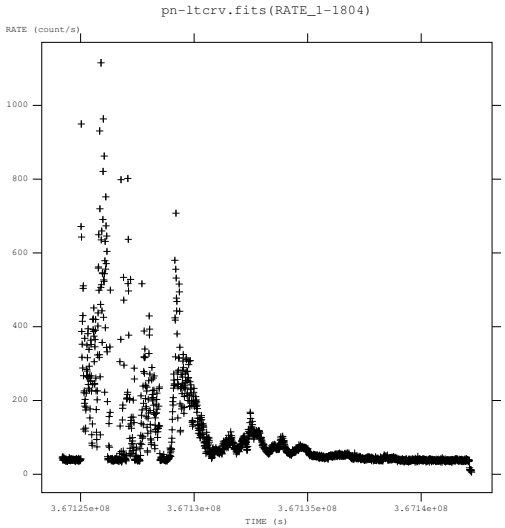

() OBS4-PN

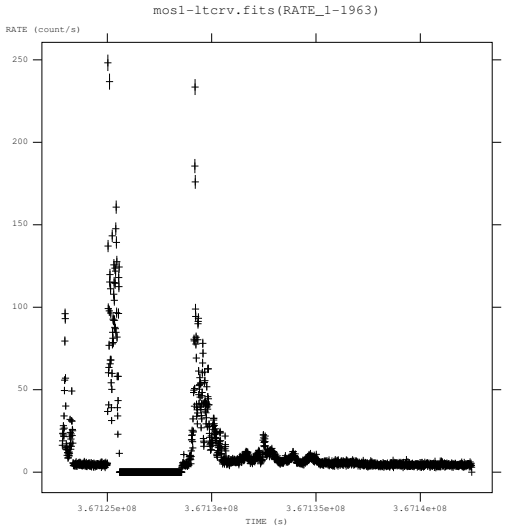

() OBS4-MOS1

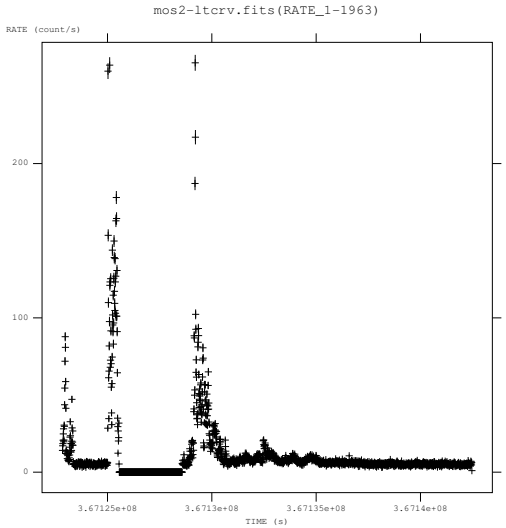

() OBS4-MOS2

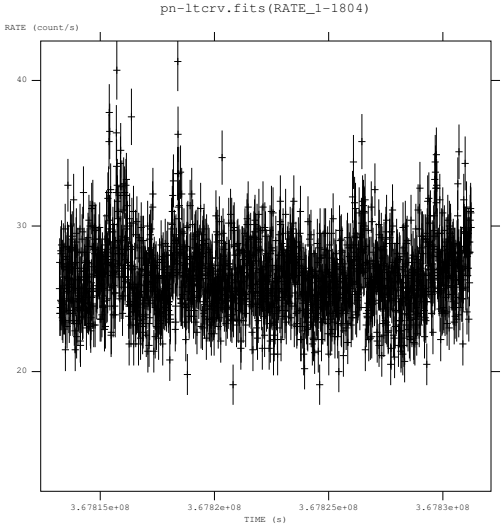

() OBS5-PN

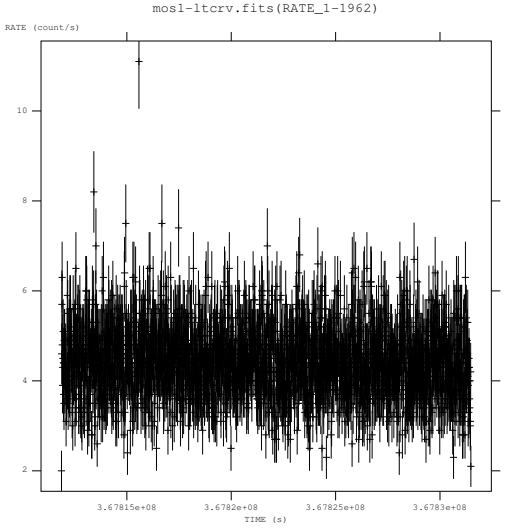

() OBS5-MOS1

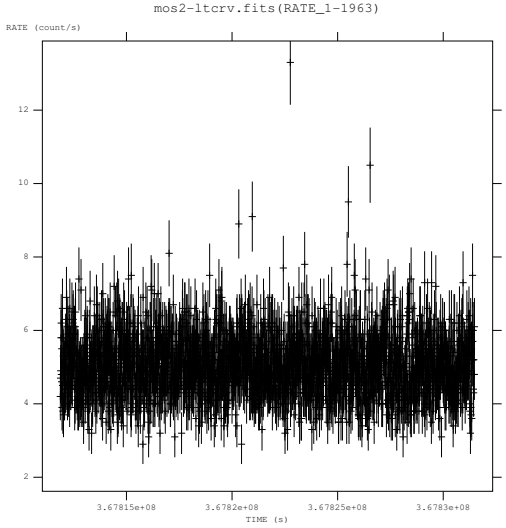

() OBS5-MOS2

Figure 11.2: The RA and Dec offsets of *XMM-Newton* observations. The optical source coordinates is set to 0.0 in RA and DEC. The plot shows differences of position of X-ray sources compared to the optical sources. the error bars are corresponding to the error of X-ray source and its optical counterpart.

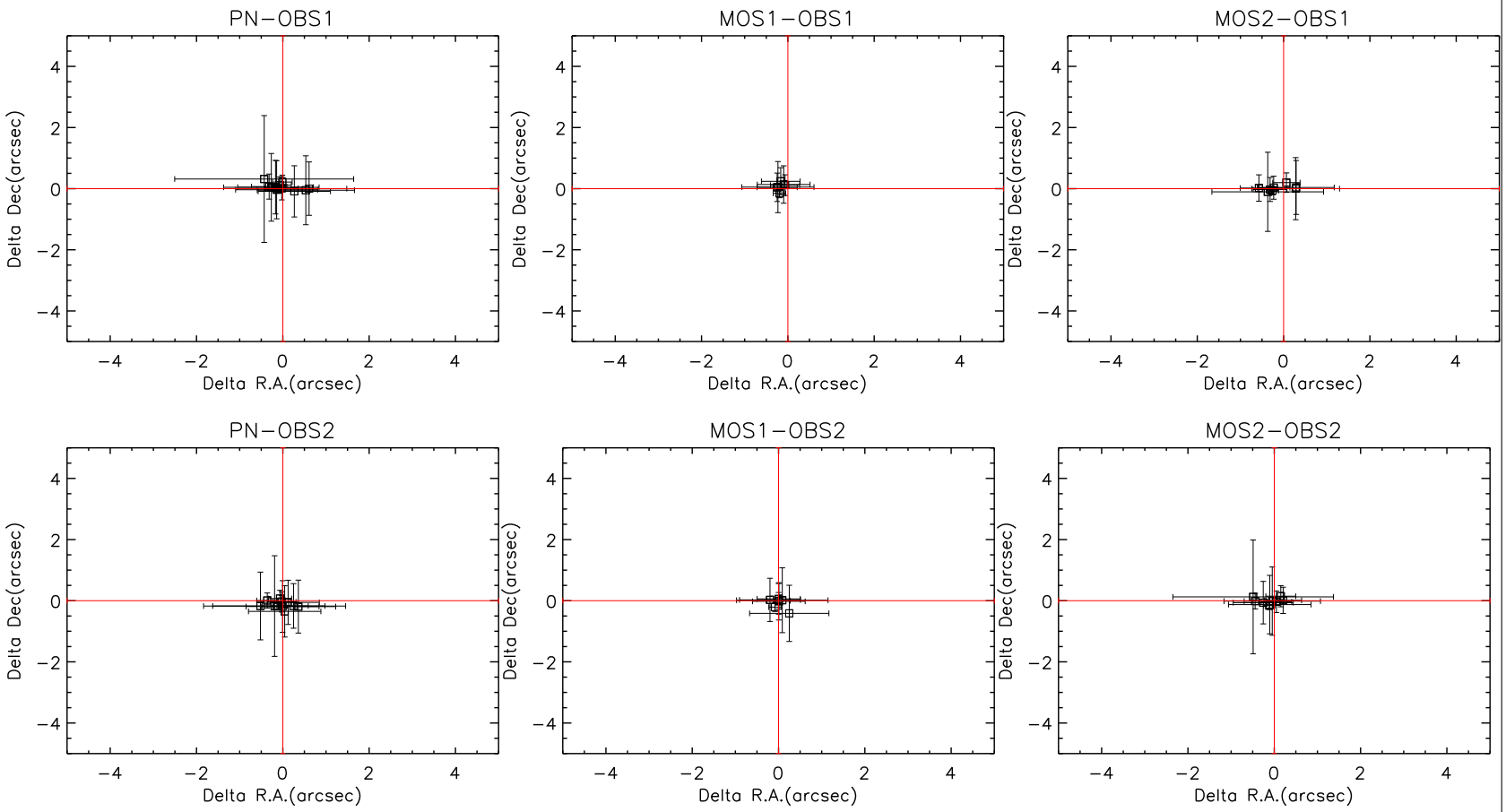

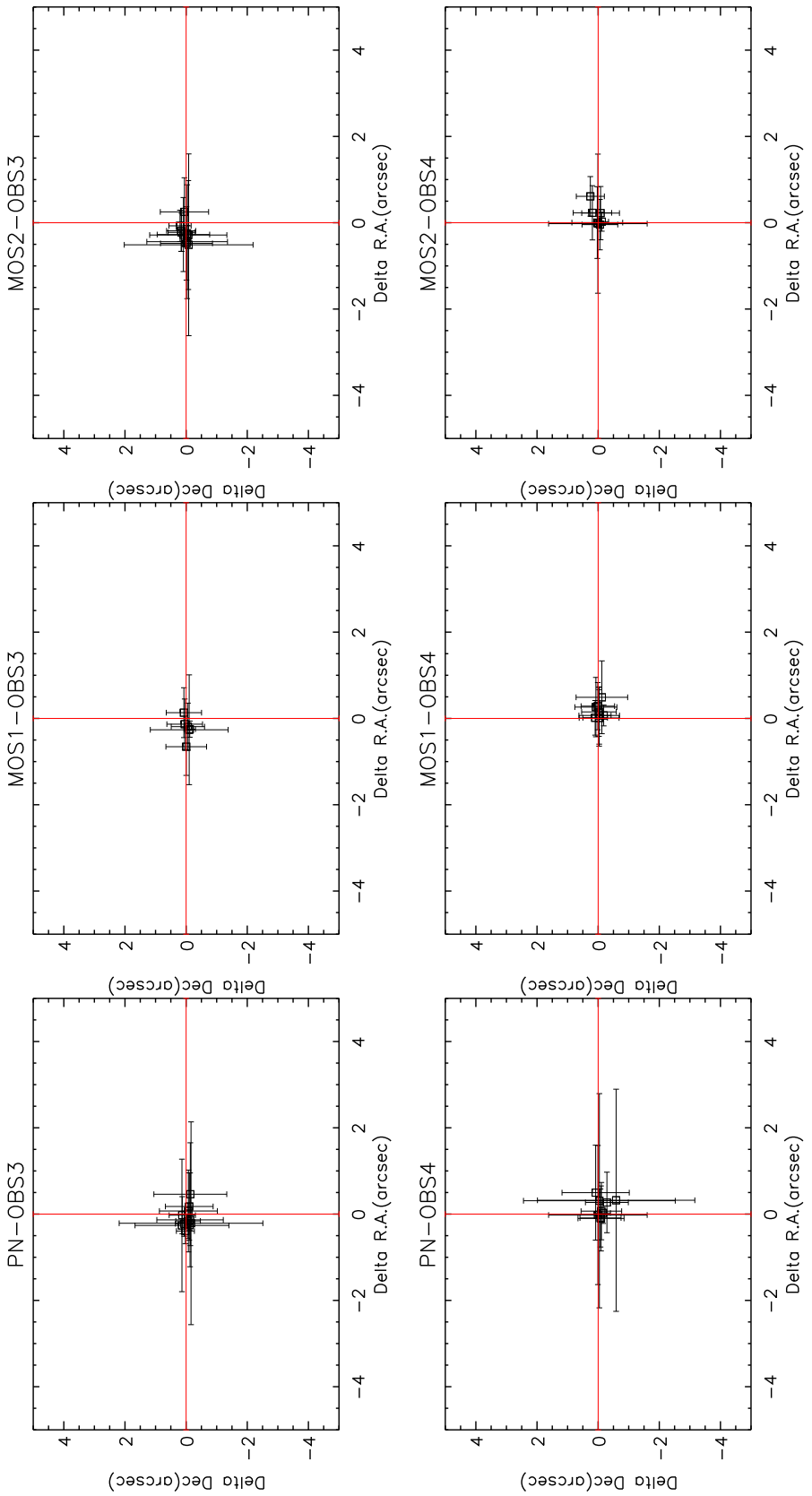
MOS2−OBS3
MOS2−OBS4
MOS1−OBS3
MOS1−OBS4
PN−OBS3
PN−OBS4
Delta Dec(arcsec)
Delta R.A.(arcsec)
4
2
0
−2
−4

PN−OBS5
MOS1−OBS5
MOS2−OBS5
mosaic
Delta Dec(arcsec)
Delta R.A.(arcsec)
4
2
0
−2
−4

Figure 11.3: The plots show the light curve of each source over five observations. The weighted (0.2 – 4.5 keV) flux of each source in different observations is plotted over time. If the source was not detected in an observation, the upper limit was calculated.

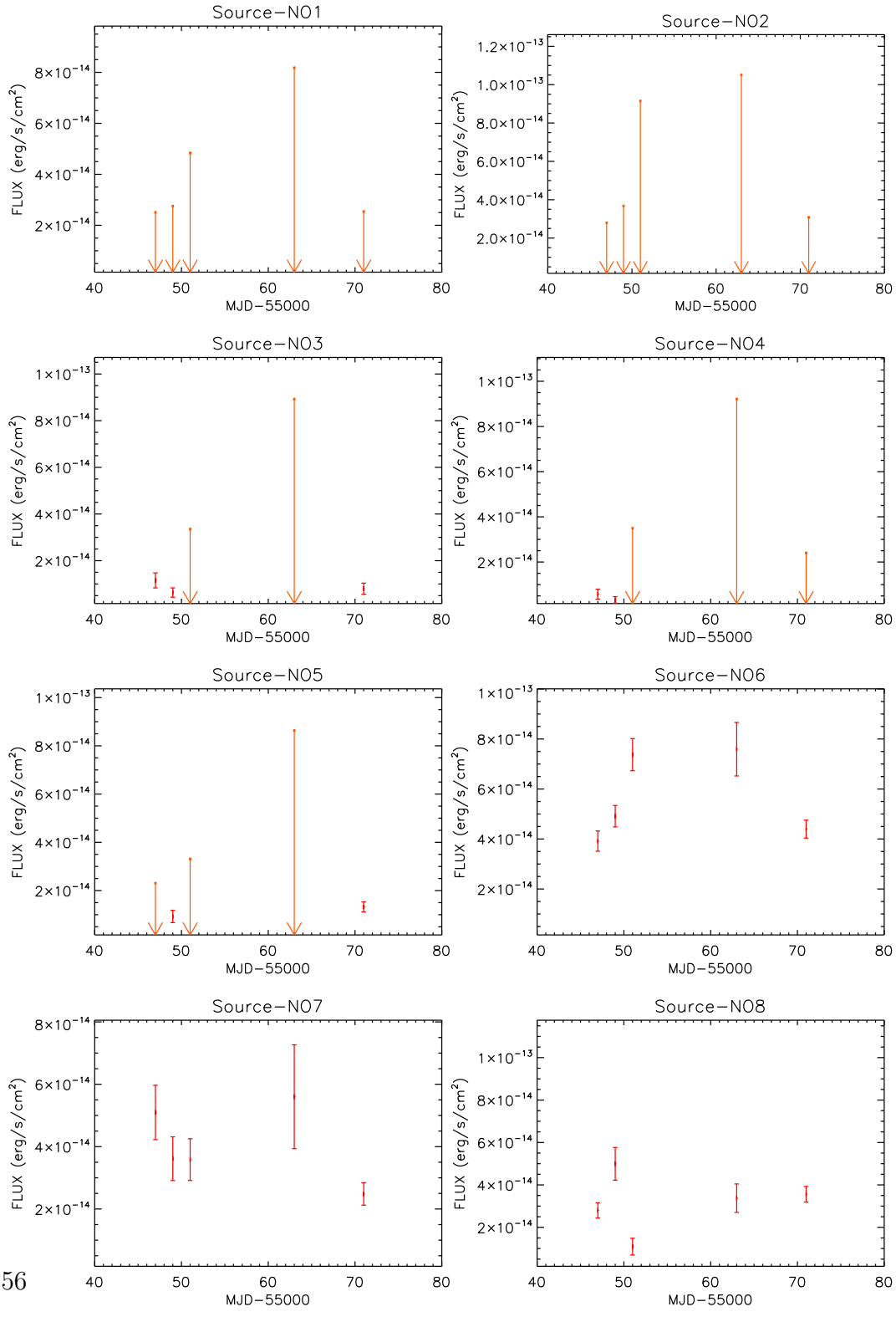

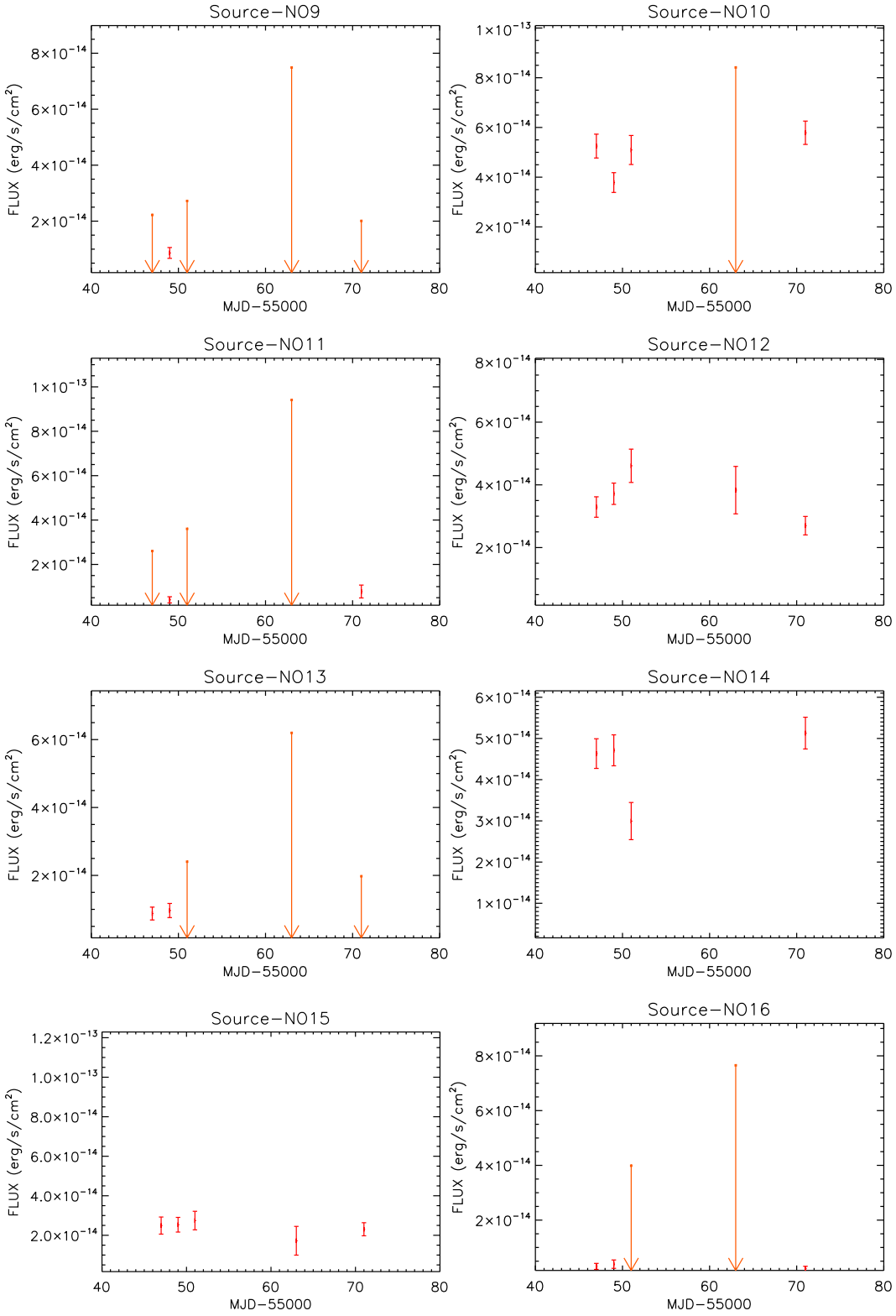
Source−NO9
Source−NO10
Source−NO11
Source−NO12
Source−NO13
Source−NO14
Source−NO15
Source−NO16
FLUX (erg/s/cm²)
MJD−55000

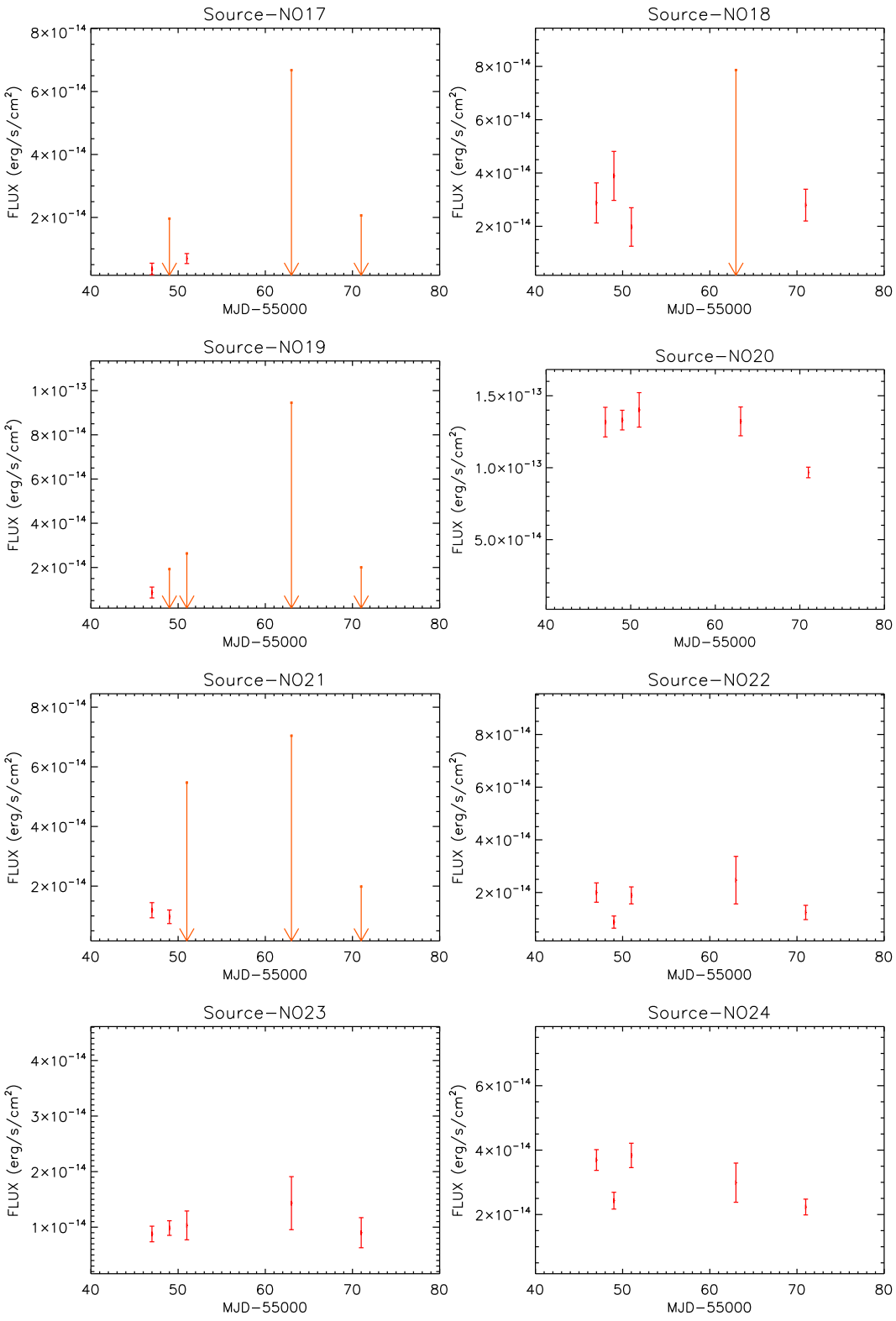
Source−NO17
Source−NO18
Source−NO19
Source−NO20
Source−NO21
Source−NO22
Source−NO23
Source−NO24
FLUX (erg/s/cm²)
MJD−55000

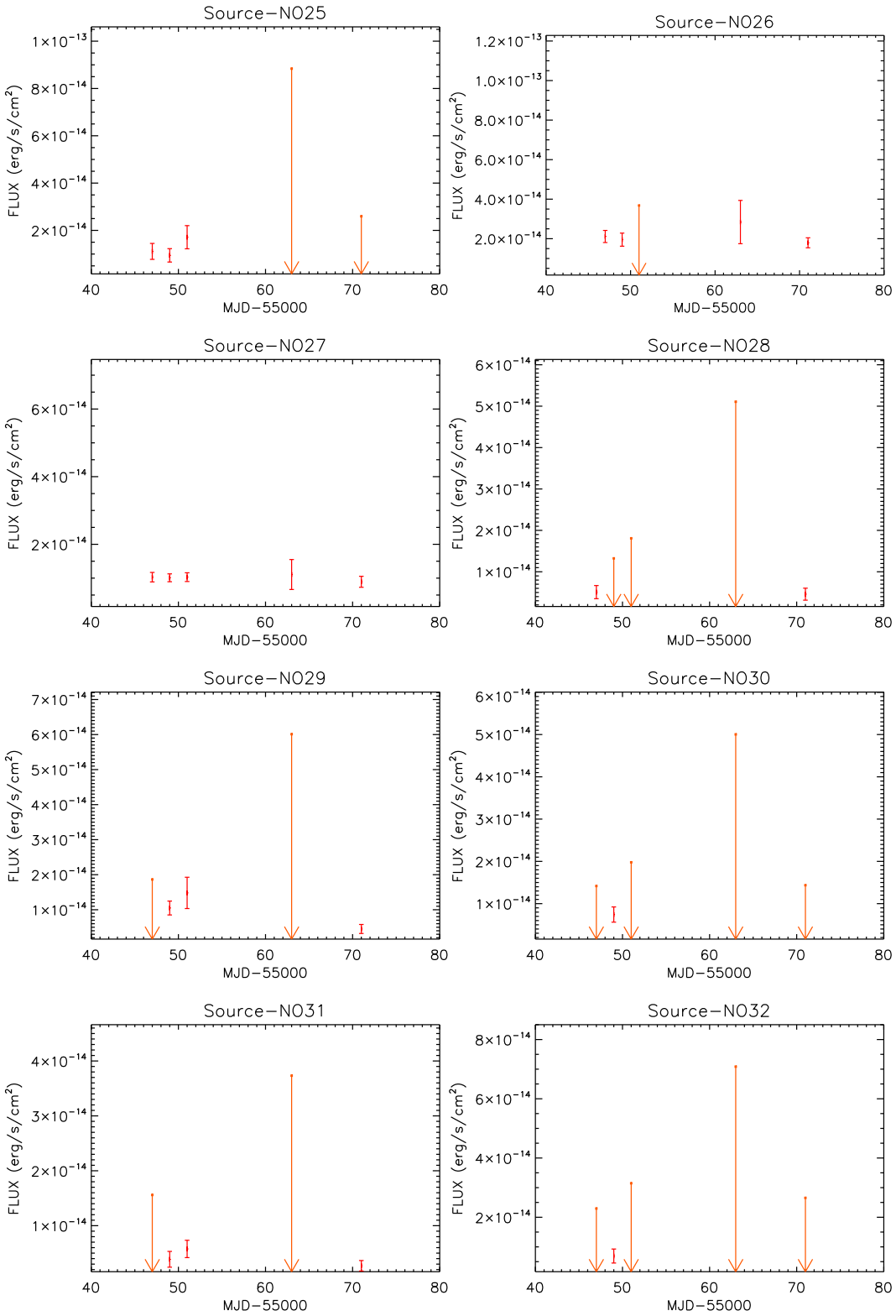
Source−NO25
Source−NO26
Source−NO27
Source−NO28
Source−NO29
Source−NO30
Source−NO31
Source−NO32
FLUX (erg/s/cm²)
MJD−55000

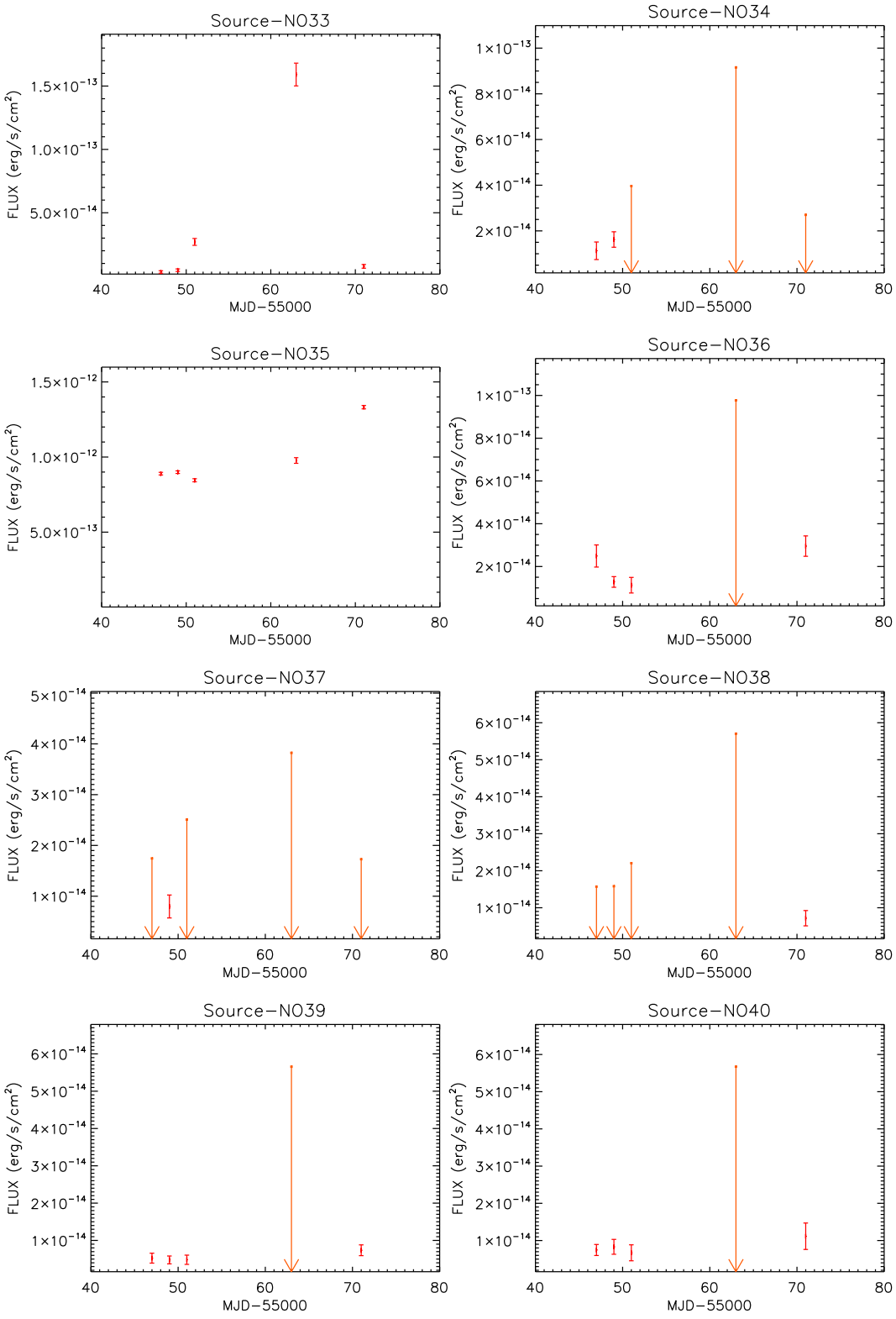
Source−N033
Source−N034
Source−N035
Source−N036
Source−N037
Source−N038
Source−N039
Source−N040
FLUX (erg/s/cm²)
MJD−55000

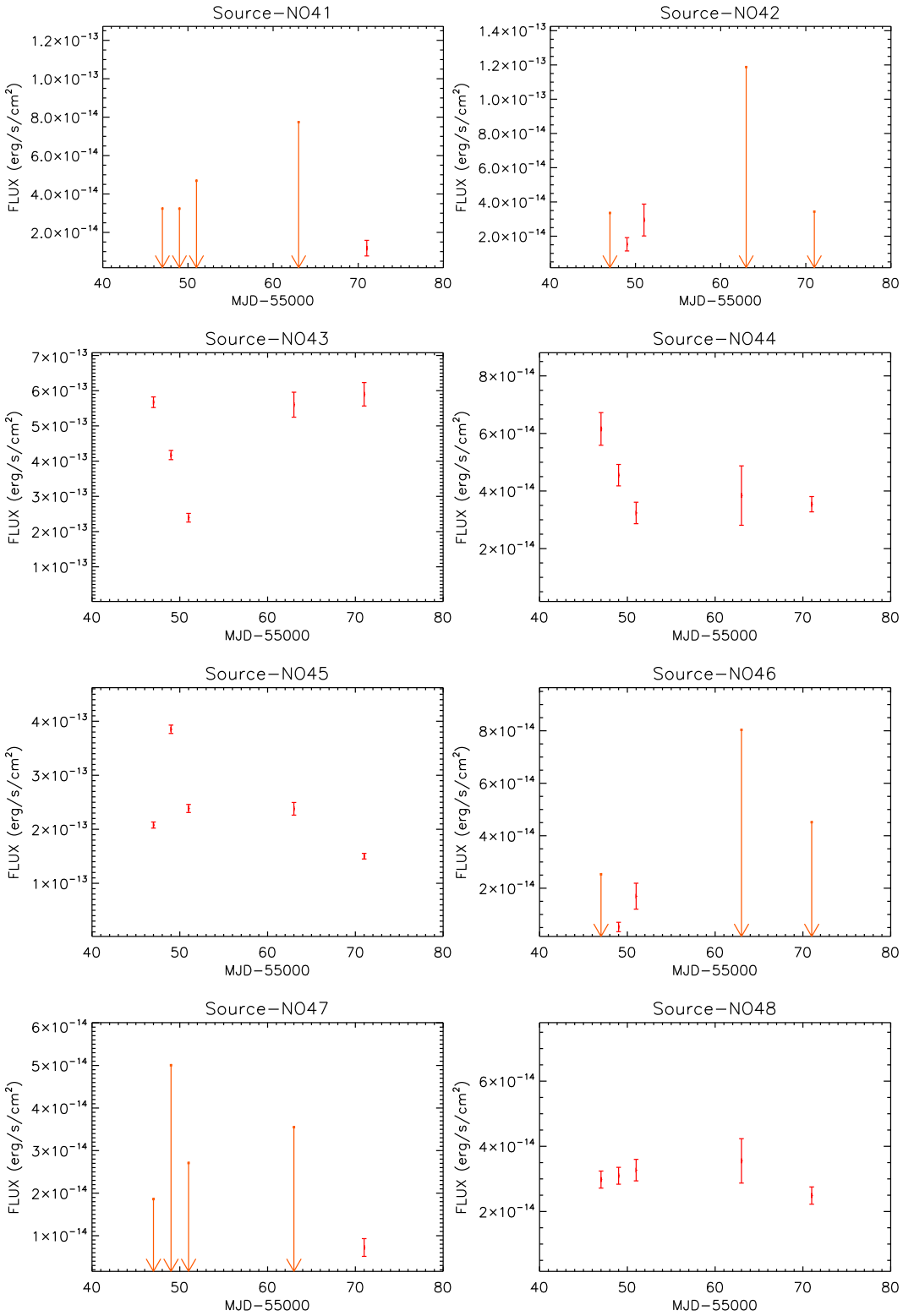
Source−NO41
Source−NO42
Source−NO43
Source−NO44
Source−NO45
Source−NO46
Source−NO47
Source−NO48
FLUX (erg/s/cm²)
MJD−55000

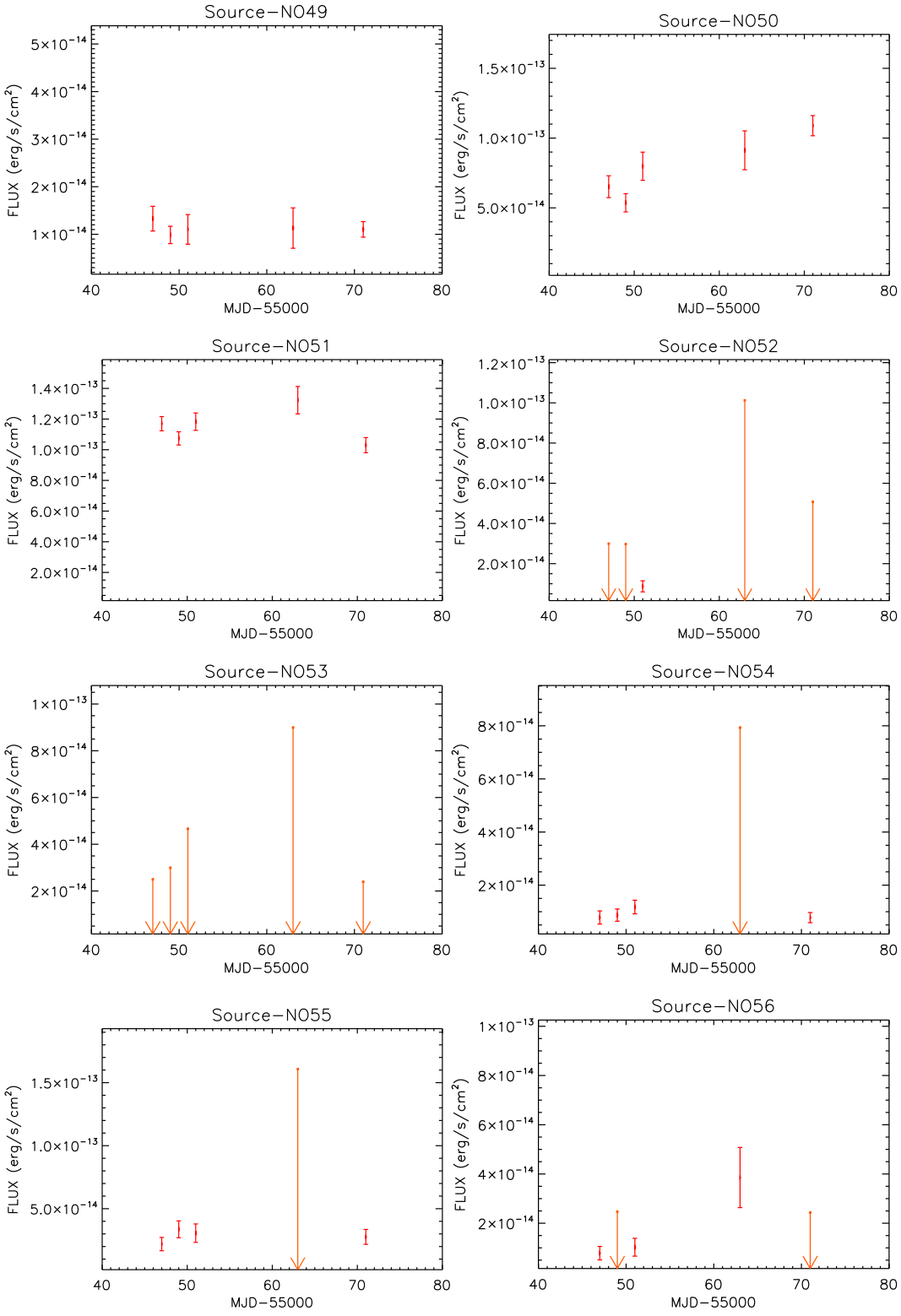
Source−N049
Source−N050
Source−N051
Source−N052
Source−N053
Source−N054
Source−N055
Source−N056
FLUX (erg/s/cm²)
MJD−55000

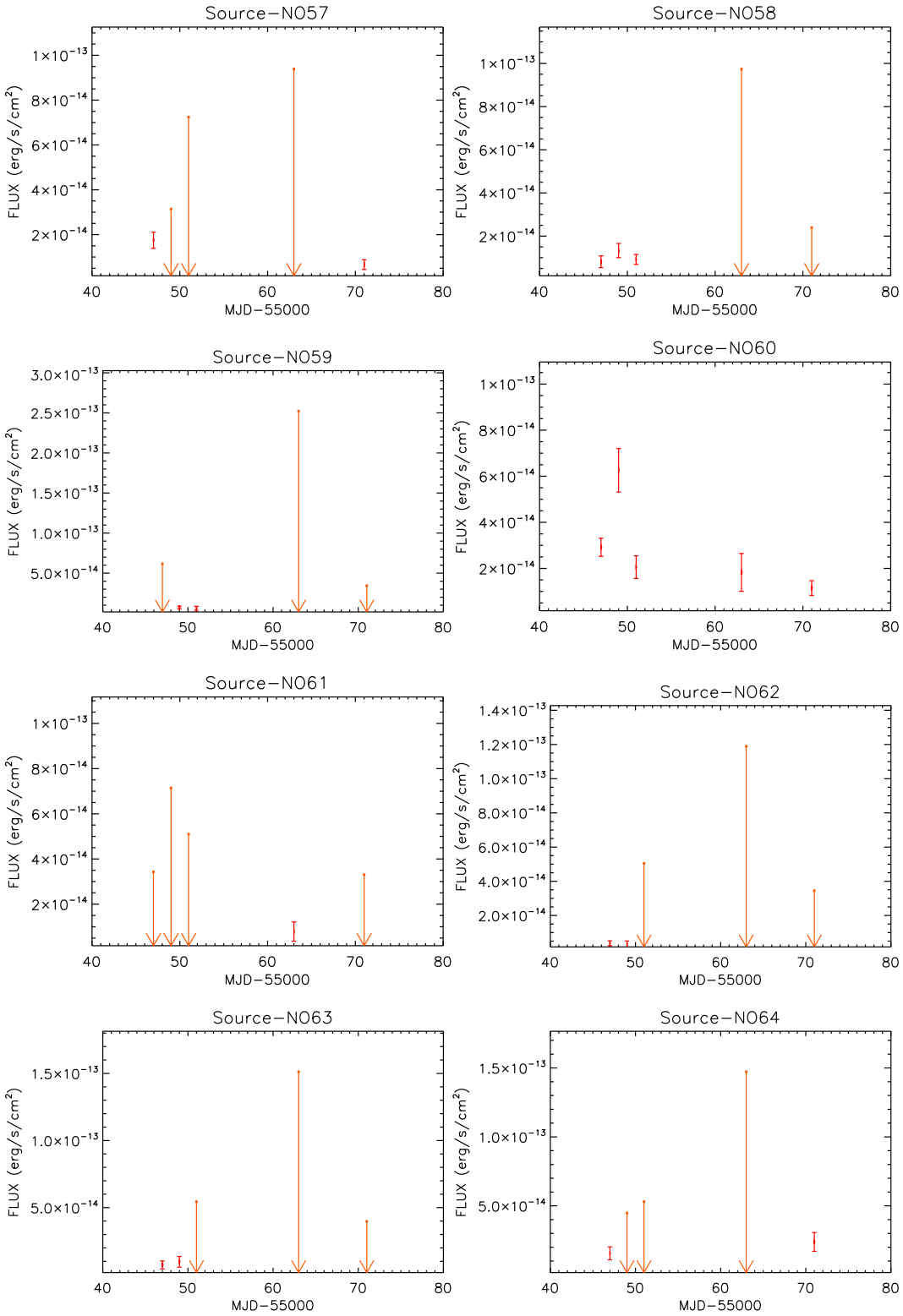
Source−NO57
Source−NO58
Source−NO59
Source−NO60
Source−NO61
Source−NO62
Source−NO63
Source−NO64
FLUX (erg/s/cm²)
MJD−55000

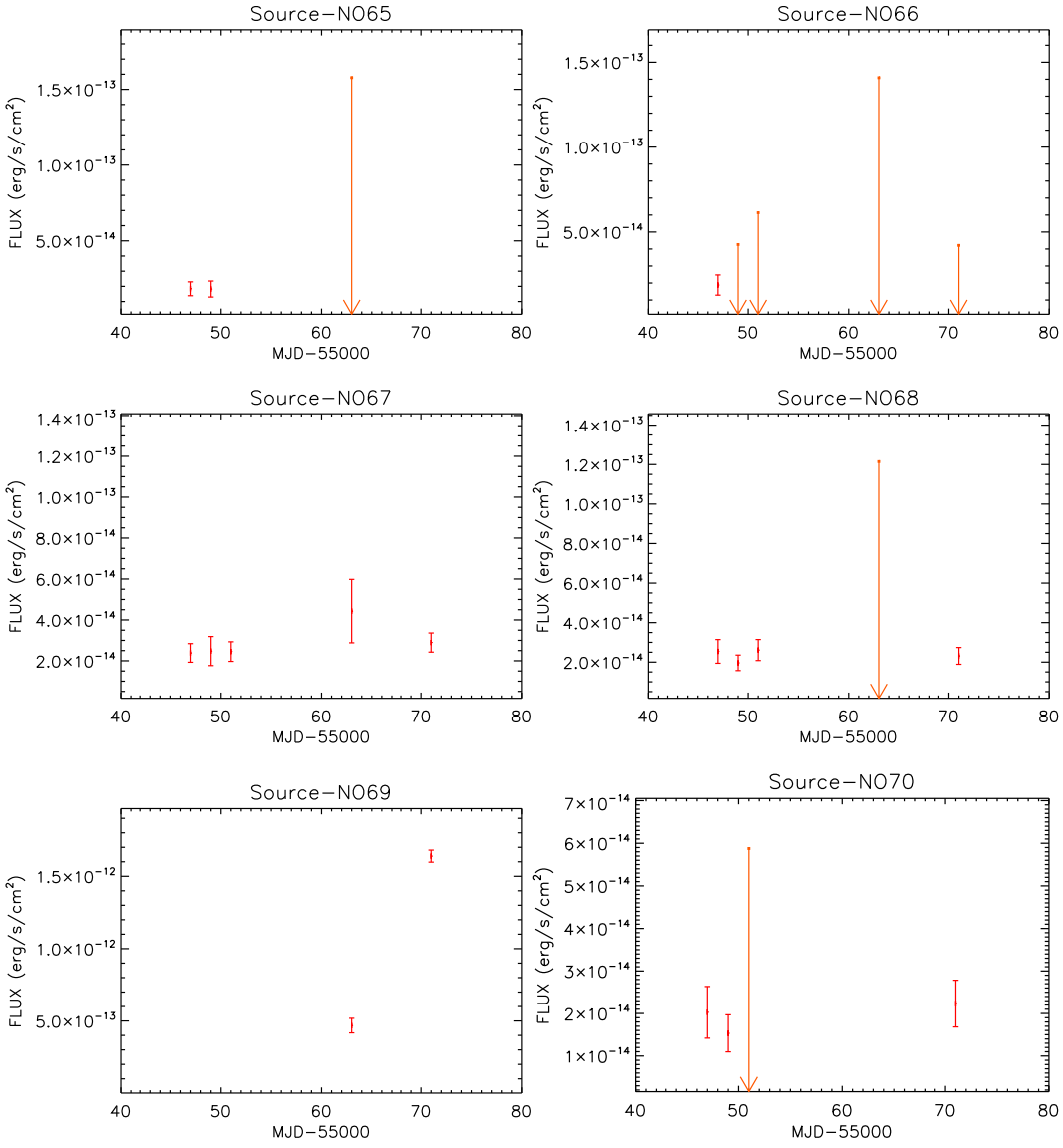
Source−NO65
Source−NO66
Source−NO67
Source−NO68
Source−NO69
Source−NO70
FLUX (erg/s/cm²)
MJD−55000

Figure 11.4: The Lomb-Scargel peridogams of the brightest X-ray sources of the Draco dSph

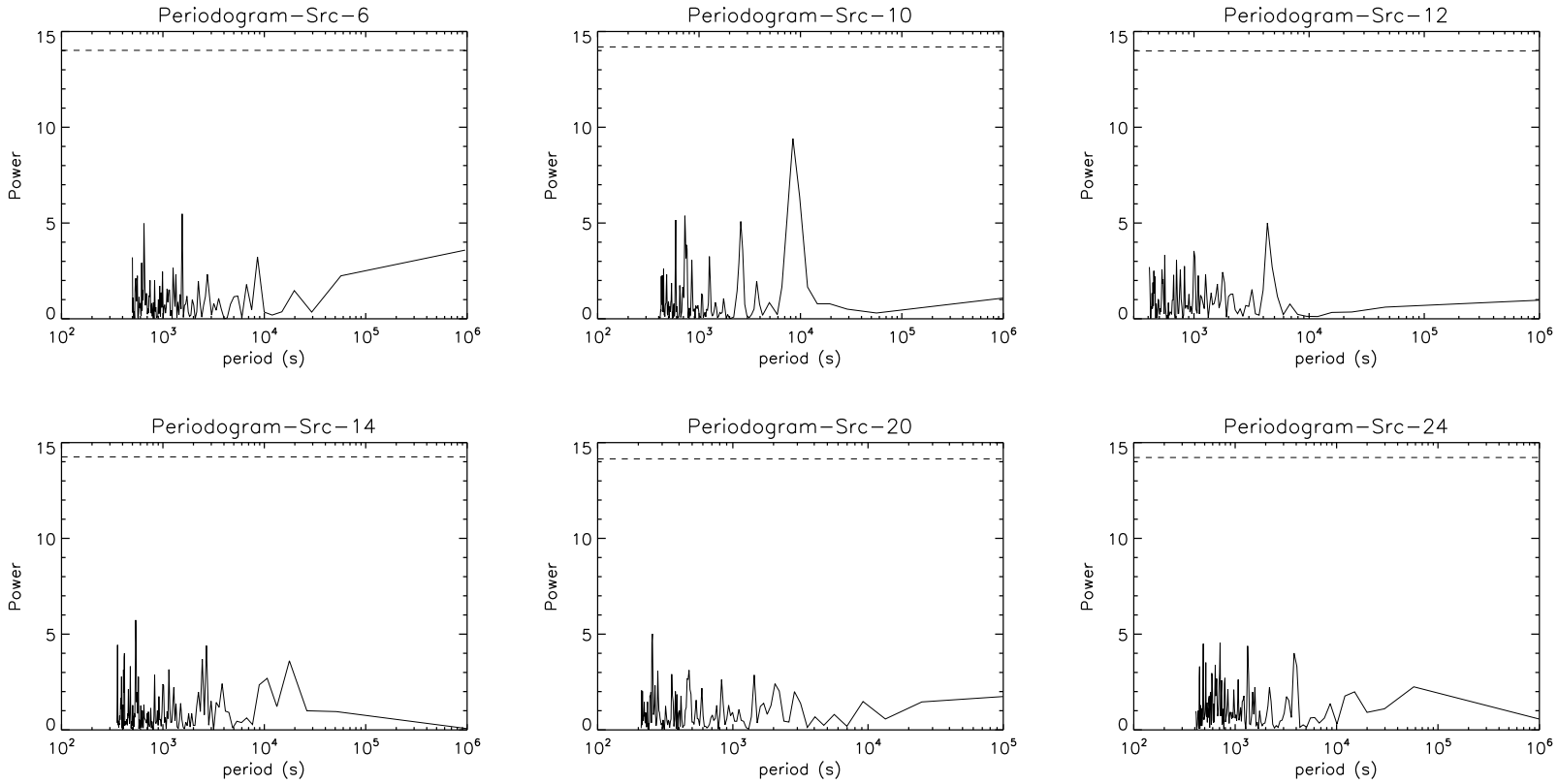

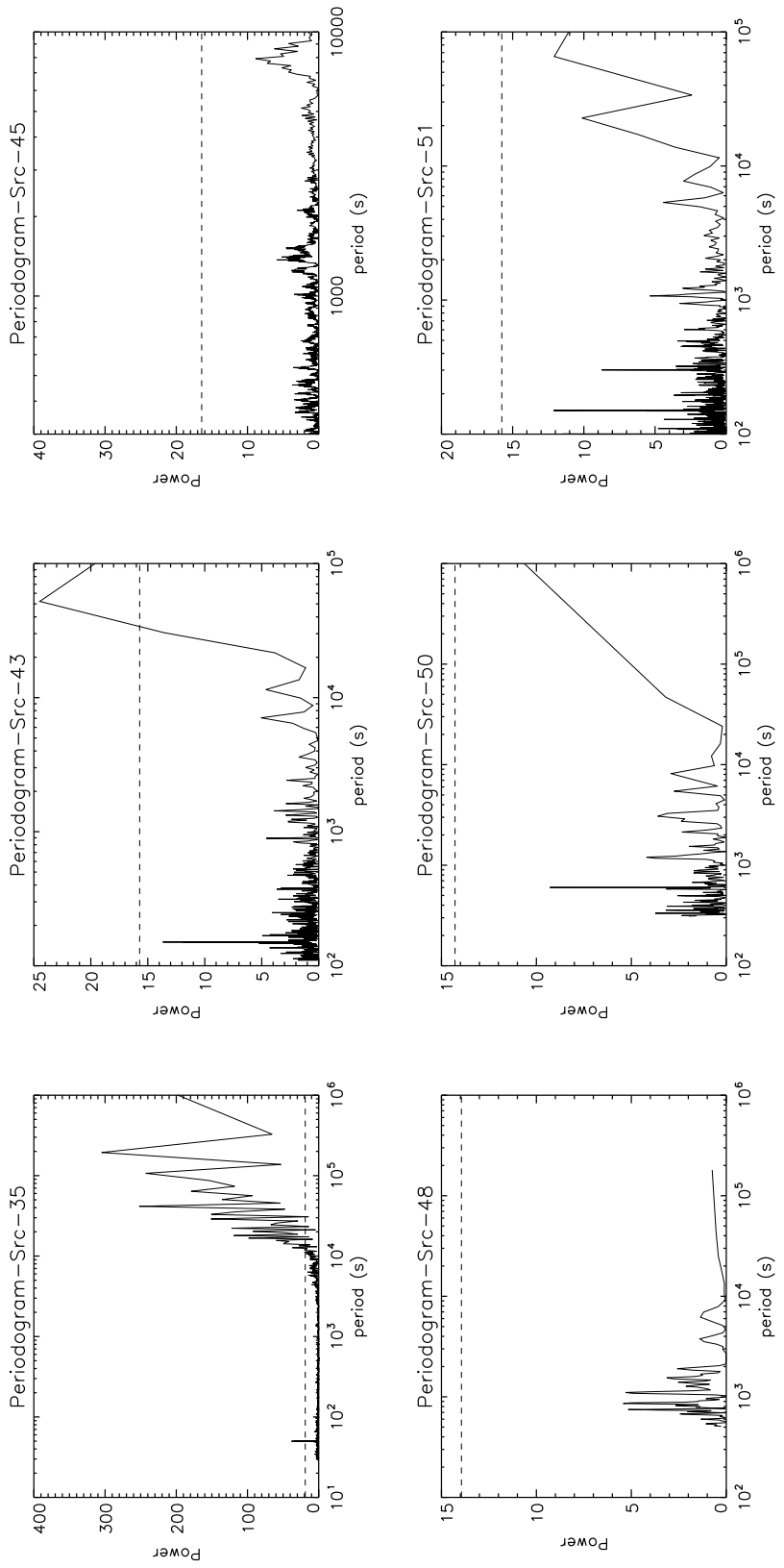
Periodogram−Src−45
Periodogram−Src−51
Periodogram−Src−43
Periodogram−Src−50
Periodogram−Src−35
Periodogram−Src−48
Power
period (s)

Figure 11.5: The simultaneous spectral fit (left plots), and merged spectral (right plots) fit of the hard bright sources. The parameter of these fit models are in Table 6.2. Sources No 14 and 43 were detected only in EPIC-pn.

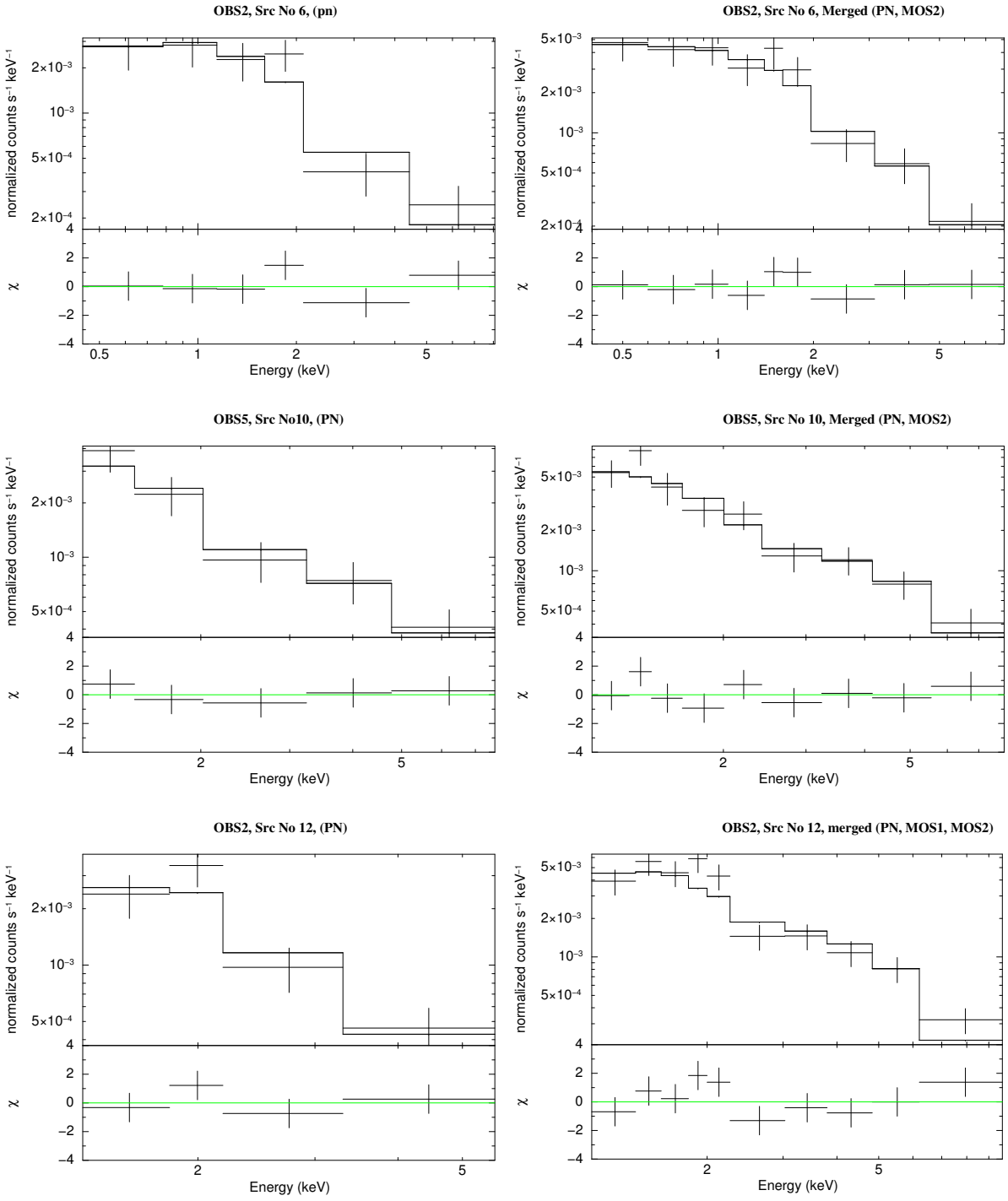

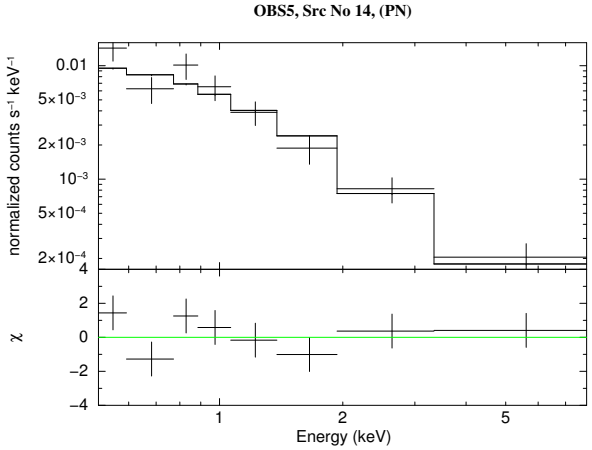
OBS5, Src No 14, (PN)
normalized counts s⁻¹ keV⁻¹
0.01
5×10⁻³
2×10⁻³
10⁻³
5×10⁻⁴
2×10⁻⁴
χ
Energy (keV)

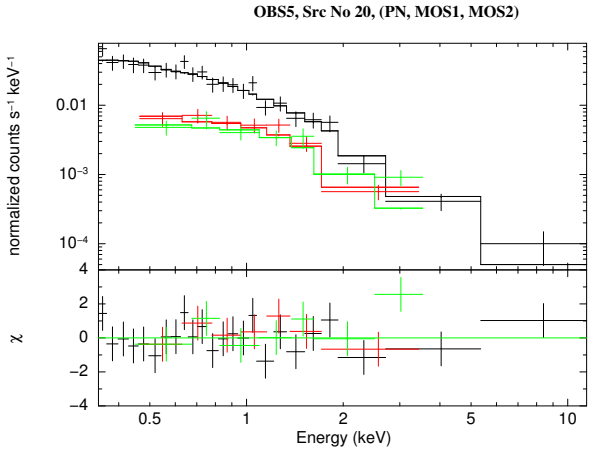
OBS5, Src No 20, (PN, MOS1, MOS2)
normalized counts s⁻¹ keV⁻¹
0.01
10⁻³
10⁻⁴
χ
Energy (keV)

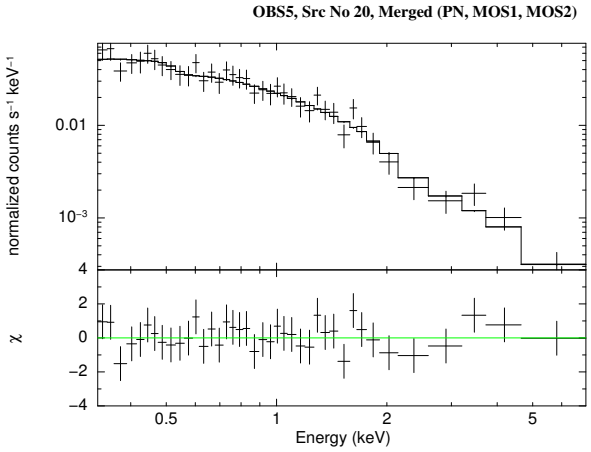
OBS5, Src No 20, Merged (PN, MOS1, MOS2)
normalized counts s⁻¹ keV⁻¹
0.01
10⁻³
χ
Energy (keV)

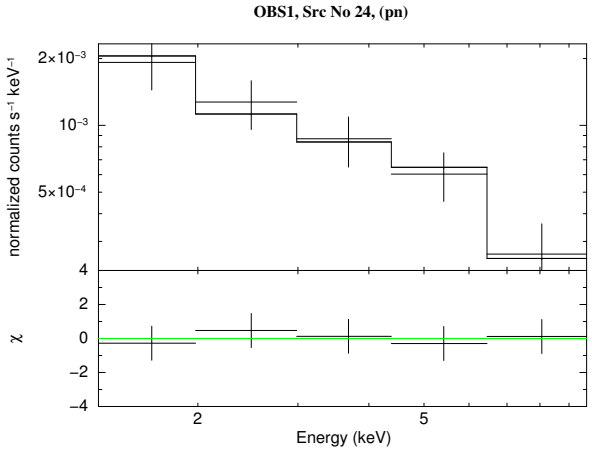
OBS1, Src No 24, (pn)
normalized counts s⁻¹ keV⁻¹
2×10⁻³
10⁻³
5×10⁻⁴
χ
Energy (keV)

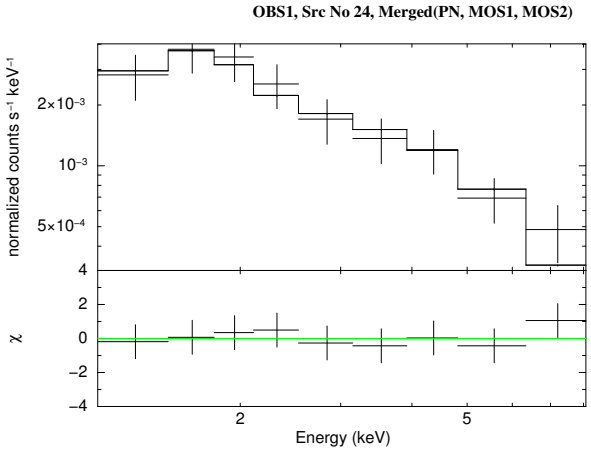
OBS1, Src No 24, Merged(PN, MOS1, MOS2)
normalized counts s⁻¹ keV⁻¹
2×10⁻³
10⁻³
5×10⁻⁴
χ
Energy (keV)

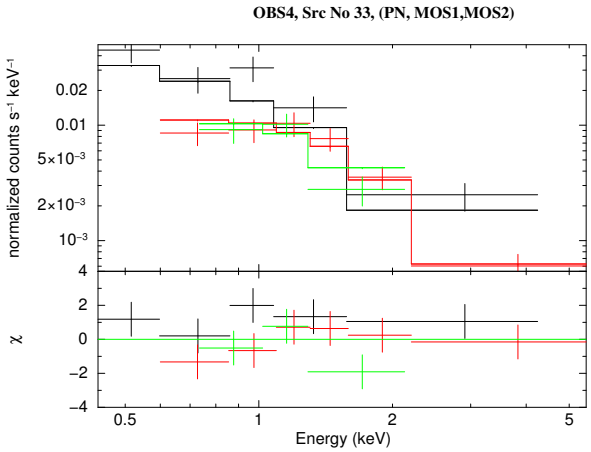
OBS4, Src No 33, (PN, MOS1,MOS2)
normalized counts s⁻¹ keV⁻¹
χ
Energy (keV)

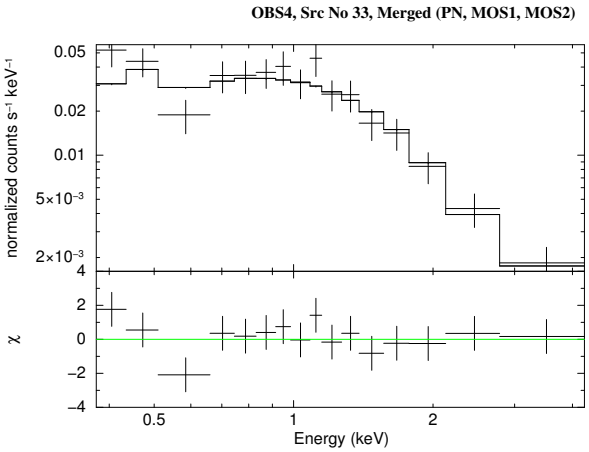
OBS4, Src No 33, Merged (PN, MOS1, MOS2)
normalized counts s⁻¹ keV⁻¹
χ
Energy (keV)

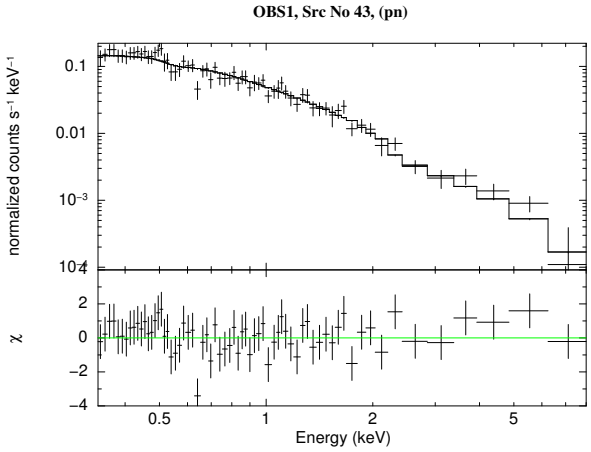
OBS1, Src No 43, (pn)
normalized counts s⁻¹ keV⁻¹
χ
Energy (keV)

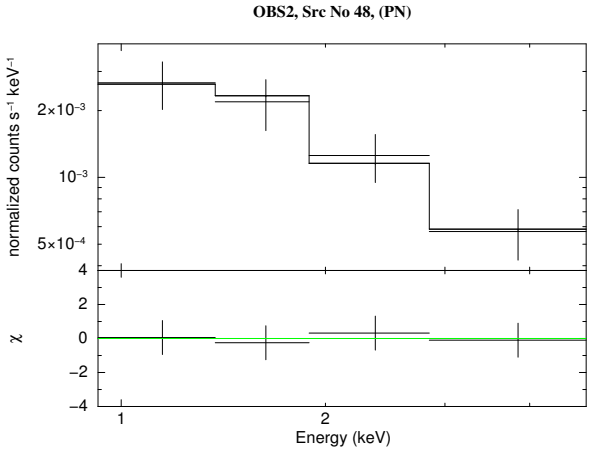
OBS2, Src No 48, (PN)
normalized counts s⁻¹ keV⁻¹
χ
Energy (keV)

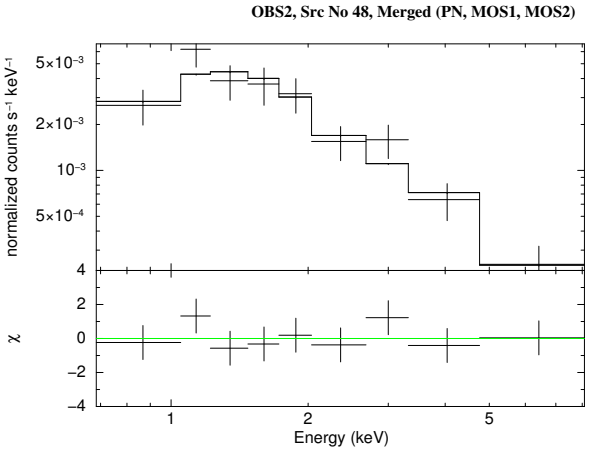
OBS2, Src No 48, Merged (PN, MOS1, MOS2)
normalized counts s⁻¹ keV⁻¹
χ
Energy (keV)

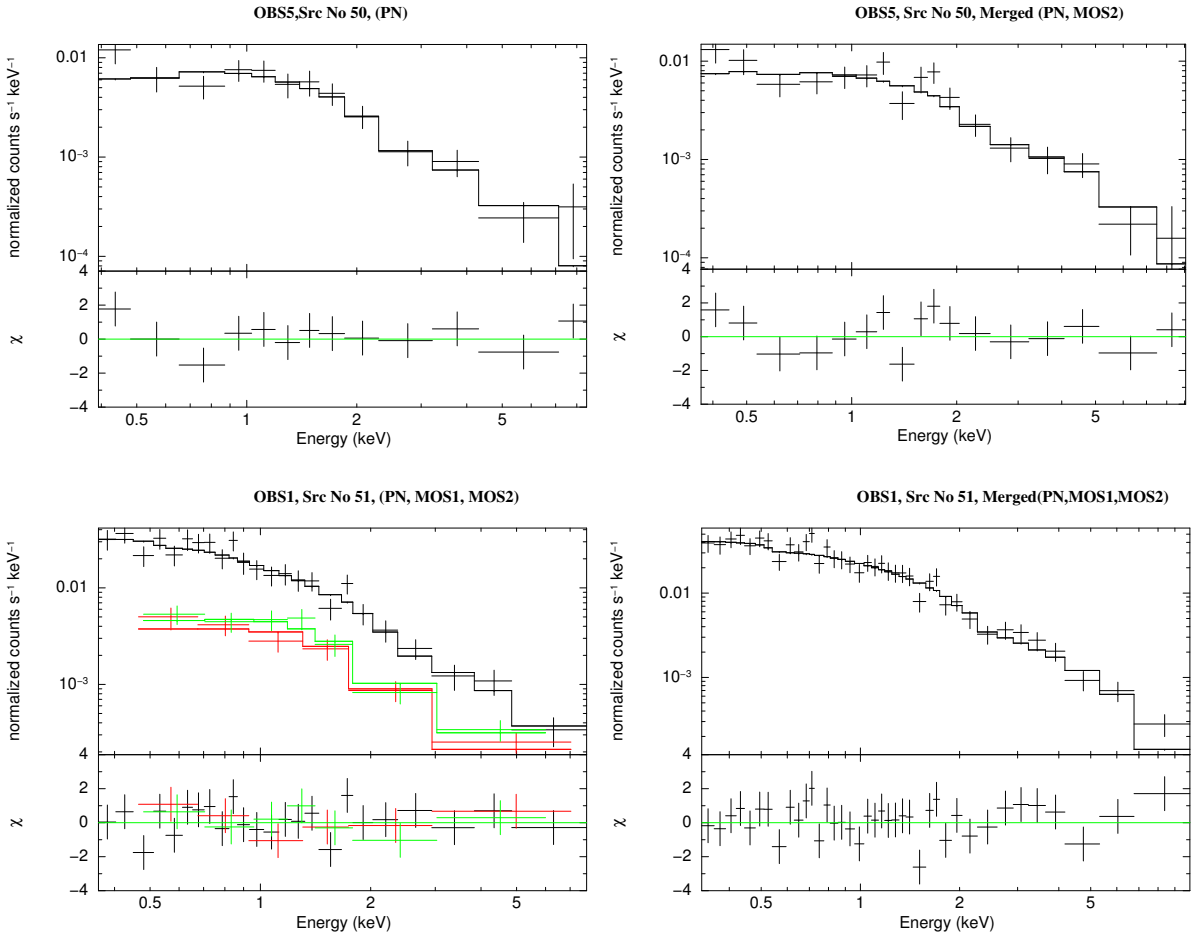
OBS5,Src No 50, (PN)
OBS5, Src No 50, Merged (PN, MOS2)
OBS1, Src No 51, (PN, MOS1, MOS2)
OBS1, Src No 51, Merged(PN,MOS1,MOS2)
normalized counts s⁻¹ keV⁻¹
χ
Energy (keV)

Chapter 12

Table 12.1: Position and detection ML for the detected sources by *XMM-Newton* in the field of the Draco dSph, in different observation in the EPIC-pn, summation and average in all EPICs., and in mosaic image

ID	RA(J2000)	Dec(J2000)	r1σ()	pn-OBS1	pn-OBS2	pn-OBS3	pn-OBS4	pn-OBS5	Sum-of-ML	Epics-Ave	Mosaic-ML
1	17 18 46.52	+57 54 46.5	1.16	–	–	–	–	–	–	–	11.5
2	17 18 48.45	+57 50 13.3	1.05	–	–	–	–	–	–	–	14.7
3	17 18 49.99	+57 54 52.9	0.88	17.5	19.9	–	–	18.7	56.1	18.7	40.3
4	17 18 56.89	+57 51 04.0	1.07	15.5	10.3	–	–	–	25.8	12.9	25.0
5	17 19 00.63	+57 51 45.7	1.19	–	23.0	–	–	69.3	114.4	38.1	64.5
6	17 19 01.51	+58 00 29.0	0.35	196.2	306.8	303.3	55.5	271.2	1592.7	144.8	1226.1
7	17 19 04.05	+58 03 29.3	1.15	–	–	–	–	97.3	360.4	51.5	374.4
8	17 19 04.54	+57 47 27.5	0.48	195.7	–	23.3	34.7	144.5	633.7	70.4	481.8
9	17 19 06.76	+57 55 48.0	0.92	–	13.7	–	–	–	26.8	13.4	23.2
10	17 19 10.33	+57 49 48.0	0.37	208.7	135.9	96.1	–	237.9	1118.6	124.3	731.8
11	17 19 11.75	+57 47 20.9	2.44	–	11.4	–	–	11.0	22.4	11.2	–
12	17 19 19.62	+57 59 42.2	0.39	117.7	153.2	94.4	34.4	97.9	894.6	68.8	586.6
13	17 19 20.17	+57 54 01.5	1.30	11.1	37.6	–	–	–	66.4	22.1	53.9
14	17 19 21.71	+57 49 43.8	0.33	418.1	463.0	48.8	–	483.9	1806.6	225.8	1265.4
15	17 19 24.84	+57 44 52.0	0.54	74.2	86.0	51.7	12.1	111.9	392.9	49.1	265.6
16	17 19 25.98	+57 50 19.1	1.39	17.5	13.2	–	–	11.6	42.2	14.1	14.5
17	17 19 26.14	+58 00 57.3	1.90	41.0	–	47.5	–	–	88.5	44.3	–
18	17 19 28.02	+57 43 12.6	0.72	–	–	–	–	–	107.5	26.9	89.4
19	17 19 29.56	+57 49 36.4	1.88	16.5	–	–	–	–	16.5	16.5	15.9
20	17 19 34.35	+57 58 50.1	0.17	–	–	–	–	1867.0	6192.5	688.1	6772.6
21	17 19 36.65	+57 49 00.2	0.78	48.0	42.0	–	–	–	9–	45.0	84.3
22	17 19 37.01	+57 46 58.7	0.66	72.6	45.6	65.8	16.8	62.3	279.8	46.6	181.6
23	17 19 45.43	+57 52 56.9	0.56	63.4	55.9	35.0	–	–	288.4	32.0	204.2
24	17 19 53.96	+57 59 50.8	0.36	157.6	139.6	132.5	–	8–	1013.0	72.4	696.1
25	17 19 56.21	+58 05 27.1	1.16	11.1	18.1	12.4	–	–	41.6	13.9	18.3
26	17 19 57.05	+57 46 17.8	0.64	54.1	88.7	–	–	105.3	310.6	51.8	207.0
27	17 19 57.76	+57 50 06.2	0.88	264.9	245.6	184.2	48.7	242.7	1124.6	140.6	–
28	17 20 02.29	+57 55 44.3	0.97	22.7	–	–	–	20.9	43.6	21.8	15.5
29	17 20 08.31	+57 58 20.4	1.07	–	–	12.0	–	15.4	65.8	16.5	46.5
30	17 20 10.16	+57 54 06.5	1.52	–	26.7	–	–	–	26.7	26.7	16.6
31	17 20 13.92	+57 50 52.4	2.20	–	13.5	10.9	–	12.0	47.8	11.9	19.6
32	17 20 14.67	+57 46 06.5	1.83	–	14.6	–	–	–	14.6	14.6	17.2
33	17 20 17.96	+57 51 04.4	0.66	19.4	32.4	163.7	731.3	11.8	1846.1	167.8	557.4
34	17 20 21.20	+57 43 59.3	2.69	14.8	14.9	–	–	–	40.5	13.5	26.8
35	17 20 21.88	+57 58 26.5	0.04	41019.3	42556.3	27957.5	7013.6	61828.7	264438.0	17629.2	186914.7
36	17 20 21.70	+57 43 27.6	0.71	37.9	38.4	29.8	–	79.3	202.0	40.4	168.2
37	17 20 23.57	+57 50 09.1	2.22	–	12.8	–	–	–	12.8	12.8	17.3

Continued in the next page

Continued from the previous page

ID	RA(J2000)	Dec(J2000)	r1σ()	pn-OBS1	pn-OBS2	pn-OBS3	pn-OBS4	pn-OBS5	Sum-of-ML	Epics-Ave	Mosaic-ML
38	17 20 25.77	+57 52 41.3	1.77	–	–	–	–	13.0	13.0	13.0	1–
39	17 20 25.64	+57 53 04.4	0.65	42.5	28.4	3–	–	44.6	182.9	30.5	166.1
40	17 20 28.33	+57 56 23.3	0.63	36.0	26.3	23.4	–	–	108.1	21.6	71.3
41	17 20 32.86	+58 07 16.0	1.85	–	–	–	–	26.8	26.8	26.8	21.4
42	17 20 33.08	+58 06 13.7	2.03	–	22.6	–	–	–	40.8	20.4	42.9
43	17 20 33.62	+58 08 29.7	0.23	6312.3	4327.5	2013.4	–	–	18031.1	2003.5	12944.7
44	17 20 37.10	+57 48 56.3	0.33	–	240.5	201.5	56.0	401.1	1878.9	156.6	1247.9
45	17 20 37.62	+58 02 12.4	0.11	3704.2	7978.2	3141.1	72–	2645.9	28610.4	2043.6	21553.7
46	17 20 38.45	+57 45 45.4	1.22	–	10.4	11.3	–	–	21.7	10.8	24.9
47	17 20 39.66	+57 56 48.8	1.62	–	–	–	–	12.9	12.9	12.9	–
48	17 20 43.08	+57 54 43.2	0.35	167.5	221.4	110.6	21.7	96.8	1167.9	83.4	759.0
49	17 20 47.27	+57 53 20.6	0.64	49.6	32.1	21.9	13.8	43.1	218.0	27.3	151.8
50	17 20 51.94	+57 41 59.0	0.41	226.1	131.0	118.8	45.8	397.5	1344.3	122.2	977.3
51	17 20 52.28	+57 55 13.2	0.17	1570.4	1689.2	1210.2	406.1	931.6	9658.4	643.9	6857.3
52	17 20 52.50	+58 04 51.1	1.05	–	–	12.7	–	–	12.7	12.7	15.3
53	17 20 56.35	+57 47 41.7	1.01	–	–	–	–	–	–	–	13.6
54	17 21 00.45	+57 51 53.5	0.66	19.9	38.7	37.9	–	34.7	141.3	28.3	117.8
55	17 21 04.38	+57 41 06.0	0.83	46.9	58.4	43.8	–	48.5	197.7	49.4	122.3
56	17 21 05.04	+57 53 38.2	2.07	–	–	–	15.8	–	41.3	13.8	89.6
57	17 21 12.02	+57 50 01.5	0.80	26.6	–	–	–	16.3	55.1	18.4	75.8
58	17 21 13.06	+57 56 15.2	0.87	17.0	22.3	15.2	–	–	66.7	16.7	37.9
59	17 21 16.66	+58 01 16.5	1.95	–	31.3	15.8	–	–	47.2	23.6	32.0
60	17 21 22.92	+57 50 29.2	0.61	96.1	90.6	39.6	11.6	29.9	291.5	48.6	193.8
61	17 21 24.66	+57 52 53.6	2.23	–	–	–	12.0	–	12.0	12.0	–
62	17 21 29.13	+57 47 08.9	1.80	21.5	11.3	–	–	–	32.8	16.4	–
63	17 21 36.11	+58 03 02.2	1.77	19.7	17.0	–	–	–	36.8	18.4	–
64	17 21 39.51	+58 01 45.2	0.87	22.7	–	–	–	18.4	41.1	20.5	55.9
65	17 21 40.60	+58 02 44.8	1.63	43.1	18.1	–	–	–	61.2	30.6	–
66	17 21 41.08	+57 45 53.2	1.61	11.1	–	–	–	–	11.1	11.1	18.6
67	17 21 41.40	+57 52 35.2	0.66	7–	–	38.8	17.0	123.0	306.6	43.8	247.8
68	17 21 48.46	+57 58 03.2	0.72	33.0	37.3	52.4	–	51.1	245.0	35.0	198.6
69	17 21 58.32	+57 49 22.7	0.11	–	–	–	428.6	7784.8	8213.4	4106.7	37602.1
70	17 22 11.69	+57 56 51.1	1.88	23.1	26.3	–	–	32.9	82.2	27.4	34.4

PN-OBS* : The ML of the source in EPIC-pn in different observation.
Sum-of-ML: The summation of ML of sources in all EPICs of all observation.
Epics-Ave: The average of ML of source in all observation.
Mosaic-ML: ML of the sources in mosaic image.

Table 12.2: 0.2–4.5 keV flux of sources detected in OBS 1 and 2 for all EPICs

ID	OBS1			OBS2		
ID	MOS1	MOS2	PN	MOS1	MOS2	PN
1	G	<2.88e-14	<2.51e-14	<2.90e-14	<2.79e-14	<2.75e-14
2	G	<3.09e-14	<2.80e-14	<3.24e-14	<2.92e-14	<3.68e-14
3	G	<2.79e-14	(1.15 ± 0.32)e-14	G	<2.67e-14	(6.33 ± 2.00)e-15
4	N	<2.73e-14	(5.79 ± 2.21)e-15	G	<3.04e-14	(3.22 ± 1.44)e-15
5	N	<2.58e-14	<2.31e-14	G	<2.46e-14	$<(9.26 \pm 2.54)$e-15
6	G	(4.29 ± 0.84)e-14	(3.81 ± 0.46)e-14	G	$(4.32 \pm 0.73)e-14$	(5.21 ± 0.52)e-14
7	G	(5.10 ± 0.87)e-14	N	G	(3.61 ± 0.70)e-14	N
8	N	(2.22 ± 0.60)e-14	(3.12 ± 0.44)e-14	N	(4.99 ± 0.77)e-14	G
9	<2.40e-14	<2.35e-14	<2.22e-14	G	(1.30 ± 0.41)e-14	(7.43 ± 2.19)e-15
10	N	(6.41 ± 0.93)e-14	(4.84 ± 0.55)e-14	N	(3.72 ± 0.67)e-14	(3.82 ± 0.49)e-14
11	N	<2.86e-14	<2.60e-14	N	<2.72e-14	(4.04 ± 1.39)e-15
12	(3.30 ± 0.66)e-14	(3.48 ± 0.68)e-14	(3.21 ± 0.44)e-14	$(3.94 \pm 0.72)e-14$	(3.73 ± 0.72)e-14	(3.62 ± 0.45)e-14
13	G	(1.22 ± 0.36)e-14	(7.53 ± 2.21)e-15	G	<1.95e-14	(9.66 ± 2.08)e-15
14	N	(4.53 ± 0.66)e-14	(4.68 ± 0.42)e-14	N	(4.08 ± 0.64)e-14	(5.04 ± 0.46)e-14
15	N	<3.27e-14	(2.49 ± 0.43)e-14	N	(2.64 ± 0.70)e-14	(2.49 ± 0.43)e-14
16	N	<2.08e-14	(3.09 ± 1.10)e-15	N	<2.11e-14	(3.91 ± 1.53)e-15
17	<2.31e-14	<2.48e-14	(3.64 ± 1.83)e-15	2.21e-14	2.37e-14	1.96e-14
18	N	(2.88 ± 0.75)e-14	N	N	(3.89 ± 0.91)e-14	N
19	N	<2.12e-14	(8.66 ± 2.47)e-15	N	<2.14e-14	<1.93e-14
20	G	(1.32 ± 0.10)e-13	G	(1.22 ± 0.09)e-13	(1.48 ± 0.10)e-13	G
21	N	G	(1.19 ± 0.24)e-14	N	<1.99e-14	(9.71 ± 2.28)e-15
22	N	<2.55e-14	(2.00 ± 0.37)e-14	N	<2.43e-14	(8.77 ± 2.31)e-15
23	(4.90 ± 2.03)e-15	(1.23 ± 0.33)e-14	(1.23 ± 0.23)e-14	(1.34 ± 0.32)e-14	(1.14 ± 0.29)e-14	(8.44 ± 1.65)e-15
24	(5.06 ± 0.84)e-14	(4.49 ± 0.70)e-14	(3.13 ± 0.40)e-14	(2.43 ± 0.62)e-14	(1.81 ± 0.46)e-14	(2.82 ± 0.36)e-14
25	<2.88e-14	<3.25e-14	$(1.11 \pm 0.33)e-14$	<2.76e-14	<3.08e-14	(9.45 ± 2.38)e-15
26	N	(1.99 ± 0.47)e-14	$(2.20 \pm 0.39)e-14$	N	<2.44e-14	(1.95 ± 0.33)e-14
27	G	<1.84e-14	(1.03 ± 0.14)e-14	(1.13 ± 0.36)e-14	(1.06 ± 0.24)e-14	(9.75 ± 1.41)e-15
28	<1.55e-14	<1.59e-14	(5.09 ± 1.58)e-15	<1.48e-14	<1.52e-14	<1.32e-14
29	G	<1.86e-14	G	(1.26 ± 0.33)e-14	$(9.30 \pm 2.47)e-15$	G
30	<1.58e-14	<1.54e-14	<1.42e-14	1.51e-14	1.47e-14	(7.43 ± 1.80)e-15
31	<1.88e-14	<1.74e-14	<1.56e-14	1.80e-14	1.67e-14	$(3.87 \pm 1.44)e-15$
32	<2.84e-14	<2.64e-14	<2.30e-14	N	G	(6.91 ± 2.36)e-15
33	<1.88e-14	<1.74e-14	(3.24 ± 0.97)e-15	<1.79e-14	<1.66e-14	(4.68 ± 0.99)e-15
34	<3.60e-14	<3.35e-14	(1.13 ± 0.38)e-14	<3.45e-14	(1.96 ± 0.64)e-14	(1.49 ± 0.40)e-14
35	(8.20 ± 0.19)e-13	(8.77 ± 0.20)e-13	(9.15 ± 0.11)e-13	(8.12 ± 0.19)e-13	(8.70 ± 0.20)e-13	(9.37 ± 0.11)e-13
36	<3.83e-14	<3.55e-14	(2.49 ± 0.51)e-14	<3.66e-14	(1.19 ± 0.38)e-14	(1.34 ± 0.32)e-14
37	<2.04e-14	<1.89e-14	<1.74e-14	<1.97e-14	<1.80e-14	(7.98 ± 2.26)e-15
38	<1.77e-14	<1.68e-14	<1.57e-14	<1.69e-14	<1.61e-14	<1.58e-14
39	<1.74e-14	<1.67e-14	(5.25 ± 1.33)e-15	(6.02 ± 2.41)e-15	<1.59e-14	$(4.49 \pm 1.17)e-15$
40	<1.73e-14	(6.51 ± 2.76)e-15	(7.83 ± 1.76)e-15	<1.61e-14	<1.75e-14	(8.31 ± 2.00)e-15
41	N	<4.08e-14	<3.24e-14	G	<3.87e-14	<3.24e-14
42	<3.36e-14	<3.74e-14	G	<3.18e-14	<3.59e-14	(1.53 ± 0.39)e-14

Continued to the next page

Continued from the previous page

ID	OBS1			OBS2		
ID	MOS1	MOS2	PN	MOS1	MOS2	PN
43	N	(6.77 ± 0.35)e-13	(5.42 ± 0.16)e-13	N	(4.50 ± 0.28)e-13	(4.08 ± 0.14)e-13
44	(5.64 ± 0.76)e-14	(6.79 ± 0.84)e-14	G	(4.56 ± 0.68)e-14	(5.67 ± 0.75)e-14	(3.96 ± 0.54)e-14
45	(2.26 ± 0.13)e-13	(2.23 ± 0.13)e-13	(1.98 ± 0.07)e-13	(3.89 ± 0.17)e-13	(4.07 ± 0.19)e-13	(3.78 ± 0.09)e-13
46	<3.28e-14	<3.09e-14	<2.53e-14	<3.12e-14	<2.96e-14	(5.21 ± 1.87)e-15
47	<1.85e-14	<1.92e-14	<1.86e-14	<1.77e-14	<1.94e-14	<5.01e-14
48	$(3.18 \pm 0.56)e-14$	(3.82 ± 0.61)e-14	(2.66 ± 0.33)e-14	(2.70 ± 0.52)e-14	(2.98 ± 0.5)e-14	(3.36 ± 0.37)e-14
49	<2.06e-14	<2.00e-14	(1.33 ± 0.26)e-14	G	$(1.21 \pm 0.33)e-14$	(8.91 ± 2.17)e-15
50	N	N	(6.52 ± 0.78)e-14	(4.73 ± 1.19)e-14	N	(5.64 ± 0.78)e-14
51	(1.16 ± 0.09)e-13	(1.25 ± 0.10)e-13	(1.14 ± 0.06)e-13	(1.07 ± 0.09)e-13	$(9.54 \pm 0.84)e-14$	(1.14 ± 0.06)e-13
52	<3.33e-14	G	<2.99e-14	<3.20e-14	G	<2.97e-14
53	<3.12e-14	<3.07e-14	<2.50e-14	<2.99e-14	<2.94e-14	<2.99e-14
54	<2.57e-14	<2.50e-14	(7.82 ± 2.48)e-15	<2.46e-14	<2.39e-14	(8.71 ± 2.30)e-15
55	N	N	(2.19 ± 0.52)e-14	N	N	(3.36 ± 0.66)e-14
56	(7.85 ± 2.37)e-15	<2.53e-14	G	<2.47e-14	<2.46e-14	G
57	<3.28e-14	(2.08 ± 0.71)e-14	(1.63 ± 0.41)e-14	<3.14e-14	G	G
58	G	G	(8.13 ± 2.72)e-15	G	G	$(1.33 \pm 0.32)e-14$
59	<3.49e-14	G	<6.17e-14	<3.28e-14	G	(7.23 ± 1.60)e-15
60	<3.67e-14	(3.49 ± 0.86)e-14	(2.77 ± 0.44)e-14	<3.51e-14	<3.42e-14	(6.26 ± 0.94)e-14
61	<3.43e-14	G	G	<3.28e-14	<3.06e-14	<7.14e-14
62	<4.80e-14	<4.38e-14	(3.79 ± 1.41)e-15	G	<4.45e-14	(3.15 ± 1.92)e-15
63	<4.68e-14	<4.87e-14	(7.29 ± 3.00)e-15	<4.53e-14	<4.47e-14	(9.63 ± 3.99)e-15
64	<4.63e-14	<4.80e-14	(1.55 ± 0.47)e-14	<4.48e-14	<4.62e-14	G
65	N	N	$(1.84 \pm 0.45)e-14$	N	N	(1.82 ± 0.52)e-14
66	N	N	(1.88 ± 0.60)e-14	N	N	<4.27e-14
67	(1.71 ± 0.60)e-14	N	$(3.31 \pm 0.70)e-14$	(2.48 ± 0.71)e-14	N	G
68	<4.49e-14	G	(2.54 ± 0.60)e-14	(3.19 ± 0.87)e-14	G	(1.65 ± 0.44)e-14
69	N	N	G	N	N	G
70	N	N	(2.03 ± 0.60)e-14	N	N	(1.53 ± 0.43)e-14

G: Source is located on a gap or damage pixel(s).
N: Source is located outside the FOV.
<: Upper limit for the flux flux of the source. In this case the source is located in the FOV but was not detected by the camera.

Table 12.3: 0.2–4.5 keV flux of sources detected in OBS 3 and 4 for all EPIC – continued of Table 12.2

ID	OBS3			OBS4		
ID	MOS1	MOS2	PN	MOS1	MOS2	PN
1	G	<3.93e-14	<4.84e-14	G	<6.72e-14	<8.18e-14
2	<4.67e-14	<4.43e-14	<9.15e-14	<6.60e-14	<6.92e-14	<1.05e-13
3	<4.21e-14	<3.79e-14	<3.35e-14	G	< 6.44e-14	<8.92e-14
4	<4.27e-14	<3.71e-14	<3.49e-14	<5.76e-14	<6.17e-14	<9.21e-14
5	<4.04e-14	<3.50e-14	<3.31e-14	<5.42e-14	<5.91e-14	<8.63e-14
6	G	$(7.15 \pm 1.22)e-14$	(7.46 ± 3.42)e-14	(8.36 ± 1.53)e-14	<6.83e-14	(6.87 ± 7.54)e-14
7	(2.90 ± 0.80)e-14	(5.28 ± 1.25)e-14	N	7 <6.06e-14	(5.60 ± 1.66)e-14	N
8	N	<4.31e-14	(1.09 ± 1.80)e-14	N	(2.93 ± 0.85)e-14	(4.10 ± 4.07)e-14
9	G	<3.18e-14	<2.72e-14	<4.19e-14	<5.45e-14	<7.49e-14
10	N	(5.19 ± 0.93)e-14	(5.03 ± 2.93)e-14	N	<5.65e-14	<8.41e-14
11	N	<4.07e-14	<3.60e-14	N	<6.30e-14	<9.41e-14
12	G	(5.27 ± 1.04)e-14	$(4.38 \pm 2.15)e-14$	(3.56 ± 0.98)e-14	<5.63e-14	(4.22 ± 7.13)e-14
13	<3.65e-14	<2.96e-14	<2.40e-14	<3.93e-14	<4.64e-14	<6.20e-14
14	N	$4.57 \pm 0.82)$e-14	(2.33 ± 1.57)e-14	N	G	
15	N	$(3.09 \pm 0.89)e-14$	(2.62 ± 3.03)e-14	N	<6.91e-14	(1.72 ± 8.92)e-14
16	N	<3.06e-14	<3.99e-14	N	<6.32e-14	<7.65e-14
17	<3.33e-14	<3.60e-14	(6.93 ± 1.57)e-15	<4.07e-14	<5.84e-14	<6.68e-14
18	N	(1.97 ± 0.72)e-14	N	N	<7.86e-14	N
19	N	<3.05e-14	<2.63e-14	N	G	<9.45e-14
20	(1.40 ± 0.12)e-13	G	G	(1.33 ± 0.13)e-13	(1.31 ± 0.15)e-13	<6.26e-14
21	N	<3.00e-14	<5.47e-14	N	G	<7.04e-14
22	N	(2.09 ± 0.63)e-14	(1.82 ± 1.81)e-14	N	<5.43e-14	(2.47 ± 2.37)e-14
23	<2.55e-14	<2.45e-14	(1.03 ± 0.48)e-14	(1.43 ± 0.47)e-14	<3.84e-14	G
24	(3.62 ± 0.78)e-14	(3.15 ± 0.68)e-14 6.88e-15	(4.39 ± 1.94)e-14	(3.01 ± 0.81)e-14	$(2.97 \pm 0.91)e-14$	<6.53e-14
25	<3.99e-14	<4.38e-14	(1.71 ± 1.34)e-14	<5.21e-14	<7.63e-14	<8.84e-14
26	N	<3.68e-14	G	N	$(2.84 \pm 1.10)e-14$	1.02e-13
27	G	(1.81 ± 0.42)e-14	(9.51 ± 5.20)e-15	<3.49e-14	<4.08e-14	(1.11 ± 2.59)e-14
28	< 2.26e-14	<2.31e-14	<1.81e-14	<2.72e-14	<3.63e-14	<5.11e-14
29	<2.43e-14	<2.60e-14	(1.48 ± 1.63)e-14	G	<4.39e-14	<6.01e-14
30	<2.30e-14	<2.23e-14	<1.98e-14	<2.94e-14	<3.49e-14	<5.00e-14
31	<2.75e-14	(9.34 ± 3.25)e-15	(4.66 ± 7.87)e-15	<3.73e-14	<3.88e-14	G
32	N	G	<3.15e-14	N	<5.78e-14	<7.08e-14
33	(3.13 ± 0.66)e-14	(2.40 ± 0.52)e-14	(2.69 ± 1.05)e-14	(1.44 ± 0.13)e-13	(1.33 ± 0.14)e-13	(2.39 ± 0.37)e-13
34	<5.20e-14	<4.81e-14	<3.96e-14	N	<7.30e-14	<9.15e-14
35	(7.09 ± 0.21)e-13	(7.61 ± 0.23)e-13	(9.23 ± 0.19)e-13	(9.01 ± 0.30)e-13	(9.56 ± 0.36)e-13	(1.09 ± 0.04)e-12
36	<5.54e-14	<5.09e-14	(1.13 ± 4.97)e-14	N	<7.68e-14	<9.77e-14
37	<3.01e-14	<2.72e-14	<2.51e-14	<3.82e-14	<4.19e-14	G
38	<2.59e-14	<2.43e-14	<2.20e-14	<3.31e-14	<3.79e-14	<5.70e-14
39	<2.54e-14	<2.42e-14	(4.82 ± 4.27)e-15	<3.26e-14	<3.74e-14	<5.66e-14
40	<2.47e-14	<2.52e-14	(6.70 ± 8.29)e-15	<3.21e-14	G	<5.67e-14
41	<5.44e-14	<5.54e-14	<4.69e-14	<7.74e-14	<1.06e-13	G
42	(2.95 ± 0.93)e-14	<4.79e-14	<4.11e-14	<7.01e-14	<8.75e-14	<1.19e-13

Continued to the next page

Continued from the previous page

ID	OBS3			OBS4		
ID	MOS1	MOS2	PN	MOS1	MOS2	PN
43	(1.20 ± 0.18)e-13	N	(3.37 ± 0.53)e-13	(5.46 ± 0.42)e-13	(5.90 ± 0.62)e-13	G
44	(2.20 ± 0.58)e-14	(4.39 ± 0.90)e-14	$(3.79 \pm 2.76)e-14$	G	G	(3.84 ± 4.60)e-14
45	(2.46 ± 0.17)e-13	(2.28 ± 0.16)e-13	(2.40 ± 0.23)e-13	(2.69 ± 0.20)e-13	(2.08 ± 0.22)e-13	(2.32 ± 0.56)e-13
46	<4.78e-14	G	(1.70 ± 2.14)e-14	<5.59e-14	G	<8.04e-14
47	<2.71e-14	<2.81e-14	G	<3.55e-14	<3.61e-14	G
48	(2.53 ± 0.56)e-14	(4.14 ± 0.75)e-14	(3.47 ± 1.91)e-14	G	(3.71 ± 0.97)e-14	(3.41 ± 1.97)e-14
49	G	<2.90e-14	(1.10 ± 1.37)e-14	<3.90e-14	<4.49e-14	(1.13 ± 2.33)e-14
50	(6.46 ± 2.02)e-14	N	(8.49 ± 6.53)e-14	(9.37 ± 2.46)e-14	(8.20 ± 2.49)e-14	(9.71 ± 11.1)e-14
51	(1.07 ± 0.11)e-13	(9.85 ± 1.11)e-14	(1.35 ± 0.24)e-13	(1.33 ± 0.14)e-13	(1.17 ± 0.11)e-13	(1.49 ± 0.55)e-13
52	<5.04e-14	<4.76e-14	(8.72 ± 31.3)e-15	<6.27e-14	<8.50e-14	<1.01e-13
53	<4.04e-14	<3.89e-14	<4.66e-14	<5.47e-14	<6.76e-14	<8.99e-14
54	$(1.60 \pm 0.57)e-14$	<3.43e-14	(1.07 ± 1.87)e-14	G	<5.57e-14	<7.93e-14
55	N 0	N	(3.06 ± 5.06)e-14	N	N	1.61e-13
56	<3.78e-14	(1.02 ± 0.36)e-14	G	<4.87e-14	<5.70e-14	(3.86 ± 1.97)e-14
57	<4.84e-14	<4.05e-14	<7.25e-14	<5.59e-14	<7.03e-14	<9.38e-14
58	<4.14e-14	(1.34 ± 0.46)e-14	(7.85 ± 11.7)e-15	<5.43e-14	G	<9.74e-14
59	<4.75e-14	G	(6.12 ± 23.7)e-15	<6.23e-14	<6.78e-14	G
60	<5.41e-14	<4.87e-14	(2.06 ± 2.86)e-14	G	<8.00e-14	(1.83 ± 4.41)e-14
61	<5.10e-14	G	G	<6.54e-14	<7.68e-14	(7.87 ± 4.96)e-15
62	<6.21e-14	<5.89e-14	<5.04e-14	<8.29e-14	<1.03e-13	<1.19e-13
63	<6.13e-14	<6.66e-14	< 5.45e-14	N	<9.48e-14	<1.51e-13
64	N	<6.52e-14	<5.31e-14	N	<9.31e-14	<1.47e-13
65	N	N	G	N	N	<1.58e-13
66	N	N	<6.14e-14	N	N	<1.41e-13
67	$(2.85 \pm 0.83)e-14$	5.97e-14	$(2.25 \pm 1.03)e-14$	<8.50e-14	<9.89e-14	(4.43 ± 11.7)e-14
68	<6.19e-14	(2.53 ± 0.85)e-14	(2.66 ± 2.85)e-14	<8.75e-14	<9.25e-14	<1.21e-13
69	N	N	G	N	N	(4.68 ± 2.27)e-13
70	N	N	<5.88e-14	N	N	N

G: Source is located on a gap or damage pixel(s).
N: Source is located outside the FOV.
<: Upper limit for the flux flux of the source. In this case the source is located in the FOV but was not detected by the camera.

Table 12.4: 0.2–4.5 keV flux of sources detected in OBS 5 for all EPIC – continued of Table 12.2

ID	MOS1	MOS2	PN
1	G	<2.83e-14	<2.54e-14
2	<3.09e-14	<2.92e-14	G
3	G	<2.72e-14	(7.99 ± 2.38)e-15
4	G	<2.61e-14	<2.40e-14
5	$(1.82 \pm 0.50)e-14$	G	(1.22 ± 0.23)e-14
6	(4.31 ± 0.73)e-14	(4.56 ± 0.77)e-14	$(4.37 \pm 0.48)e-14$
7	(2.38 ± 0.61)e-14	N	$(2.54 \pm 0.44)e-14$
8	(4.17 ± 0.79)e-14	(2.84 ± 0.67)e-14	(3.73 ± 0.52)e-14
9	G	<2.33e-14	<2.01e-14
10	$(5.03 \pm 0.90)e-14$	(6.25 ± 0.89)e-14	(5.96 ± 0.69)e-14
11	N	<2.65e-14	(7.79 ± 2.90)e-15
12	(2.77 ± 0.60)e-14	(3.27 ± 0.68)e-14	(2.48 ± 0.38)e-14
13	G	<1.97e-14	G
14	N	(5.45 ± 0.76)e-14	$(5.02 \pm 0.44)e-14$
15	N	(1.65 ± 0.50)e-14	(2.79 ± 0.43)e-14
16	N	<2.10e-14	(2.24 ± 8.96)e-15
17	<2.25e-14	<2.48e-14	<2.06e-14
18	N	(2.80 ± 0.60)e-14	N
19	N	<2.00e-14	G
20	(1.06 ± 0.83)e-13	(1.20 ± 0.98)e-13	(8.90 ± 0.44)e-14
21	N	<1.98e-14	G
22	N	<2.27e-14	(1.24 ± 0.27)e-14
23	<1.63e-14	(9.00 ± 2.71)e-15	G
24	(2.50 ± 0.50)e-14	(2.26 ± 0.5)e-14	(2.10 ± 0.33)e-14
25	<2.87e-14	<3.26e-14	<2.60e-14
26	N	(1.53 ± 0.44)e-14	(1.92 ± 0.30)e-14 3.06e-15
27	1.84e-14	G	(8.92 ± 1.62)e-15
28	<1.47e-14	<1.53e-14	(4.59 ± 1.45)e-15
29	G	<1.79e-14	(4.50 ± 1.28)e-15
30	<1.48e-14	<1.46e-14	<1.44e-14
31	<1.74e-14	<1.62e-14	(2.70 ± 0.95)e-15
32	N	<2.38e-14	<2.65e-14
33	(8.48 ± 2.62)e-15	(1.13 ± 0.28)e-14	(4.94 ± 2.25)e-15
34	N	<2.97e-14	<2.70e-14
35	(1.31 ± 0.02)e-12	$(1.16 \pm 0.02)e-12$	(1.39 ± 0.01)e-12
36	N	<3.13e-14	(2.96 ± 0.47)e-14
37	<1.89e-14	<1.74e-14	<1.73e-14
38	<1.65e-14	<1.57e-14	(7.18 ± 2.07)e-15
39	<1.64e-14	$(7.57 \pm 2.21)e-15$	(7.21 ± 1.91)e-15
40	<1.62e-14	(1.11 ± 0.35)e-14	G
41	<3.74e-14	<4.07e-14	(1.18 ± 0.40)e-14
42	<3.44e-14	<3.74e-14	G
43	(5.90 ± 0.33)e-13	G	N
44	(3.81 ± 0.64)e-14	(3.39 ± 0.50)e-14	(3.54 ± 0.36)e-14
45	(1.65 ± 0.10)e-13	G	(1.46 ± 0.05)e-13

Continued to the next page

Continued from the previous page

ID	MOS1	MOS2	PN
46	<2.96e-14	<2.72e-14	<4.52e-14
47	<1.83e-14	<1.86e-14	(7.23 ± 2.08)e-15
48	(2.25 ± 0.46)e-14	(2.42 ± 0.50)e-14	(2.73 ± 0.42)e-14
49	(9.96 ± 3.27)e-15	(1.42 ± 0.36)e-14	$1.04 \pm 0,22)$e-14
50	(1.15 ± 0.17)e-13	(1.30 ± 0.16)e-13	(1.01 ± 0.09)e-13
51	(1.04 ± 0.09)e-13	$(1.07 \pm 0.10)e - 13$	(1.01 ± 0.07)e-13
52	<3.44e-14	<3.38e-14	<5.07e-14
53	<2.90e-14	<2.75e-14	<2.39e-14
54	<2.33e-14	<2.29e-14	(7.77 ± 1.91)e-15
55	N	N	(2.76 ± 0.60)e-14
56	<2.43e-14	<2.35e-14	G
57	<3.00e-14	<2.89e-14	(6.60 ± 2.16)e-15
58	<2.72e-14	<2.69e-14	<2.39e-14
59	N	N	N
60	<3.68e-14	<3.29e-14	(1.15 ± 0.31)e-14
61	<3.30e-14	<3.18e-14	G
62	<4.42e-14	<4.26e-14	<3.45e-14
63	N	N	<3.98e-14
64	<4.73e-14	<4.79e-14	$(2.38 \pm 0.68)e - 14$
65	N	N	G
66	N	N	<4.21e-14
67	<4.24e-14	G	(2.89 ± 0.49)e-14
68	(3.26 ± 1.01)e-14	N	(2.11 ± 0.47)e-14
69N	N	(1.64 ± 0.04)e-12	
70	N	N	(2.23 ± 0.55)e-14

G: Source is located on a gap or damage pixel(s).
N: Source is located outside the FOV.
<: Upper limit for the flux flux of the source. In this case the source is located in the FOV but was not detected by the camera.

Table 12.5: The extinction in the direction of the Draco dSph in different optical and inferred bands

Filter name [1]	Eff-λ [2]	A/E(B-V)[3]	A^c(mag)[4]
CTIO U	0.3734	4.107	0.113
CTIO B	0.4309	3.641	0.101
CTIO V	0.5517	2.682	0.074
CTIO R	0.6520	2.119	0.059
CTIO I	0.8007	1.516	0.042
DSS-II g	0.4621	3.381	0.093
DSS-II r	0.6546	2.088	0.058
DSS-II i	0.8111	1.487	0.041
SDSS u	0.3587	4.239	0.117
SDSS g	0.4717	3.303	0.091
SDSS r	0.6165	2.285	0.063
SDSS i	0.7476	1.698	0.047
SDSS z	0.8923	1.263	0.035
UKIRT J	1.248	0.709	0.020
UKIRT H	1.659	0.449	0.012
UKIRT K	2.190	0.302	0.008
2MASS J	1.23	0.723	0.020
2MASS H	1.64	0.460	0.013
2MASS Ks	2.16	0.310	0.009
IRAC-1	3.52	0.178	0.005
IRAC-2	4.46	0.148	0.004
IRAC-3	5.66	0.130	0.004
IRAC-4	7.68	0.122	0.003
WISE-1	3.32	0.189	0.005
WISE-2	4.57	0.146	0.004

1: The name of filter of different optical and infrared surveys.
2: Eff-λ is the effective wavelength of the filter as defined in Schlafly and Finkbeiner (2011).
3: A/E(B-V) is the ratio of band extinction to reddening.
4: A is the band extinction in magnitudes.Extinction law is from Fitzpatrick (1999) and from Indebetouw et al. (2005) for IRAC, WISE.

Reference: This table was extract from online data, available on IPAC infrared since archive: http://irsa.ipac.caltech.edu/

Table 12.6: List of optical counterparts from the SDSS9 catalogue.

ID	Class	SDSS9 ID	g (mag)	r (mag)	i (mag)	$log_{10}(\frac{F_{\rm x}}{F_{\rm opt}})$
1		-	-	-	-	-
2		-	-	-	-	-
3		J171850.16+575453.0	21.74± 0.09	20.86 ± 0.06	21.11 ± 0.14	-0.03 ± 0.21
4	GLX	J171856.97+575102.5	18.10 ± 0.01	16.96 ± 0.01	16.52 ± 0.01	-1.75 ± 0.64
5	GLX	J171900.84+575147.0	20.27 ± 0.02	19.57 ± 0.01	19.18 ± 0.02	-0.21 ± 0.20
6	AGN	J171901.68+580028.9	18.79 ± 0.01	18.67 ± 0.01	18.68 ± 0.01	-0.17 ± 0.04
7	AGN	J171904.16+580329.3	20.35 ± 0.02	20.33 ± 0.02	20.29 ± 0.04	0.07 ± 0.12
8	GLX	J171904.62+574728.1	20.49 ± 0.02	19.55 ± 0.02	19.12 ± 0.02	0.18 ± 0.09
9		-	-	-	-	-
10	GLX	J171910.45+574948.0	18.96 ± 0.01	18.00 ± 0.01	17.45 ± 0.01	0.07 ± 0.03
11		J171910.90+574718.1	23.71 ± 0.2	22.00 ± 0.10	21.67 ± 0.12	0.71 ± 0.58
12	AGN (r)	-	-	-	-	-
13	AGN (r)	J171919.93+575401.3	15.94 ± 0.00	15.11 ± 0.01	14.68 ± 0.01	-2.15 ± 0.17
14	XRB-CAN	J171921.82+574943.7	22.76 ± 0.13	22.48 ± 0.15	21.68 ± 0.12	1.26 ± 0.04
15		-	-	-	-	-
16	FG	J171925.97+575020.1	14.74 ± 0.01	14.52 ± 0.01	12.38 ± 0.01	-3.21 ± 0.27
17		J171925.68+580100.3	19.39 ± 0.01	18.67 ± 0.01	18.37 ± 0.01	-0.79 ± 0.37
18	AGN-CAN	J171928.00+574313.3	20.85 ± 0.03	20.76 ± 0.04	20.42 ± 0.04	0.33 ± 0.18
19		-	-	-	-	-
20	AGN	J171934.41+575849.6	19.34 ± 0.01	19.27 ± 0.01	19.02 ± 0.01	0.29 ± 0.02
21	H	-	-	-	-	-
22		J171936.97+574659.0	22.84 ± 0.14	21.84 ± 0.09	21.35 ± 0.09	0.80 ± 0.10
23		J171945.41+575257.3	22.93 ± 0.18	21.47 ± 0.06	21.56 ± 0.11	0.63 ± 0.07
24	XRB-CAN	J171954.02+575951.3	22.96 ± 0.20	22.27 ± 0.15	21.88 ± 0.16	1.52 ± 0.02
25	H	-	-	-	-	-
26		-	-	-	-	-
27	SYM	J171957.64+575005.7	17.75 ± 0.01	16.47 ± 0.01	16.19 ± 0.01	-1.51 ± 0.10
28	H	-	-	-	-	-
29		-	-	-	-	-
30	H	J172010.50+575404.9	22.45 ± 0.13	23.05 ± 0.29	23.04 ± 0.46	0.22 ± 0.17
31	BS-CAN	J172013.37+575051.9	18.61 ± 0.01	17.74 ± 0.01	17.38 ± 0.01	-1.02 ± 0.13
32		J172015.25+574604.7	22.28 ± 0.10	21.94 ± 0.10	21.77 ± 0.14	0.12 ± 0.44
33	BS-CAN	J172018.01+575105.5	19.48 ± 0.01	17.98 ± 0.01	16.84 ± 0.01	-0.74 ± 0.08
34	AGN-CAN	J172021.04+574401.4	21.56 ± 0.05	21.17 ± 0.05	20.87 ± 0.06	0.72 ± 0.13
35	FG	J172021.83+575827.3	12.80 ± 0.01	12.79± 0.01	11.81 ± 0.01	-1.52 ± 0.01
36	AGN-CAN	J172021.63+574327.0	21.34 ± 0.04	21.14 ± 0.04	20.8± 0.06	0.37 ± 0.11
37	H	J172023.92+575009.9	24.27 ± 0.48	24.50± 0.62	24.19 ± 0.70	1.16 ± 0.24
38	H	-	-	-	-	-
39	FG	J172025.65+575304.4	11.82 ± 0.01	14.19 ± 0.01	11.34 ± 0.01	-4.07 ± 0.14
40		-	-	-	-	-
41	GLX-CAN	J172033.09+580714.9	22.60 ± 0.16	21.80 ± 0.11	20.91 ± 0.08	1.22 ± 0.25
42	GLX-CAN	J172033.71+580612.6	24.12 ± 0.57	22.26 ± 0.17	21.66± 0.16	1.74 ± 0.20
43	AGN	J172033.61+580829.7	17.33 ± 0.01	16.66 ± 0.01	16.24± 0.01	0.12 ± 0.01
44	AGN	J172037.13+574856.3	19.32 ± 0.01	18.64 ± 0.01	18.27 ± 0.01	0.12 ± 0.03
45	FG	J172037.64+580211.9	11.39 ± 0.01	13.95 ± 0.01	12.98 ± 0.01	-2.67 ± 0.01
46		-	-	-	-	-

Continued on the next page

Continued from previous page

ID	Class	SDSS9 ID	g (mag)	r (mag)	i (mag)	$log_{10}(\frac{F_x}{F_{opt}})$
47	H	-	-	-	-	-
48	AGN-CAN	J172043.09+575443.2	20.92 ± 0.03	20.44 ± 0.03	20.21 ± 0.03	0.57 ± 0.03
49	H	-	-	-	-	-
50	AGN-CAN	J172051.91+574159.7	19.84 ± 0.01	19.89 ± 0.02	19.72± 0.02	0.62 ± 0.04
51	AGN (r)	J172052.30+575513.4	20.28± 0.02	19.99 ± 0.02	19.95 ± 0.03	0.77 ± 0.01
52		-	-	-	-	-
53	GLX-CAN	J172056.48+574739.6	24.23 ± 0.58	22.35 ± 0.18	21.14± 0.10	1.31 ± 0.09
54	AGN-CAN	J172100.52+575152.9	21.44 ± 0.05	21.51 ± 0.07	21.52 ± 0.15	0.10 ± 0.15
55	AGN-CAN	J172104.23+574106.2	20.58 ± 0.02	20.73± 0.03	20.56 ± 0.05	0.40 ± 0.13
56		J172104.75+575335.1	15.97 ± 0.01	15.30 ± 0.01	15.03 ± 0.01	-2.13 ± 0.23
57*		J172112.06+575002.0	20.58 ± 0.03	20.88± 0.04	22.80 ± 0.35	-0.03 ± 0.22
58	H	-	-	-	-	-
59	FG	J172116.97+580113.6	11.66 ± 0.01	13.67 ± 0.01	14.55± 0.01	-4.04 ± 0.65
60	AGN	J172122.81+575029.6	18.04 ± 0.01	18.01 ± 0.01	17.81 ± 0.01	-0.59 ± 0.09
61		J172124.61+575253.6	20.35 ± 0.02	19.99 ± 0.02	19.87 ± 0.02	0.21 ± 0.42
62		-	-	-	-	-
63		-	-	-	-	-
64	XRB-CAN	J172139.48+580145.1	23.73 ± 0.30	23.16 ± 0.29	22.20 ± 0.21	1.32 ± 0.30
65	XRB-CAN	-	-	-	-	-
66	GLX-CAN	J172141.18+574555.6	23.12 ±0.23	22.43 ± 0.18	22.52 ±0.33	0.89 ± 0.74
67	AGN-CAN	J172141.43+575235.5	21.53 ± 0.05	21.12 ± 0.06	20.69 ± 0.05	0.51 ± 0.11
68	AGN	J172148.27+575805.3	20.19 ± 0.01	20.09 ± 0.02	19.73 ± 0.02	0.03 ± 0.15
69	FG	J172158.29+574922.5	11.21 ± 0.01	13.03 ± 0.01	10.1 ± 0.01	-1.88 ± 0.02
70	AGN	J172211.64+575652.1	20.50 ± 0.02	20.37± 0.03	20.14± 0.03	0.27 ± 0.18

ID : ID of *XMM-Newton* source.
SDSS9 ID : ID of the optical source according to the SDSS9 catalogue.
Source class : Source class is the same as Table 7.3.
g, r, i :Apparent magnitudes of the counterparts in different optical energy bands of SDSS9. The extinction was applied for the magnitude according to Schlafly and Finkbeiner (2011).
*****: For source No 57 the data is taken from SDSS7 (see Sect. 5.4.4).

Table 12.7: Catalogue of optical counterparts of the INT catalogue

ID	Catalogue-ID	RA(J2000)	Dec(J2000)	I (mag)	V (mag)
1	138035	17 18 46.75	+57 54 46.9	24.31 ± 0.17	22.99 ± 0.11
2	137758	17 18 46.29	+57 54 44.0	23.73 ± 0.10	-
3	138603	17 18 50.15	+57 54 53.0	22.37 ± 0.03	21.92 ± 0.04
4	118407	17 18 56.96	+57 51 02.3	18.56 ± 0.01	17.68 ± 0.01
5	122064	17 19 00.84	+57 51 46.8	19.95 ± 0.01	19.23 ± 0.01
6	168047	17 19 01.70	+58 00 28.9	19.16 ± 0.01	19.03 ± 0.01
7	180217	17 19 04.20	+58 03 29.2	20.48 ± 0.01	20.47 ± 0.01
8	102889	17 19 04.64	+57 47 28.2	20.44 ± 0.01	19.55 ± 0.01
9	143841	17 19 06.79	+57 55 47.2	24.29 ± 0.16	23.61 ± 0.19
10	112873	17 19 10.47	+57 49 47.7	19.21 ± 0.01	18.20 ± 0.01
11	102318	17 19 12.16	+57 47 20.1	22.29 ± 0.03	21.85 ± 0.04
13	133969	17 19 19.91	+57 54 00.6	18.45 ± 0.01	17.27 ± 0.01
14	112603	17 19 21.83	+57 49 43.6	22.50 ± 0.04	21.57 ± 0.03
15	92419	17 19 24.89	+57 44 52.5	22.06 ± 0.02	21.14 ± 0.02
16	115210	17 19 25.92	+57 50 19.8	15.93 ± 0.01	15.66 ± 0.01
18	86525	17 19 28.04	+57 43 13.4	21.07± 0.01	20.55 ± 0.01
19	112040	17 19 29.66	+57 49 35.6	21.86 ± 0.02	22.93 ± 0.10
20	159900	17 19 34.43	+57 58 49.6	19.42 ± 0.01	19.10 ± 0.01
21	109850	17 19 36.65	+57 49 00.2	24.60 ± 0.21	23.77 ± 0.22
22	100830	17 19 37.02	+57 46 59.1	22.15 ± 0.03	21.37 ± 0.03
23	128300	17 19 45.45	+57 52 57.2	21.98 ± 0.02	21.29 ± 0.02
24	165057	17 19 54.05	+57 59 51.1	22.69 ± 0.04	21.68 ± 0.03
27	114149	17 19 57.66	+57 50 05.7	17.28 ± 0.01	16.57 ± 0.01
28	143800	17 20 02.54	+57 55 46.8	22.99 ± 0.05	23.84 ± 0.22
29	157635	17 20 08.50	+57 58 20.5	22.84 ± 0.05	22.38 ± 0.06
30	134301	17 20 10.55	+57 54 05.1	22.47 ± 0.03	22.54 ± 0.07
31	117617	17 20 13.40	+57 50 51.9	18.10 ± 0.01	17.41 ± 0.01
32	97170	17 20 15.30	+57 46 04.8	22.12 ± 0.03	21.71 ± 0.03
33	118675	17 20 18.05	+57 51 05.6	18.66 ± 0.01	16.97 ± 0.01
34	89447	17 20 21.08	+57 44 01.5	21.18 ± 0.01	20.78 ± 0.02
36	87344	17 20 21.68	+57 43 27.1	21.00 ± 0.01	20.68 ± 0.02
37	114557	17 20 24.01	+57 50 11.5	23.82 ± 0.11	-
38	127370	17 20 25.92	+57 52 46.9	-	21.90 ± 0.04
40	147406	17 20 28.60	+57 56 24.9	23.55 ± 0.09	23.16 ± 0.13
41	194897	17 20 33.14	+58 07 15.0	22.25 ± 0.03	21.10 ± 0.02
42	190976	17 20 33.77	+58 06 12.5	23.17 ± 0.06	21.60 ± 0.03
43	199382	17 20 33.69	+58 08 29.5	18.06 ± 0.01	17.28 ± 0.01
44	109521	17 20 37.18	+57 48 56.5	19.49 ± 0.01	18.79 ± 0.01
47	149827	17 20 39.14	+57 56 51.2	23.65 ± 0.09	23.70 ± 0.20
48	137694	17 20 43.10	+57 54 43.4	20.84 ± 0.01	20.46 ± 0.02
49	130626	17 20 47.15	+57 53 23.1	23.77 ± 0.10	22.88 ± 0.09
50	82425	17 20 51.96	+57 41 59.9	19.96 ± 0.01	19.71 ± 0.01
51	140628	17 20 52.32	+57 55 13.5	19.91 ± 0.01	19.87 ± 0.01
52	185592	17 20 52.56	+58 04 51.3	23.17± 0.06	22.53 ± 0.01
53	103674	17 20 56.46	+57 47 39.9	23.10 ± 0.05	21.26± 0.02
54	122627	17 21 00.55	+57 51 53.1	21.18 ± 0.01	21.19 ± 0.02

Continued in the next page

Continued from previous page

ID	Catalogue-ID	RA(J2000)	Dec(J2000)	I (mag)	V (mag)
55	79410	17 21 04.27	+57 41 06.4	21.10 ± 0.01	20.65 ± 0.02
56	131756	17 21 04.76	+57 53 35.2	16.22 ± 0.01	15.94 ± 0.01
57	113881	17 21 12.10	+57 50 02.2	20.94 ± 0.01	-
58	146787	17 21 13.08	+57 56 18.2	23.25 ± 0.06	23.88 ± 0.23
60	115947	17 21 22.84	+57 50 29.8	18.22 ± 0.01	17.92 ± 0.01
61	127975	17 21 24.63	+57 52 53.8	20.17 ± 0.01	19.84 ± 0.01
63	178117	17 21 35.89	+58 02 57.1	23.91 ± 0.12	22.99 ± 0.11
64	173256	17 21 39.52	+58 01 44.9	23.64 ± 0.09	22.13 ± 0.05
67	126303	17 21 41.45	+57 52 35.7	21.52 ± 0.01	20.87 ± 0.02
68	156404	17 21 48.28	+57 58 05.6	20.24 ± 0.01	19.75 ± 0.02
70	149930	17 22 11.67	+57 56 52.3	20.60 ± 0.01	20.18 ± 0.01

Continued in the next page

ID : The ID of *XMM-Newton* source.
RA, Dec : The position of the optical source.
catalogue ID : The ID of the optical source in the INT catalogue.
I, V : Magnitudes of the counterpart in different optical energy bands of the INT. The extinction was applied for the magnitudes according to Table 12.5.
$\star$: In some energy bands the magnitude has been not reported in the optical catalogue.

Table 12.8: Catalogue of optical counterpart of the MegaCam catalogue

ID	Cataloge-ID	RA(J2000)	Dec (J2000)	g (mag)	r (mag)	i (mag)
1	617733	17 18 46.28	+57 54 43.6	23.86 ± 0.04	23.83 ± 0.08	23.78 ± 0.11
2	571040	17 18 48.27	+57 50 15.6	23.88 ± 0.04	-	-
3	619624	17 18 50.15	+57 54 52.7	22.32 ± 0.01	22.02 ± 0.02	21.78 ± 0.02
4	578735	17 18 56.97	+57 51 02.4	19.22 ± 0.01	18.30 ± 0.01	17.79 ± 0.01
5	586523	17 19 00.85	+57 51 46.9	20.38 ± 0.01	19.74 ± 0.01	19.29 ± 0.01
6	692999	17 19 01.71	+58 00 28.8	19.47 ± 0.01	19.38 ± 0.01	19.26 ± 0.01
7	720529	17 19 04.19	+58 03 29.2	20.69 ± 0.01	20.71 ± 0.01	20.64 ± 0.01
8	544220	17 19 04.62	+57 47 28.1	20.73 ± 0.01	20.04 ± 0.01	19.63 ± 0.01
9	631655	17 19 06.78	+57 55 47.3	24.57 ± 0.07	23.89 ± 0.09	23.40 ± 0.08
10	566425	17 19 10.47	+57 49 47.8	19.80 ± 0.01	18.98 ±0.01	18.38 ± 0.01
11	542974	17 19 12.13	+57 47 19.9	22.53 ± 0.01	22.23 ± 0.02	21.95 ± 0.02
12	683999	17 19 19.63	+57 59 41.8	24.06 ± 0.05	-	23.37 ± 0.065
13	609607	17 19 19.92	+57 54 00.7	19.09 ± 0.01	18.14 ± 0.01	17.44 ± 0.01
14	565744	17 19 21.82	+57 49 43.6	23.06 ± 0.02	22.56 ± 0.03	21.95 ± 0.02
15	529878	17 19 24.84	+57 44 52.1	22.20 ± 0.01	21.77 ± 0.02	21.13 ± 0.01
16	571741	17 19 25.99	+57 50 19.7	13.24 ± 0.01	12.62 ± 0.01	-
17	698097	17 19 25.69	+58 01 00.1	19.30 ± 0.01	18.70 ± 0.01	18.35 ± 0.01
18	517936	17 19 27.99	+57 43 13.1	21.72 ± 0.01	21.42 ± 0.01	21.11 ± 0.01
19	564460	17 19 29.61	+57 49 35.4	23.20 ± 0.02	23.48 ± 0.06	22.98 ± 0.05
20	672692	17 19 34.43	+57 58 49.4	19.27 ± 0.01	19.25 ± 0.01	19.02 ± 0.01
21	558833	17 19 36.62	+57 49 00.0	23.82 ± 0.03	23.28 ± 0.05	22.94 ± 0.05
22	539738	17 19 36.99	+57 46 58.9	22.55 ± 0.02	22.10 ± 0.02	21.44 ± 0.02
23	598631	17 19 45.43	+57 52 57.0	22.54 ± 0.02	21.35 ± 0.01	21.14 ± 0.01
24	685825	17 19 54.04	+57 59 50.9	23.18 ± 0.02	22.28 ± 0.02	21.74 ± 0.02
25	737221	17 19 56.35	+58 05 26.0	25.29 ± 0.14	-	24.49 ± 0.174
27	569394	17 19 57.64	+57 50 05.5	17.78 ± 0.01	16.61 ± 0.01	16.24 ± 0.01
28	631508	17 20 02.53	+57 55 46.6	23.40 ± 0.03	22.90 ± 0.04	22.82 ± 0.04
29	666428	17 20 08.48	+57 58 20.2	23.05 ± 0.02	22.89 ± 0.04	22.53 ± 0.03
30	610274	17 20 10.54	+57 54 04.8	22.53 ± 0.02	22.57 ± 0.03	22.62 ± 0.04
31	576943	17 20 13.37	+57 50 51.8	18.48 ± 0.01	17.75 ± 0.01	17.36 ± 0.01
33	579292	17 20 18.01	+57 51 05.5	19.26 ± 0.01	18.03 ± 0.01	16.76 ± 0.01
34	524268	17 20 21.04	+57 44 01.2	21.26 ± 0.01	21.01 ± 0.01	20.76 ± 0.01
36	519804	17 20 21.63	+57 43 26.9	20.80 ± 0.01	20.85 ± 0.01	20.61 ± 0.01
37	570322	17 20 23.97	+57 50 11.2	23.99 ± 0.05	23.80 ± 0.08	23.66 ± 0.10
39	600121	17 20 25.64	+57 53 06.0	13.20 ± 0.01	12.68 ± 0.01	-
40	640008	17 20 28.36	+57 56 22.9	24.78 ± 0.09	23.63 ± 0.06	22.91 ± 0.04
41	752594	17 20 33.12	+58 07 14.8	22.27 ± 0.01	21.75 ± 0.01	21.16 ± 0.01
42	743824	17 20 33.73	+58 06 12.3	23.97 ± 0.04	22.56 ± 0.03	21.75 ± 0.02
43	762716	17 20 33.62	+58 08 29.7	18.40 ± 0.01	18.14 ± 0.01	17.74 ± 0.01
44	558186	17 20 37.14	+57 48 56.1	19.94 ± 0.01	19.45 ± 0.01	19.01 ± 0.01
47	645311	17 20 39.99	+57 56 45.9	24.37 ± 0.06	23.38 ± 0.06	23.16 ± 0.06
48	617599	17 20 43.08	+57 54 43.0	20.74 ± 0.01	20.35 ± 0.01	20.13 ± 0.01
49	603002	17 20 47.27	+57 53 20.6	23.72 ± 0.04	23.06 ± 0.04	22.83 ± 0.05
50	508553	17 20 51.92	+57 41 59.6	19.96 ± 0.01	19.91 ± 0.01	19.85 ± 0.01
51	624168	17 20 52.30	+57 55 13.2	19.34 ± 0.01	19.24 ± 0.01	19.29 ± 0.01
52	732143	17 20 52.53	+58 04 51.1	23.73 ± 0.04	23.80 ± 0.07	23.22 ± 0.06

Continued in the next page

Continued from previous page

ID	Catalogue-ID	RA(J2000)	Dec(J2000)	g(mag)	r(mag)	i(mag)
53	545924	17 20 56.43	+57 47 39.5	23.62 ± 0.03	22.68 ± 0.03	21.46 ± 0.02
54	587506	17 21 00.53	+57 51 52.8	21.20 ± 0.01	21.22 ± 0.01	21.12 ± 0.01
56	605038	17 21 04.75	+57 53 34.9	15.92 ± 0.01	15.34 ± 0.01	14.94 ± 0.01
57	568743	17 21 12.07	+57 50 01.9	20.48 ± 0.01	20.31 ± 0.01	20.36 ± 0.01
58	638058	17 21 12.99	+57 56 14.8	24.69 ± 0.08	24.09 ± 0.09	24.019 ± 0.11
59	701528	17 21 16.34	+58 01 20.0	-	21.557 ± 0.012	-
60	573308	17 21 22.81	+57 50 29.4	18.18 ± 0.01	18.17 ± 0.01	17.94 ± 0.01
61	598030	17 21 24.61	+57 52 53.5	20.33 ± 0.01	20.07 ± 0.01	19.86 ± 0.01
62	540753	17 21 29.61	+57 47 05.3	25.48 ± 0.15	-	-
63	715961	17 21 35.88	+58 02 57.1	23.89 ± 0.04	23.67 ± 0.07	23.46 ± 0.07
64	705529	17 21 39.49	+58 01 44.8	24.38 ± 0.06	23.23 ± 0.05	22.27 ± 0.03
65	714330	17 21 40.69	+58 02 45.2	25.37 ± 0.14	24.22 ± 0.1	24.13 ± 0.13
67	594813	17 21 41.43	+57 52 35.5	22.37 ± 0.01	21.87 ± 0.02	21.29 ± 0.01
68	663249	17 21 48.27	+57 58 05.4	20.49 ± 0.01	20.33 ± 0.01	19.98 ± 0.01
69	562354	17 21 58.30	+57 49 22.4	13.04 ± 0.01	12.44 ± 0.01	12.90 ± 0.01
70	646728	17 22 11.63	+57 56 52.0	20.92 ± 0.01	20.73 ± 0.01	20.37 ± 0.01

ID : The ID of *XMM-Newton* source.
RA, Dec : The position of the optical source.
catalogue ID : The ID of the optical source in the MegaCam catalogue.
g, r, i : Magnitudes of the counterpart in different optical energy bands of the MegaCam. The extinction was applied for the magnitudes according to Table 12.5.
$\star$: In some energy bands the magnitude has been not reported in the optical catalogue.

Table 12.9: Catalogue of infrared counterparts of the WISE(2012) catalogue

ID	RA(J2000) (Degree)	Dec(J2000) (Degree)	W1 (mag)	W2 (mag)	W3 (mag)	W4 (mag)
2	17 18 46.76	+57 54 45.8	16.65 ± 0.07	15.27 ± 0.07	12.75 ± 0.34	9.25 ± 0.01
3	17 18 48.37	+57 50 13.7	18.45 ± 0.36	16.35 ± 0.19	13.28±0.01	9.61 ± 0.01
4	17 18 56.99	+57 51 02.3	13.89 ± 0.02	13.71 ± 0.03	13.13 ± 0.45	9.57 ± 0.01
5	17 19 00.85	+57 51 46.7	16.34 ± 0.06	16.05 ± 0.14	12.58 ± 0.01	9.08 ± 0.01
6	17 19 01.70	+58 00 28.9	15.22 ± 0.03	14.24 ± 0.04	11.10 ± 0.07	8.54 ± 0.21
7	17 19 04.22	+58 03 29.7	16.06 ± 0.05	15.01 ± 0.06	12.52± 0.28	9.43 ± 0.53
8	17 19 04.64	+57 47 28.1	15.90 ± 0.04	15.25 ± 0.07	12.22 ± 0.21	8.81 ± 0.01
9	17 19 06.75	+57 55 47.5	17.61 ± 0.17	17.15 ± 0.42	12.53 ± 0.01	9.56 ± 0.01
10	17 19 10.46	+57 49 47.8	13.90 ± 0.02	13.40 ± 0.02	9.73 ± 0.03	8.18 ± 0.15
12	17 19 19.96	+57 59 42.9	15.48 ± 0.03	15.03 ± 0.06	12.46± 0.25	9.07 ± 0.33
13	17 19 20.01	+57 54 00.9	11.90 ± 0.02	11.69 ± 0.02	7.95 ± 0.02	5.66 ± 0.03
14	17 19 21.78	+57 49 44.1	16.61 ± 0.07	15.68 ± 0.10	12.81 ± 0.01	9.62 ± 0.52
16	17 19 25.99	+57 50 19.9	10.57 ± 0.02	10.63 ± 0.02	10.58± 0.05	9.06 ± 0.01
17	17 19 25.69	+58 01 00.4	16.82 ± 0.08	16.78 ± 0.27	13.30 ± 0.01	9.53 ± 0.01
18	17 19 28.05	+57 43 13.3	17.69 ± 0.17	16.37 ± 0.19	12.87 ± 0.01	9.37 ± 0.44
20	17 19 34.42	+57 58 49.6	14.44 ± 0.03	13.54 ± 0.03	10.84± 0.06	9.10 ± 0.39
23	17 19 45.40	+57 52 57.3	16.88 ± 0.09	16.67 ± 0.25	13.18 ± 0.01	9.63 ± 0.01
26	17 19 57.10	+57 46 16.4	16.66 ± 0.08	15.90 ± 0.13	12.81±0.01	9.57 ± 0.01
27	17 19 57.66	+57 50 05.5	13.25 ± 0.02	13.26 ± 0.02	12.68± 0.31	9.67 ± 0.01
28	17 20 02.55	+57 55 44.4	17.01 ± 0.10	16.13 ± 0.15	12.84 ± 0.31	8.88 ± 0.01
31	17 20 13.37	+57 50 51.7	15.34 ± 0.03	15.55 ± 0.09	13.10 ± 0.01	9.51 ± 0.01
33	17 20 18.03	+57 51 05.5	13.90 ± 0.02	13.74 ± 0.03	12.55 ± 0.01	9.482 ± 0.01
34	17 20 21.06	+57 44 01.6	16.09 ± 0.05	15.44 ± 0.091	12.66 ± 0.01	8.98 ± 0.01
35	17 20 21.98	+57 58 26.5	7.39 ± 0.02	7.40 ± 0.02	7.38 ± 0.016	7.31 ± 0.077
36	17 20 21.66	+57 43 27.5	17.19 ± 0.11	15.81 ± 0.11	13.18 ± 0.49	9.59 ± 0.01
37	17 20 23.42	+57 50 07.7	17.28 ± 0.12	16.70 ± 0.25	13.26 ± 0.01	9.55 ± 0.01
39	17 20 25.65	+57 53 04.5	10.16 ± 0.02	10.18 ± 0.02	10.21 ± 0.04	8.92 ± 0.01
41	17 20 33.09	+58 07 15.3	16.78 ± 0.08	17.18 ± 0.41	12.73 ± 0.33	9.24 ± 0.01
42	17 20 32.83	+58 06 13.3	17.41 ± 0.14	16.05 ± 0.14	13.30 ± 0.01	9.53 ± 0.01
43	17 20 33.64	+58 08 29.5	12.87 ± 0.02	12.17 ± 0.02	9.50 ± 0.02	6.68 ± 0.050
44	17 20 37.16	+57 48 56.3	13.98 ± 0.02	12.74 ± 0.02	10.01 ± 0.03	7.99 ± 0.13
45	17 20 37.68	+58 02 12.0	7.67 ± 0.02	7.77 ± 0.02	7.65 ± 0.02	7.67 ± 0.09
48	17 20 43.18	+57 54 43.6	16.35 ± 0.06	15.24 ± 0.07	12.75 ± 0.33	9.43 ± 0.01
49	17 20 47.38	+57 53 22.5	16.92 ± 0.09	15.91 ± 0.13	12.72 ± 0.32	9.18 ± 0.01
50	17 20 51.95	+57 41 59.6	15.46 ± 0.04	14.46 ± 0.04	11.91 ± 0.16	9.62 ± 0.51
51	17 20 52.34	+57 55 12.2	15.27 ± 0.03	14.45 ± 0.04	12.13 ± 0.18	9.37 ± 0.44
53	17 20 56.42	+57 47 39.4	16.51 ± 0.07	16.24 ± 0.16	13.26 ± 0.01	9.64 ± 0.01
56	17 21 04.75	+57 53 34.8	13.27 ± 0.02	13.24 ± 0.02	13.04 ± 0.42	9.50 ± 0.01
58	17 21 12.92	+57 56 14.7	16.91 ± 0.09	15.86 ± 0.11	13.12 ± 0.45	9.45 ± 0.01
59	17 21 16.98	+58 01 13.3	10.09 ± 0.02	10.12 ± 0.02	10.10 ± 0.03	8.95 ± 0.01
60	17 21 22.84	+57 50 29.5	14.95 ± 0.03	13.46 ± 0.02	10.26 ± 0.04	8.26 ± 0.16
67	17 21 41.51	+57 52 35.5	16.18 ± 0.05	15.90 ± 0.12	12.60 ± 0.01	9.09 ± 0.01
68	17 21 48.28	+57 58 05.3	16.27 ± 0.06	14.81± 0.05	11.66 ± 0.12	9.03 ± 0.01
69	17 21 58.31	+57 49 22.5	8.23 ± 0.02	8.24 ± 0.02	8.12 ± 0.01	8.14 ± 0.16
70	17 22 11.74	+57 56 52.7	17.02 ± 0.11	15.78 ± 0.11	12.26 ± 0.20	9.25 ± 0.01

ID : The ID of the *XMM-Newton*sources.
RA, Dec : The position of inferred source.
$W1, W2, W3, W4$: Magnitudes of the counterparts in different infrared energy bands of the WISE . The extinction applied for the magnitude according to Table 12.5.

Table 12.10: Catalogue of infrared counterpart of 2MASS(2003) catalogue

ID	RA(J2000) (Degree)	Dec(J2000) (Degree)	J (mag)	K (mag)
4	17 18 56.89	+57 51 04.1	15.72 ± 0.07	14.44 ± 0.10
10	17 19 10.33	+57 49 48.1	15.96 ± 0.09	14.61 ± 0.08
13	17 19 20.17	+57 54 01.5	14.39 ± 0.08	13.15 ± 0.07
16	17 19 25.98	+57 50 19.1	11.19 ± 0.02	10.71 ± 0.02
27	17 19 57.76	+57 50 06.2	14.40 ± 0.03	13.47 ± 0.04
31	17 20 13.92	+57 50 52.4	16.33 ± 0.11	15.43 ± 0.17
33	17 20 17.96	+57 51 04.5	14.97 ± 0.05	14.13 ± 0.079
35	17 20 21.88	+57 58 26.6	7.76 ± 0.03	7.45 ± 0.01
39	17 20 25.64	+57 53 04.5	10.42 ± 0.02	10.21 ± 0.01
43	17 20 33.62	+58 08 29.8	15.24 ± 0.06	13.87± 0.07
45	17 20 37.62	+58 02 12.4	8.49 ± 0.02	7.79 ± 0.02
56	17 21 05.04	+57 53 38.3	13.98 ± 0.03	13.33 ± 0.03
59	17 21 16.66	+58 01 16.5	10.45 ± 0.02	10.12 ± 0.02
60	17 21 22.92	+57 50 29.3	16.66 ± 0.16	15.39 ± 0.01
69	17 21 58.32	+57 49 22.7	9.01± 0.02	8.31 ± 0.03

ID: The ID of the *XMM-Newton* source.
RA, Dec: The position of infrared source in 2MASS catalogue.
J, K**:** Magnitudes of the counterparts in different infrared energy bands of 2MASS.

Table 12.11: Catalogue of radio counterparts of 1.4GHz NRAO VLA Sky Survey(NVSS-1998) catalogue

ID	NVSS-ID	RA(J2000) (Degree)	Dec(J2000) (Degree)	Flux mJy	Major-Axis ($''$)	Mijor-Axis ($''$)
12	171919+575940	259.83200	57.994690	8.7±0.5	26.2	24.8
13	171920+575359	259.83471	57.899890	3.5±0.4	47.6	42.0
51	172051+575517	260.21479	57.921500	56.7±2.1	26.0	15.9

ID: The ID of the *XMM-Newton* source.
NVSS-ID: ID of the radio source in NVSS catalogue.
RA, Dec: The position of radio source.
Flux: Integrated 1.4GHz flux density of radio source in milliJansky (10-26W/m2/Hz).
Major-Axis: fit(deconvolved) Major axis of radio source .
Minor-Axis: fit (deconvolved) Minor axis of radio source.

Table 12.12: Catalogue of X-ray counterparts of ROSAT(2000) catalogue

ID	RA(J2000) (Degree)	Dec(J2000) (Degree)	r1σ ()	Count-Rate (ct s^{-1})	HR1	HR2
14	17 19 21.60	+57 49 41.9	8.5	3.680e-03 ± 1.01e-03	0.00 ± 0.31	0.47± 0.33
20	17 19 34.80	+57 58 49.1	6.3	1.146e-02 ± 1.71e-03	-0.08 ± 0.15	0.37 ± 0.19
27	17 19 57.79	+57 50 06.0	5.2	4.189e-02 ± 3.31e-03	-1.03 ± 0.01	-
35	17 20 21.60	+57 58 26.0	3.7	1.083e-01 ± 4.96e-03	0.51 ± 0.04	-0.07 ± 0.05
43	17 20 34.01	+58 08 33.0	13.9	3.501e-02± 3.33e-03	0.10 ± 0.1	0.11 ± 0.12
44	17 20 37.20	+57 48 54.0	6.9	3.137e-02 ± 2.73e-03	-0.57 ± 0.07	-0.58 ± 0.15
45	17 20 37.61	+58 02 08.9	7.9	2.770e-02 ± 2.61e-03	0.77 ± 0.07	0.13 ± 0.10
50	17 20 53.30	+57 41 53.9	14.1	3.130e-03 ± 9.65e-04	1.56 ± 0.70	0.79 ± 0.24
51	17 20 52.01	+57 55 09.8	5.3	3.639e-03 ± 1.01e-03	0.31 ± 0.38	0.58 ± 0.30
69	17 21 56.90	+57 49 23.9	14.9	5.528e-02± 3.77e-03	0.51 ± 0.06	0.22 ± 0.08

ID: The ID of the *XMM-Newton* source.
RA, Dec: the position of X-ray the ROSAT source.
Count-Rate: the flux of X-ray sources in ROSAT catalogue.
HR1, HR2: Calculation of hardness ratio has been explained in 5.4.7.

Table 12.13: Catalogue of X-ray counterparts of Chandra Catalogue

ID	RA(J2000) (Degree)	Dec(J2000) (Degree)	r1σ ()	FLUX(b-band) (erg s^{-1} m^{-2})	hr1	hr2
13	17 19 19.77	+57 53 56.4	7.05	$8.30^{1.01}_{6.13}$e-15	-0.22	0.04
20	17 19 34.54	+57 58 50.4	0.78	$1.10^{1.17}_{1.04}$e-13	-0.02	-0.30
23	17 19 45.38	+57 52 57.3	1.00	$1.86^{2.11}_{1.60}$e-14	-0.01	-0.06
29	17 20 08.51	+57 58 21.1	1.17	$4.04^{5.47}_{2.61}$e-15	-0.07	-0.18
30	17 20 09.95	+57 54 08.6	0.87	$6.23^{7.76}_{4.70}$e-15	0.05	-0.12
33	17 20 18.03	+57 51 05.0	1.11	$4.35^{5.54}_{3.16}$e-15	-0.01	-0.49
35	17 20 21.97	+57 58 26.8	0.30	$1.12^{1.14}_{1.11}$e-12	-0.12	-0.61
38	17 20 25.48	+57 52 39.6	0.60	$7.27^{8.55}_{6.01}$e-15	-0.05	-0.02
39	17 20 25.66	+57 53 04.7	0.54	$4.19^{4.92}_{3.47}$e-15	-0.06	-0.73
40	17 20 28.43	+57 56 23.2	0.43	$8.83^{1.01}_{7.55}$e-15	-0.03	-0.26
47	17 20 40.24	+57 56 47.9	0.88	$1.15^{1.46}_{0.87}$e-14	-0.03	0.02
48	17 20 43.08	+57 54 43.2	0.35	$5.47^{5.95}_{4.98}$e-14	0.33	-0.03
49	17 20 47.15	+57 53 23.2	0.50	$1.90^{2.15}_{1.66}$e-14	-0.08	-0.10
51	17 20 52.32	+57 55 13.3	0.32	$1.17^{1.23}_{1.12}$e-13	0.01	-0.18
54	17 21 00.47	+57 51 53.2	1.31	$8.13^{10.1}_{6.13}$e-15	0.03	-0.07
56	17 21 04.75	+57 53 35.2	1.04	$8.89^{1.05}_{7.34}$e-15	-0.05	-0.49
58	17 21 12.96	+57 56 15.1	1.99	$7.44^{9.83}_{5.05}$e-15	-0.11	-0.11
67	17 21 41.14	+57 52 36.4	2.75	$2.85^{3.31}_{2.38}$e-14	0.01	-0.23
68	17 21 48.07	+57 58 05.2	7.92	$2.85^{4.59}_{1.11}$e-14	0.18	-0.12
70	17 22 12.41	+57 56 51.5	7.92	$0.00^{2.90}$e+14	-0.16	-0.15

ID: The ID of the *XMM-Newton* source.
RA, Dec: The position of X-ray the Chandra source.
Flux: The flux of X-ray sources in the Chandra catalogue.
HR1, HR2: Calculation of hardness ratio has been explained in 5.4.7.

Chapter 13

Figure 13.1: SDSS9 optical images at the position of the *XMM-Newton* X-ray sources in the field of the Draco dSph. The details of the counterparts are given in Table 12.6

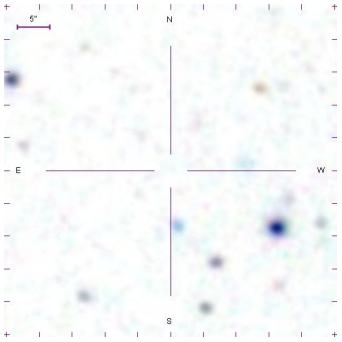
(a) src No 1

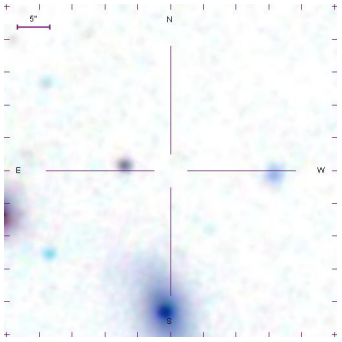
(b) src No 2

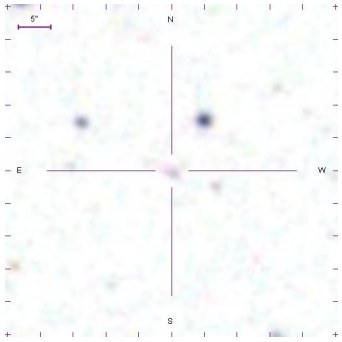
(c) src No 3

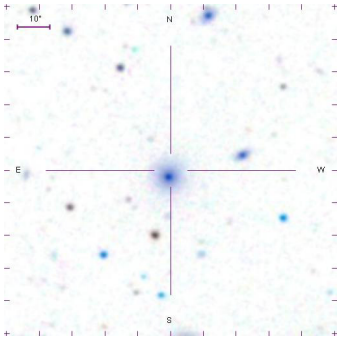
(d) src No 4

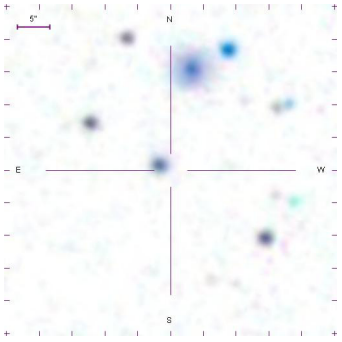
(e) src No 5

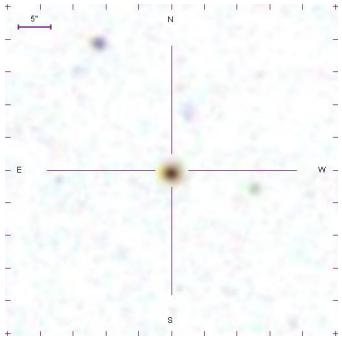
(f) src No 6

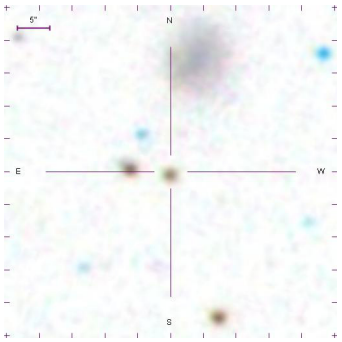
(g) src No 7

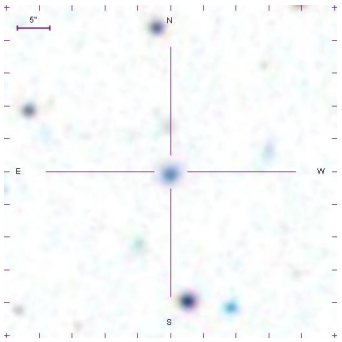
(h) src No 8

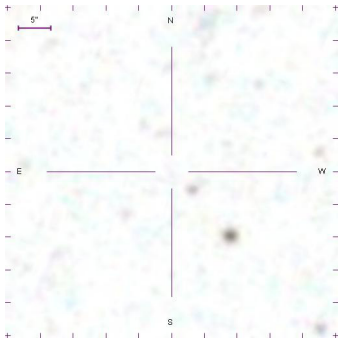
(i) src No 9

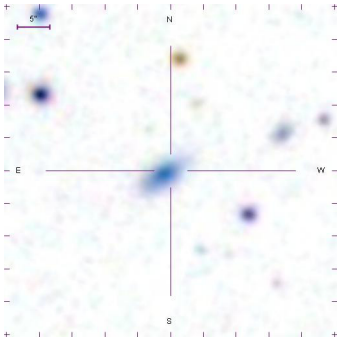
(j) src No 10

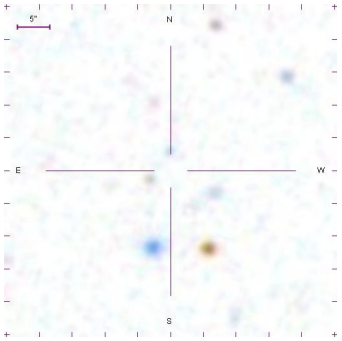
(k) src No 11

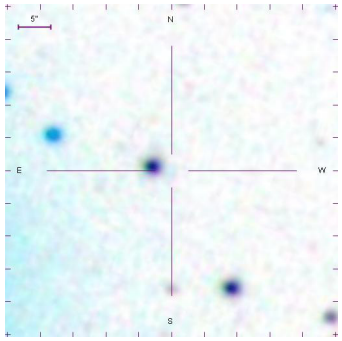
(l) src No 12

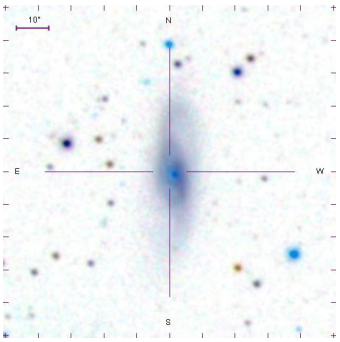

(a) src No 13

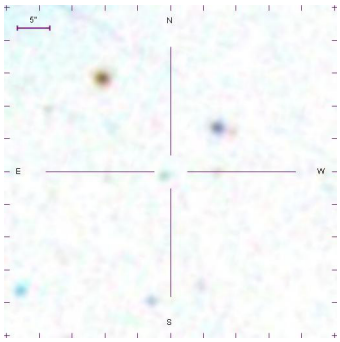

(b) src No 14

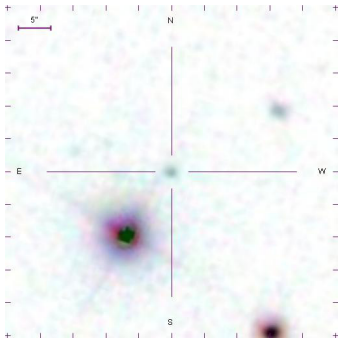

(c) src No 15

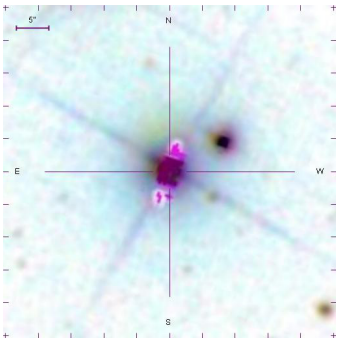

(d) src No 16

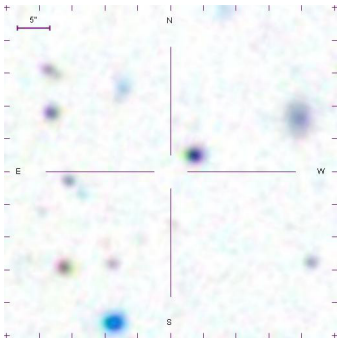

(e) src No 17

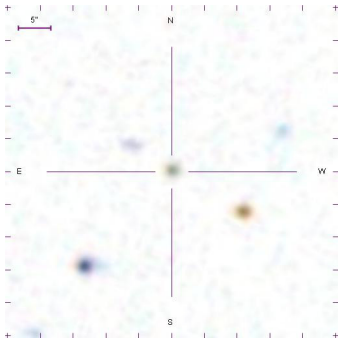

(f) src No 18

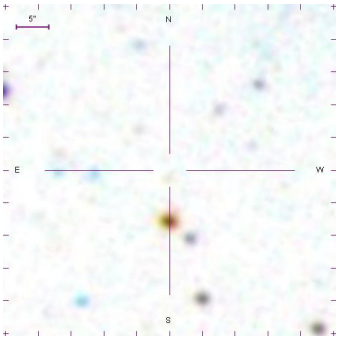

(g) src No 19

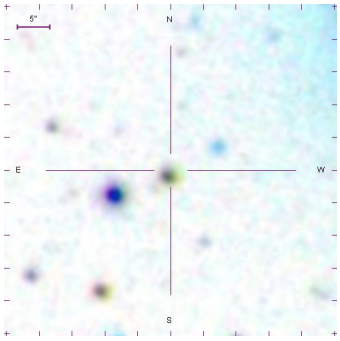

(h) src No 20

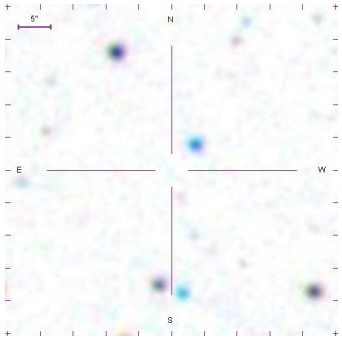

(i) src No 21

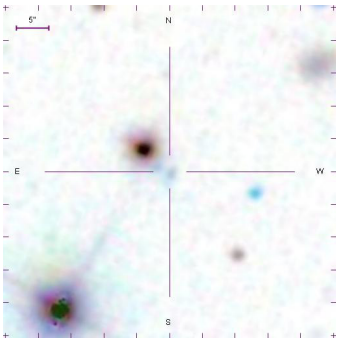

(j) src No 22

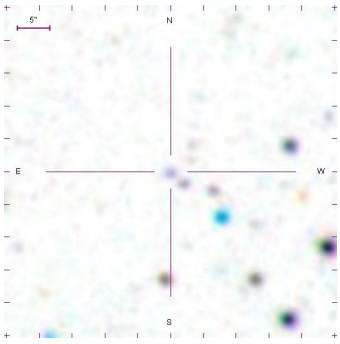

(k) src No 23

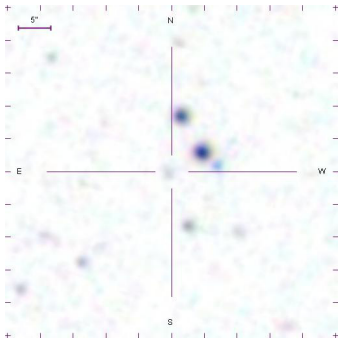

(l) src No 24

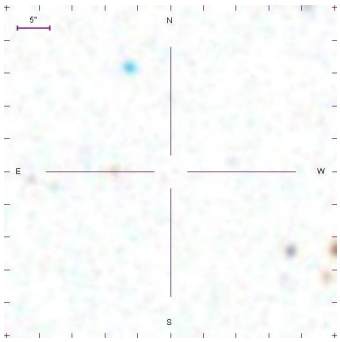

(a) src No 25

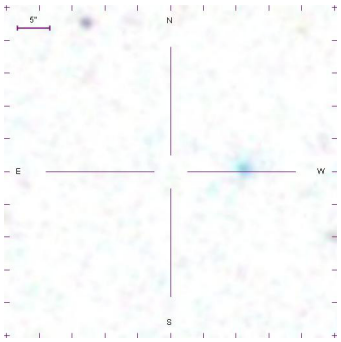

(b) src No 26

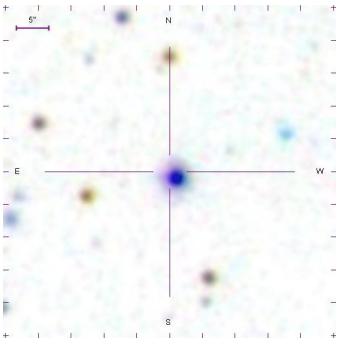

(c) src No 27

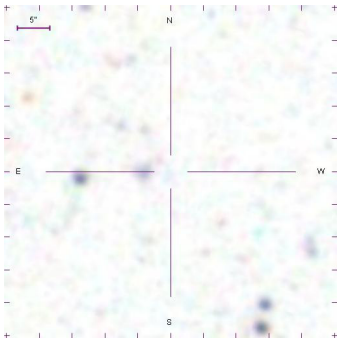

(d) src No 28

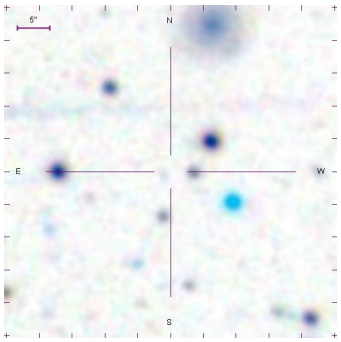

(e) src No 29

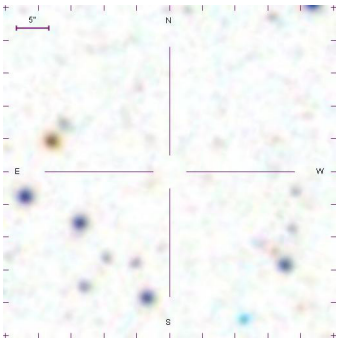

(f) src No 30

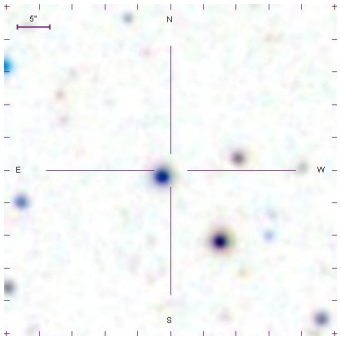

(g) src No 31

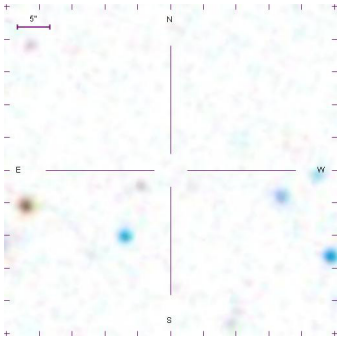

(h) src No 32

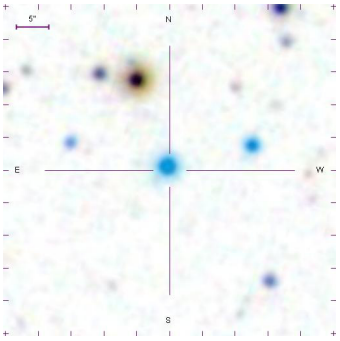

(i) src No 33

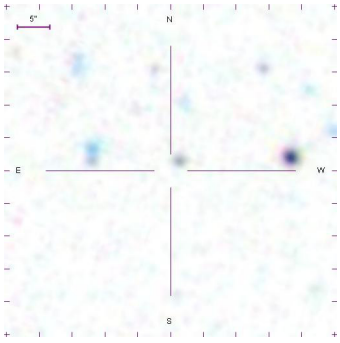

(j) src No 34

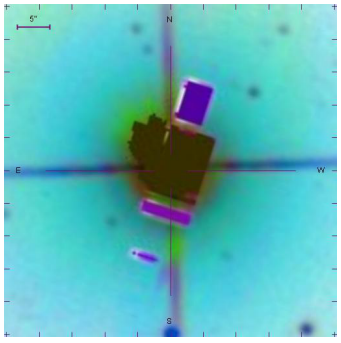

(k) src No 35

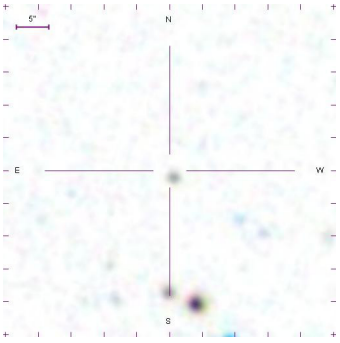

(l) src No 36

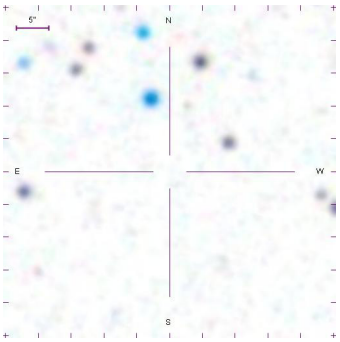

(a) src No 37

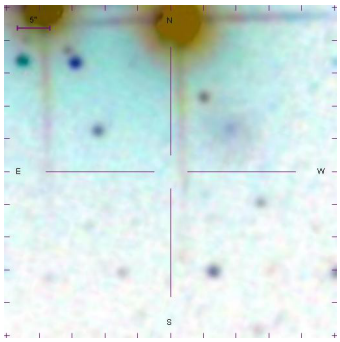

(b) src No 38

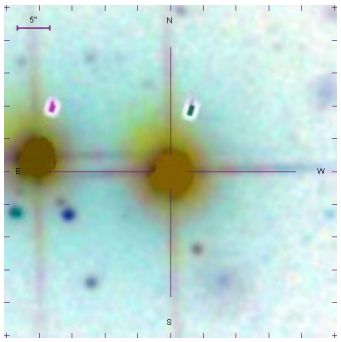

(c) src No 39

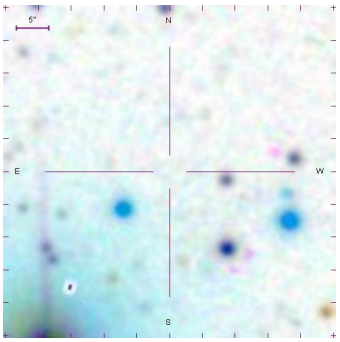

(d) src No 40

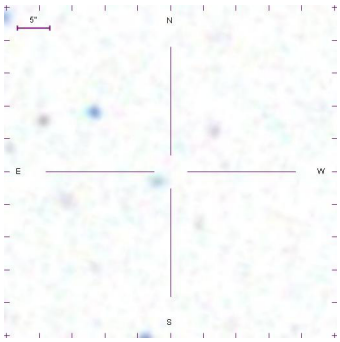

(e) src No 41

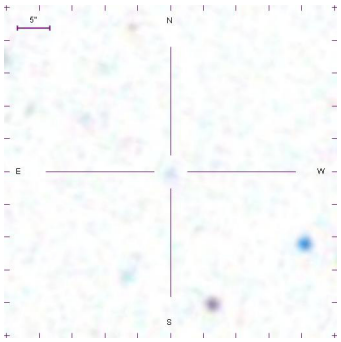

(f) src No 42

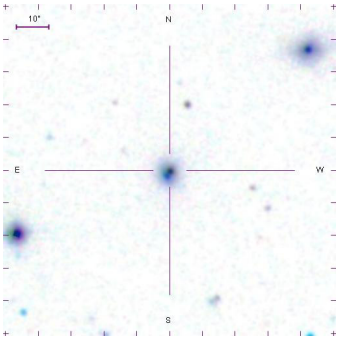

(g) src No 43

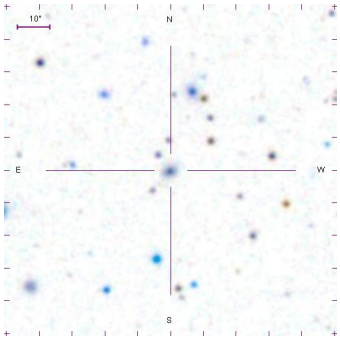

(h) src No 44

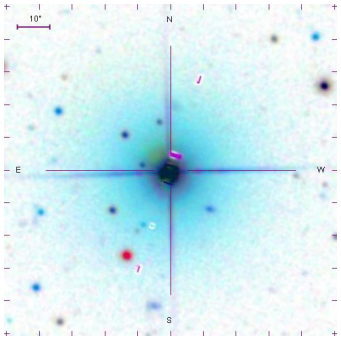

(i) src No 45

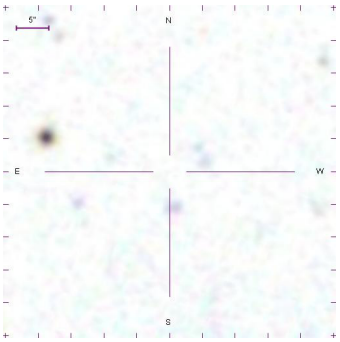

(j) src No 46

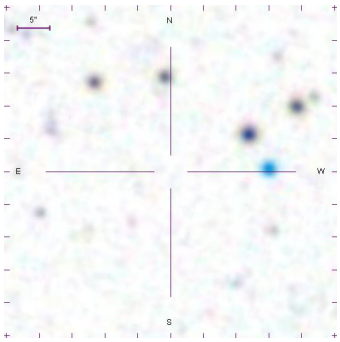

(k) src No 47

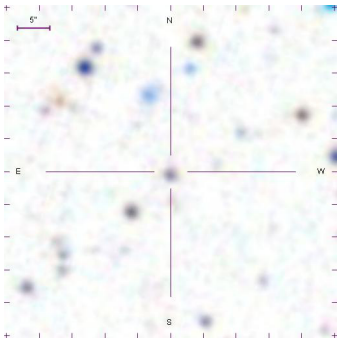

(l) src No 48

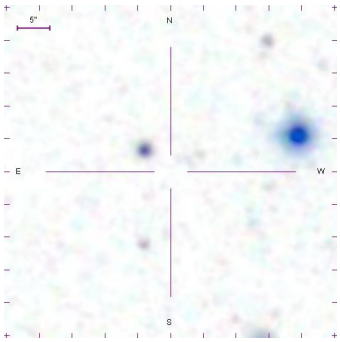
(a) src No 49

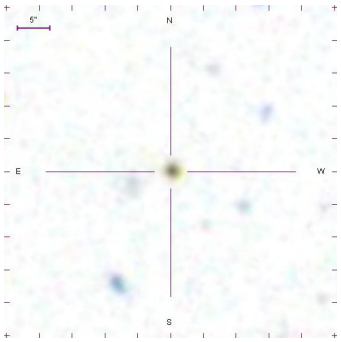
(b) src No 50

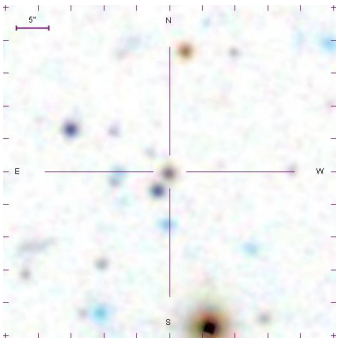
(c) src No 51

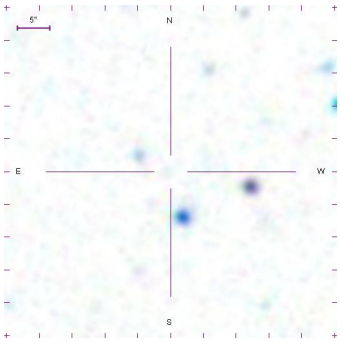
(d) src No 52

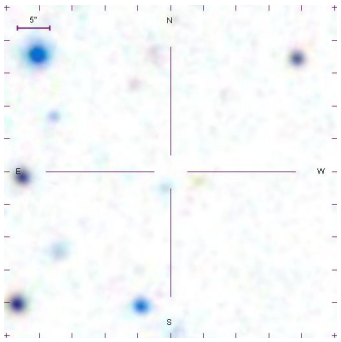
(e) src No 53

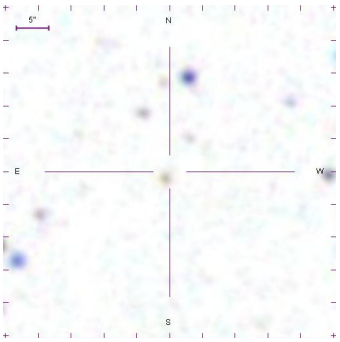
(f) src No 54

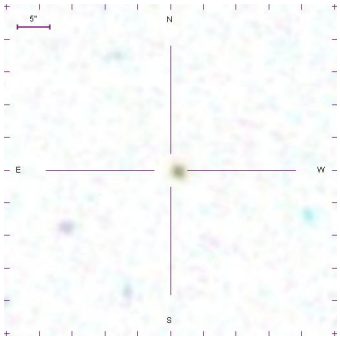
(g) src No 55

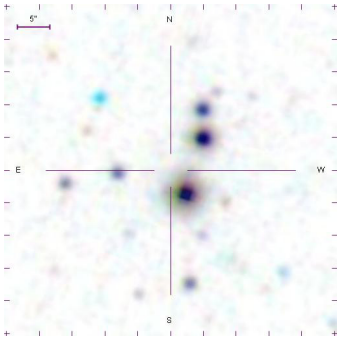
(h) src No 56

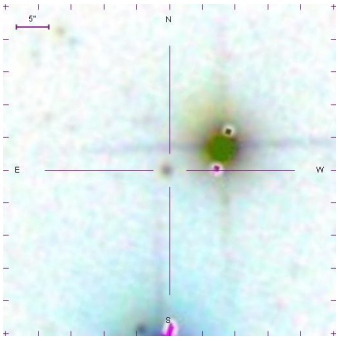
(i) src No 57

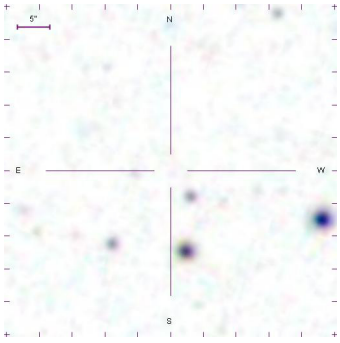
(j) src No 58

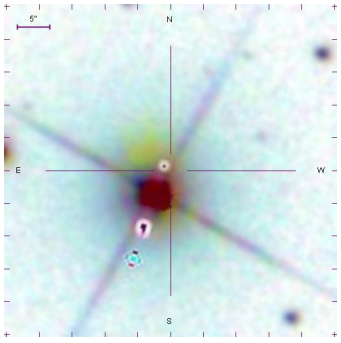
(k) src No 59

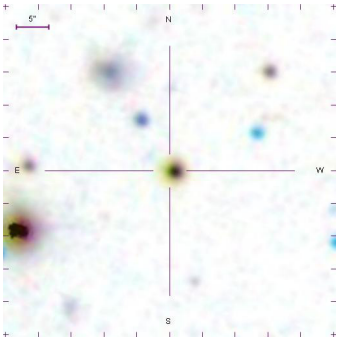
(l) src No 60

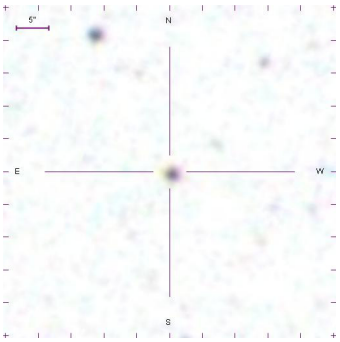

(a) src No 61

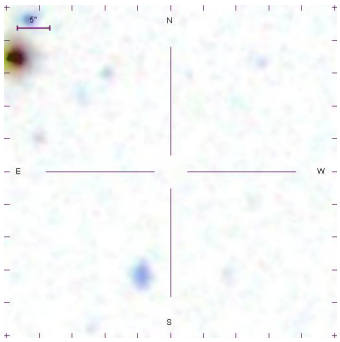

(b) src No 62

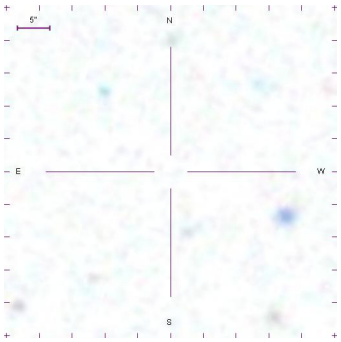

(c) src No 63

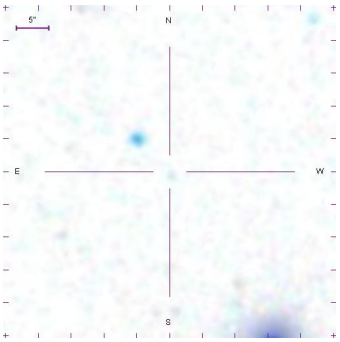

(d) src No 64

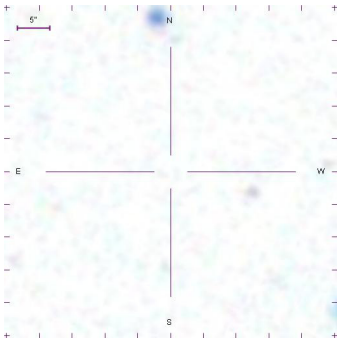

(e) src No 65

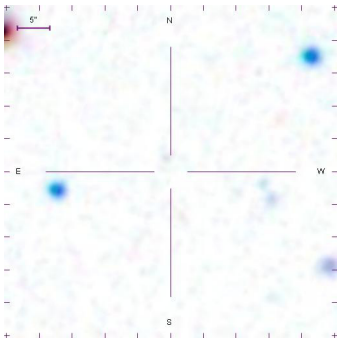

(f) src No 66

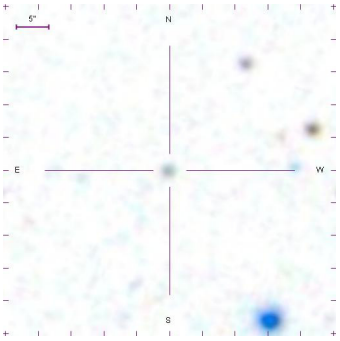

(g) src No 67

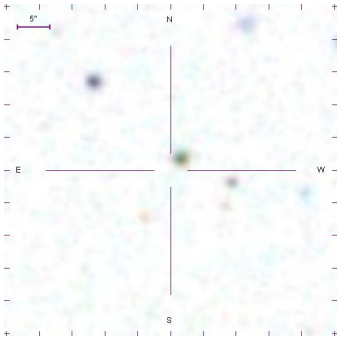

(h) src No 68

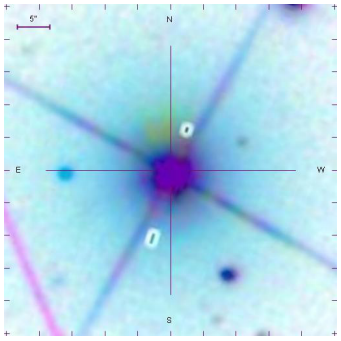

(i) src No 69

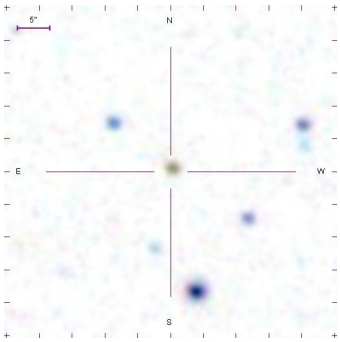

(j) src No 70

Bibliography

Availability of the Digitized Sky Survey on CD-ROMs. *Publications of the Astronomical Society of the Pacific*, 106:108, January 1994. doi: 10.1086/133354.

K. N. Abazajian, J. K. Adelman-McCarthy, M. A. Agüeros, S. S. Allam, C. Allende Prieto, D. An, K. S. J. Anderson, S. F. Anderson, J. Annis, N. A. Bahcall, and et al. The Seventh Data Release of the Sloan Digital Sky Survey. *The Astrophysical Journal Supplement Series*, 182:543, June 2009. doi: 10.1088/0067-0049/182/2/543.

S. Abraham, N. S. Philip, A. Kembhavi, Y. G. Wadadekar, and R. Sinha. A photometric catalogue of quasars and other point sources in the Sloan Digital Sky Survey. *Monthly Notices of the Royal Astronomical Society*, 419:80–94, January 2012. doi: 10.1111/j.1365-2966.2011.19674.x.

F. Aharonian, A. Akhperjanian, M. Beilicke, K. Bernlöhr, H.-G. Börst, H. Bojahr, O. Bolz, T. Coarasa, J. L. Contreras, J. Cortina, S. Denninghoff, M. V. Fonseca, M. Girma, N. Götting, G. Heinzelmann, G. Hermann, A. Heusler, W. Hofmann, D. Horns, I. Jung, R. Kankanyan, M. Kestel, A. Kohnle, A. Konopelko, D. Kranich, H. Lampeitl, M. Lopez, E. Lorenz, F. Lucarelli, O. Mang, D. Mazin, H. Meyer, R. Mirzoyan, A. Moralejo, E. Oña-Wilhelmi, M. Panter, A. Plyasheshnikov, G. Pühlhofer, R. de los Reyes, W. Rhode, J. Ripken, G. Rowell, V. Sahakian, M. Samorski, M. Schilling, M. Siems, D. Sobzynska, W. Stamm, M. Tluczykont, V. Vitale, H. J. Völk, C. A. Wiedner, and W. Wittek. The Crab Nebula and Pulsar between 500 GeV and 80 TeV: Observations with the HEGRA Stereoscopic Air Cerenkov Telescopes. *The Astrophysical Journal*, 614:897–913, October 2004. doi: 10.1086/423931.

C. P. Ahn, R. Alexandroff, C. Allende Prieto, S. F. Anderson, T. Anderton, B. H. Andrews, É. Aubourg, S. Bailey, E. Balbinot, R. Barnes, and et al. The Ninth Data Release of the Sloan Digital Sky Survey: First Spectroscopic Data from the SDSS-III Baryon Oscillation Spectroscopic Survey. *The Astrophysical Journal Supplement Series*, 203:21, December 2012. doi: 10.1088/0067-0049/203/2/21.

N. C. Amorisco, J. Zavala, and T. J. L. de Boer. Dark Matter Cores in the Fornax and Sculptor Dwarf Galaxies: Joining Halo Assembly and Detailed Star For-

mation Histories. *The Astrophysical Journal Letters*, 782:L39, February 2014. doi: 10.1088/2041-8205/782/2/L39.

A. Aparicio, R. Carrera, and D. Martinez-Delgado. The Star Formation History and Morphological Evolution of the Draco Dwarf Spheroidal Galaxy. *The Astronomical Journal*, 122:2524–2537, November 2001. doi: 10.1086/323535.

K. A. Arnaud. XSPEC: The First Ten Years. In G. H. Jacoby and J. Barnes, editors, *Astronomical Data Analysis Software and Systems V*, volume 101 of *Astronomical Society of the Pacific Conference Series*, page 17, 1996.

K. Asai, T. Dotani, R. Hoshi, Y. Tanaka, C. R. Robinson, and K. Terada. ASCA Observations of Transient X-Ray Sources in Quiescence. *Publications of the Astronomical Society of Japan*, 50:611–619, December 1998. doi: 10.1093/pasj/50.6.611.

W. Baade and H. H. Swope. The Draco system, a dwarf galaxy. *The Astronomical Journal*, 66:300–347, September 1961. doi: 10.1086/108431.

M. Balucinska-Church and D. McCammon. Photoelectric absorption cross sections with variable abundances. *The Astrophysical Journal*, 400:699, December 1992. doi: 10.1086/172032.

S. D. Barthelmy. Burst Alert Telescope (BAT) on the Swift MIDEX mission. In K. A. Flanagan and O. H. W. Siegmund, editors, *X-Ray and Gamma-Ray Instrumentation for Astronomy XIII*, volume 5165 of *Society of Photo-Optical Instrumentation Engineers (SPIE) Conference Series*, pages 175–189, February 2004. doi: 10.1117/12.506779.

E. S. Bartlett, M. J. Coe, F. Haberl, V. A. McBride, and R. H. D. Corbet. The search for high-mass X-ray binaries in the Phoenix dwarf galaxy. *Monthly Notices of the Royal Astronomical Society*, 422:2302–2313, May 2012. doi: 10.1111/j.1365-2966.2012.20791.x.

G. Battaglia, A. Helmi, E. Tolstoy, M. Irwin, V. Hill, and P. Jablonka. The Kinematic Status and Mass Content of the Sculptor Dwarf Spheroidal Galaxy. *The Astrophysical Journal Letters*, 681:L13–L16, July 2008. doi: 10.1086/590179.

G. Battaglia, A. Helmi, and M. Breddels. Internal kinematics and dynamical models of dwarf spheroidal galaxies around the Milky Way. , 57:52–79, September 2013. doi: 10.1016/j.newar.2013.05.003.

K. Belczyński, J. Mikołajewska, U. Munari, R. J. Ivison, and M. Friedjung. A catalogue of symbiotic stars. *Astronomy & Astrophysics Supplement*, 146:407–435, November 2000. doi: 10.1051/aas:2000280.

K. Belczynski, V. Kalogera, and T. Bulik. A Comprehensive Study of Binary Compact Objects as Gravitational Wave Sources: Evolutionary Channels, Rates, and Physical Properties. *The Astrophysical Journal*, 572:407–431, June 2002. doi: 10.1086/340304.

K. Belczynski, V. Kalogera, A. Zezas, and G. Fabbiano. X-Ray Binary Populations: The Luminosity Function of NGC 1569. *The Astrophysical Journal Letters*, 601:L147–L150, February 2004. doi: 10.1086/382131.

K. Belczynski, V. Kalogera, F. A. Rasio, R. E. Taam, A. Zezas, T. Bulik, T. J. Maccarone, and N. Ivanova. Compact Object Modeling with the StarTrack Population Synthesis Code. *The Astrophysical Journal Supplement Series*, 174: 223–260, January 2008. doi: 10.1086/521026.

E. F. Bell and R. S. de Jong. Stellar Mass-to-Light Ratios and the Tully-Fisher Relation. *The Astrophysical Journal*, 550:212–229, March 2001. doi: 10.1086/319728.

M. Bellazzini, F. R. Ferraro, L. Origlia, E. Pancino, L. Monaco, and E. Oliva. The Draco and Ursa Minor Dwarf Spheroidal Galaxies: A Comparative Study. *The Astronomical Journal*, 124:3222–3240, December 2002. doi: 10.1086/344794.

R. Bender. Supermassive Black Holes in Nearby Galaxy Centers. In A. Merloni, S. Nayakshin, and R. A. Sunyaev, editors, *Growing Black Holes: Accretion in a Cosmological Context*, pages 147–153, 2005. doi: 10.1007/11403913_25.

G. Bertelli, A. Bressan, C. Chiosi, F. Fagotto, and E. Nasi. Theoretical isochrones from models with new radiative opacities. *Astronomy & Astrophysics Supplement*, 106:275–302, August 1994.

L. Bianchi, B. Efremova, J. Herald, L. Girardi, A. Zabot, P. Marigo, and C. Martin. Catalogues of hot white dwarfs in the Milky Way from GALEX's ultraviolet sky surveys: constraining stellar evolution. *Monthly Notices of the Royal Astronomical Society*, 411:2770–2791, March 2011. doi: 10.1111/j.1365-2966.2010.17890.x.

L. Bildsten and C. J. Deloye. Ultracompact Binaries as Bright X-Ray Sources in Elliptical Galaxies. *The Astrophysical Journal Letters*, 607:L119–L122, June 2004. doi: 10.1086/421844.

A. Blaauw. On the origin of the O- and B-type stars with high velocities (the "run-away" stars), and some related problems. *Provided by the SAO/NASA Astrophysics Data System*, 15:265, May 1961.

J. K. Blackburn. FTOOLS: A FITS Data Processing and Analysis Software Package. 77:367, 1995.

J. Boersma. Mathematical theory of the two-body problem with one of the masses decreasing with time. *Provided by the SAO/NASA Astrophysics Data System*, 15:291–301, May 1961.

A. I. Bogomazov and V. M. Lipunov. Population synthesis for the luminosity functions of X-ray binaries made using the "Scenario Machine". *Astronomy Reports*, 52:299–310, April 2008. doi: 10.1134/S1063772908040045.

H. Böhringer, W. Voges, J. P. Huchra, B. McLean, R. Giacconi, P. Rosati, R. Burg, J. Mader, P. Schuecker, D. Simiç, S. Komossa, T. H. Reiprich, J. Retzlaff, and J. Trümper. The Northern ROSAT All-Sky (NORAS) Galaxy Cluster Survey. I. X-Ray Properties of Clusters Detected as Extended X-Ray Sources. *The Astrophysical Journal Supplement Series*, 129:435–474, August 2000. doi: 10.1086/313427.

B. W. Bopp, F. C. Fekel, J. P. Aufdenberg, R. Dempsey, and V. Dadonas. Extremely active long-period RS CVn binary HD 12545. *The Astronomical Journal*, 106:2502–2509, December 1993. doi: 10.1086/116818.

F. Bournaud, P.-A. Duc, and F. Masset. The large extent of dark matter haloes probed by the formation of tidal dwarf galaxies. *Astronomy & Astrophysics*, 411:L469–L472, December 2003. doi: 10.1051/0004-6361:20031520.

A. Boyarsky, O. Ruchayskiy, D. Iakubovskyi, and J. Franse. Unidentified Line in X-Ray Spectra of the Andromeda Galaxy and Perseus Galaxy Cluster. *Physical Review Letters*, 113(25):251301, December 2014. doi: 10.1103/PhysRevLett.113.251301.

H. Bradt. *Astrophysics Processes*. September 2008.

N. Brandt and P. Podsiadlowski. The effects of high-velocity supernova kicks on the orbital properties and sky distributions of neutron-star binaries. *Monthly Notices of the Royal Astronomical Society*, 274:461–484, May 1995.

N. S. Brickhouse. Spectral Modeling with Apec. In *IAU Joint Discussion*, volume 17 of *IAU Joint Discussion*, page 23, 2003.

N. S. Brickhouse, R. K. Smith, J. C. Raymond, and D. A. Liedahl. The Astrophysical Plasma Emission Code. In *AAS/High Energy Astrophysics Division #5*, volume 32 of *Bulletin of the American Astronomical Society*, page 1227, October 2000.

T. M. Brown, J. Tumlinson, M. Geha, J. D. Simon, L. C. Vargas, D. A. VandenBerg, E. N. Kirby, J. S. Kalirai, R. J. Avila, M. Gennaro, H. C. Ferguson, R. R. Muñoz, P. Guhathakurta, and A. Renzini. The Quenching of the Ultra-faint Dwarf Galaxies in the Reionization Era. *The Astrophysical Journal*, 796:91, December 2014. doi: 10.1088/0004-637X/796/2/91.

R. Buccheri, K. Bennett, G. F. Bignami, J. B. G. M. Bloemen, V. Boriakoff, P. A. Caraveo, W. Hermsen, G. Kanbach, R. N. Manchester, J. L. Masnou, H. A. Mayer-Hasselwander, M. E. Ozel, J. A. Paul, B. Sacco, L. Scarsi, and A. W. Strong. Search for pulsed gamma-ray emission from radio pulsars in the COS-B data. *Astronomy & Astrophysics*, 128:245–251, November 1983.

R. Buccheri, M. C. Maccarone, B. Sacco, and V. di Gesu. High resolution cluster method for topological studies of the light curves of gamma-ray pulsars. *Astronomy & Astrophysics*, 201:194–198, July 1988.

Y. L. Bukhmastova. Properties of Quasar-Galaxy Associations and Gravitational Mesolensing by Halo Objects. *Astronomy Reports*, 45:581–590, August 2001. doi: 10.1134/1.1388923.

E. Bulbul, M. Markevitch, A. R. Foster, R. K. Smith, M. Loewenstein, and S. W. Randall. Comment on "Dark matter searches going bananas: the contribution of Potassium (and Chlorine) to the 3.5 keV line". *ArXiv e-prints*, September 2014.

D. N. Burrows, J. E. Hill, J. A. Nousek, J. A. Kennea, A. Wells, J. P. Osborne, A. F. Abbey, A. Beardmore, K. Mukerjee, A. D. T. Short, G. Chincarini, S. Campana, O. Citterio, A. Moretti, C. Pagani, G. Tagliaferri, P. Giommi, M. Capalbi, F. Tamburelli, L. Angelini, G. Cusumano, H. W. Bräuninger, W. Burkert, and G. D. Hartner. The Swift X-Ray Telescope. *Space Science Reviews*, 120:165–195, October 2005. doi: 10.1007/s11214-005-5097-2.

N. Cappelluti, M. Brusa, G. Hasinger, A. Comastri, G. Zamorani, A. Finoguenov, R. Gilli, S. Puccetti, T. Miyaji, M. Salvato, C. Vignali, T. Aldcroft, H. Böhringer, H. Brunner, F. Civano, M. Elvis, F. Fiore, A. Fruscione, R. E. Griffiths, L. Guzzo, A. Iovino, A. M. Koekemoer, V. Mainieri, N. Z. Scoville, P. Shopbell, J. Silverman, and C. M. Urry. The XMM-Newton wide-field survey in the COSMOS field. The point-like X-ray source catalogue. *Astronomy & Astrophysics*, 497:635–648, April 2009. doi: 10.1051/0004-6361/200810794.

R. Carrera, A. Aparicio, D. Martinez-Delgado, and J. Alonso-García. The Star Formation History and Spatial Distribution of Stellar Populations in the Ursa Minor Dwarf Spheroidal Galaxy. *The Astronomical Journal*, 123:3199–3209, June 2002. doi: 10.1086/340702.

M.-R. L. Cioni and H. J. Habing. The Draco dwarf galaxy in the near-infrared. *Astronomy & Astrophysics*, 442:165–176, October 2005. doi: 10.1051/0004-6361:20053368.

D. H. Cohen, M. A. Kuhn, M. Gagné, E. L. N. Jensen, and N. A. Miller. Chandra spectroscopy of the hot star βCrucis and the discovery of a pre-main-sequence

companion. *Monthly Notices of the Royal Astronomical Society*, 386:1855–1871, June 2008. doi: 10.1111/j.1365-2966.2008.13176.x.

E. J. M. Colbert and R. F. Mushotzky. The Nature of Accreting Black Holes in Nearby Galaxy Nuclei. *The Astrophysical Journal*, 519:89–107, July 1999. doi: 10.1086/307356.

M. G. Coleman and J. T. A. de Jong. A Deep Survey of the Fornax dSph. I. Star Formation History. *The Astrophysical Journal*, 685:933–946, October 2008. doi: 10.1086/589992.

J. J. Condon, W. D. Cotton, E. W. Greisen, Q. F. Yin, R. A. Perley, G. B. Taylor, and J. J. Broderick. The NRAO VLA Sky Survey. *The Astronomical Journal*, 115:1693–1716, May 1998. doi: 10.1086/300337.

R. Connon Smith. Cataclysmic Variables. *ArXiv Astrophysics e-prints*, January 2007.

M. F. Corcoran, W. L. Waldron, J. J. Macfarlane, W. Chen, A. M. T. Pollock, K. Torii, S. Kitamoto, N. Miura, M. Egoshi, and Y. Ohno. ASCA solid state imaging spectrometer observations of O stars. *The Astrophysical Journal Letters*, 436:L95–L98, November 1994. doi: 10.1086/187641.

R. M. Cutri and et al. WISE All-Sky Data Release (Cutri+ 2012). *VizieR Online Data Catalog*, 2311:0, 2012.

R. M. Cutri, M. F. Skrutskie, S. van Dyk, C. A. Beichman, J. M. Carpenter, T. Chester, L. Cambresy, T. Evans, J. Fowler, J. Gizis, E. Howard, J. Huchra, T. Jarrett, E. L. Kopan, J. D. Kirkpatrick, R. M. Light, K. A. Marsh, H. McCallon, S. Schneider, R. Stiening, M. Sykes, M. Weinberg, W. A. Wheaton, S. Wheelock, and N. Zacarias. 2MASS All-Sky Catalog of Point Sources (Cutri+ 2003). *VizieR Online Data Catalog*, 2246:0, March 2003.

R. D'Abrusco, G. Longo, and N. A. Walton. Quasar candidates selection in the Virtual Observatory era. *Monthly Notices of the Royal Astronomical Society*, 396:223–262, June 2009. doi: 10.1111/j.1365-2966.2009.14754.x.

M. Dall'Ora, K. Kinemuchi, V. Ripepi, C. T. Rodgers, G. Clementini, L. Di Fabrizio, H. A. Smith, M. Marconi, I. Musella, C. Greco, C. A. Kuehn, M. Catelan, B. J. Pritzl, and T. C. Beers. Stellar Archaeology in the Galactic Halo with the Ultra-faint Dwarfs. VI. Ursa Major II. *The Astrophysical Journal*, 752:42, June 2012. doi: 10.1088/0004-637X/752/1/42.

T. J. L. de Boer, E. Tolstoy, V. Hill, A. Saha, E. W. Olszewski, M. Mateo, E. Starkenburg, G. Battaglia, and M. G. Walker. The star formation and chemical evolution history of the Fornax dwarf spheroidal galaxy. *Astronomy & Astrophysics*, 544:A73, August 2012. doi: 10.1051/0004-6361/201219547.

D. de Chambure, R. Laine, and K. van Katwijk. X-ray telescopes for the ESA XMM spacecraft. In R. B. Hoover and A. B. Walker, editors, *X-Ray Optics, Instruments, and Missions*, volume 3444 of *Society of Photo-Optical Instrumentation Engineers (SPIE) Conference Series*, pages 313–326, November 1998.

W. Dehnen and A. King. Probing dark matter with X-ray binaries. *Monthly Notices of the Royal Astronomical Society*, 367:L29–L31, March 2006. doi: 10.1111/j.1745-3933.2005.00132.x.

A. Dekel and J. Silk. The origin of dwarf galaxies, cold dark matter, and biased galaxy formation. *The Astrophysical Journal*, 303:39–55, April 1986. doi: 10.1086/164050.

A. del Pino, S. L. Hidalgo, A. Aparicio, C. Gallart, R. Carrera, M. Monelli, R. Buonanno, and G. Marconi. Spatial dependence of the star formation history in the central regions of the Fornax dwarf spheroidal galaxy. *Monthly Notices of the Royal Astronomical Society*, 433:1505–1516, August 2013. doi: 10.1093/mnras/stt833.

J. W. den Herder, A. C. Brinkman, S. M. Kahn, G. Branduardi-Raymont, K. Thomsen, H. Aarts, M. Audard, J. V. Bixler, A. J. den Boggende, J. Cottam, T. Decker, L. Dubbeldam, C. Erd, H. Goulooze, M. Güdel, P. Guttridge, C. J. Hailey, K. A. Janabi, J. S. Kaastra, P. A. J. de Korte, B. J. van Leeuwen, C. Mauche, A. J. McCalden, R. Mewe, A. Naber, F. B. Paerels, J. R. Peterson, A. P. Rasmussen, K. Rees, I. Sakelliou, M. Sako, J. Spodek, M. Stern, T. Tamura, J. Tandy, C. P. de Vries, S. Welch, and A. Zehnder. The Reflection Grating Spectrometer on board XMM-Newton. *Astronomy & Astrophysics*, 365: L7–L17, January 2001. doi: 10.1051/0004-6361:20000058.

A. E. Dolphin. Numerical methods of star formation history measurement and applications to seven dwarf spheroidals. *Monthly Notices of the Royal Astronomical Society*, 332:91–108, May 2002. doi: 10.1046/j.1365-8711.2002.05271.x.

A. E. Dolphin, D. R. Weisz, E. D. Skillman, and J. A. Holtzman. Star Formation Histories of Local Group Dwarf Galaxies. *ArXiv Astrophysics e-prints*, June 2005.

P.-A. Duc, F. Bournaud, and F. Masset. A top-down scenario for the formation of massive Tidal Dwarf Galaxies. *Astronomy & Astrophysics*, 427:803–814, December 2004. doi: 10.1051/0004-6361:20041410.

L. Ducci, M. Sasaki, F. Haberl, and W. Pietsch. X-ray source population study of the starburst galaxy M 83 with XMM-Newton. *Astronomy & Astrophysics*, 553:A7, May 2013. doi: 10.1051/0004-6361/201321035.

D. Eichler, M. Livio, T. Piran, and D. N. Schramm. Nucleosynthesis, neutrino bursts and gamma-rays from coalescing neutron stars. *Nature*, 340:126–128, July 1989. doi: 10.1038/340126a0.

M. Elvis, F. Civano, C. Vignali, S. Puccetti, F. Fiore, N. Cappelluti, T. L. Aldcroft, A. Fruscione, G. Zamorani, A. Comastri, M. Brusa, R. Gilli, T. Miyaji, F. Damiani, A. M. Koekemoer, A. Finoguenov, H. Brunner, C. M. Urry, J. Silverman, V. Mainieri, G. Hasinger, R. Griffiths, C. M. Carollo, H. Hao, L. Guzzo, A. Blain, D. Calzetti, C. Carilli, P. Capak, S. Ettori, G. Fabbiano, C. Impey, S. Lilly, B. Mobasher, M. Rich, M. Salvato, D. B. Sanders, E. Schinnerer, N. Scoville, P. Shopbell, J. E. Taylor, Y. Taniguchi, and M. Volonteri. The Chandra COSMOS Survey. I. Overview and Point Source Catalog. *The Astrophysical Journal Supplement Series*, 184:158–171, September 2009. doi: 10.1088/0067-0049/184/1/158.

I. N. Evans, F. A. Primini, K. J. Glotfelty, C. S. Anderson, N. R. Bonaventura, J. C. Chen, J. E. Davis, S. M. Doe, J. D. Evans, G. Fabbiano, E. C. Galle, D. G. Gibbs, II, J. D. Grier, R. M. Hain, D. M. Hall, P. N. Harbo, X. (Helen He, J. C. Houck, M. Karovska, V. L. Kashyap, J. Lauer, M. L. McCollough, J. C. McDowell, J. B. Miller, A. W. Mitschang, D. L. Morgan, A. E. Mossman, J. S. Nichols, M. A. Nowak, D. A. Plummer, B. L. Refsdal, A. H. Rots, A. Siemiginowska, B. A. Sundheim, M. S. Tibbetts, D. W. Van Stone, S. L. Winkelman, and P. Zografou. The Chandra Source Catalog. *The Astrophysical Journal Supplement Series*, 189:37, July 2010. doi: 10.1088/0067-0049/189/1/37.

G. Fabbiano. Populations of X-Ray Sources in Galaxies. *Annual Review of Astronomy & Astrophysics*, 44:323–366, September 2006. doi: 10.1146/annurev.astro.44.051905.092519.

G. Fabbiano, E. Feigelson, and G. Zamorani. X-ray observations of peculiar galaxies with the Einstein Observatory. *The Astrophysical Journal*, 256:397–409, May 1982. doi: 10.1086/159917.

G. Fabbiano, I. M. Gioia, and G. Trinchieri. Radio emission and the hot interstellar medium of early-type galaxies. *The Astrophysical Journal*, 347:127–143, December 1989. doi: 10.1086/168103.

A. C. Fabian. UHURU - The first X-ray astronomy satellite. *Journal of the British Interplanetary Society*, 28:343–346, May 1975.

A. C. Fabian. The origin of the continuum of AGN and the X ray background. In J. Hunt and B. Battrick, editors, *Two Topics in X-Ray Astronomy, Volume 1: X Ray Binaries. Volume 2: AGN and the X Ray Background*, volume 296 of *ESA Special Publication*, pages 1097–1104, November 1989.

A. C. Fabian. Obscured AGN and galaxy formation. In *AAS/High Energy Astrophysics Division #5*, volume 32 of *Bulletin of the American Astronomical Society*, page 1194, October 2000.

D. Fadda, B. T. Jannuzi, A. Ford, and L. J. Storrie-Lombardi. The Spitzer Space Telescope First-Look Survey: KPNO Mosaic-1 R-Band Images and Source Catalogs. *The Astronomical Journal*, 128:1–15, July 2004. doi: 10.1086/421366.

E. E. Falco, M. J. Kurtz, M. J. Geller, J. P. Huchra, J. Peters, P. Berlind, D. J. Mink, S. P. Tokarz, and B. Elwell. The Updated Zwicky Catalog (UZC). *Publications of the Astronomical Society of the Pacific*, 111:438–452, April 1999. doi: 10.1086/316343.

Y.-Z. Fan, T. Piran, R. Narayan, and D.-M. Wei. High-energy afterglow emission from gamma-ray bursts. *Monthly Notices of the Royal Astronomical Society*, 384:1483–1501, March 2008. doi: 10.1111/j.1365-2966.2007.12765.x.

D. Faria, S. Feltzing, I. Lundström, G. Gilmore, G. M. Wahlgren, A. Ardeberg, and P. Linde. The usage of Strömgren photometry in studies of local group dwarf spheroidal galaxies. Application to Draco: a new catalogue of Draco members and a study of the metallicity distribution function and radial gradients. *Astronomy & Astrophysics*, 465:357–373, April 2007. doi: 10.1051/0004-6361:20065244.

Y. Fenner, B. K. Gibson, R. Gallino, and M. Lugaro. Cosmological Implications of Dwarf Spheroidal Chemical Evolution. *The Astrophysical Journal*, 646:184–191, July 2006. doi: 10.1086/504893.

E. L. Fitzpatrick. Correcting for the Effects of Interstellar Extinction. *Publications of the Astronomical Society of the Pacific*, 111:63–75, January 1999. doi: 10.1086/316293.

E. Flesch. An All-Sky Atlas of Radio/X-ray Associations. *Publications of the Astron. Soc. of Australia*, 27:283–289, June 2010. doi: 10.1071/AS09060.

C. Gallart, D. Martinez-Delgado, M. A. Gómez-Flechoso, and M. Mateo. Radial Velocity of the Phoenix Dwarf Galaxy: Linking Stars and H I Gas. *The Astronomical Journal*, 121:2572–2583, May 2001. doi: 10.1086/320395.

K. D. Gazeas, A. Baran, P. Niarchos, S. Zola, J. M. Kreiner, W. Ogloza, S. M. Rucinski, B. Zakrzewski, M. Siwak, A. Pigulski, and M. Drozdz. Physical Parameters of Components in Close Binary Systems: IV. *Acta Astronomica*, 55: 123–140, March 2005.

N. Gehrels, G. Chincarini, P. Giommi, K. O. Mason, J. A. Nousek, A. A. Wells, N. E. White, S. D. Barthelmy, D. N. Burrows, L. R. Cominsky, K. C. Hurley, F. E. Marshall, P. Mészáros, P. W. A. Roming, L. Angelini, L. M. Barbier, T. Belloni, S. Campana, P. A. Caraveo, M. M. Chester, O. Citterio, T. L. Cline, M. S. Cropper, J. R. Cummings, A. J. Dean, E. D. Feigelson, E. E. Fenimore, D. A. Frail, A. S. Fruchter, G. P. Garmire, K. Gendreau, G. Ghisellini, J. Greiner, J. E. Hill, S. D. Hunsberger, H. A. Krimm, S. R. Kulkarni, P. Kumar, F. Lebrun, N. M. Lloyd-Ronning, C. B. Markwardt, B. J. Mattson, R. F. Mushotzky, J. P. Norris, J. Osborne, B. Paczynski, D. M. Palmer, H.-S. Park, A. M. Parsons, J. Paul, M. J. Rees, C. S. Reynolds, J. E. Rhoads, T. P. Sasseen, B. E. Schaefer, A. T. Short, A. P. Smale, I. A. Smith, L. Stella, G. Tagliaferri, T. Takahashi, M. Tashiro, L. K. Townsley, J. Tueller, M. J. L. Turner, M. Vietri, W. Voges, M. J. Ward, R. Willingale, F. M. Zerbi, and W. W. Zhang. The Swift Gamma-Ray Burst Mission. *The Astrophysical Journal*, 611:1005–1020, August 2004. doi: 10.1086/422091.

H. Gerola, P. Carnevali, and E. E. Salpeter. Dwarf elliptical galaxies. *The Astrophysical Journal Letters*, 268:L75–L78, May 1983. doi: 10.1086/184032.

M. T. Geske, S. J. Gettel, and T. A. McKay. A ROSAT Survey of Contact Binary Stars. *The Astronomical Journal*, 131:633–637, January 2006. doi: 10.1086/498018.

K. K. Ghosh, V. Suleymanov, I. Bikmaev, S. Shimansky, and N. Sakhibullin. RBS 1032: a dwarf-nucleated spheroidal galaxy with an intermediate-mass black hole hosted in a globular cluster. *Monthly Notices of the Royal Astronomical Society*, 371:1587–1593, October 2006. doi: 10.1111/j.1365-2966.2006.10723.x.

M. Gilfanov. Low-mass X-ray binaries as a stellar mass indicator for the host galaxy. *Monthly Notices of the Royal Astronomical Society*, 349:146–168, March 2004. doi: 10.1111/j.1365-2966.2004.07473.x.

P. Giommi, A. J. Blustin, M. Capalbi, S. Colafrancesco, A. Cucchiara, L. Fuhrmann, H. A. Krimm, N. Marchili, E. Massaro, M. Perri, G. Tagliaferri, G. Tosti, A. Tramacere, D. N. Burrows, G. Chincarini, A. Falcone, N. Gehrels, J. Kennea, and R. Sambruna. Swift and infra-red observations of the blazar 3C 454.3 during the giant X-ray flare of May 2005. *Astronomy & Astrophysics*, 456:911–916, September 2006. doi: 10.1051/0004-6361:20064874.

T. M. Girard, W. F. van Altena, N. Zacharias, K. Vieira, D. I. Casetti-Dinescu, D. Castillo, D. Herrera, Y. S. Lee, T. C. Beers, D. G. Monet, and C. E. López. The Southern Proper Motion Program. IV. The SPM4 Catalog. *The Astronomical Journal*, 142:15, July 2011. doi: 10.1088/0004-6256/142/1/15.

L. Girardi, E. K. Grebel, M. Odenkirchen, and C. Chiosi. Theoretical isochrones in several photometric systems. II. The Sloan Digital Sky Survey ugriz system. *Astronomy & Astrophysics*, 422:205–215, July 2004. doi: 10.1051/0004-6361:20040250.

P. Gondoin. X-ray spectroscopy of the W UMa-type binary VW Cephei. *Astronomy & Astrophysics*, 415:1113–1121, March 2004a. doi: 10.1051/0004-6361:20034416.

P. Gondoin. X-ray spectroscopy of the W UMa-type binary 44 Bootis. *Astronomy & Astrophysics*, 426:1035–1045, November 2004b. doi: 10.1051/0004-6361:20040494.

E. K. Grebel, J. S. Gallagher, III, and D. Harbeck. The Progenitors of Dwarf Spheroidal Galaxies. *The Astronomical Journal*, 125:1926–1939, April 2003. doi: 10.1086/368363.

H.-J. Grimm, M. Gilfanov, and R. Sunyaev. The Milky Way in X-rays for an outside observer. Log(N)-Log(S) and luminosity function of X-ray binaries from RXTE/ASM data. *Astronomy & Astrophysics*, 391:923–944, September 2002. doi: 10.1051/0004-6361:20020826.

H.-J. Grimm, M. Gilfanov, and R. Sunyaev. High-mass X-ray binaries as a star formation rate indicator in distant galaxies. *Monthly Notices of the Royal Astronomical Society*, 339:793–809, March 2003. doi: 10.1046/j.1365-8711.2003.06224.x.

M. Güdel. X-ray astronomy of stellar coronae. *The Astronomy & Astrophysics Review*, 12:71–237, September 2004. doi: 10.1007/s00159-004-0023-2.

M. Güdel and Y. Nazé. X-ray spectroscopy of stars. *The Astronomy & Astrophysics Review*, 17:309–408, September 2009. doi: 10.1007/s00159-009-0022-4.

M. Gullieuszik, E. V. Held, I. Saviane, and L. Rizzi. New constraints on the chemical evolution of the dwarf spheroidal galaxy Leo I from VLT spectroscopy. *Astronomy & Astrophysics*, 500:735–747, June 2009. doi: 10.1051/0004-6361/200811578.

H. Gursky, E. Kellogg, S. Murray, C. Leong, H. Tananbaum, and R. Giacconi. A Strong X-Ray Source in the Coma Cluster Observed by UHURU. *The Astrophysical Journal Letters*, 167:L81, August 1971. doi: 10.1086/180765.

S. D. J. Gwyn. MegaPipe: The MegaCam Image Stacking Pipeline at the Canadian Astronomical Data Centre. *Publications of the Astronomical Society of the Pacific*, 120:212–223, February 2008. doi: 10.1086/526794.

E. Hayashi, J. F. Navarro, J. E. Taylor, J. Stadel, and T. Quinn. The Structural Evolution of Substructure. *The Astrophysical Journal*, 584:541–558, February 2003. doi: 10.1086/345788.

E. V. Held, M. Gullieuszik, L. Rizzi, L. Girardi, P. Marigo, and I. Saviane. A near-infrared study of AGB and red giant stars in the Leo I dSph galaxy. *Monthly Notices of the Royal Astronomical Society*, 404:1475–1489, May 2010. doi: 10.1111/j.1365-2966.2010.16358.x.

A. Henden and U. Munari. Multi-Epoch UBVRcIc Photometric Catalog of Symbiotic Stars. *Baltic Astronomy*, 17:293–300, 2008.

S. L. Hidalgo, A. Aparicio, D. Martínez-Delgado, and C. Gallart. On the Extended Structure of the Phoenix Dwarf Galaxy. *The Astrophysical Journal*, 705:704–716, November 2009. doi: 10.1088/0004-637X/705/1/704.

S. L. Hidalgo, M. Monelli, A. Aparicio, C. Gallart, E. D. Skillman, S. Cassisi, E. J. Bernard, L. Mayer, P. Stetson, A. Cole, and A. Dolphin. The ACS LCID Project. IX. Imprints of the Early Universe in the Radial Variation of the Star Formation History of Dwarf Galaxies. *The Astrophysical Journal*, 778:103, December 2013. doi: 10.1088/0004-637X/778/2/103.

J. G. Hills. The formation of binaries containing black holes by the exchange of companions and the X-ray sources in globular clusters. *Monthly Notices of the Royal Astronomical Society*, 175:1P–4P, April 1976.

M. Hunsch, J. H. M. M. Schmitt, K.-P. Schroder, and F.-J. Zickgraf. On the X-ray emission from M-type giants. *Astronomy & Astrophysics*, 330:225–231, February 1998.

R. Indebetouw, J. S. Mathis, B. L. Babler, M. R. Meade, C. Watson, B. A. Whitney, M. J. Wolff, M. G. Wolfire, M. Cohen, T. M. Bania, R. A. Benjamin, D. P. Clemens, J. M. Dickey, J. M. Jackson, H. A. Kobulnicky, A. P. Marston, E. P. Mercer, J. R. Stauffer, S. R. Stolovy, and E. Churchwell. The Wavelength Dependence of Interstellar Extinction from 1.25 to 8.0 μm Using GLIMPSE Data. *The Astrophysical Journal*, 619:931–938, February 2005. doi: 10.1086/426679.

J. A. Irwin, A. E. Athey, and J. N. Bregman. X-Ray Spectral Properties of Low-Mass X-Ray Binaries in Nearby Galaxies. *The Astrophysical Journal*, 587:356–366, April 2003. doi: 10.1086/368179.

M. Irwin and D. Hatzidimitriou. Structural parameters for the Galactic dwarf spheroidals. *Monthly Notices of the Royal Astronomical Society*, 277:1354–1378, December 1995.

F. Jansen, D. Lumb, B. Altieri, J. Clavel, M. Ehle, C. Erd, C. Gabriel, M. Guainazzi, P. Gondoin, R. Much, R. Munoz, M. Santos, N. Schartel, D. Texier, and G. Vacanti. XMM-Newton observatory. I. The spacecraft and operations. *Astronomy & Astrophysics*, 365:L1–L6, January 2001. doi: 10.1051/0004-6361:20000036.

J. R. Jardel, K. Gebhardt, M. H. Fabricius, N. Drory, and M. J. Williams. Measuring Dark Matter Profiles Non-Parametrically in Dwarf Spheroidals: An Application to Draco. *The Astrophysical Journal*, 763:91, February 2013. doi: 10.1088/0004-637X/763/2/91.

T. E. Jeltema and S. Profumo. Searching for Dark Matter with X-Ray Observations of Local Dwarf Galaxies. *The Astrophysical Journal*, 686:1045–1055, October 2008. doi: 10.1086/591495.

D. H. Jones, M. A. Read, W. Saunders, M. Colless, T. Jarrett, Q. A. Parker, A. P. Fairall, T. Mauch, E. M. Sadler, F. G. Watson, D. Burton, L. A. Campbell, P. Cass, S. M. Croom, J. Dawe, K. Fiegert, L. Frankcombe, M. Hartley, J. Huchra, D. James, E. Kirby, O. Lahav, J. Lucey, G. A. Mamon, L. Moore, B. A. Peterson, S. Prior, D. Proust, K. Russell, V. Safouris, K.-I. Wakamatsu, E. Westra, and M. Williams. The 6dF Galaxy Survey: final redshift release (DR3) and southern large-scale structures. *Monthly Notices of the Royal Astronomical Society*, 399:683–698, October 2009. doi: 10.1111/j.1365-2966.2009.15338.x.

P. Jovanović and L. Č. Popović. X-ray Emission From Accretion Disks of AGN: Signatures of Supermassive Black Holes. *ArXiv e-prints*, March 2009.

W. A. Joye and E. Mandel. New Features of SAOImage DS9. In H. E. Payne, R. I. Jedrzejewski, and R. N. Hook, editors, *Astronomical Data Analysis Software and Systems XII*, volume 295 of *Astronomical Society of the Pacific Conference Series*, page 489, 2003.

J. S. Kaastra and R. Mewe. Coronal Plasmas Modeling and the MEKAL code. In M. A. Bautista, T. R. Kallman, and A. K. Pradhan, editors, *Atomic Data Needs for X-ray Astronomy*, page 161, October 2000.

P. M. W. Kalberla, W. B. Burton, D. Hartmann, E. M. Arnal, E. Bajaja, R. Morras, and W. G. L. Pöppel. The Leiden/Argentine/Bonn (LAB) Survey of Galactic HI. Final data release of the combined LDS and IAR surveys with improved stray-radiation corrections. *Astronomy & Astrophysics*, 440:775–782, September 2005. doi: 10.1051/0004-6361:20041864.

V. Kalogera. Orbital Characteristics of Binary Systems after Asymmetric Supernova Explosions. *The Astrophysical Journal*, 471:352, November 1996. doi: 10.1086/177974.

S. Kazantzidis, L. Mayer, C. Mastropietro, J. Diemand, J. Stadel, and B. Moore. Density Profiles of Cold Dark Matter Substructure: Implications for the Missing-Satellites Problem. *The Astrophysical Journal*, 608:663–679, June 2004. doi: 10.1086/420840.

S. J. Kenyon. *The symbiotic stars*. 1986.

D.-W. Kim and G. Fabbiano. X-Ray Luminosity Function and Total Luminosity of Low-Mass X-Ray Binaries in Early-Type Galaxies. *The Astrophysical Journal*, 611:846–857, August 2004. doi: 10.1086/422210.

K. Kinemuchi, H. C. Harris, H. A. Smith, N. A. Silbermann, L. A. Snyder, A. P. La Cluyzé, and C. L. Clark. The Variable Stars of the Draco Dwarf Spheroidal Galaxy: Revisited. *The Astronomical Journal*, 136:1921–1939, November 2008. doi: 10.1088/0004-6256/136/5/1921.

I. King. The structure of star clusters. I. an empirical density law. *The Astronomical Journal*, 67:471, October 1962. doi: 10.1086/108756.

E. N. Kirby, J. G. Cohen, P. Guhathakurta, L. Cheng, J. S. Bullock, and A. Gallazzi. The Universal Stellar Mass-Stellar Metallicity Relation for Dwarf Galaxies. *The Astrophysical Journal*, 779:102, December 2013. doi: 10.1088/0004-637X/779/2/102.

R. S. Klessen, E. K. Grebel, and D. Harbeck. Draco: A Failure of the Tidal Model. *The Astrophysical Journal*, 589:798–809, June 2003. doi: 10.1086/374816.

J. Kleyna, M. I. Wilkinson, N. W. Evans, G. Gilmore, and C. Frayn. Dark matter in dwarf spheroidals - II. Observations and modelling of Draco. *Monthly Notices of the Royal Astronomical Society*, 330:792–806, March 2002. doi: 10.1046/j.1365-8711.2002.05155.x.

J. T. Kleyna, M. I. Wilkinson, N. W. Evans, and G. Gilmore. First Clear Signature of an Extended Dark Matter Halo in the Draco Dwarf Spheroidal. *The Astrophysical Journal Letters*, 563:L115–L118, December 2001. doi: 10.1086/338603.

A. Klypin, A. V. Kravtsov, O. Valenzuela, and F. Prada. Where Are the Missing Galactic Satellites? *The Astrophysical Journal*, 522:82–92, September 1999. doi: 10.1086/307643.

J. H. Knapen, S. Erroz-Ferrer, J. Roa, J. Bakos, M. Cisternas, R. Leaman, and N. Szymanek. Optical imaging for the Spitzer Survey of Stellar Structure in Galaxies. Data release and notes on interacting galaxies. *Astronomy & Astrophysics*, 569:A91, September 2014. doi: 10.1051/0004-6361/201322954.

R. P. Kraft, J. M. Kregenow, W. R. Forman, C. Jones, and S. S. Murray. Chandra Observations of the X-Ray Point Source Population in Centaurus A. *The Astrophysical Journal*, 560:675–688, October 2001. doi: 10.1086/323056.

J. H. Krolik. *Active galactic nuclei : from the central black hole to the galactic environment*. 1999.

P. Kroupa. Dwarf spheroidal satellite galaxies without dark matter. *New Astronomy*, 2:139–164, July 1997. doi: 10.1016/S1384-1076(97)00012-2.

S. Kwok and D. A. Leahy. X-ray emissions from symbiotic novae. *The Astrophysical Journal*, 283:675–678, August 1984. doi: 10.1086/162353.

J. G. Laros, J. L. Matteson, and R. M. Pelling. A Search for Hard X-Rays from Extragalactic Objects. *The Astrophysical Journal*, 179:375–380, January 1973. doi: 10.1086/151876.

M. D. Lehnert, R. A. Bell, J. E. Hesser, and J. B. Oke. Abundances for giant stars in the Draco dwarf galaxy. *The Astrophysical Journal*, 395:466–474, August 1992. doi: 10.1086/171666.

W. H. G. Lewin and P. C. Joss. X-Ray Bursters and the X-Ray Sources of the Galactic Bulge. In W. H. G. Lewin and E. P. J. van den Heuvel, editors, *Accretion-Driven Stellar X-ray Sources*, page 41, 1983.

V. M. Lipunov, K. A. Postnov, and M. E. Prokhorov. The Scenario Machine: restrictions on key parameters of binary evolution. *Astronomy & Astrophysics*, 310:489–507, June 1996.

E. L. Łokas. Dark matter distribution in dwarf spheroidal galaxies. *Monthly Notices of the Royal Astronomical Society*, 333:697–708, July 2002. doi: 10.1046/j.1365-8711.2002.05457.x.

E. L. Łokas. The mass and velocity anisotropy of the Carina, Fornax, Sculptor and Sextans dwarf spheroidal galaxies. *Monthly Notices of the Royal Astronomical Society*, 394:L102–L106, March 2009. doi: 10.1111/j.1745-3933.2009.00620.x.

E. L. Łokas, G. A. Mamon, and F. Prada. Dark matter distribution in the Draco dwarf from velocity moments. *Monthly Notices of the Royal Astronomical Society*, 363:918–928, November 2005. doi: 10.1111/j.1365-2966.2005.09497.x.

N. R. Lomb. Least-squares frequency analysis of unequally spaced data. *Provided by the SAO/NASA Astrophysics Data System*, 39:447–462, February 1976. doi: 10.1007/BF00648343.

K. S. Long, D. J. Helfand, and D. A. Grabelsky. A soft X-ray study of the Large Magellanic Cloud. *The Astrophysical Journal*, 248:925–944, September 1981. doi: 10.1086/159222.

M. S. Longair. *High Energy Astrophysics*. February 2011.

L. B. Lucy. The Structure of Contact Binaries. *The Astrophysical Journal*, 151: 1123, March 1968. doi: 10.1086/149510.

D. H Lumb, N. Schartel, and F. A Jansen. XMM-Newton (X-Ray Mulit-Mirror Mission) Observatory. *ArXiv e-prints*, February 2012.

A. G. Lyne and D. R. Lorimer. High birth velocities of radio pulsars. *Nature*, 369: 127–129, May 1994. doi: 10.1038/369127a0.

T. Maccacaro, I. M. Gioia, A. Wolter, G. Zamorani, and J. T. Stocke. The X-ray spectra of the extragalactic sources in the Einstein extended medium sensitivity survey. *The Astrophysical Journal*, 326:680–690, March 1988. doi: 10.1086/166127.

T. J. Maccarone, A. Kundu, S. E. Zepf, A. L. Piro, and L. Bildsten. The discovery of X-ray binaries in the Sculptor dwarf spheroidal galaxy. *Monthly Notices of the Royal Astronomical Society*, 364:L61–L65, November 2005. doi: 10.1111/j.1745-3933.2005.00106.x.

T. J. Maccarone, T. M. Girard, and D. I. Casetti-Dinescu. High proper motion X-ray binaries from the Yale Southern Proper Motion Survey. *Monthly Notices of the Royal Astronomical Society*, 440:1626–1633, May 2014. doi: 10.1093/mnras/stu320.

J. Magorrian, S. Tremaine, D. Richstone, R. Bender, G. Bower, A. Dressler, S. M. Faber, K. Gebhardt, R. Green, C. Grillmair, J. Kormendy, and T. Lauer. The Demography of Massive Dark Objects in Galaxy Centers. *The Astronomical Journal*, 115:2285–2305, June 1998. doi: 10.1086/300353.

D. Malyshev, A. Neronov, and D. Eckert. Constraints on 3.55 keV line emission from stacked observations of dwarf spheroidal galaxies. *Provided by the SAO/NASA Astrophysics Data System*, 90(10):103506, November 2014. doi: 10.1103/PhysRevD.90.103506.

L. Manni, A. A. Nucita, F. De Paolis, V. Testa, and G. Ingrosso. A XMM-Newton observation of a sample of four close dwarf spheroidal galaxies. *Monthly Notices of the Royal Astronomical Society*, 451:2735–2749, August 2015. doi: 10.1093/mnras/stv1009.

B. Margon, S. F. Anderson, H. C. Harris, M. A. Strauss, G. R. Knapp, X. Fan, D. P. Schneider, D. E. Vanden Berk, D. J. Schlegel, E. W. Deutsch, Ž. Ivezić, P. B. Hall, B. F. Williams, A. F. Davidsen, J. Brinkmann, I. Csabai, J. J. E. Hayes, G. Hennessy, E. K. Kinney, S. J. Kleinman, D. Q. Lamb, D. Long, E. H. Neilsen, R. Nichol, A. Nitta, S. A. Snedden, and D. G. York. Faint High-Latitude Carbon Stars Discovered by the Sloan Digital Sky Survey: Methods and Initial Results. *The Astronomical Journal*, 124:1651–1669, September 2002. doi: 10.1086/342284.

D. Martinez-Delgado, C. Gallart, and A. Aparicio. The Stellar Content of the Local Group Dwarf Galaxy PHOENIX. *The Astronomical Journal*, 118:862–882, August 1999. doi: 10.1086/300967.

R. O. Marzke and L. N. da Costa. The Galaxy Luminosity Function. *The Astronomical Journal*, 113:185, January 1997. doi: 10.1086/118243.

S. Mashchenko, H. M. P. Couchman, and A. Sills. Modeling Star Formation in Dwarf Spheroidal Galaxies: A Case for Extended Dark Matter Halos. *The Astrophysical Journal*, 624:726–741, May 2005. doi: 10.1086/429403.

S. Mashchenko, A. Sills, and H. M. Couchman. Constraining Global Properties of the Draco Dwarf Spheroidal Galaxy. *The Astrophysical Journal*, 640:252–269, March 2006. doi: 10.1086/499940.

K. O. Mason, A. Breeveld, R. Much, M. Carter, F. A. Cordova, M. S. Cropper, J. Fordham, H. Huckle, C. Ho, H. Kawakami, J. Kennea, T. Kennedy, J. Mittaz, D. Pandel, W. C. Priedhorsky, T. Sasseen, R. Shirey, P. Smith, and J.-M. Vreux. The XMM-Newton optical/UV monitor telescope. *Astronomy & Astrophysics*, 365:L36–L44, January 2001. doi: 10.1051/0004-6361:20000044.

P. Massey, K. A. G. Olsen, P. W. Hodge, G. H. Jacoby, R. T. McNeill, R. C. Smith, and S. B. Strong. A Survey of Local Group Galaxies Currently Forming Stars. II. UBVRI Photometry of Stars in Seven Dwarfs and a Comparison of the Entire Sample. *The Astronomical Journal*, 133:2393–2417, May 2007a. doi: 10.1086/513319.

R. Massey, J. Rhodes, R. Ellis, N. Scoville, A. Leauthaud, A. Finoguenov, P. Capak, D. Bacon, H. Aussel, J.-P. Kneib, A. Koekemoer, H. McCracken, B. Mobasher, S. Pires, A. Refregier, S. Sasaki, J.-L. Starck, Y. Taniguchi, A. Taylor, and J. Taylor. Dark matter maps reveal cosmic scaffolding. *Nature*, 445:286–290, January 2007b. doi: 10.1038/nature05497.

M. Mateo, E. W. Olszewski, and M. G. Walker. The Velocity Dispersion Profile of the Remote Dwarf Spheroidal Galaxy Leo I: A Tidal Hit and Run? *The Astrophysical Journal*, 675:201–233, March 2008. doi: 10.1086/522326.

M. L. Mateo. Dwarf Galaxies of the Local Group. *Annual Review of Astronomy & Astrophysics*, 36:435–506, 1998. doi: 10.1146/annurev.astro.36.1.435.

L. Mayer, F. Governato, M. Colpi, B. Moore, T. Quinn, J. Wadsley, J. Stadel, and G. Lake. Tidal Stirring and the Origin of Dwarf Spheroidals in the Local Group. *The Astrophysical Journal Letters*, 547:L123–L127, February 2001a. doi: 10.1086/318898.

L. Mayer, F. Governato, M. Colpi, B. Moore, T. Quinn, J. Wadsley, J. Stadel, and G. Lake. The Metamorphosis of Tidally Stirred Dwarf Galaxies. *The Astrophysical Journal*, 559:754–784, October 2001b. doi: 10.1086/322356.

A. W. McConnachie. The Observed Properties of Dwarf Galaxies in and around the Local Group. *The Astronomical Journal*, 144:4, July 2012. doi: 10.1088/0004-6256/144/1/4.

M. Metz and P. Kroupa. Dwarf spheroidal satellites: are they of tidal origin? *Monthly Notices of the Royal Astronomical Society*, 376:387–392, March 2007. doi: 10.1111/j.1365-2966.2007.11438.x.

R. R. Muñoz, P. M. Frinchaboy, S. R. Majewski, J. R. Kuhn, M.-Y. Chou, C. Palma, S. T. Sohn, R. J. Patterson, and M. H. Siegel. Exploring Halo Substructure with Giant Stars: The Velocity Dispersion Profiles of the Ursa Minor and Draco Dwarf Spheroidal Galaxies at Large Angular Separations. *The Astrophysical Journal Letters*, 631:L137–L141, October 2005. doi: 10.1086/497396.

U. Munari and L. M. Buson. The ultraviolet spectra of the symbiotic stars MWC 960, FN Sgr, SS 29 and Draco C-1. *Astronomy & Astrophysics*, 287:87–94, July 1994.

R. Narayan, T. Piran, and P. Kumar. Accretion Models of Gamma-Ray Bursts. *The Astrophysical Journal*, 557:949–957, August 2001. doi: 10.1086/322267.

J. M. Nemec. Double-Mode Rr-Lyrae Stars in the Draco Dwarf Galaxy and in Other Stellar Systems. In A. Maeder and A. Renzini, editors, *Observational Tests of the Stellar Evolution Theory*, volume 105 of *IAU Symposium*, page 465, 1984.

A. A. Nucita, L. Manni, F. De Paolis, D. Vetrugno, and G. Ingrosso. An XMM-Newton search for X-ray sources in the Fornax dwarf galaxy. *Astronomy & Astrophysics*, 550:A18, February 2013. doi: 10.1051/0004-6361/201220152.

M. Odenkirchen, E. K. Grebel, D. Harbeck, W. Dehnen, H.-W. Rix, H. J. Newberg, B. Yanny, J. Holtzman, J. Brinkmann, B. Chen, I. Csabai, J. J. E. Hayes, G. Hennessy, R. B. Hindsley, Ž. Ivezić, E. K. Kinney, S. J. Kleinman, D. Long, R. H. Lupton, E. H. Neilsen, A. Nitta, S. A. Snedden, and D. G. York. New Insights on the Draco Dwarf Spheroidal Galaxy from the Sloan Digital Sky

Survey: A Larger Radius and No Tidal Tails. *The Astronomical Journal*, 122: 2538–2553, November 2001. doi: 10.1086/323715.

E. W. Olszewski, M. Aaronson, and J. M. Hill. Nine Seasons of Velocity Measurements in the Draco and Ursa Minor Dwarf Spheroidal Galaxies with the MMT Echelle. *The Astronomical Journal*, 110:2120, November 1995. doi: 10.1086/117674.

B. Paczyński. Evolutionary Processes in Close Binary Systems. *Annual Review of Astronomy & Astrophysics*, 9:183, 1971. doi: 10.1146/annurev.aa.09.090171.001151.

B. Paczyński. Are Gamma-Ray Bursts in Star-Forming Regions? *The Astrophysical Journal Letters*, 494:L45–L48, February 1998. doi: 10.1086/311148.

T. Padmanabhan. *Theoretical Astrophysics - Volume 3, Galaxies and Cosmology*. December 2002.

J. Peñarrubia, J. F. Navarro, A. W. McConnachie, and N. F. Martin. The Signature of Galactic Tides in Local Group Dwarf Spheroidals. *The Astrophysical Journal*, 698:222–232, June 2009. doi: 10.1088/0004-637X/698/1/222.

E. Pfahl, S. Rappaport, P. Podsiadlowski, and H. Spruit. A New Class of High-Mass X-Ray Binaries: Implications for Core Collapse and Neutron Star Recoil. *The Astrophysical Journal*, 574:364–376, July 2002. doi: 10.1086/340794.

S. Piatek, C. Pryor, T. E. Armandroff, and E. W. Olszewski. Stars of the Draco Dwarf Spheroidal Galaxy Beyond Its Measured Tidal Boundary. *The Astronomical Journal*, 121:841–860, February 2001. doi: 10.1086/318755.

S. Piatek, C. Pryor, E. W. Olszewski, H. C. Harris, M. Mateo, D. Minniti, D. G. Monet, H. Morrison, and C. G. Tinney. Proper Motions of Dwarf Spheroidal Galaxies from Hubble Space Telescope Imaging. I. Method and a Preliminary Measurement for Fornax. *The Astronomical Journal*, 124:3198–3221, December 2002. doi: 10.1086/344767.

W. Pietsch, M. Freyberg, and F. Haberl. An XMM-Newton survey of M 31 (Pietsch+, 2005). *VizieR Online Data Catalog*, 343:40483, November 2004.

T. Piran. The physics of gamma-ray bursts. *Reviews of Modern Physics*, 76: 1143–1210, October 2004. doi: 10.1103/RevModPhys.76.1143.

A. L. Piro and L. Bildsten. Transient X-Ray Binaries in Elliptical Galaxies. *The Astrophysical Journal Letters*, 571:L103–L106, June 2002. doi: 10.1086/341341.

E. Pointecouteau, M. Arnaud, and G. W. Pratt. The structural and scaling properties of nearby galaxy clusters. I. The universal mass profile. *Astronomy & Astrophysics*, 435:1–7, May 2005. doi: 10.1051/0004-6361:20042569.

K. A. Postnov and L. R. Yungelson. The Evolution of Compact Binary Star Systems. *Living Reviews in Relativity*, 9:6, December 2006. doi: 10.12942/lrr-2006-6.

W. H. Press, S. A. Teukolsky, W. T. Vetterling, and B. P. Flannery. *Numerical recipes in FORTRAN. The art of scientific computing*. 1992.

S. Randich. Supersaturation in X-ray Emission of Cluster Stars. In R. A. Donahue and J. A. Bookbinder, editors, *Cool Stars, Stellar Systems, and the Sun*, volume 154 of *Astronomical Society of the Pacific Conference Series*, page 501, 1998.

H. A. Rave, C. Zhao, H. J. Newberg, B. Yanny, D. P. Schneider, J. Brinkman, and D. Q. Lamb. Sloan Digital Sky Survey Catalog of Stars in the Draco Dwarf Spheroidal Galaxy. *The Astrophysical Journal Supplement Series*, 145:245–258, April 2003. doi: 10.1086/367724.

A. M. Read, S. R. Rosen, R. D. Saxton, and J. Ramirez. A new comprehensive 2D model of the point spread functions of the XMM-Newton EPIC telescopes: spurious source suppression and improved positional accuracy. *Astronomy & Astrophysics*, 534:A34, October 2011. doi: 10.1051/0004-6361/201117525.

J. I. Read, M. I. Wilkinson, N. W. Evans, G. Gilmore, and J. T. Kleyna. The importance of tides for the Local Group dwarf spheroidals. *Monthly Notices of the Royal Astronomical Society*, 367:387–399, March 2006. doi: 10.1111/j.1365-2966.2005.09959.x.

P. Reig. Be/X-ray binaries. *Provided by the SAO/NASA Astrophysics Data System*, 332:1–29, March 2011. doi: 10.1007/s10509-010-0575-8.

G. T. Richards, A. D. Myers, A. G. Gray, R. N. Riegel, R. C. Nichol, R. J. Brunner, A. S. Szalay, D. P. Schneider, and S. F. Anderson. Efficient Photometric Selection of Quasars from the Sloan Digital Sky Survey. II. ˜1,000,000 Quasars from Data Release 6. *The Astrophysical Journal Supplement Series*, 180:67–83, January 2009. doi: 10.1088/0067-0049/180/1/67.

P. L. Richards. Fourier Transform Spectroscopy. In D. H. Martin, editor, *Spectroscopic Techniques for Far Infra-red, Submillimetre and Millimetre Waves*, page 33, 1967.

G. R. Ricker, J.-L. Atteia, G. B. Crew, J. P. Doty, E. E. Fenimore, M. Galassi, C. Graziani, K. Hurley, J. G. Jernigan, N. Kawai, D. Q. Lamb, M. Matsuoka, G. Pizzichini, Y. Shirasaki, T. Tamagawa, R. Vanderspek, G. Vedrenne, J. Villasenor, S. E. Woosley, and A. Yoshida. The High Energy Transient Explorer

(HETE): Mission and Science Overview. In G. R. Ricker and R. K. Vanderspek, editors, *Gamma-Ray Burst and Afterglow Astronomy 2001: A Workshop Celebrating the First Year of the HETE Mission*, volume 662 of *American Institute of Physics Conference Series*, pages 3–16, April 2003. doi: 10.1063/1.1579291.

S. Riemer-Sørensen and S. H. Hansen. Decaying dark matter in the Draco dwarf galaxy. *Astronomy & Astrophysics*, 500:L37–L40, June 2009. doi: 10.1051/0004-6361/200912430.

V. Ripepi, M. Marconi, M. I. Moretti, G. Clementini, M.-R. L. Cioni, R. de Grijs, J. P. Emerson, M. A. T. Groenewegen, V. D. Ivanov, and J. M. Oliveira. The VMC Survey - VIII. First results for anomalous Cepheids. *Monthly Notices of the Royal Astronomical Society*, 437:2307–2319, January 2014. doi: 10.1093/mnras/stt2047.

P. W. A. Roming, T. E. Kennedy, K. O. Mason, J. A. Nousek, L. Ahr, R. E. Bingham, P. S. Broos, M. J. Carter, B. K. Hancock, H. E. Huckle, S. D. Hunsberger, H. Kawakami, R. Killough, T. S. Koch, M. K. McLelland, K. Smith, P. J. Smith, J. C. Soto, P. T. Boyd, A. A. Breeveld, S. T. Holland, M. Ivanushkina, M. S. Pryzby, M. D. Still, and J. Stock. The Swift Ultra-Violet/Optical Telescope. *Space Science Reviews*, 120:95–142, October 2005. doi: 10.1007/s11214-005-5095-4.

S. Röser, E. Schilbach, H. Schwan, N. V. Kharchenko, A. E. Piskunov, and R.-D. Scholz. PPM-Extended (PPMX) - a catalogue of positions and proper motions. *Astronomy & Astrophysics*, 488:401–408, September 2008. doi: 10.1051/0004-6361:200809775.

S. M. Rucinski. Eclipsing Binaries in the OGLE Variable Star Catalog. III. Long-Period Contact Systems. *The Astronomical Journal*, 115:1135–1144, March 1998. doi: 10.1086/300266.

C. L. Sarazin. X-ray emission from clusters of galaxies. *Reviews of Modern Physics*, 58:1–115, January 1986. doi: 10.1103/RevModPhys.58.1.

J. D. Scargle. Studies in astronomical time series analysis. II - Statistical aspects of spectral analysis of unevenly spaced data. *The Astrophysical Journal*, 263: 835–853, December 1982. doi: 10.1086/160554.

E. F. Schlafly and D. P. Finkbeiner. Measuring Reddening with Sloan Digital Sky Survey Stellar Spectra and Recalibrating SFD. *The Astrophysical Journal*, 737: 103, August 2011. doi: 10.1088/0004-637X/737/2/103.

C. Schröder and J. H. M. M. Schmitt. X-ray emission from A-type stars. *Astronomy & Astrophysics*, 475:677–684, November 2007. doi: 10.1051/0004-6361:20077429.

N. S. Schulz, G. Hasinger, and J. Truemper. Spectral classification of low-mass X-ray binary (LMXB) energy spectra with color-color diagrams. *Astronomy & Astrophysics*, 225:48–68, November 1989.

A. E. Schweitzer, K. M. Cudworth, S. R. Majewski, and N. B. Suntzeff. The Absolute Proper Motion and a Membership Survey of the Sculptor Dwarf Spheroidal Galaxy. *The Astronomical Journal*, 110:2747, December 1995. doi: 10.1086/117727.

M. Ségall, R. A. Ibata, M. J. Irwin, N. F. Martin, and S. Chapman. Draco, a flawless dwarf galaxy. *Monthly Notices of the Royal Astronomical Society*, 375: 831–842, March 2007. doi: 10.1111/j.1365-2966.2006.11356.x.

F. D. Seward and P. A. Charles. *Exploring the X-ray Universe*. August 2010.

M. M. Shara, D. Prialnik, and G. Shaviv. Non-ejecting novae as EUV sources. *Astronomy & Astrophysics*, 61:363–367, November 1977.

J. S. Shaw, J.-P. Caillault, and J. H. M. M. Schmitt. Near-Contact Binary Systems in the ROSAT All-Sky Survey. *The Astrophysical Journal*, 461:951, April 1996. doi: 10.1086/177116.

M. D. Shetrone, P. Côté, and W. L. W. Sargent. Abundance Patterns in the Draco, Sextans, and Ursa Minor Dwarf Spheroidal Galaxies. *The Astrophysical Journal*, 548:592–608, February 2001. doi: 10.1086/319022.

V. Smolčić, D. B. Zucker, E. F. Bell, M. G. Coleman, H. W. Rix, E. Schinnerer, Ž. Ivezić, and A. Kniazev. Improved Photometry of Sloan Digital Sky Survey Crowded-Field Images: Structure and Dark Matter Content in the Dwarf Spheroidal Galaxy Leo I. *The Astronomical Journal*, 134:1901–1915, November 2007. doi: 10.1086/522369.

Y. Sofue. Ram-pressure stripping of gas from companions and accretion onto a spiral galaxy: A gaseous merger. *The Astrophysical Journal*, 423:207–222, March 1994. doi: 10.1086/173800.

J. Souchay, A. H. Andrei, C. Barache, S. Bouquillon, D. Suchet, F. Taris, and R. Peralta. The second release of the Large Quasar Astrometric Catalog (LQAC-2). *Astronomy & Astrophysics*, 537:A99, January 2012. doi: 10.1051/0004-6361/201117954.

P. B. Stetson. The dwarf spheroidal galaxy in Draco. I - New BV photometry. *The Astronomical Journal*, 84:1149–1172, August 1979. doi: 10.1086/112522.

P. B. Stetson, G. Fiorentino, G. Bono, E. J. Bernard, M. Monelli, G. Iannicola, C. Gallart, and I. Ferraro. Homogeneous Photometry VI: Variable Stars in the Leo I Dwarf Spheroidal Galaxy. *Publications of the Astronomical Society of the Pacific*, 126:616–641, July 2014. doi: 10.1086/677352.

H. Stiele, W. Pietsch, F. Haberl, D. Hatzidimitriou, R. Barnard, B. F. Williams, A. K. H. Kong, and U. Kolb. Deep XMM-Newton Survey of M31 (Stiele+, 2011). *VizieR Online Data Catalog*, 353:49055, August 2011.

F. Stoehr, S. D. M. White, G. Tormen, and V. Springel. The satellite population of the Milky Way in a ΛCDM universe. *Monthly Notices of the Royal Astronomical Society*, 335:L84–L88, October 2002. doi: 10.1046/j.1365-8711.2002.05891.x.

L. Strüder et al. The European Photon Imaging Camera on XMM-Newton: The pn-CCD camera. *Astronomy & Astrophysics*, 365:L18–L26, January 2001. doi: 10.1051/0004-6361:20000066.

T. M. Tauris and E. P. J. van den Heuvel. *Formation and evolution of compact stellar X-ray sources*, pages 623–665. April 2006.

J. E. Trümper and G. Hasinger. *The Universe in X-Rays*. 2008.

M. J. L. Turner, A. Abbey, M. Arnaud, M. Balasini, M. Barbera, E. Belsole, P. J. Bennie, J. P. Bernard, G. F. Bignami, M. Boer, U. Briel, I. Butler, C. Cara, C. Chabaud, R. Cole, A. Collura, M. Conte, A. Cros, M. Denby, P. Dhez, G. Di Coco, J. Dowson, P. Ferrando, S. Ghizzardi, F. Gianotti, C. V. Goodall, L. Gretton, R. G. Griffiths, O. Hainaut, J. F. Hochedez, A. D. Holland, E. Jourdain, E. Kendziorra, A. Lagostina, R. Laine, N. La Palombara, M. Lortholary, D. Lumb, P. Marty, S. Molendi, C. Pigot, E. Poindron, K. A. Pounds, J. N. Reeves, C. Reppin, R. Rothenflug, P. Salvetat, J. L. Sauvageot, D. Schmitt, S. Sembay, A. D. T. Short, J. Spragg, J. Stephen, L. Strüder, A. Tiengo, M. Trifoglio, J. Trümper, S. Vercellone, L. Vigroux, G. Villa, M. J. Ward, S. Whitehead, and E. Zonca. The European Photon Imaging Camera on XMM-Newton: The MOS cameras : The MOS cameras. *Astronomy & Astrophysics*, 365:L27–L35, January 2001. doi: 10.1051/0004-6361:20000087.

A. ud-Doula and S. P. Owocki. Dynamical Simulations of Magnetically Channeled Line-driven Stellar Winds. I. Isothermal, Nonrotating, Radially Driven Flow. *The Astrophysical Journal*, 576:413–428, September 2002. doi: 10.1086/341543.

C. M. Urry and P. Padovani. Unified Schemes for Radio-Loud Active Galactic Nuclei. *Publications of the Astronomical Society of the Pacific*, 107:803, September 1995. doi: 10.1086/133630.

V. V. Usov. Millisecond pulsars with extremely strong magnetic fields as a cosmological source of gamma-ray bursts. *Nature*, 357:472–474, June 1992. doi: 10.1038/357472a0.

G. S. Vaiana, J. P. Cassinelli, G. Fabbiano, R. Giacconi, L. Golub, P. Gorenstein, B. M. Haisch, F. R. Harnden, Jr., H. M. Johnson, J. L. Linsky, C. W. Maxson, R. Mewe, R. Rosner, F. Seward, K. Topka, and C. Zwaan. Results from an extensive Einstein stellar survey. *The Astrophysical Journal*, 245:163–182, April 1981. doi: 10.1086/158797.

E. P. J. van den Heuvel, D. Bhattacharya, K. Nomoto, and S. A. Rappaport. Accreting white dwarf models for CAL 83, CAL 87 and other ultrasoft X-ray sources in the LMC. *Astronomy & Astrophysics*, 262:97–105, August 1992.

E. C. Vasconcellos, R. R. de Carvalho, R. R. Gal, F. L. LaBarbera, H. V. Capelato, H. Frago Campos Velho, M. Trevisan, and R. S. R. Ruiz. Decision Tree Classifiers for Star/Galaxy Separation. *The Astronomical Journal*, 141:189, June 2011. doi: 10.1088/0004-6256/141/6/189.

M.-P. Véron-Cetty and P. Véron. A catalogue of quasars and active nuclei: 13th edition. *Astronomy & Astrophysics*, 518:A10, July 2010. doi: 10.1051/0004-6361/201014188.

M. P. Veron-Cetty and P. Veron. Quasars and Active Galactic Nuclei (13th Ed.) (Veron+ 2010). *VizieR Online Data Catalog*, 7258:0, February 2010.

M. Vietri and L. Stella. A Gamma-Ray Burst Model with Small Baryon Contamination. *The Astrophysical Journal Letters*, 507:L45–L48, November 1998. doi: 10.1086/311674.

O. Vilhu. What can we learn about contact binaries with the help of far UV and X-ray observations? *Highlights of Astronomy*, 6:643–644, 1983.

J. Vink. Supernova remnants: the X-ray perspective. *The Astronomy & Astrophysics Review*, 20:49, December 2012. doi: 10.1007/s00159-011-0049-1.

G. M. Voit. Tracing cosmic evolution with clusters of galaxies. *Reviews of Modern Physics*, 77:207–258, April 2005. doi: 10.1103/RevModPhys.77.207.

M. G. Walker and J. Peñarrubia. A Method for Measuring (Slopes of) the Mass Profiles of Dwarf Spheroidal Galaxies. *The Astrophysical Journal*, 742: 20, November 2011. doi: 10.1088/0004-637X/742/1/20.

M. G. Walker, M. Mateo, E. W. Olszewski, O. Y. Gnedin, X. Wang, B. Sen, and M. Woodroofe. Velocity Dispersion Profiles of Seven Dwarf Spheroidal Galaxies. *The Astrophysical Journal Letters*, 667:L53–L56, September 2007. doi: 10.1086/521998.

M. G. Watson, A. C. Schröder, D. Fyfe, C. G. Page, G. Lamer, S. Mateos, J. Pye, M. Sakano, S. Rosen, J. Ballet, X. Barcons, D. Barret, T. Boller, H. Brunner, M. Brusa, A. Caccianiga, F. J. Carrera, M. Ceballos, R. Della Ceca, M. Denby, G. Denkinson, S. Dupuy, S. Farrell, F. Fraschetti, M. J. Freyberg, P. Guillout, V. Hambaryan, T. Maccacaro, B. Mathiesen, R. McMahon, L. Michel, C. Motch, J. P. Osborne, M. Page, M. W. Pakull, W. Pietsch, R. Saxton, A. Schwope, P. Severgnini, M. Simpson, G. Sironi, G. Stewart, I. M. Stewart, A.-M. Stobbart, J. Tedds, R. Warwick, N. Webb, R. West, D. Worrall, and W. Yuan. The XMM-Newton serendipitous survey. V. The Second XMM-Newton serendipitous source catalogue. *Astronomy & Astrophysics*, 493:339–373, January 2009. doi: 10.1051/0004-6361:200810534.

M. C. Weisskopf, H. D. Tananbaum, L. P. Van Speybroeck, and S. L. O'Dell. Chandra X-ray Observatory (CXO): overview. In J. E. Truemper and B. Aschenbach, editors, *X-Ray Optics, Instruments, and Missions III*, volume 4012 of *Society of Photo-Optical Instrumentation Engineers (SPIE) Conference Series*, pages 2–16, July 2000.

D. R. Weisz, A. E. Dolphin, E. D. Skillman, J. Holtzman, K. M. Gilbert, J. J. Dalcanton, and B. F. Williams. The Star Formation Histories of Local Group Dwarf Galaxies. I. Hubble Space Telescope/Wide Field Planetary Camera 2 Observations. *The Astrophysical Journal*, 789:147, July 2014. doi: 10.1088/0004-637X/789/2/147.

S. D. M. White and M. J. Rees. Core condensation in heavy halos - A two-stage theory for galaxy formation and clustering. *Monthly Notices of the Royal Astronomical Society*, 183:341–358, May 1978.

M. I. Wilkinson, J. T. Kleyna, N. W. Evans, G. F. Gilmore, M. J. Irwin, and E. K. Grebel. Kinematically Cold Populations at Large Radii in the Draco and Ursa Minor Dwarf Spheroidal Galaxies. *The Astrophysical Journal Letters*, 611: L21–L24, August 2004. doi: 10.1086/423619.

R. Willingale, R. L. C. Starling, A. P. Beardmore, N. R. Tanvir, and P. T. O'Brien. Calibration of X-ray absorption in our Galaxy. *Monthly Notices of the Royal Astronomical Society*, 431:394–404, May 2013. doi: 10.1093/mnras/stt175.

C. Winkler, T. J.-L. Courvoisier, G. Di Cocco, N. Gehrels, A. Giménez, S. Grebenev, W. Hermsen, J. M. Mas-Hesse, F. Lebrun, N. Lund, G. G. C. Palumbo, J. Paul, J.-P. Roques, H. Schnopper, V. Schönfelder, R. Sunyaev, B. Teegarden, P. Ubertini, G. Vedrenne, and A. J. Dean. The INTEGRAL mission. *Astronomy & Astrophysics*, 411:L1–L6, November 2003. doi: 10.1051/0004-6361:20031288.

H. Wolter. Spiegelsysteme streifenden Einfalls als abbildende Optiken für Röntgenstrahlen. *Annalen der Physik*, 445:94–114, 1952a. doi: 10.1002/andp.19524450108.

H. Wolter. Verallgemeinerte Schwarzschildsche Spiegelsysteme streifender Reflexion als Optiken für Röntgenstrahlen. *Annalen der Physik*, 445:286–295, 1952b. doi: 10.1002/andp.19524450410.

S. E. Woosley. Gamma-ray bursts from stellar mass accretion disks around black holes. *The Astrophysical Journal*, 405:273–277, March 1993. doi: 10.1086/172359.

L. M. Young, E. D. Skillman, D. R. Weisz, and A. E. Dolphin. The Aptly Named Phoenix Dwarf Galaxy. *The Astrophysical Journal*, 659:331–338, April 2007. doi: 10.1086/512153.

C. Zhu, G. Lü, Z. Wang, and N. Wang. Donors of Persistent Neutron-Star Low-Mass X-Ray Binaries. *Publications of the Astronomical Society of the Pacific*, 124:195–203, March 2012. doi: 10.1086/664833.

D. B. Zucker, V. Belokurov, N. W. Evans, J. T. Kleyna, M. J. Irwin, M. I. Wilkinson, M. Fellhauer, D. M. Bramich, G. Gilmore, H. J. Newberg, B. Yanny, J. A. Smith, P. C. Hewett, E. F. Bell, H.-W. Rix, O. Y. Gnedin, S. Vidrih, R. F. G. Wyse, B. Willman, E. K. Grebel, D. P. Schneider, T. C. Beers, A. Y. Kniazev, J. C. Barentine, H. Brewington, J. Brinkmann, M. Harvanek, S. J. Kleinman, J. Krzesinski, D. Long, A. Nitta, and S. A. Snedden. A Curious Milky Way Satellite in Ursa Major. *The Astrophysical Journal Letters*, 650:L41–L44, October 2006. doi: 10.1086/508628.

List of Figures

List of Tables

Acronyms

AGNs active galactic nuclei
BAT Burst alert telescope
BeXBs Be/X-ray binaries
BH black hole
CAL calibration access layer
CCDs charged coupled devices
CVs cataclysmic variables
Dec Declination
dSphs spheroidal dwarf galaxies
ECF energy conversion factor
ESA European Space Agency
FOV field of view
FPA focal plane assembly
GRB Gamma-ray burst
GTI good time intervals
HMXBs High mass X-ray binaries
HR Hertzsprung-Russell
HST Hubble space telescope
INT Isaac Newton telescope
IMBHs intermediate mass black holes
LMXBs low mass X-ray binaries
MegaCam new Canada-France-Hawaii telescope wide-field imaging Camera
ML maximum likelihood
MSP mirror support platform
NVSS 1.4GHz NRAO VLA sky survey
NS neutron star
OM optical monitor
PSF Point-Spread function
RA Right Ascension
RGA reflection grating array
RGS reflection grating spectrometer
ROSAT ROentgen SATellite
SAS science analysis system
SDSS9 Sloan digital sky survey

SGXBs super-giant X-ray binaries
SNR supernova remnant
2MASS two micron all sky survey
XLF X-ray luminosity function
XRBs X-ray binary systems
XRT X-ray telescope
WISE wide-field infrared survey explorer
EPICs European Photon Imaging Cameras
ESA European Space Agency
FOV field of view
GRB gamma-ray burst
PSF point spread function
RGS Reflection Grating Spectrometer
SAS Scientific Analysis System
GALEX Galaxy Evolution Explorer

Acknolegment

There are many, who scientifically and emotionally helped me to conduct this research and to write my Ph.D dissertation:
First of all, I wish to express my sincerest gratitude to my supervisor, Dr. Manami Sasaki, for her endless support, understanding, and patience. Her guidance and immense knowledge helped me throughout all stages of the research and writing. By doing research under her supervision, I learned what it means to be committed to a project and how creativity opens up new ways for looking at the same project from several viewpoints and brings out novel ideas.
Also, I would like to express my deepest regards and sincerest thanks to Prof. Andrea Santangelo. Besides appreciating his support throughout the project, I am so grateful to him for providing a motivating and energetic scientific atmosphere for doing researches and precursor projects.
My sincere thanks also go to Dr. Lorenzo Ducci for his cooperation in this project, his knowledgeable comments, meticulous attention and support during the work. I learned so much from working with him.
I also place on record, my sense of gratitude to Dr. Chris Tenzer, for his prompt helps, attentions and explanations in several scientific and official issues.
It is impossible to forget the memories of two years, in the same office with Gabriella Warth. This opportunity gave me the chance to experience kindness and sympathy in its sincerest form. Thanks Gabi for every thing! I also have to thank my little sister Eva. My days simply got shiny, any time we were together! A special thank goes to my great friend Nicole Reindl, for those nice evenings, when we cooked together and talked about the details of works, life, white dwarfs, and dwarf galaxies!
I want to portray the picture which will always remain in my mind. This picture comes with a background of IAAT building, its yellow ocher colour, spectacular location in a meadow over Sand hill, surrounded by trees, with a view of old Tübingen from balconies. I thank ALL friends and colleagues for making this picture bright and alive. Over more than three years, beside talks about physics and astrophysics, which has always encouraged me to know more, I would like to specifically appreciate friends with whom I spent more time... I always keep in my mind: Antonio. B, with his humility and accuracy; Alejandro. G, with his cleverness; Alejandro. M, with his honesty; Angela. H, with her hospitality and also attention to environmental problems; Beppe. D, with his sincerity and calmness; Cornelia. H, with her politeness and power in organising; Daniel. G, with his brotherly supportive behaviour; Emma. W, with her kindness and serenity; Jörg. B, with his responsible and gentle character; Laura. R, with her happily motivating mood; Ruth. G, with her cordiality and passion to horses; and Thomas. M, with his open mind and decent personality.
I also place on record, my sense of gratitude to my wonderful flat mates, who has made my days memorable in lovely Neckarhalde, all my dears: Laura and Erik, Esteban, Giuseppe, Nicolas and Jana, Charlotte, Robert, Eva, Felix, and of course Stefilein and her lovely family.

Last but not the least, I would like to thank my family, my parents, my brother and sister for supporting me spiritually throughout my life and my studies in Germany.

عزیزترین هایم مامان، بابا، سینا و سروش! از همین دور ممنون به خاطر همه چیز!

This research was founded by the Deutsche Forschungsgemeinschaft, through the Emmy Noether Research Grant SA 2131/1-1. L.D. Based on observations obtained with XMM-Newton, an ESA science mission with instruments and contributions directly funded by ESA Member States and NASA. This research has made use of the SIMBAD and VIZIER database, operated at CDS, Strasbourg, France, and of the NASA/IPAC Extragalactic Database (NED), which is operated by the Jet Propulsion Laboratory, California Institute of Technology, under contract with the National Aeronautics and Space Administration. This publication makes use of data products from the Wide-field Infrared Survey Explorer, which is a joint project of the University of California, Los Angeles, and the Jet Propulsion Laboratory/California Institute of Technology, funded by the National Aeronautics and Space Administration. This thesis has made use of data products from the Two Micron All Sky Survey, which is a joint project of the University of Massachusetts and the Infrared Processing and Analysis Center, funded by the National Aeronautics and Space Administration and the National Science Foundation. Funding for SDSS and SDSS-III has been provided by the Alfred P. Sloan Foundation, the Participating Institutions, the National Science Foundation, and the U.S. Department of Energy Office of Science. The SDSS-III web site is http://www.sdss3.org/. SDSS-III is managed by the Astrophysical Research Consortium for the Participating Institutions of the SDSS-III Collaboration including the University of Arizona, the Brazilian Participation Group, Brookhaven National Laboratory, University of Cambridge, University of Florida, the French Participation Group, the German Participation Group, the Instituto de Astrofisica de Canarias, the Michigan State/Notre Dame/JINA Participation Group, Johns Hopkins University, Lawrence Berkeley National Laboratory, Max Planck Institute for Astrophysics, New Mexico State University, New York University, Ohio State University, Pennsylvania State University, University of Portsmouth, Princeton University, the Spanish Participation Group, University of Tokyo, University of Utah, Vanderbilt University, University of Virginia, University of Washington, and Yale University. This research has made use of data obtained from the Chandra Source Catalogue, provided by the Chandra X-ray Centre (CXC) as part of the Chandra Data Archive. This research has made use of SAOImage DS9, developed by Smithsonian Astrophysical Observatory. The National Radio Astronomy Observatory is a facility of the National Science Foundation operated under cooperative agreement by Associated Universities, Inc.